

**EXTENDED HIGGS SECTORS, VACUUM STABILITY
AND RELATED ISSUES**

By
NABARUN CHAKRABARTY
PHYS08201104007

Harish-Chandra Research Institute, Allahabad

*A thesis submitted to the
Board of Studies in Physical Sciences
In partial fulfillment of requirements
for the Degree of*
DOCTOR OF PHILOSOPHY
of
HOMI BHABHA NATIONAL INSTITUTE

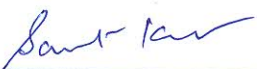
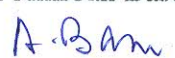


August, 2017

Homi Bhabha National Institute¹

Recommendations of the Viva Voce Committee

As members of the Viva Voce Committee, we certify that we have read the dissertation prepared by **Nabarun Chakrabarty** entitled “**Extended Higgs sectors, vacuum stability and related issues**” and recommend that it may be accepted as fulfilling the thesis requirement for the award of Degree of Doctor of Philosophy.

Chairman - Prof. Raj Gandhi		Date: 7/8/17
Guide / Convener - Prof. B. Mukhopadhyaya		Date: 7/8/17
Co-guide -		Date:
Examiner – Prof. B. Ananthanarayan		Date: 7/8/2017
Member 1- Prof. Santosh Kumar Rai		Date: 7/8/17
Member 2- Prof. Anirban Basu		Date: 7/8/17
Member 3- Prof. Pinaki Majumdar		Date: 7/8/17

Final approval and acceptance of this thesis is contingent upon the candidate's submission of the final copies of the thesis to HBNI.

I/We hereby certify that I/we have read this thesis prepared under my/our direction and recommend that it may be accepted as fulfilling the thesis requirement.

Date: 07/08/2017

Place: Allahabad


Prof. B. Mukhopadhyaya

¹ This page is to be included only for final submission after successful completion of viva voce.

STATEMENT BY AUTHOR

This dissertation has been submitted in partial fulfillment of requirements for an advanced degree at Homi Bhabha National Institute (HBNI) and is deposited in the Library to be made available to borrowers under rules of the HBNI.

Brief quotations from this dissertation are allowable without special permission, provided that accurate acknowledgement of source is made. Requests for permission for extended quotation from or reproduction of this manuscript in whole or in part may be granted by the Competent Authority of HBNI when in his or her judgment the proposed use of the material is in the interests of scholarship. In all other instances, however, permission must be obtained from the author.

Nabarun Chakrabarty
Nabarun Chakrabarty

DECLARATION

I, hereby declare that the investigation presented in the thesis has been carried out by me. The work is original and has not been submitted earlier as a whole or in part for a degree / diploma at this or any other Institution / University.

Nabarun Chakrabarty
Nabarun Chakrabarty

List of publications arising from the thesis

Journal

1. "High-scale validity of a two-Higgs doublet scenario: a study including LHC data", Nabarun Chakrabarty, Ujjal Kumar Dey, Biswarup Mukhopadhyaya, *Journal of High Energy Physics*, **2014**, *12*, 166.
2. "Dark matter, neutrino masses and high scale validity of an inert Higgs doublet model", Nabarun Chakrabarty, Dilip Kumar Ghosh, Biswarup Mukhopadhyaya, Ipsita Saha, *Physical Review D*, **2015**, *92*, 015002.
3. "High-scale validity of a model with Three-Higgs-doublets, Nabarun Chakrabarty, *Physical Review D*, **2016**, *93*, 075025.
4. "High-scale validity of a two Higgs doublet scenario: metastability included", Nabarun Chakrabarty, Biswarup Mukhopadhyaya, *The European Physical Journal C*, **2017**, *77*, 153.
5. "High-scale validity of a two Higgs doublet scenario: predicting collider signals", Nabarun Chakrabarty, Biswarup Mukhopadhyaya, accepted for publication in *Physical Review D*


Nabarun Chakrabarty

Other publications

Journal

1. "Radiative Return for Heavy Higgs Boson at a Muon Collider",
Nabarun Chakrabarty, Tao Han, Zhen Liu, Biswarup Mukhopadhyaya,
Physical Review D, **2015**, *91*, 015008.
2. "Same-sign trileptons as a signal of sneutrino lightest supersymmetric particle",
Arindam Chatterjee, Nabarun Chakrabarty, Biswarup Mukhopadhyaya,
Physics Letters B, **2016**, *754*, 14-17.
3. "Phenomenological signatures of additional scalar bosons at the LHC",
Stefan von Buddenbrock, Nabarun Chakrabarty, Alan S. Cornell, Deepak Kar,
Mukesh Kumar, Tanumoy Mandal, Bruce Mellado, Biswarup Mukhopadhyaya,
Robert G. Reed, Xifeng Ruan,
The European Physical Journal C, **2016**, *76*, 580.
4. "Diphoton signal via Chern-Simons interaction in a warped geometry scenario",
Nabarun Chakrabarty, Biswarup Mukhopadhyaya, Soumitra Sengupta
Physical Review D, **2017**, *95*, 015007.

Communicated

1. "A revisit to scalar dark matter with radiative corrections",
Shankha Banerjee, Nabarun Chakrabarty, arXiv:1612.01973


Nabarun Chakrabarty

Dedicated to

Dada

My dear grandfather, who, I feel, is always watching over me.

ACKNOWLEDGEMENTS

It saddens me to embark upon writing an acknowledgement in the thesis, since, this very task signals, in a way, the end of my stay in HRI. At the risk of forgetting someone's name, I shall try my best to thank all whom I interacted with in this institute.

First and foremost, I convey my gratitude towards my supervisor Prof. Biswarup Mukhopadhyaya for his superb guidance throughout my doctoral tenure. His encouraging stance has always helped me carry forward whenever I got stuck. I have always looked up to his deep physics insight, and, to his uncanny ability of identifying a relevant problem. I am also deeply indebted to Prof. Rajesh Gopakumar, Prof. Ashoke Sen, Prof. Raj Gandhi, Prof. Andreas Nyffeler, Prof. V. Ravindran, Prof. G.V. Pai, Prof. Anirban Basu, Prof. S. Naik and Prof. Ujjwal Sen for their excellent teaching that indeed served as a groundwork to start research. I take this opportunity to earnestly thank my collaborators Prof. Tao Han, Prof. Dilip Kumar Ghosh, Prof. Bruce Mellado, Prof. Soumitra Sengupta, Dr. Ujjal Kumar Dey, Dr. Ipsita Saha, Dr. Tanumoy Mondal and Dr. Shankha Banerjee, from whom I have gained academically in various undefined ways.

I express my gratefulness to the Regional Centre for Accelerator- based Particle Physics (RECAPP) for providing computational resources and much needed travel support on several occasions.

HRI has been a *home away from home* for me for the last six years. The reminiscences of my stay in HRI are numerous enough to fill up a separate thesis by themselves! I shall forever remain indebted to my dear friends for all the wonderful moments they have gifted me. I was fortunate to have befriended Dibya, Sauri, Shankha-da and Arijit who not only were wonderful friends, but also stood by my side whenever needed. I express my heartfelt good wishes to Aritra, Samrat, Saikat, Aditya, Ashis, Uttam, Debasis, Asutosh, Udit, Krashna Mohan, Soumyadeep, Subhronel, Siddharth, Kasinath, Jyotiranjana, Titas, Arif, Juhi, Sudipto, Baby(Debasis), Satadal, Ritabrata, Arpan, Avirup, Nirnoy, Swapnamay, Masud, Soumyarup, Subhadeep-da, Tanumoy-da, Animesh-da, Anirban (Biswas)-da, Atri-da, Satya-da, Bhuru-da, Ushoshi-di, Avinanda-di, Niyogi-da, Jonthu(Arunabha)-da, Bhatta-da, Anirban (Basu)-da, Rambha(Saurabh)-da, Tarat-da, Paromita-di and Hochi(Ujjal)-da. I can safely say that each one of them has helped shape me up to what I am today. Chats, eat-outs, movie-watching as well as occasional games of cricket and table-tennis were indispensable parts of my stay in HRI, whose memories I shall forever cherish. I also acknowledge the

support received from the administrative and technical sections of HRI, in particular from Seema-ji, Archana-ji, Chandan and Rajiv.

I acknowledge Indrani for her continuous support throughout. I also must thank her for a patient proof-reading of this manuscript. Further, it was the love and care of my parents that strengthened me to tread this (*sometimes difficult*) path.

Contents

SYNOPSIS	1
LIST OF FIGURES	4
LIST OF TABLES	10
1 Introduction	13
1.1 What is the Standard Model?	13
1.2 Particle content of the SM	14
1.2.1 Fermionic fields	14
1.2.2 Gauge fields	16
1.3 Towards the SM Lagrangian	17
1.4 Generation of mass: The Higgs mechanism	18
1.5 The SM Higgs and its interactions	20
1.6 Need for physics beyond the SM	21
1.6.1 Experimental evidences	21
1.6.2 Theoretical shortcomings	22
1.7 Extended Higgs sectors	24
1.7.1 $SU(2)$ singlet(s)	24
1.7.2 $SU(2)$ doublet(s)	24
1.7.3 $SU(2)$ triplet(s)	28
2 Vacuum stability and related issues: The role of the Higgs boson mass	30
2.1 Vacuum stability in the SM	30
2.1.1 Tunnelling probability	34
2.2 Bound from triviality	36

2.3	Bound from unitarity	37
2.4	Need for an extended Higgs sector	40
3	High-scale validity of a two-Higgs-doublet scenario: a study including LHC data	41
3.1	Introduction	41
3.2	The two-Higgs-doublet scenario and the scalar potential: basic features . . .	44
3.3	Theoretical and experimental constraints	46
3.3.1	Perturbativity, unitarity and vacuum stability	47
3.3.2	Higgs mass constraints	48
3.3.3	Oblique parameter constraints	48
3.3.4	Collider constraints	49
3.4	Results with exact discrete symmetry	50
3.5	Results with softly broken discrete symmetry	55
3.6	Results with quartic terms breaking the discrete symmetry	63
3.7	Summary and conclusions	67
4	High-scale validity of a two-Higgs-doublet scenario: metastability included	69
4.1	Introduction	69
4.2	Model features.	71
4.3	The computation of tunnelling probability.	71
4.4	A metastable vacuum and the 2HDM parameter space.	75
4.4.1	Analysis strategy.	75
4.5	Results and discussions.	76
4.6	Summary and conclusions.	85
5	High-scale validity of a two Higgs doublet scenario: predicting collider signals	88
5.1	Introduction	88
5.2	2HDM and high scale validity.	89
5.2.1	Perturbativity, unitarity and vacuum stability	90
5.3	Type-I 2HDM: Allowed parameter space for stable vacuum	92
5.4	Signals at the LHC: Types I and II.	94
5.4.1	$pp \rightarrow H \rightarrow ZZ \rightarrow 4l$	96
5.4.2	$pp \rightarrow A \rightarrow hZ \rightarrow l^+l^-b\bar{b}$	100

5.5	Prospects at other colliders	105
5.5.1	$\mu^+\mu^-$ collisions and radiative return	106
5.6	Summary and conclusions.	109
6	Particle dark matter: An introduction	111
6.1	What is dark matter?	111
6.2	Some evidences for dark matter	112
6.3	Some properties of dark matter	114
6.4	Types of dark matter	115
6.4.1	From thermal history	115
6.4.2	From particle content	115
6.4.3	From mass and speed	116
6.5	Some popular models for dark matter	116
6.6	Calculation of relic abundance	118
6.7	Search for dark matter	120
6.7.1	Direct search	121
6.7.2	Indirect search	122
6.7.3	Collider search	124
6.8	Summary	124
7	Dark matter, neutrino masses and high scale validity of an inert Higgs doublet model	125
7.1	Introduction	125
7.2	The Radiative Neutrino Mass Model with an inert doublet	127
7.3	Constraints from perturbativity, unitarity, vacuum stability and collider data	129
7.3.1	Vacuum stability	129
7.3.2	Perturbativity	130
7.3.3	Unitarity	130
7.3.4	Collider data	130
7.4	Dark Matter Issues	131
7.4.1	Case-A: Low mass DM ($50 \text{ GeV} < M_H < 90 \text{ GeV}$)	132
7.4.2	Case-B: High mass DM ($M_H > 500 \text{ GeV}$)	132
7.5	Analysis strategy	133
7.6	Numerical results	134
7.6.1	Low mass DM region	134

7.6.2	High mass DM region	140
7.7	Summary and Conclusions	144
8	High-scale validity of a model with Three-Higgs-doublets	148
8.1	Introduction	148
8.2	The S_3 symmetric three-Higgs-doublet model (S_3 HDM) in brief.	150
8.2.1	Scalar sector.	150
8.2.2	Yukawa Sector.	154
8.3	Constraints imposed.	155
8.3.1	Theoretical constraints.	155
8.3.2	Oblique parameters.	157
8.3.3	Higgs Signal-strengths	157
8.3.4	Dark matter relic density and direct detection	158
8.3.5	Evolution under renormalisation group.	159
8.4	Impact of the constraints on the parameter space.	159
8.4.1	Scenario A: $v_1 = \sqrt{3}v_2$	159
8.4.2	Scenario B: $v_1 = v_2 = 0, v_3 = 246$ GeV.	162
8.5	Conclusions and future work	173
9	Summary and conclusions	175
	Appendices	178
A	Type-I and Type-II 2HDM	179
A.1	Renormalisation group (RG) equations for Type-II 2HDM	179
A.2	Renormalisation group (RG) equations for Type-I 2HDM	180
A.3	Unitarity bounds	181
B	The inert doublet model with right handed neutrinos	184
B.1	One-loop Renormalisation group (RG) equations	184
C	S_3HDM: RG equations and oblique parameters	186
C.1	Renormalisation group (RG) equations	186
C.2	Oblique parameters	187
C.3	$h \rightarrow \gamma\gamma$ decay width	188

SYNOPSIS

With the observation of a scalar resonance around 125 GeV at the LHC, and hence its identification with a Higgs boson, the particle spectrum of the Standard Model (SM) appears to be complete. However, issues ranging from the existence of Dark Matter (DM) to the pattern of neutrino mass continue to suggest physics beyond the SM. While the quest for such new physics remains on, a rather pertinent question to ask is whether the SM by itself can ensure vacuum stability at scales above that of electroweak symmetry breaking (EWSB). This is because the Higgs quartic coupling evolving via SM interactions alone tends to turn negative in between the Electroweak (EW) and Planck scales, thereby making the scalar potential unbounded from below. This exact location of this instability scale crucially depends on the pole masses of the top quark and the Higgs. However, the EW vacuum can be stabilised till the Planck scale even for a top-mass near the upper edge of its allowed band, by introducing additional bosonic degrees of freedom. In my thesis, I have explored this possibility through several Higgs-sector extensions. I summarise the work carried out in the following sections.

In one work, we have investigated the high-scale behaviour of a 2HDM. The results were illustrated in the context of a Type-II scenario. We have used the theoretical constraints of perturbativity, unitarity and vacuum stability to constrain the parameter space of the model. The relatively less stringent constraints from oblique parameters, and also the LHC constraints on the signal strength in each decay channel of a Higgs around 125 GeV have also been taken into account. We found that a 2HDM with a discrete \mathbb{Z}_2 symmetry (thereby forbidding some cross-terms in the two doublets in the potential) cannot be valid beyond 10 TeV, since otherwise the requirement of keeping one neutral scalar mass around 125 GeV cannot be met. With the discrete symmetry broken, on the other hand, it is possible to fulfill all the constraints over a much larger region of the parameter space. Thus the theory with a 2HDM can distinctly be valid up to energies as high as 10^{16} GeV or even the Planck scale, without the intervention of any additional physics. This feature holds irrespectively of the uncertainty in the measured value of the top quark mass, which is in contrast to what is expected in the standard model with a single Higgs doublet. In addition, high-scale validity of this scenario is not affected by the uncertainty in the strong coupling $\alpha_s(M_Z)$. The effect of a CP -violating phase in the potential is also considered, it is found that one can find regions in the parameter space valid up to high scales for at least one illustrative value (viz. $\frac{\pi}{4}$). The allowed regions of the parameter space, in terms of the various quartic

couplings as well as the scalar mass eigenvalues were presented by us in detail, in the light of theoretical as well as collider bounds. The inclusion of \mathbb{Z}_2 -breaking quartic couplings, too, is found to retain the high-scale validity of the theory over a large region. Though the study is based on a Type II 2HDM, many of the results obtained here are expected to hold for a more general 2HDM as well. A situation where some departure can take place is, for example one where the Yukawa coupling of the bottom quark becomes comparable to, or more than, that of the top quark. One possibility to explore in such a case is to look for those regions where the large number of quartic couplings can rescue the scenario from an unstable vacuum. The results presented here are based on one-loop RG equations, in consonance with most similar studies in the context of 2HDM. It should also be noted that we call those regions in the parameter space as allowed, where the vacuum is strictly stable. The inclusion of a metastable vacuum, with lifetime greater than the age of the universe, will lead to larger allowed regions. On the whole, our conclusion is that it is possible to validate a 2HDM till scales as high as the Planck mass without any additional physics. While the issue of naturalness remains unaddressed in this statement, it is interesting to see that no current experimental measurement or theoretical restriction can affect high-scale validity, which is not the case for the single-doublet scenario. In another work, we have looked at the possibility of a metastable vacuum in a Type-II 2HDM. Once the parameters occurring in the scalar potential are subjected to RG evolution, additional global minima may indeed occur at high scales. In a 2HDM, the strength of the fermionic contribution is controlled by not only the top quark pole mass, but also by the ratio of vacuum expectation values of the two doublets, which is named $\tan\beta$. The t -quark Yukawa coupling can get enhanced with respect to the SM. This can render the electroweak vacuum unstable or metastable. This is found to happen in the direction of the scalar field h_2 , because the quartic coupling λ_2 can be driven to negative values by the top-Yukawa coupling, at high scales. Based on the results of this work, one would always expect a metastable model point in the vicinity of a point allowing for absolute stability. However, $\tan\beta$ picks up a lower bound from the requirement of metastability, which is tightened when one demands absolute stability of the EW vacuum. The sensitivity of the results to the top pole mass has also been emphasised. In an ongoing study, we are exploring the observability at the present and future colliders, of a 2HDM that ensures a stable vacuum and a perturbative theory till the Planck scale. As highlighted earlier, stringent constraints are put on the 2HDM parameter space in the process. Particularly, the couplings of the non-standard scalars to other bosonic states become small. In addition the mass spectrum of the non-standard scalar

bosons becomes quasi-degenerate. These constraints limit the observability of such a 2HDM at colliders. In this study, we aim to study in detail the interplay between high-scale validity and the discernibility of the scenario at the LHC and at a future muon collider. In the LHC, signatures of the the CP -even boson H and CP -odd boson A are studied through their decays into the $4l$ and $l^+l^-b\bar{b}$ channel respectively. The search turns challenging given the suppressed values of the interactions of H and A with the 125 GeV scalar h and the SM gauge bosons. An analysis at the 14 TeV LHC, including detector effects, reveals that H and A of masses around 500 GeV can be simultaneously observed with 3σ confidence or greater when the integrated luminosity is 3000 fb^{-1} . The observability improves upon de-escalating the cutoff scale. Radiative return at the muon collider yields sizeable production rates of H or A . We have studied the observation their prospects through their subsequent decay to the $b\bar{b}$ final state. The possibility to identify the CP of the decaying boson by studying their decays into separate final states, however, remains still open. In another work, we have examined the high-scale validity of a scenario that (a) offers a scalar dark matter, (b) radiatively generates Majorana masses for neutrinos, and (c) is responsible for leptogenesis. For this, we extended the SM fields with one additional inert Higgs doublet field (ϕ_2) and three right handed neutrinos (N_i). These new particles are odd under a discrete \mathbb{Z}_2 symmetry, while all the SM particles are even. Because of this discrete symmetry, ϕ_2 does not acquire any vacuum expectation value (VEV) and has no tree-level couplings to fermions. In this scenario, one has five physical scalars (h, H, A, H^\pm), where, h is denoted as the SM like Higgs boson with a mass of 125 GeV. The lightest state between H and A is the dark matter candidate due to built in \mathbb{Z}_2 symmetry. In our analysis we have assumed H to be the dark matter candidate. The neutrino masses and mixing angles are determined in terms of Yukawa couplings, new Higgs particle masses (M_H, M_A) and three heavy Majorana masses ($M_{1,2,3}$). In our numerical analysis we have assumed M_1 is mass of the lightest state and considered two values, namely, $M_1 = M = 110 \text{ TeV}$ and 10^9 TeV . These two mass scales are consistent with leptogenesis. For simplicity, in our analysis, we have considered only one diagonal Yukawa coupling and to determine the value of this coupling, we have scanned over M_H and M_A for a given value of M , by keeping $M_\nu \simeq \text{O}(0.1 \text{ eV})$. An analysis combining all the above physics issues was carried out. It was found that it is indeed possible to find a parameter space that generates an 0.1 eV neutrino mass, keeps the dark matter relic density and direct detection cross sections within their respective experimental limits, and, ensures a stable EW vacuum and a perturbative theory till the Planck scale, simultaneously. One more work in similar lines has been completed, which looks into the high-scale behaviour of

the scalar potential of a three-Higgs-doublet model (3HDM). In that study, we considered a three-Higgs doublet scenario, invariant under the discrete group S_3 . We chose two particular alignments of vacuum expectation values for our study, out of a set of several such possible ones. All three doublets receive non-zero vacuum expectation values in the first case, and in the second case, two of the doublets remain without VEV. The constraints on the parameter space at low energy, including the measured value of the Higgs mass and the signal strengths, oblique corrections and also measurements of relic density and direct detection rates were juxtaposed with the conditions of vacuum stability, perturbativity and unitarity at various scales. We found that the scenario with three non-zero VEVs is not valid beyond 10^7 GeV, assuming no additional physics participates at the intermediate scales. On the contrary, the scenario with only one non-zero VEV can be a successful model for cold dark matter phenomenology, which also turns out to be valid up to the Planck scale at the same time. Stringent restrictions were obtained on the model parameter space in each case. Thus, the S_3 symmetric scalar sector was deemed to be an ultraviolet complete theory.

List of Figures

1.1	The elementary particles forming the Standard Model.	14
3.1	Theoretically allowed parameter spaces at $\Lambda_{UV} = 1$ TeV, $\tan\beta = 2$ and $m_{12} = 0$ GeV for $M_t = 173.1$ GeV. The region in the figure on the left is allowed concomitantly with that in the figure on the right. Note that the allowed region shown will expand further if $\tan\beta$ too is allowed to vary. . . .	52
3.2	Region allowed in the $m_{H^\pm-\alpha}$ and m_H-m_A planes, by the theoretical constraints and the recent Higgs data. In each case, the chosen benchmark values of the two other parameters are given in the legend.	53
3.3	RG running of λ_i , the LQT eigenvalues and the stability conditions with the energy scale for $\tan\beta = 2$ and $m_{12} = 0$. The horizontal lines in the leftmost figure (Fig.3.3a) denote the perturbative limit and unitarity limit in the second figure (Fig.3.3b). Also a_+ , b_+ and c_+ in the second figure (Fig.3.3b) are the LQT eigenvalues explained in Appendix A.3 . In the rightmost figure (Fig.3.3c), vsc3 and vsc4 represent the two stability conditions that are defined in eqns.(3.3.1a)-(3.3.1e).	54
3.4	The allowed parameter spaces in the soft \mathbb{Z}_2 breaking case for $\Lambda_{UV} = 10^{11}$ (green), 10^{16} (grey) and 10^{19} GeV (red). The $\tan\beta$ and m_{12} values are shown in the plots. The shaded region (blue) in the top left figure denotes the exclusion coming from flavour constraints.	56
3.5	A comparison of the allowed parameter spaces at $\Lambda_{UV} = 10^{19}$ GeV, $\tan\beta = 2$ and $m_{12} = 1000$ GeV for two values of M_t , in the soft \mathbb{Z}_2 breaking case. . . .	57
3.6	Regions in the $m_{H^\pm-\alpha}$ plane allowed by the Higgs data in the soft \mathbb{Z}_2 breaking case.	58
3.7	RG running of λ_i , the LQT eigenvalues and the stability conditions with the energy scale for $\tan\beta = 2$ and $m_{12} = 1000$ GeV in the soft \mathbb{Z}_2 breaking case.	59
3.8	Running of λ_2 for three different values for $\alpha_s(M_Z)$ in the soft \mathbb{Z}_2 breaking case.	60

3.9	The allowed regions in mass plane as a function of Λ_{UV} in the soft \mathbb{Z}_2 breaking case. The upper and lower two plots correspond to $\delta = \frac{\pi}{4}$ and $\delta = 0$ respectively.	62
3.10	The allowed parameter spaces for $\Lambda_{UV} = 10^{11}$ (green), 10^{16} (grey) and 10^{19} GeV (red), in the $\lambda_6, \lambda_7 \neq 0$ case. The $\tan \beta$ and m_{12} values are shown in the plots.	64
3.11	Results for $\Lambda_{UV} = 1$ TeV, in the $\lambda_6, \lambda_7 \neq 0$ case. The regions in red denote the part of the parameter space allowed by the Higgs data.	65
3.12	RG running of λ_i and the stability conditions with the energy scale for $\tan \beta = 2$ and $m_{12} = 1000$ GeV, in the $\lambda_6, \lambda_7 \neq 0$ case.	66
4.1	RG evolution of λ_2^{eff} for the benchmarks listed in Table 4.1, for more than one value of M_t . The colour coding is explained in the legends.	77
4.2	Behaviour of $V_{\text{eff}}(h_2)$ in BP6 for $M_t = 173$ GeV.	79
4.3	Distribution of points in the parameter space perturbative till 10^{16} GeV that lead to an either stable or metastable EW vacuum. The upper (lower) plots correspond to $M_t = 171$ (175) GeV. The colour coding is explained in the legends. 2HDM II refers to a Type-II 2HDM.	81
4.4	Distribution of points in the parameter space perturbative till 10^{19} GeV that lead to an either stable or metastable EW vacuum. The upper (lower) plots correspond to $M_t = 171$ (175) GeV. The colour coding is explained in the legends. 2HDM II refers to a Type-II 2HDM.	83
4.5	Distribution of parameter space points in the $m_H - m_A$ ($m_H - m_{H^+}$) plane as shown in the left (right) plots, for $M_t = 175$ GeV. The upper (lower) plots correspond to perturbativity till 10^{16} (10^{19}) GeV.	84
4.6	Distribution of points in the parameter space in the $m_H - \tan\beta$ plane that are perturbative till 10^{19} GeV and lead to an either stable or metastable EW vacuum. The mass splitting amongst the non-standard scalars is forced to stay within 2 GeV during these scans. The upper (lower) plots correspond to $M_t = 171$ (175) GeV. The colour coding is explained in the legends. 2HDM II refers to a Type-II 2HDM.	86

5.1	Distribution of the parameter points valid till Λ in the $m_H - m_A$ (left) and $m_H - m_{H^+}$ (right) planes for the Type-I 2HDM. The colour coding can be read from the legends. We fix $\tan\beta = 2.5$ as a benchmark. The upper(lower) plots correspond to $\lambda_6 = \lambda_7 = 0$ ($\lambda_6, \lambda_7 \neq 0$). We have varied λ_6, λ_7 in the interval $[-1,1]$ for the lower plots.	93
5.2	The parameter space in the $\tan\beta$ vs. $c_{\beta-\alpha}$ plane for $m_H = 500$ GeV and $m_A = 501$ GeV that allows for validity till 10^{11} GeV(red), 10^{14} GeV(green) and 10^{19} GeV(black). The region inside the blue curve corresponds to a signal significance greater than or equal to 3σ . The upper and lower plots are for $\lambda_6 = \lambda_7 = 0$ and $\lambda_6, \lambda_7 \neq 0$ respectively.	99
5.3	The parameter space in the $\tan\beta$ vs. $c_{\beta-\alpha}$ plane for $m_H = 550$ GeV and $m_A = 551$ GeV that allows for validity till 10^{11} GeV(red), 10^{14} GeV(green) and 10^{19} GeV(black). The region inside the blue curve corresponds to a signal significance greater than or equal to 3σ . The upper and lower plots are for $\lambda_6 = \lambda_7 = 0$ and $\lambda_6, \lambda_7 \neq 0$ respectively.	101
5.4	The parameter space in the $\tan\beta$ vs. $c_{\beta-\alpha}$ plane for $m_H = 500$ GeV and $m_A = 501$ GeV that allows for validity till 10^{11} GeV(red), 10^{14} GeV(green) and 10^{19} GeV(black). The region inside the solid (broken) blue curve corresponds to a signal significance greater than or equal to $3(5)\sigma$. The upper and lower plots are for $\lambda_6 = \lambda_7 = 0$ and $\lambda_6, \lambda_7 \neq 0$ respectively.	103
5.5	The parameter space in the $\tan\beta$ vs. $c_{\beta-\alpha}$ plane for $m_H = 550$ GeV and $m_A = 551$ GeV that allows for validity till 10^{11} GeV(red), 10^{14} GeV(green) and 10^{19} GeV(black). The region inside the solid (broken) blue curve corresponds to a signal significance greater than or equal to $3(5)\sigma$. The upper and lower plots are for $\lambda_6 = \lambda_7 = 0$ and $\lambda_6, \lambda_7 \neq 0$ respectively.	104
7.1	Regions compatible with the theoretical constraints for $M = 110$ TeV (left panel) and 10^9 TeV (right panel) with three different choices of Λ_{UV} and two values of λ_2 . The regions denoted by A (red), B (cyan) and C (green) obey these constraints up to $\Lambda_{UV} = 10^6, 10^{16}$ and 10^{19} GeV respectively. The grey region denoted by D keeps the Higgs to diphoton signal strength within 2σ limits of the current data.	135

7.2	Region allowed by imposing the constraints on relic density(RC) and spin-independent cross section(SI) for DM-nucleon scattering. The red(gray) region is allowed only by the requirement of $\Omega_{\text{DM}}h^2$ being in the correct range. The black region is allowed by both the $\Omega_{\text{DM}}h^2$ and direct detection constraints. The shaded horizontal band below is disallowed by vacuum stability conditions. Here, $M_{H^\pm} = M_A = 200$ GeV.	137
7.3	Regions allowed by the theoretical constraints projected in the $\lambda_L - M_A$ and $\lambda_3 - M_H^\pm$ planes. The regions denoted by A (red), B (cyan) and C (green) obey those constraints up to $\Lambda_{UV} = 10^6, 10^{16}$ and 10^{19} GeV respectively. The grey region denoted by D shows the 2σ allowed limit of the Higgs to diphoton signal strength.	138
7.4	Regions allowed by the theoretical constraints projected in the $\lambda_L - M_A$ and $\lambda_3 - M_H^\pm$ planes. The regions denoted by A (red), B (cyan) and C (green) obey those constraints up to $\Lambda_{UV} = 10^6, 10^{16}$ and 10^{19} GeV respectively. The grey region denoted by D shows the 2σ allowed limit of the Higgs to diphoton signal strength.	139
7.5	Region(s) allowed in the M_H - λ_L plane obeying the various constraints for $M = 10^4$ GeV (left panel) and $M = 10^{12}$ GeV (right panel). The full region (marked by ‘ RC + SI ’) (magenta) is allowed by the DM constraints alone. The overlapped regions labelled by A (red), B (cyan) and C (green) are consistent with the theoretical constraints up to $\Lambda_{UV} = 10^6, 10^{16}$ and 10^{19} GeV respectively.	141
7.6	Region(s) allowed in the M_{H^\pm} - λ_3 plane obeying the various constraints . The full region (marked by ‘ RC + SI ’) (magenta) is allowed by the DM constraints alone. The overlapped regions labelled by A (red), B (cyan) and C (green) are consistent with the theoretical constraints up to $\Lambda_{UV} = 10^6, 10^{16}$ and 10^{19} GeV respectively.	143
7.7	RG running of different scalar quartic couplings corresponding to BP1. The solid, dashed, dashed dotted and dotted lines denote the evolution curves of the stability conditions vsc1, vsc2, vsc3 and vsc4 respectively.	144
7.8	Same as Fig. 7.7 but for the benchmark point BP2.	145
8.1	Running of λ_8 corresponding to BP1 (left) and λ_1 corresponding to BP2 (right). $m_h = 125$ GeV and an exact alignment $\sin(\beta - \alpha) = 1.0$ taken in both.	161

8.2	Contribution of the S_3 HDM scalars to the oblique parameters for $\sin(\beta - \alpha) = 1.0$ (Left) and $\sin(\beta - \alpha) = 0.98$ (Right). The ellipses denote the 1σ (solid), 2σ (dashed) and 3σ (dotted) limits. The green and red points indicate validity till 10^4 GeV and 10^6 GeV respectively. We notice that the oblique parameters do not change appreciably for a slight departure from exact alignment.	162
8.3	$h \rightarrow \gamma\gamma$ rates for an S_3 HDM valid till a cutoff Λ . The cyan, green and red points are respectively for $\Lambda = 10^3, 10^4$ and 10^6 GeV. The solid and dotted lines denote the 2σ limits below the central value given by ATLAS and CMS respectively	163
8.4	Regions consistent with the theoretical constraints up to a given cutoff. The cyan, green and red points are valid till 10^3 GeV, 10^4 GeV and 10^6 GeV respectively. Oblique parameter and diphoton constraints are also taken into account. Points valid till 10^7 GeV get disallowed by the diphoton constraint and are hence not displayed. An exact alignment is chosen and it has been checked that the bounds do not change for a small deviation from exact alignment.	164
8.5	Evolution of BP3 under RG. Colour coding is explained in the legends and the vacuum instability line is highlighted.	166
8.6	The dark matter relic density versus m_{H_1} (left) and the coupling of H_1 pair to the Higgs boson λ_L (right). The grey, green and red points preserve validity up to 1TeV, the GUT scale 10^{16} GeV and the Planck scale 10^{19} GeV respectively. The horizontal black lines denote the 3σ limits of the PLANCK data.	167
8.7	Spin-independent WIMP-nucleon scattering cross section vs m_{H_1} (left) and the coupling of H_1 pair to the Higgs boson λ_L (right). The grey, green and red points preserve validity up to 1 TeV, the GUT scale 10^{16} GeV and the Planck scale 10^{19} GeV respectively. Note that a large proportion of model points do obey the LUX upper bound while fulfilling stability requirements.	168
8.8	The viable S_3 HDM parameter space projected on the λ_L vs m_{H_1} (top left), $m_{A_1} - m_{H_1}$ vs m_{H_1} (top right), $m_{H_1^+} - m_{H_1}$ vs m_{H_1} (bottom) planes. " $\Lambda + \text{DM} + \mu_{\gamma\gamma}$ " in the legends refers to validity up to Λ as well as consistency with DM searches and diphoton signal strength. The green and red points correspond to $\Lambda = 10^{16}$ GeV and $\Lambda = 10^{19}$ GeV respectively.	170

8.9	Distribution of parameter points valid till 10^3 GeV (grey), 10^{16} (red) GeV and 10^{19} (green) GeV in the $\mu_{\gamma\gamma}$ vs $m_{H_1^+}$ plane. The solid and dotted lines denote the 2σ limits below the central value given by ATLAS and CMS respectively .	171
8.10	RG Evolution of BP4, BP5, BP6 and BP7. Colour coding is explained in the legends and the vacuum instability line is highlighted. Note that vsc5 and vsc6 are not defined whenever $\lambda_8 < 0$	172

List of Tables

1.1	<i>Charges of the SM fermions and scalars. C is the colour charge under $SU(3)_C$ group, T_3 is the third component of weak isospin of $SU(2)_L$ group, Y is the hypercharge quantum number of $U(1)_Y$ group and Q is the electric charge.</i>	15
3.1	The signal strengths in various channels with their 1σ uncertainties.	51
4.1	Benchmark points chosen to illustrate the behaviour under renormalisation group equations (RGE). Λ denotes the maximum extrapolation scale up to which perturbativity remains intact. The stability/metastability of the EW vacuum corresponding to these benchmarks is dictated by the value of M_t taken.	78
5.1	Benchmarks chosen for simulating the proposed channels. We have taken $m_h = 125$ GeV and $\tan\beta = 2.5$ throughout. Any higher $\tan\beta$ would lead to a lower ggF rate and so was not chosen.	95
5.2	A record of the number of surviving events in the $H \rightarrow 4l$ channel after the selection cuts at the $\sqrt{s} = 14$ TeV LHC for a Type-I 2HDM. Here $\mathcal{N}_S^{100(3000)}$ and $\mathcal{N}_B^{100(3000)}$ respectively denote the number of signal and background events at $\mathcal{L} = 100(3000) \text{ fb}^{-1}$. Besides, $\text{CL}_{100(3000)}$ denotes the confidence level at $\mathcal{L} = 100(3000) \text{ fb}^{-1}$.	97
5.3	A record of the number of surviving events in the $H \rightarrow 4l$ channel after the selection cuts at the $\sqrt{s} = 14$ TeV LHC for a Type-II 2HDM. Here $\mathcal{N}_S^{100(3000)}$ and $\mathcal{N}_B^{100(3000)}$ respectively denote the number of signal and background events at $\mathcal{L} = 100(3000) \text{ fb}^{-1}$. Besides, $\text{CL}_{100(3000)}$ denotes the confidence level at $\mathcal{L} = 100(3000) \text{ fb}^{-1}$.	98

5.4	A record of the number of surviving events in the $A \rightarrow l^+l^-b\bar{b}$ channel after the selection cuts at the $\sqrt{s} = 14$ TeV LHC for a Type-I 2HDM. Here $\mathcal{N}_S^{100(3000)}$ and $\mathcal{N}_B^{100(3000)}$ and respectively denote the number of signal and background events with $\mathcal{L} = 100(3000) \text{ fb}^{-1}$. Besides, $\text{CL}_{100(3000)}$ denotes the confidence level for $\mathcal{L} = 100(3000) \text{ fb}^{-1}$	105
5.5	A record of the number of surviving events in the $A \rightarrow l^+l^-b\bar{b}$ channel after the selection cuts at the $\sqrt{s} = 14$ TeV LHC for a Type-II 2HDM. Here $\mathcal{N}_S^{100(3000)}$ and $\mathcal{N}_B^{100(3000)}$ respectively denote the number of signal and background events with $\mathcal{L} = 100(3000) \text{ fb}^{-1}$. Besides, $\text{CL}_{100(3000)}$ denotes the confidence level at for $\mathcal{L} = 100(3000) \text{ fb}^{-1}$	106
5.6	The values of m_H , m_A and $\tan\beta$ chosen to probe the radiative return channel. The values of \sqrt{s} are also shown.	108
5.7	Number of signal and background surviving events in the radiative return process at the muon collider. Here $\mathcal{N}_S^{500(1000)}$ and $\mathcal{N}_B^{500(1000)}$ and respectively denote the number of signal and background events $\mathcal{L} = 500(1000) \text{ fb}^{-1}$. Besides, $\text{CL}_{500(1000)}$ denotes the confidence level at $\mathcal{L} = 500(1000) \text{ fb}^{-1}$	108
7.1	Benchmark values (BP) of parameters affecting the RG evolution of the quartic couplings. For each BP, two values of M , namely, 110 TeV and 10^9 TeV, have been used.	142
8.1	Benchmark points chosen to illustrate the behaviour under RGE. Λ denotes the maximum extrapolation scale up to which vacuum stability and perturbativity are ensured.	160
8.2	Bounds on the quartic couplings, for $\Lambda = 10^3, 10^4, 10^6$ GeV. Oblique parameter and diphoton constraints are also taken into account. We show the numbers up to the first decimal place.	165
8.3	Benchmark point illustrating the behaviour under RGE. Λ denotes the maximum extrapolation scale up to which vacuum stability and perturbativity are ensured.	165
8.4	Benchmark points chosen to illustrate the behaviour under RGE. Λ denotes the maximum extrapolation scale up to which vacuum stability and perturbativity are ensured.	173

Chapter 1

Introduction

1.1 What is the Standard Model?

In nature, all phenomena at the fundamental level can be described in terms of the following interactions among elementary particles :

- Strong Interaction
- Weak Interaction
- Electromagnetic interaction
- Gravitational Interaction

The Standard Model (SM) [1–5] of particle physics is a theory describing the electromagnetic, weak, and strong interactions. It also classifies all the elementary particles discovered till date. It is a Yang-Mills theory [6] based on the $SU(3)_C \times SU(2)_L \times U(1)_Y$ gauge group. The theory of strong interactions is encoded in the gauge group $SU(3)_C$, where 'C' stands for the colour quantum number. The electromagnetic and weak interactions have a common origin in the $SU(2)_L \times U(1)_Y$ product group and are collectively referred to as "electroweak(EW) interactions". The $U(1)$ charge "Y" is named as the "hypercharge" in the SM¹. Gravity is not included in the SM framework; in fact, no proven quantum theory of gravity exists yet.

¹The Standard Model has been reviewed comprehensively in [7–9]. Excellent books on the subject are [10–13]

Standard Model of Elementary Particles

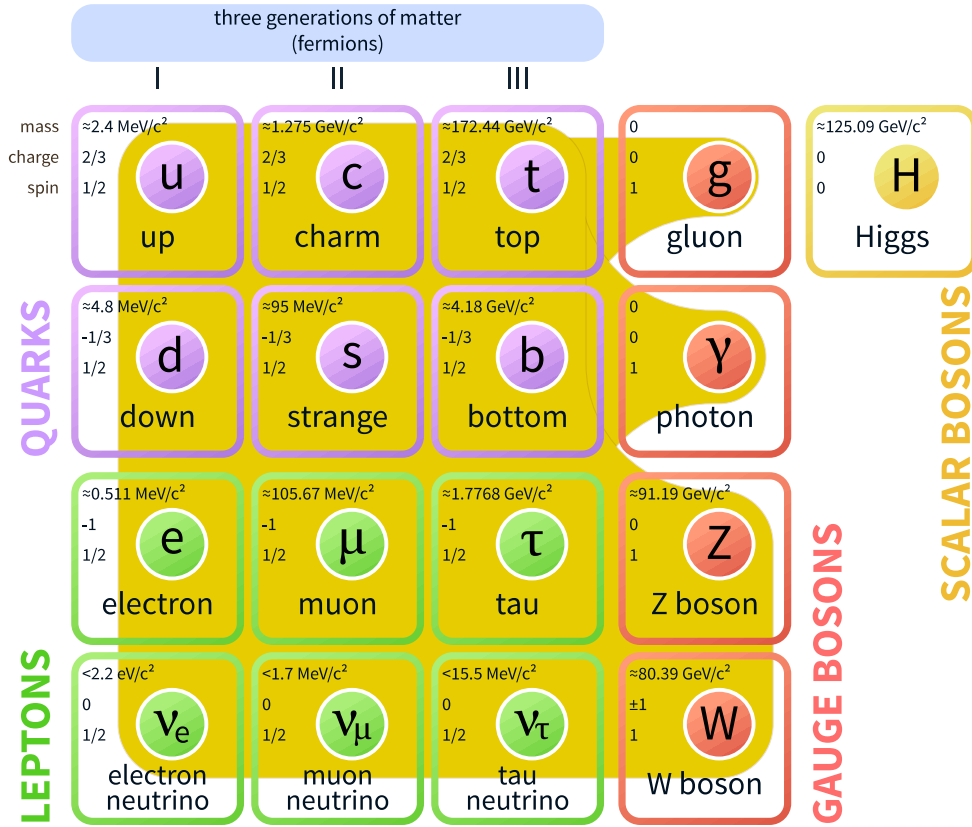


Figure 1.1: The elementary particles forming the Standard Model.

1.2 Particle content of the SM

The SM is built of quarks, leptons, gauge bosons and the Higgs boson. Fig.1.1 below lists all the particles and their masses. We discuss the various component fields one by one in the following.

1.2.1 Fermionic fields

The matter content of the SM comprises quarks and leptons which are arranged in three generations. The quarks and leptons transform respectively as triplets and singlets under $SU(3)_C$. An SM fermion f is chiral, implying that its left-handed ($f_L = \frac{1}{2}(1 - \gamma_5)f$) and right-handed ($f_R = \frac{1}{2}(1 + \gamma_5)f$) components transform differently under the electroweak gauge group. The left-handed fermions transform as doublets under $SU(2)_L$, whereas the

Field	$SU(3)_C$	$SU(2)_L$	T_3	$U(1)_Y$	$Q = T_3 + Y$
$Q_L = \begin{pmatrix} u_L \\ d_L \end{pmatrix}$	3	2	$\begin{pmatrix} \frac{1}{2} \\ -\frac{1}{2} \end{pmatrix}$	$\frac{1}{6}$	$\begin{pmatrix} \frac{2}{3} \\ -\frac{1}{3} \end{pmatrix}$
u_R	3	1	0	$\frac{2}{3}$	$\frac{2}{3}$
d_R	3	1	0	$-\frac{1}{3}$	$-\frac{1}{3}$
$L_L = \begin{pmatrix} \nu_L \\ l_L \end{pmatrix}$	1	2	$\begin{pmatrix} \frac{1}{2} \\ -\frac{1}{2} \end{pmatrix}$	$-\frac{1}{2}$	$\begin{pmatrix} 0 \\ -1 \end{pmatrix}$
l_R	1	1	0	-1	-1

Table 1.1: Charges of the SM fermions and scalars. C is the colour charge under $SU(3)_C$ group, T_3 is the third component of weak isospin of $SU(2)_L$ group, Y is the hypercharge quantum number of $U(1)_Y$ group and Q is the electric charge.

right-handed ones are singlets under the same. Moreover, the hypercharges of the left- and right-handed components are also different. The third component of the $SU(2)$ isospin (T_3) is related to the $U(1)$ hypercharge Y and the electric charge Q by $Q = T_3 + Y$.

The left-handed quark doublet Q_L and lepton doublet L_L are denoted as

$$Q_L \equiv \begin{pmatrix} u_L \\ d_L \end{pmatrix} \quad \text{and} \quad L_L \equiv \begin{pmatrix} \nu_{lL} \\ l_L \end{pmatrix}, \quad (1.2.1)$$

Right-handed quark singlet q_R and lepton singlet l_R are given by,

$$q_R = u_R, d_R \text{ and } l_R, \quad (1.2.2)$$

where u represents the *up-type* quarks of the three generations u, c, t ; and d stands for the respective *down-type* quarks d, s, b . The charged leptons are denoted by $l = e, \mu, \tau$ with the corresponding left-handed neutrinos $\nu_l = \nu_e, \nu_\mu, \nu_\tau$. Right-handed neutrinos are absent in the SM. We list below the fermionic quantum numbers in Table 1.1.

Various anomalies possible in the $SU(2)_L \times U(1)_Y$ framework actually get cancelled due to the fact that the SM fermions are chiral. Anomalies connecting one axial and two vector couplings are bound to arise. The ones involving only $SU(2)$ and $SU(3)$ bosons are trivially zero. This follows from the algebra corresponding to these gauge groups. However one expects anomalies involving one $U(1)$ boson and two $SU(2)$ bosons. This comes out to

be proportional to $\sum_{fL} Y_{fL}$, where the sum is over the left-handed SM fermions. Such an anomaly cancels due to the fact that

$$\sum_{fL} Y_{fL} = -\left(-\frac{1}{2}\right) - 3\left(\frac{1}{6}\right) = 0. \quad (1.2.3)$$

Therefore the SM is a chiral gauge theory free of axial vector anomalies [14–17], and, this is a direct fallout of the occurrence of an equal number of quark and lepton generations. The same charge assignments are found to save one from other anomalies as well. For instance, the anomaly involving one $U(1)$ boson with two $SU(3)$ bosons is proportional to $\sum_q Y_q$, where the sum is over all quarks. For any one fermionic generation, this is found to vanish since²

$$\sum_q Y_q = -\frac{1}{6} - \frac{1}{6} + \left(\frac{2}{3}\right) + \left(-\frac{1}{3}\right) = 0. \quad (1.2.4)$$

Moreover, the anomaly involving three $U(1)$ bosons is proportional to $\sum_f Y_f^3$, where the summation is over all the fermions. This also turns out to be zero since

$$\begin{aligned} \sum_f Y_f^3 &= -\left(-\frac{1}{2}\right)^3 - \left(-\frac{1}{2}\right)^3 + (-1)^3 \\ &\quad - 3\left[2\left(\frac{1}{6}\right)^3 - \left(\frac{2}{3}\right)^3 - \left(-\frac{1}{3}\right)^3\right] = 0. \end{aligned} \quad (1.2.5)$$

In eqns.(1.2.3), (1.2.4) and (1.2.5), the sum was carried out over a single fermion generation.

1.2.2 Gauge fields

Then there are also gauge fields that ensure invariance under G_{SM} . These are spin-1 entities that bear one-to-one correspondence with the corresponding group generators. In the electroweak sector, the field B_μ corresponds to the generator Y of the $U(1)_Y$ group and the three fields $W_\mu^{1,2,3}$ which correspond to the generators T^a (with $a = 1,2,3$) of the $SU(2)_L$ group. The four gauge bosons B_μ, W_μ^a are thus mediators of electroweak interactions. The Lie algebra spanned by T^a is thus

$$[T^a, T^b] = \epsilon^{abc} T^c \quad \text{with} \quad Tr[T^a T^b] = \frac{1}{2} \delta^{ab}, \quad (1.2.6)$$

²An extra (-1) comes for left-handed fermions.

where ϵ^{abc} denotes the structure constant for $SU(2)$, which coincides with the antisymmetric tensor in three dimensions. The generators of the fundamental representation of $SU(2)_L$ are thus $T^a = \frac{1}{2}\sigma^a$, where σ^a are the Pauli matrices.

Strong interaction is mediated by an octet of gluons, G_μ^A [with $A = 1, 2, \dots, 8$] which correspond to the eight generators λ^A of the $SU(3)_C$, which in the fundamental representation, are 3×3 matrices known as the Gell-Mann matrices. These satisfy

$$[\lambda^A, \lambda^B] = f^{ABC}\lambda^C \quad \text{with} \quad \text{Tr}[\lambda^A\lambda^B] = \frac{1}{2}\delta^{AB}. \quad (1.2.7)$$

Here f^{ABC} is the corresponding structure constant. To have a consistent dynamics of the gauge fields, one needs kinetic terms of the gauge fields which are expressible in terms of the following field strengths.

$$B_{\mu\nu} = \partial_\mu B_\nu - \partial_\nu B_\mu \quad (1.2.8)$$

$$W_{\mu\nu}^a = \partial_\mu W_\nu^a - \partial_\nu W_\mu^a + g_2 f^{abc} W_\mu^b W_\nu^c \quad (1.2.9)$$

$$G_{\mu\nu}^A = \partial_\mu G_\nu^A - \partial_\nu G_\mu^A + g_3 f^{ABC} G_\mu^B G_\nu^C \quad (1.2.10)$$

In the above, g_2 and g_3 denote respectively the coupling constants of the $SU(2)_L$ and the $SU(3)_C$ groups. Having introduced the spin- $\frac{1}{2}$ and spin-1 fields of the SM, and their transformation properties under G_{SM} , we set out to construct a gauge invariant Lagrangian for the SM.

1.3 Towards the SM Lagrangian

The kinetic terms for the gauge fields can be written as

$$\mathcal{L}_G = -\frac{1}{4}B^{\mu\nu}B_{\mu\nu} - \frac{1}{4}W^{a\mu\nu}W_{\mu\nu}^a - \frac{1}{4}G^{A\mu\nu}G_{\mu\nu}^A. \quad (1.3.1)$$

By virtue of their non-Abelian origin, the gluons and the $SU(2)_L$ gauge bosons exhibit three- and four-point interactions among themselves, unlike an abelian theory such as Quantum Electrodynamics (QED). To construct the kinetic term of an SM fermion f of hypercharge Y_f , one defines the covariant derivative

$$D_\mu f = \left(\partial_\mu - ig_1 Y_f B_\mu - ig_2 T^a W_\mu^a - ig_3 \lambda^A G_\mu^A \right) f. \quad (1.3.2)$$

In case f transforms trivially under any of $SU(3)_C$, $SU(2)_L$ or $U(1)_Y$, the corresponding term is absent from the covariant derivative. Given this definition and the quantum numbers of the

different SM fermions under G_{SM} , following becomes the kinetic Lagrangian of the fermions. That is.

$$\mathcal{L}_f = \bar{Q}_L^i i\gamma^\mu D_\mu Q_L^i + \bar{u}_R^i i\gamma^\mu D_\mu u_R^i + \bar{d}_R^i i\gamma^\mu D_\mu d_R^i + \bar{L}_L^i i\gamma^\mu D_\mu L_L^i + \bar{l}_R^i i\gamma^\mu D_\mu l_R^i. \quad (1.3.3)$$

In eqn.(1.3.3), $i = 1, 2, 3$ denotes the generation (or family) index. Up to this point, the fermions and the gauge bosons are massless since mass terms are disallowed by gauge invariance. While this is in compliance with QED and QCD (Quantum Chromodynamics), where both photons and gluons are massless, it is unacceptable for the gauge theory of weak interactions, since both the charged (W^\pm) and neutral (Z) gauge bosons have masses ($M_W \approx 80$ GeV, $M_Z \approx 91$ GeV). In addition, it has been also known for long that the electron also carries a small mass of about 0.5 MeV.

A novel way to give masses to the fermions and electroweak gauge bosons is through a spontaneous breakdown of the $SU(2)_L \times U(1)_Y$ gauge symmetry. This is popularly known as the Higgs mechanism [18–20] and will be discussed in the subsequent section.

1.4 Generation of mass: The Higgs mechanism

The Higgs mechanism is implemented in the Standard Model by introducing a complex scalar field Φ which is a doublet of $SU(2)_L$ with $Y = \frac{1}{2}$, being expressed as

$$\Phi = \begin{pmatrix} \phi^+ \\ \phi^0 \end{pmatrix}. \quad (1.4.1)$$

Therefore, $D_\mu \Phi = \left(\partial_\mu - i\frac{1}{2}g_1 B_\mu - ig_2 T^a W_\mu^a \right) \Phi$. Defining a corresponding scalar potential $V(\Phi)$, the Lagrangian for the scalar doublet is then written as

$$\mathcal{L}_\Phi = (D^\mu \Phi)^\dagger (D_\mu \Phi) - V(\Phi), \quad (1.4.2a)$$

$$V(\Phi) = \mu^2 \Phi^\dagger \Phi + \lambda (\Phi^\dagger \Phi)^2. \quad (1.4.2b)$$

Whenever $\mu^2 < 0, \lambda > 0$, Φ develops a vacuum expectation value (VEV) given by $\Phi_0 = \langle 0 | \Phi | 0 \rangle$. The symmetry group $SU(2)_L \times U(1)_Y$ is spontaneously broken down to $U(1)_Q$ if a specific VEV is chosen. Then,

$$\Phi_0 = \frac{1}{\sqrt{2}} \begin{pmatrix} 0 \\ v \end{pmatrix} \quad (1.4.3)$$

Minimising $V(\Phi)$ about the VEV leads to $\mu^2 = -\lambda v^2$. Upon spontaneous symmetry breaking, the kinetic term in eqn.(1.4.2a) is responsible for generating the gauge boson masses.

$$\begin{aligned}
(D^\mu \Phi)^\dagger (D_\mu \Phi) &\longrightarrow \cdots + \frac{1}{8} (0 \ v) (g_2 W_\mu^a \sigma^a + g_1 B_\mu) (g_2 W^{b\mu} \sigma^b + g_1 B^\mu) \begin{pmatrix} 0 \\ v \end{pmatrix} + \cdots \\
&\longrightarrow \cdots + \frac{1}{2} \frac{v^2}{4} [g_2^2 (W_\mu^1)^2 + g_2^2 (W_\mu^2)^2 + (-g_2 W_\mu^3 + g_1 B_\mu)^2] + \cdots
\end{aligned} \tag{1.4.4}$$

One recognises in eqn.(1.4.4) the mass terms for the charged gauge bosons W_μ^\pm :

$$W_\mu^\pm = \frac{1}{\sqrt{2}} (W_\mu^1 \pm W_\mu^2) \longrightarrow M_W = g_2 \frac{v}{2}, \tag{1.4.5}$$

and for the neutral gauge boson Z_μ :

$$Z_\mu = \frac{1}{\sqrt{g_2^2 + g_1^2}} (g_2 W_\mu^3 - g_1 B_\mu) \longrightarrow M_Z = \sqrt{g_2^2 + g_1^2} \frac{v}{2}, \tag{1.4.6}$$

while the orthogonal linear combination of W_μ^3 and B_μ remains massless and corresponds to the photon field (A_μ):

$$A_\mu = \frac{1}{\sqrt{g_2^2 + g_1^2}} (g_1 W_\mu^3 + g_2 B_\mu) \longrightarrow M_A = 0, \tag{1.4.7}$$

the gauge boson of the residual $U(1)_Q$ gauge symmetry. θ_W , also known as the Weinberg angle, is the angle by which the $\{W_\mu^a, B_\mu\}$ fields must be rotated to obtain $\{W_\mu^\pm, Z_\mu, A_\mu\}$. One then has

$$\tan \theta_W = \frac{g_1}{g_2}. \tag{1.4.8}$$

The photon A_μ interacts with the other SM fields with the electromagnetic coupling $e = g_1 \cos \theta_W = g_2 \sin \theta_W$. Thus, e becomes the coupling corresponding to the unbroken $U(1)_Q$. The relative strengths of the charged and neutral current interactions in a spontaneously broken theory is measured by the ρ -parameter defined to be

$$\rho = \frac{M_W^2}{M_Z^2 \cos^2 \theta_W} = 1. \tag{1.4.9}$$

Non-zero masses of the SM fermions are generated through Yukawa interactions involving Φ .

$$\mathcal{L}_Y = -y_u^{ij} Q_L^i \tilde{\Phi} u_R^j - y_d^{ij} Q_L^i \Phi d_R^j - y_e^{ij} L_L^i \Phi l_R^j. \tag{1.4.10}$$

In eqn.(1.4.10), $y_{u,d,e}^{ij}$ denote the respective Yukawa couplings. Here, $\tilde{\Phi} = i\sigma_2\Phi^*$ is again an $SU(2)_L$ doublet with $Y = -\frac{1}{2}$. When Φ develops a VEV v , in terms of the flavour basis the fermion-masses are $m_{u,d,e} = \frac{1}{\sqrt{2}}y_{u,d,e}v$. These mass matrices are not in general diagonal, they can be brought to diagonal forms by rotating to the "mass basis". Denoting the mass basis using primed fields,

$$u_L^{i'} = U_L^{ij}u_L^j, \quad (1.4.11)$$

$$d_L^{i'} = V_L^{ij}d_L^j, \quad (1.4.12)$$

$$u_R^{i'} = U_R^{ij}u_R^j, \quad (1.4.13)$$

$$d_R^{i'} = V_R^{ij}d_R^j. \quad (1.4.14)$$

In the above $U_{L,R}$ and $V_{L,R}$ are unitary matrices. As a result of this mixing, the charged current interactions, i.e., the interactions of the quarks with W^\pm are not flavour diagonal. They assume the following form.

$$-\frac{g_2}{\sqrt{2}}(\bar{u}'_L \bar{c}'_L \bar{t}'_L)\gamma^\mu W_\mu^+ V_{CKM}(d'_L s'_L b'_L)^T + h.c. \quad (1.4.15)$$

where $V_{CKM} = U_L^\dagger V_L$, stands for the Cabibbo-Kobayashi-Maskawa matrix (CKM) [21,22], and has off-diagonal entries (as found in experiments) because the up- and down-quark mass matrices are not diagonal in the same basis. It is parametrised by three mixing angles and a phase and is given by [23]

$$V_{CKM} = \begin{pmatrix} |V_{ud}| = 0.97425 \pm 0.00022 & |V_{us}| = 0.2253 \pm 0.0008 & |V_{ub}| = 0.00413 \pm 0.00049 \\ |V_{cd}| = 0.225 \pm 0.008 & |V_{cs}| = 0.986 \pm 0.016 & |V_{cb}| = 0.0411 \pm 0.0013 \\ |V_{td}| = 0.0084 \pm 0.0006 & |V_{ts}| = 0.0400 \pm 0.0027 & |V_{tb}| = 1.021 \pm 0.032 \end{pmatrix}. \quad (1.4.16)$$

It should be noted that neutrinos still remain massless due to the absence of their right-handed partners.

1.5 The SM Higgs and its interactions

The doublet Φ can be expressed as

$$\Phi(x) = \frac{e^{\frac{i}{v}\vec{w}(x)\cdot\vec{\tau}}}{\sqrt{2}} \begin{pmatrix} 0 \\ v + h(x) \end{pmatrix} \xrightarrow{SU(2)} \Phi(x) = \frac{1}{\sqrt{2}} \begin{pmatrix} 0 \\ v + h(x) \end{pmatrix}, \quad (1.5.1)$$

after which the scalar potential in eqn.(1.4.2a) becomes:

$$\mathcal{L}_\phi = \mu^2 h^2 - \lambda v h^3 - \frac{1}{4}h^4 = -\frac{1}{2}M_h^2 h^2 - \sqrt{\frac{\lambda}{2}}M_h h^3 - \frac{1}{4}\lambda h^4. \quad (1.5.2)$$

Three degrees of freedom, the $w^a(x)$ Goldstone bosons, have been absorbed as the longitudinal components of the W_μ^\pm and Z_μ weak gauge bosons. One real scalar field remains as the *Higgs boson* h , with mass $M_h^2 = -2\mu^2 = 2\lambda v^2$ and self-couplings. The following scalar self-interactions then follow.

$$h - h - h \longrightarrow -3i \frac{M_h^2}{v} \quad (1.5.3a)$$

$$h - h - h - h \longrightarrow -3i \frac{M_h^2}{v^2} \quad (1.5.3b)$$

Furthermore, some of the terms that we omitted in eqn.(1.4.4), define the coupling of the SM Higgs boson to the gauge field $V = W, Z$:

$$h - V^\mu - V^\nu \longrightarrow 2i \frac{M_V^2}{v} g^{\mu\nu} \quad (1.5.4a)$$

$$h - h - V^\mu - V^\nu \longrightarrow 2i \frac{M_V^2}{v^2} g^{\mu\nu} \quad (1.5.4b)$$

In addition, h does not couple to the photon at tree level. It is however important to remark that couplings that are absent at tree level may be induced at higher order in the gauge couplings by loop corrections.

1.6 Need for physics beyond the SM

The SM is not believed to be a complete description of nature for several compelling reasons, some of which are directly connected to experiments. The others are primarily indicative of certain theoretical inconsistencies. It therefore falls short of being a complete theory of fundamental interactions. Such drawbacks are discussed briefly below.

1.6.1 Experimental evidences

- *Fermion masses and mixings*: A wide hierarchy amongst the fermion masses is noted within the SM. In fact, the masses of the SM fermions range from sub-eV (neutrinos) to 100 GeV (top quark) spanning six orders of magnitude. The mixing in the quark sector also has a generational structure, i.e, the largest mixing occurs between the generations one and two, followed by mixing of two and three and finally, mixing between one and three, which are the feeblest ones. There is nothing in the SM that explains this mass hierarchy and the mixing amongst its fermions.

- *Non-zero neutrino masses*: One of the most important findings suggesting the existence of physics beyond the SM is the evidence for non-zero neutrino masses and mixings, deciphered through neutrino oscillations. In SM, a neutrino is massless because of the absence of the corresponding right-handed partner. In principle, neutrino masses can be easily accommodated in the SM framework by postulating the existence of right-handed heavy sterile neutrinos. But, the extreme smallness of neutrino mass, calls for a deeper understanding. Also, the bi-large mixing pattern of neutrinos, as evident from oscillation data, is very different from what is noticed in the quark sector.
- *Dark matter*: The standard model of cosmology indicates that the total mass-energy of the universe contains 4.9% ordinary matter, 26.8% dark matter and 68.3% dark energy. Although dark matter has not been directly observed, its existence and properties are inferred from its gravitational effects. These include motion of visible matter, gravitational lensing, as well as its influence on the large-scale structure formation in the universe and on the cosmic microwave background. The SM fails to provide a suitable candidate for particle dark matter.
- *Baryon asymmetry*: The baryon asymmetry problem in physics refers to the imbalance in baryonic matter and antibaryonic matter in the observable universe. The Big Bang should have produced equal amounts of matter and antimatter. However, an asymmetry measuring $\eta_b \sim 10^{-9}$ is observed in the present day. According to the Sakharov conditions, one possible explanation could come from CP -violation. In the SM, CP -violation arises mainly from the phase in the CKM matrix. However, it does not have the requisite magnitude so as to account for the observed baryon asymmetry. Dynamics beyond the SM therefore becomes necessary in explaining the observed asymmetry.
- *Anomalous magnetic moment of the muon*: The measurement of the anomalous magnetic moment of the muon disagrees with the SM by $\simeq 3.4\sigma$ [24]. This observation also necessarily calls for physics beyond the SM.

1.6.2 Theoretical shortcomings

- *The absence of a fully unified framework*: Although the SM is a framework describing the strong, weak and electromagnetic interactions, it fails to predict a common origin of the three. In case of such a common origin, one would identify a bigger symmetry

group in which G_{SM} could be possibly embedded. Then, the gauge couplings g_1, g_2 and g_3 should unify at the breaking scale of the bigger group. However, assuming no other dynamics apart from the SM participates till that scale, no such unification is observed. Moreover, the SM model also fails to unify gravity with the rest of the interactions, and thus, cannot be used to describe physics near the Planck scale.

- *The naturalness problem:* In theoretical physics, a naturalness problem refers to the presence of two separate energy scales corresponding to those of weak and gravitational interactions. These scales are separated by an astounding seventeen orders of magnitude. In such a setting, the Higgs boson mass is susceptible to large radiative corrections. For instance, if the SM has a natural ultraviolet (UV) cutoff at Λ_{UV} , then adopting the cutoff regularisation and working in the Feynman gauge leads to the following one loop correction to the Higgs mass.

$$\delta M_h^2 = \frac{\Lambda_{UV}^2}{16\pi^2} \left(12\lambda + \frac{3}{4}g_1^2 + \frac{9}{4}g_2^2 - 6y_t^2 \right) \quad (1.6.1)$$

A quadratic sensitivity to the UV cutoff is noted in case of the Higgs [25]. Whereas, the corresponding corrections to the SM fermions and gauge bosons display only a logarithmic dependence on the same. This is due to the fact that the fermion and gauge boson masses are "screened" by the gauge and chiral symmetries respectively and there is no such symmetry in case of the Higgs. The coefficient of Λ_{UV}^2 does not vanish in the SM and upon taking $\Lambda_{UV} \sim M_{Pl}$, one gets $\delta M_h^2 \sim 10^{35} \text{ GeV}^2$.

Any attempt to tame the naturalness problem necessitates the presence of physics beyond the SM. The additional physics could be a theory like supersymmetry where owing to identical interaction strengths of the Higgs with supersymmetric partner particles, the quadratic contribution to its mass gets identically cancelled. Also attractive is the idea that the SM is a theory with spacetime dimensions higher than four with the extra dimensions being compactified. Apart from these novel scenarios, one can in principle address the hierarchy problem by introducing additional fields and relying upon fine tuning.

- *The strong CP problem:* Theoretically it can be argued that the standard model should contain a term that breaks CP symmetry relating matter to antimatter in the strong interaction sector. Experimentally, however, no such violation has been found, implying that the coefficient of this term is very close to zero. This fine tuning is considered unnatural.

- *Vacuum instability*: In the SM, the Higgs quartic coupling can become negative around 10^{11} GeV while evolving under renormalisation group, thereby rendering the EW vacuum unstable. In that case, the SM loses its attractiveness as a tool to describe dynamics all the way up to the Planck scale.

1.7 Extended Higgs sectors

In the present section, we outline how the above shortcomings of the SM can be addressed by just extending the scalar sector only. We discuss a few cases where the additional scalars transform as multiplets of $SU(2)$.

1.7.1 $SU(2)$ singlet(s)

The SM is augmented by a complex singlet S [26] by adding the following terms to the SM Lagrangian.

$$\mathcal{L}_S = (\partial_\mu S)^\dagger (\partial^\mu S) - \mu_S^2 S^\dagger S - \lambda_{SH} S^\dagger S \Phi^\dagger \Phi - \lambda_S (S^\dagger S)^2 \quad (1.7.1)$$

The singlet can have interesting phenomenological implications. The physical scalars emerging in this case are the CP -even neutral scalars h_1 and h_2 and a CP -odd A . In the post Higgs discovery era, one always chooses either h_1 or h_2 to be SM-like. When S does not acquire a VEV, it does not mix with Φ , and consequently has a zero decay width. Therefore, its CP -even and odd components can be dark matter candidates. In the case when S does receive a VEV, it potentially alters the interactions of the 125 GeV Higgs through $\Phi - S$ mixing. Along with a modified phenomenology of the 125 GeV scalar, this scenario can also open up new signals at the colliders. A particularly interesting variant of this model is one where S is gauged under an $U(1)_X$ [27], thereby enlarging also the gauge sector of the SM.

1.7.2 $SU(2)$ doublet(s)

The SM Higgs sector augmented by additional $SU(2)_L$ doublets has some spectacular features. One of them is that being the ρ -parameter remains unity at tree-level. This becomes clear upon writing down the general expression for the tree level ρ -parameter for an $SU(2) \times U(1)$ gauge theory in terms of the quantum numbers of the scalar multiplets. That

is,

$$\rho = \frac{\sum_{i=1}^N [T_i(T_i + 1) - Y_i^2] v_i}{2 \sum_{i=1}^N Y_i^2 v_i}. \quad (1.7.2)$$

In the above, T_i and Y_i denote the weak isospin and hypercharge of the i -th scalar multiplet respectively, and v_i is the VEV acquired by the neutral component of the corresponding multiplet.

An N-Higgs doublet model (NHDM) is set apart from the other Higgs sector extensions through its Yukawa sector. In an NHDM, a particular fermion has *prima facie* the scope of coupling to all of the doublets. This can not only modify the Yukawa couplings of the scalar identified with the 125 GeV Higgs, but also lead to unsuppressed fermionic interactions of the additional scalars. This offers a multitude of testable predictions. Firstly, flavour changing interactions can arise at the tree-level itself. Secondly, the scalar sector participates radiatively in a precision calculation of the flavour physics observables.

The two simplest version of the NHDM are the 2HDM and 3HDM. We outline their main features below³.

Two Higgs Doublet Models (2HDM)

The 2HDM is a well motivated scenario and have an indispensable presence in supersymmetric models. There, the scalars are part of chiral multiplets and their complex conjugates belong to multiplets of the opposite chirality. As multiplets of different chiralities cannot couple together in the Lagrangian, a single Higgs doublet is unable to give mass simultaneously to the charge 2/3 and charge 1/3 quarks. Moreover, since scalars sit in chiral multiplets together with chiral spin-1/2 fields, the cancellation of anomalies also requires that an additional doublet be added. Therefore, the MSSM contains two Higgs doublets.

Another motivation for 2HDMs comes from axion models. Peccei and Quinn noted that a possible CP -violating term in the QCD Lagrangian, which is phenomenologically known to be very small, can be rotated away if the Lagrangian contains a global $U(1)$ symmetry. However, this symmetry can only be imposed if there are two Higgs doublets in place of one. Yet another interesting feature is that the 2HDM can account for the observed baryon asymmetry in the universe owing to possible CP -violating phases in the scalar potential.

2HDMs are also attractive from the perspective of dark matter and neutrino mass generation. The *inert* version of the 2HDM is a popular scenario predicting a scalar dark matter

³Most of the relevant references are given in the subsequent chapters.

candidate. Besides, the well known Type-I seesaw mechanism requires two scalar doublets for generating a correct neutrino mass. Some versions of the 2HDM are also known to bridge the discrepancy between the experimentally measured value of the anomalous muon magnetic moment and the corresponding SM prediction.

The most general renormalisable scalar potential for two doublets Φ_1 and Φ_2 , each having hypercharge (+1),

$$\begin{aligned}
V(\Phi_1, \Phi_2) = & m_{11}^2 \Phi_1^\dagger \Phi_1 + m_{22}^2 \Phi_2^\dagger \Phi_2 - m_{12}^2 \left(\Phi_1^\dagger \Phi_2 + \Phi_2^\dagger \Phi_1 \right) + \frac{\lambda_1}{2} \left(\Phi_1^\dagger \Phi_1 \right)^2 + \frac{\lambda_2}{2} \left(\Phi_2^\dagger \Phi_2 \right)^2 \\
& + \lambda_3 \Phi_1^\dagger \Phi_1 \Phi_2^\dagger \Phi_2 + \lambda_4 \Phi_1^\dagger \Phi_2 \Phi_2^\dagger \Phi_1 + \frac{\lambda_5}{2} \left[\left(\Phi_1^\dagger \Phi_2 \right)^2 + \left(\Phi_2^\dagger \Phi_1 \right)^2 \right] \\
& + \lambda_6 \Phi_1^\dagger \Phi_1 \left(\Phi_1^\dagger \Phi_2 + \Phi_2^\dagger \Phi_1 \right) + \lambda_7 \Phi_2^\dagger \Phi_2 \left(\Phi_1^\dagger \Phi_2 + \Phi_2^\dagger \Phi_1 \right). \tag{1.7.3}
\end{aligned}$$

The doublets can be parametrised in the following fashion,

$$\Phi_i = \frac{1}{\sqrt{2}} \begin{pmatrix} \sqrt{2} w_i^+ \\ v_i + h_i + i z_i \end{pmatrix} \text{ for } i = 1, 2. \tag{1.7.4}$$

Here, v_1 and v_2 denote the vacuum expectation values acquired by the CP -even neutral components Φ_1 and Φ_2 respectively, with $\tan\beta = \frac{v_2}{v_1}$. Out of the 8 real scalar degrees of freedom furnished by the two doublets, 3 get identified with the longitudinal modes of W^\pm and Z . In other words, they become the Goldstone bosons. The remaining 5 real scalars are the physical fields and they manifest themselves as two CP -even neutral scalars H, h , a CP -odd scalar A , and, a charged scalar H^\pm . The physical fields and the Goldstone bosons are expressed as linear combinations of w_i^\pm, h_i, z_i as under:

$$\begin{pmatrix} G^\pm \\ H^\pm \end{pmatrix} = \begin{pmatrix} \cos\beta & \sin\beta \\ -\sin\beta & \cos\beta \end{pmatrix} \begin{pmatrix} w_1^\pm \\ w_2^\pm \end{pmatrix}, \tag{1.7.5}$$

$$\begin{pmatrix} G^0 \\ A \end{pmatrix} = \begin{pmatrix} \cos\beta & \sin\beta \\ -\sin\beta & \cos\beta \end{pmatrix} \begin{pmatrix} z_1 \\ z_2 \end{pmatrix}. \tag{1.7.6}$$

$$\begin{pmatrix} H \\ h \end{pmatrix} = \begin{pmatrix} \cos\alpha & \sin\alpha \\ -\sin\alpha & \cos\alpha \end{pmatrix} \begin{pmatrix} h_1 \\ h_2 \end{pmatrix}. \tag{1.7.7}$$

In eqns.(1.7.5) and (1.7.6), G^\pm, G^0 refer to the Goldstones. The mixing angle α is determined in terms of the quartic couplings and $\tan\beta$. A more elaborate account on the scalar

spectrum can be seen in [28, 29]. Moreover, the expressions for the masses of the physical scalars are also given in **Chapter 3**.

Turning to the fermionic interactions, one finds that a particular fermion doublet can couple to both Φ_1 and Φ_2 in this case. For instance, the most general Yukawa interactions involving the down-type quarks can now be of the following form:

$$-\mathcal{L}_Y = y_{ij}^1 \bar{Q}_L^i \Phi_1 d_R^j + y_{ij}^2 \bar{Q}_L^i \Phi_2 d_R^j. \quad (1.7.8)$$

An immediate consequence of eqn.(1.7.8) is the occurrence of tree level flavour changing neutral currents (FCNC) mediated by h, H and A . These are severely constrained by the measurements on meson mixing. However, a 2HDM can still be salvaged by means of the Glashow-Weinberg- Paschos theorem [30, 31], which states that the tree level FCNCs can be annulled by ensuring that a particular fermion doublet couples to only any one of the Higgs doublets. This is realized by introducing a \mathbb{Z}_2 symmetry which assigns respective charges to the scalars and fermions. One example is where Φ_1 , the lepton doublets Q_L^i and the d -quark singlets d_R^i carry a positive \mathbb{Z}_2 charge while Φ_2 and the u -quark singlets d_R^i have negative \mathbb{Z}_2 charges. This gives rise to a particular scheme of couplings where the u -quarks couple to Φ_2 and the d -quarks couple to Φ_1 , thereby eliminating FCNCs. One obtains more such schemes by changing the \mathbb{Z}_2 assignments. This leads to the following four flavour conserving types of 2HDMs [28]:

- Type I: all quarks and leptons couple to only one scalar doublet Φ_2 ;
- Type II: Φ_2 couples to up-type quarks, while Φ_1 couples to down-type quarks and charged leptons (MSSM conforms to this category);
- Type X or lepton specific: Φ_2 couples to all quarks, while Φ_1 couples to all leptons;
- Type Y or flipped: Φ_2 couples to up-type quarks and leptons, while Φ_1 couples to down-type quarks.

There is also the option for preventing tree level FCNC by assuming the two Yukawa matrices proportional to each other. This gives rise to the so called aligned 2HDM. However Branco, Grimus and Lavoura (BGL) employed a global $U(1)$ symmetry which textures both Yukawa matrices in a certain way [28]. As a result of this the tree level Higgs FCNC couplings get related to the off diagonal elements of the CKM matrix and thereby are naturally suppressed.

Various relevant aspects of the 2HDM shall be discussed in **Chapter 3**, **Chapter 4** and **Chapter 5**. Important formulae are relegated to the **Appendix A**.

Three Higgs Doublet Models (3HDM)

A 3HDM can be made to possess all the features of a 2HDM by virtue of the higher field content of the former. However the 3HDM stands apart for two distinct cases. First, there is scope of spontaneous CP -violation in a framework with three Higgs doublets. However this may lead to a conflict with the experimental limit on the electric dipole moment of the neutron, and the CP -violating phase has to be somehow suppressed in order to alleviate the problem. Second, a 3HDM can offer a solution to the fermion mass hierarchy problem. This is possible since the three scalar doublets can replicate the three fermion generations if the doublets are tied together by some discrete symmetry which also connects the fermion generations. Such symmetries are generally called 'family symmetries' [32, 33], important examples of which are A_4 , S_4 , S_3 and $\Delta(27)$. A 3HDM endowed with an S_3 symmetry is what forms the content of **Chapter 8**. Important formulae related to it can be found in **Appendix C**.

1.7.3 $SU(2)$ triplet(s)

The principal motivation a $SU(2)_L$ triplet scalar (Δ) is the generation of the masses of the SM neutrinos through the Type-II seesaw mechanism [34, 35]. For a $Y = 1$ triplet, the kinetic term and the scalar potential are

$$\begin{aligned} \mathcal{L}_\Delta = & Tr[D_\mu \Delta]^\dagger (D^\mu \Delta) - m_\Phi^2 (\Phi^\dagger \Phi) + M^2 Tr(\Delta^\dagger \Delta) + \{\mu (\Phi^T i\sigma_2 \Delta^\dagger \Phi) + \text{h.c.}\} + \frac{\lambda}{4} (\Phi^\dagger \Phi)^2 \\ & + \lambda_1 (\Phi^\dagger \Phi) Tr(\Delta^\dagger \Delta) + \lambda_2 \{Tr(\Delta^\dagger \Delta)\}^2 + \lambda_3 Tr[(\Delta^\dagger \Delta)^2] \\ & + \lambda_4 (\Phi^\dagger \Delta \Delta^\dagger \Phi) + \frac{1}{\sqrt{2}} \lambda_6 (M_\Delta \Phi^T C i\sigma_2 \Delta^\dagger \Phi + \text{h.c.}). \end{aligned} \quad (1.7.9)$$

Denoting the triplet VEV as v_Δ , the ρ parameter in this model is

$$\rho = (1 + \frac{2v_\Delta^2}{v^2}) / (1 + \frac{4v_\Delta^2}{v^2}). \quad (1.7.10)$$

The electroweak precision data constraints require the ρ parameter to be very close to its SM value of unity: $\rho = 1.0004_{-0.0004}^{+0.0003}$. For this model, it accordingly translates to $v_\Delta < 5$ GeV.

One can write down an Yukawa interaction between the scalar triplet and the lepton doublet in this scenario:

$$\mathcal{L}_Y = -\frac{1}{\sqrt{2}} Y_\Delta^{ij} (L_L^i)^T C i\sigma_2 \Delta L_L^j. \quad (1.7.11)$$

the Majorana mass matrix for the light neutrinos obtained is

$$M_\nu^{ij} = \frac{\lambda_6 v^2}{2M_\Delta} Y_\Delta^{ij} \text{ for } v_\Delta \ll v \quad (1.7.12a)$$

Therefore, $Y_\Delta^{ij} v_\Delta$ can be fixed using the low energy neutrino oscillation data as well as bounds on lepton flavour violating processes. The current experimental observations allow a wide region in the space spanned by Y_Δ^{ij} and v_Δ , so long as their products are consistent with data in the neutrino sector.

Apart from the aspects of neutrino mass generation, the scalar sector of the Type-II scenario is also of interest. In particular, the presence of a doubly charged scalar in this scenario leads to interesting signals at the colliders with lepton-rich final states.

Chapter 2

Vacuum stability and related issues: The role of the Higgs boson mass

As has been mentioned in the last chapters, along with several experimental observations, some pressing theoretical issues also suggest the presence of physics beyond the SM. One such issue is the instability of the SM vacuum under quantum corrections. In other words, if there is no other dynamics other than the SM till the Planck scale (M_{Pl}), the EW vacuum can get destabilised at an intermediate scale. This takes place under the effect of renormalisation group (RG). Moreover, the conclusions in this regard crucially depend on the masses of the t -quark and the Higgs. Also closely connected to the Higgs mass are the notions of triviality and perturbative unitarity. In this chapter, we seek to explore these connections and the possible scope of physics beyond the SM in alleviating the vacuum instability.

2.1 Vacuum stability in the SM

As elaborated in the previous chapter, the Higgs potential in the SM is

$$V(\Phi) = \mu^2 \Phi^\dagger \Phi + \lambda (\Phi^\dagger \Phi)^2. \quad (2.1.1)$$

Spontaneous breakdown of the gauge symmetry is triggered whenever $\mu^2 < 0, \lambda > 0$ in eqn.(2.1.1), with the minimum of $V(\Phi)$ lying at $v = 246$ GeV. For $\lambda < 0$, the potential becomes unbounded from below thereby leading to tachyonic states. In other words, the positiveness of the Higgs quartic coupling is directly connected to the generation of mass.

The SM being a renormalisable theory, the parameters therein vary with the dimensional regularisation scale μ . The running of the parameters is dictated by the RG equations. Using

$t^1 = \log \frac{Q}{v}$, we list below the RG equations at one loop for the parameters SM $\lambda, y_t, g_1, g_2, g_3$,

$$16\pi^2 \frac{d\lambda}{dt} = 24\lambda^2 - (3g_1^2 + 9g_2^2 - 12y_t^2)\lambda + \frac{3}{8}g_1^2 + \frac{3}{4}g_1^2g_2^2 + \frac{9}{8}g_2^4 - 6y_t^4, \quad (2.1.2a)$$

$$16\pi^2 \frac{dy_t}{dt} = \frac{9}{2}y_t^3 - y_t\left(\frac{9}{4}g_2^2 + \frac{17}{12}g_1^2 + 8g_3^2\right), \quad (2.1.2b)$$

$$16\pi^2 \frac{dg_1}{dt} = \frac{41}{6}g_1^3, \quad (2.1.2c)$$

$$16\pi^2 \frac{dg_2}{dt} = \frac{-19}{6}g_2^3, \quad (2.1.2d)$$

$$16\pi^2 \frac{dg_3}{dt} = -7g_3^3. \quad (2.1.2e)$$

In eqns.(2.1.2a) and (2.1.2b), y_t denotes the t -quark Yukawa coupling². Negative signs in the beta functions of g_2 and g_3 (see eqns.(2.1.2d) and (2.1.2e)) indicate that these gauge couplings are "asymptotically free", that is, the higher is the energy scale μ , the smaller they become [36, 37]³. A participation of all the quark flavours was assumed while deriving $\frac{dg_i}{dt}$ with $i = 1, 2, 3$. Among the SM fermions, the dominant contribution to the evolution of λ of course comes from the t -quark owing to its large value compared to the others. This, in combination with the fact the t -quark contributes with a negative term in the beta function for λ (β_λ), leads to $\lambda(Q) < 0$ at some energy scale $\mu = Q$, thereby signalling a loss of the stability of the EW vacuum [49–56]. Crucial to determining the exact location of the instability case are the boundary conditions for the SM couplings, particularly those of λ and y_t . The EW scale values of λ and y_t (at the input scale $\mu = M_t$) can be expressed in terms of the masses of h and the t -quark as follows.

$$\lambda(M_t) = \frac{M_h^2}{2v^2}(1 + \delta_h(M_t)), \quad (2.1.3a)$$

$$y_t(M_t) = \frac{\sqrt{2}M_t}{v}(1 + \delta_t(M_t)). \quad (2.1.3b)$$

In the above M_h and M_t are the pole masses of the Higgs and the t -quark [57–59], and, $\delta_h(M_t)$ and $\delta_t(M_t)$ are the corresponding threshold corrections [60–62]. These arise when the tree-level relations connecting λ and y_t respectively to M_h and M_t are modified by incorporating loop effects [58, 59, 63, 64]. A higher M_h implies a larger value of λ at the input scale and thereby a larger bosonic contribution to β_λ . This aids towards stabilising the EW vacuum.

¹Not to be confused with the t -quark.

²The Yukawa couplings of the t -quark, b -quark and τ -lepton are denoted as y_t, y_b and y_τ respectively here onwards.

³Computational details of two-loop beta functions in gauge theories can be found in [38–48].

On the other hand, a higher value for M_t signals the onset of an unstable vacuum at a lower scale.

In the recent past, sophisticated analyses of the fate of the EW vacuum within the SM have occurred. For instance, [65] employs three-loop beta functions for the λ and y_t and the respective threshold effects up to two-loop order. Such being the sensitivity, the following threshold corrections were obtained:

$$\begin{aligned} \lambda(\mu = M_t) &= 0.12604 + 0.00206\left(\frac{M_h}{\text{GeV}} - 125.15\right) \\ &\quad - 0.00004\left(\frac{M_t}{\text{GeV}} - 173.34\right) \pm 0.00030_{\text{th}}, \end{aligned} \quad (2.1.4a)$$

$$\begin{aligned} y_t(\mu = M_t) &= 0.93690 + 0.00556\left(\frac{M_t}{\text{GeV}} - 173.34\right) - 0.00042\left(\frac{\alpha_s(M_Z) - 0.1184}{0.0007}\right) \\ &\quad \pm 0.00050_{\text{th}}, \end{aligned} \quad (2.1.4b)$$

$$\begin{aligned} g_1(\mu = M_t) &= 0.35830 + 0.00011\left(\frac{M_t}{\text{GeV}} - 173.34\right) \\ &\quad - 0.00020\left(\frac{M_W - 80.384 \text{ GeV}}{0.014 \text{ GeV}}\right), \end{aligned} \quad (2.1.4c)$$

$$\begin{aligned} g_2(\mu = M_t) &= 0.64779 + 0.00004\left(\frac{M_t}{\text{GeV}} - 173.34\right) \\ &\quad + 0.00011\left(\frac{M_W - 80.384 \text{ GeV}}{0.014 \text{ GeV}}\right), \end{aligned} \quad (2.1.4d)$$

$$\begin{aligned} g_3(\mu = M_t) &= 1.1666 + 0.00314\left(\frac{\alpha_s(M_Z) - 0.1184}{0.0007}\right) \\ &\quad - 0.00046\left(\frac{M_t}{\text{GeV}} - 173.34\right). \end{aligned} \quad (2.1.4e)$$

In eqns.(2.1.4b)-(2.1.4e), $\alpha_s(M_Z)$ stands for the strong coupling constant at the energy scale $\mu = M_Z$. The precision of the analysis is further enhanced by computing the radiative corrections to λ such that one obtains a $\lambda_{\text{eff}} = \lambda +$ finite corrections. In that case the Higgs potential becomes $V(h \gg v) = \frac{1}{4}\lambda_{\text{eff}}(h)h^4$. Two loop corrections to the SM Higgs potential are calculated in [62]. Along with the corresponding two-loop corrected input scale values of the gauge couplings, the dependence of the evolution trajectory of λ_{eff} on the pole masses and $\alpha_s(M_Z)$ can be determined [66]. This is illustrated in Fig.2.1.

The evolutions of y_t and g_i are not shown separately in Fig.2.1. However, we mention in this context that they remain perturbative and are fairly weak at high energy, becoming roughly equal in the vicinity of the Planck mass. As the running of the Yukawa couplings of the other quarks and leptons are very small, these are not included in this analysis. Upon RG evolution, it is seen that value of λ at the Planck scale is negative [65], albeit small.

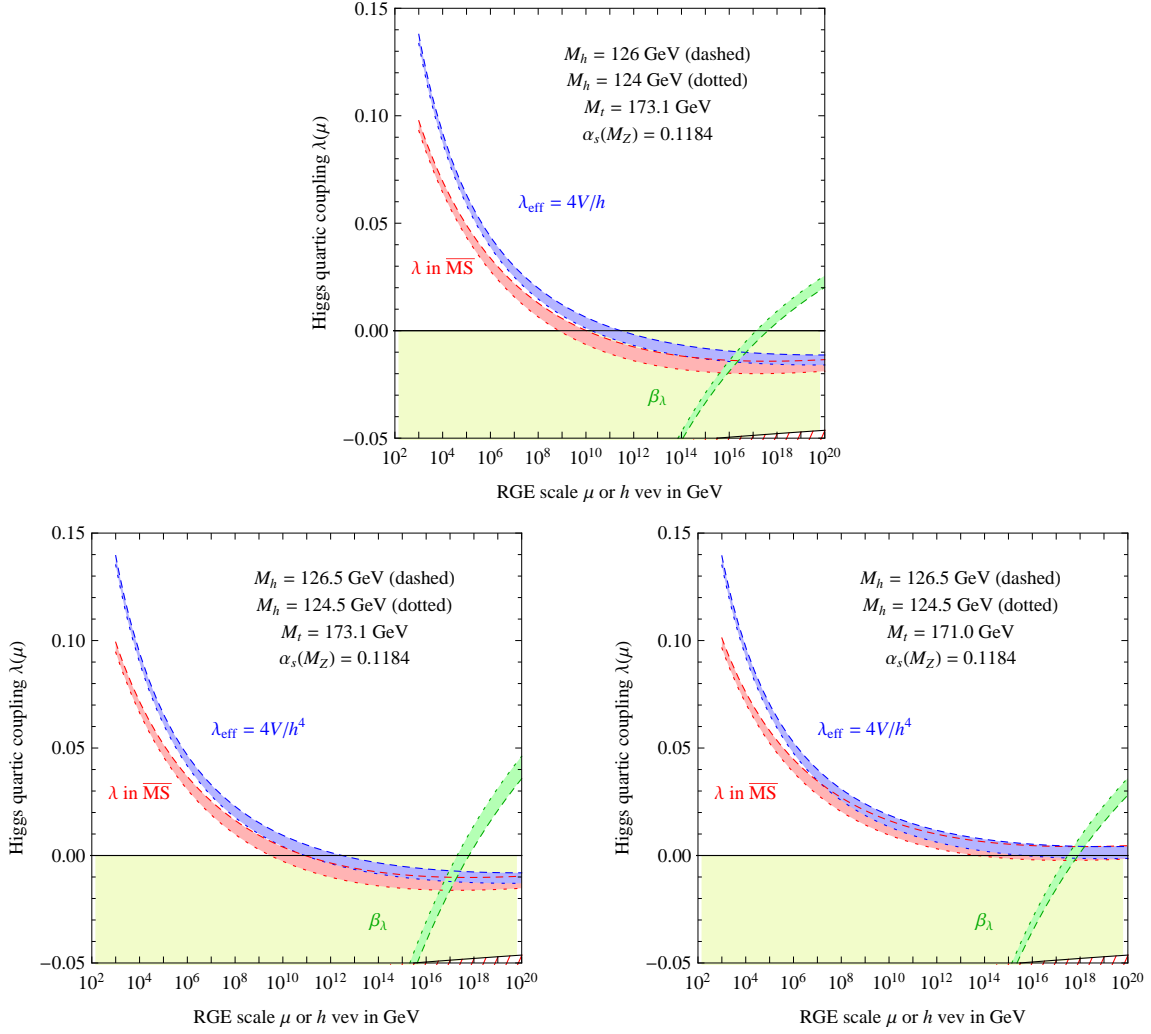


Figure 2.1: The RG evolution of λ as a function of the energy scale μ for a fixed M_h and three different sets of M_t and $\alpha_s(M_Z)$. This figure is taken from [65]

$$\begin{aligned} \lambda(M_{Pl}) = & -0.0143 - 0.0066\left(\frac{M_t}{\text{GeV}} - 173.34\right) + 0.0018\left(\frac{\alpha_s(M_Z) - 0.1184}{0.0007}\right) \\ & + 0.0029\left(\frac{M_h}{\text{GeV}} - 125.15\right). \end{aligned} \quad (2.1.5)$$

In eqn.(2.1.5), M_{Pl} denotes the Planck scale. Therefore in the current framework, the EW vacuum ceases to be the global minimum whenever $V(h \gg v) < V(h = v)$. The condition for $\lambda_{\text{eff}} > 0$ up to the Planck scale translates into the following bound on the Higgs boson mass [65].

$$M_h > 129.6 \text{ GeV} + 2.0(M_t - 173.34 \text{ GeV}) - 0.5\text{GeV}\frac{(\alpha_s(M_Z) - 0.1184)}{0.0007} \pm 0.3_{\text{th}}\text{GeV} \quad (2.1.6)$$

It is inferred from eqn.(2.1.6) that whenever M_t is at the upper edge of its allowed band, M_h too has to be correspondingly high so as to allow for a stable EW vacuum till the Planck scale. One uses $M_t = (173.34 \pm 0.76_{\text{exp}} \pm 0.3_{\text{th}})$ GeV to take into account the uncertainty in the t -quark pole mass [67]. The experimental error on the Higgs mass is already fairly small and is expected to get further reduced by future measurements in the LHC. The main source of uncertainty in eqn.(2.1.6) comes from M_t . Therefore, any refinement in the measurement of the t -mass is of great importance for the question of EW vacuum stability. Therefore, in the wake of a situation where a more precise value of the t -mass is awaited, one finds that the central values of M_h and M_t do not stabilise the vacuum all the way up to the Planck scale. Then, the effective quartic coupling λ_{eff} becomes negative around $\simeq 10^{11}$ GeV, thereby ruling out the candidature of the SM as a consistent theory till the Planck scale.

However, one may still rescue the SM, if the EW vacuum is shallower than the ‘deeper vacuum’ at a high scale, and the lifetime of tunnelling from the former to the latter is larger than the age of the universe. This corresponds to a scenario with a ‘metastable’ vacuum. In order to understand the point better, an outline of the computation of the tunnelling probability is in order.

2.1.1 Tunnelling probability

In a scalar field theory permitting two vacua, the solution to the classical equation of motion in the Euclidean form is commonly known as the ‘bounce’ [68, 69]. It actually interpolates the two vacua. Now, the SM Higgs potential in eqn.(1.4.2b) of **Chapter 1** is expressed as

$$V(h) = \frac{1}{2}m^2h^2 + \lambda vh^3 + \frac{1}{4}\lambda h^4 + \dots \quad (2.1.7)$$

where the dots in eqn.(2.1.7) stand for the Goldstone terms that vanish in the unitary gauge. We assume that the quantum corrections to $V(h)$ can be absorbed in the running coupling $\lambda_{\text{eff}}(\mu)$, renormalized at a scale $\mu \approx h$. To a good accuracy, $V(h \gg v) = \frac{1}{4}\lambda_{\text{eff}}(h)h^4$. In general, the bounce $H_b(r)$ depends only on the radial coordinate $r^2 \equiv x_\mu x_\mu$ [68]. In that case, it becomes invariant under an $SO(4)$ symmetry which is indeed a manifestation of the Lorentz symmetry in an Euclidean spacetime. In such a case, the classical equation of motion reads [70]

$$-\partial_\mu \partial_\mu H_b + V'(H_b) = -\frac{d^2 H_b}{dr^2} - \frac{3}{r} \frac{dH_b}{dr} + V'(H_b) = 0. \quad (2.1.8)$$

The appropriate boundary condition is

$$H'_b(0) = 0, H_b(\infty) = v \rightarrow 0. \quad (2.1.9)$$

Solving for the bounce gives

$$H_b(r) = \sqrt{\frac{2}{|\lambda_{\text{eff}}|} \frac{2R}{r^2 + R^2}}. \quad (2.1.10)$$

The arbitrary parameter R [70] appears in the expression of the bounce since, because of our approximations, the potential is scale-invariant: at this level, there is an infinite set of bounces of different sizes that lead to the same action. In fact, this can also be related to the dimensional regularisation scale μ . The 'classical action' denoted by $S_0[H_b]$ is defined as the Euclidean action evaluated on the classical trajectory given by $H_b(r)$. One obtains in this case

$$S_0[H_b] = \frac{8\pi^2}{3|\lambda_{\text{eff}}|}. \quad (2.1.11)$$

We then use the following classic formula for tunnelling probability (p):

$$p = T_U^4 \mu^4 \exp[-S_0[H_b]]. \quad (2.1.12)$$

In eqn.(2.1.12), T_U refers to the universe's age. In case of the Higgs, the probability of tunnelling to the deeper vacuum therefore is given by [70]

$$p = T_U^4 \mu^4 \exp\left[-\frac{8\pi^2}{3|\lambda_{\text{eff}}(\mu)|}\right]. \quad (2.1.13)$$

One fixes μ to the scale where the probability is maximised, and, it turns out that $\frac{d\lambda_{\text{eff}}}{d\log(Q)} = 0$ at $Q = \mu$. Using $T_U \simeq 10^{10}$ yr and requiring that the vacuum tunnelling lifetime is always higher than the lifetime of the universe is tantamount to the condition [70]

$$\lambda_{\text{eff}}(h) \geq \frac{-0.065}{1 - 0.01 \ln(v/\mu)}. \quad (2.1.14)$$

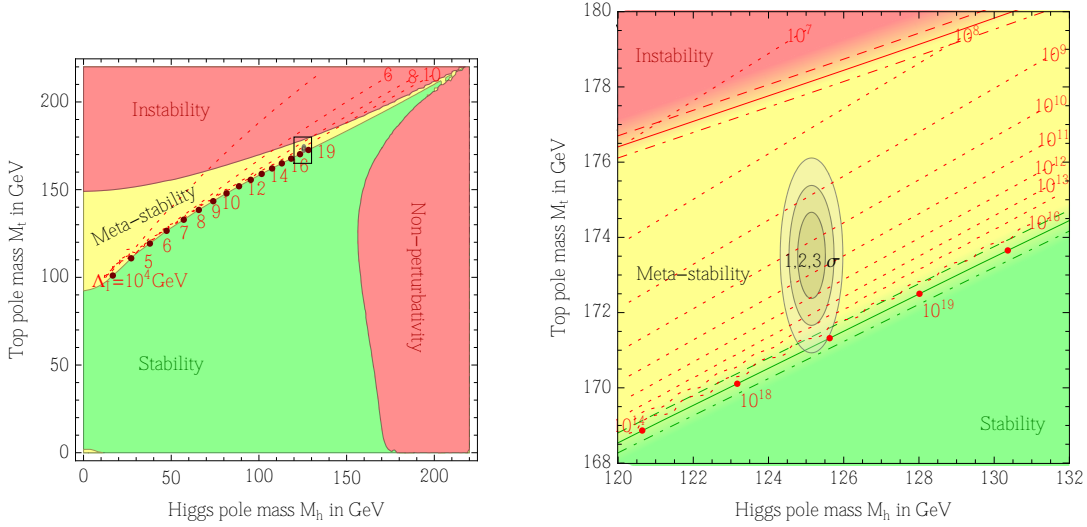


Figure 2.2: Left: SM phase diagram in terms of Higgs and top pole masses. The plane is divided into regions of absolute stability, meta-stability, instability of the SM vacuum, and nonperturbativity of the Higgs quartic coupling. The top Yukawa coupling becomes non-perturbative for $M_t \geq 230$ GeV. The dotted contour-lines show the instability scale Λ_I in GeV assuming $\alpha_s(M_Z) = 0.1184$. Right: Zoom in the region of the preferred experimental range of M_h and M_t (the grey areas denote the allowed region at 1, 2, and 3σ). The three boundary lines correspond to 1σ variations of $\alpha_s(M_Z) = 0.1184 \pm 0.0007$, and the grading of the colours indicates the size of the theoretical error. This figure has been taken from [65]

In other words, whenever $\lambda < 0$, the EW vacuum can be metastable if λ_{eff} does not take far too negative values. Therefore, for certain values of M_t and M_h , the EW vacuum in the SM is metastable. This apparent criticality is seen in Fig.2.2.

2.2 Bound from triviality

In case, h strongly couples to itself and λ is larger than the other SM interaction strengths, all terms but the $\mathcal{O}(\lambda^2)$ one can be dropped from eqn.(2.1.2a). Then, eqn.(2.1.2a) can be exactly solved to give

$$\lambda(Q) = \lambda(v) \left[1 - \frac{3}{4\pi^2} \lambda(v) \log \frac{Q^2}{v^2} \right]^{-1} \quad (2.2.1)$$

Thus, the Higgs quartic coupling varies logarithmically with the squared energy Q^2 . For energies much smaller than the EWSB scale, i.e., for $Q \ll v$, the quartic coupling becomes

extremely small and eventually vanishes. It is then said that the theory is trivial, i.e. non interacting since the coupling is zero (see [71–74] for more details). In the opposite limit of $Q \gg v$, the quartic coupling grows and eventually becomes infinite around the energy scale $Q_P = v \exp\left(\frac{4\pi^2 v^2}{3M_h^2}\right)$, commonly known as the Landau pole. This could be circumvented in the following two ways. First, one could demand $\lambda(v) = 0$, i.e., the SM to be trivial theory again. Alternatively, since the location of Q_P depends critically on M_h , one could predict a corresponding bound on it such that $Q_P < \Lambda$ is ensured, where Λ denotes an hitherto unknown cutoff of the SM. As seen from the expression for Q_P , if Λ is large, the Higgs must be accordingly light to avoid hitting the Landau pole prior to the cutoff. For instance with $\Lambda = 10^{16}$ GeV, one requires, $M_h < 200$ GeV. In turn, if the cutoff is small, the Higgs boson mass can be rather large and for $\Lambda \sim 10^3$ GeV for instance, the Higgs mass is allowed to be of the order of 1 TeV.

In particular, if the cutoff is at the Higgs mass itself, then demanding a finite Λ implies $M_h < 700$ GeV. But then, there is the following caveat: when λ is too large, one cannot use perturbation theory any more and therefore, this constraint is lost. However, from simulations of gauge theories on the lattice, where the non-perturbative effects are properly taken into account, a more rigorous bound of $M_h < 740$ GeV is obtained. One can of course adhere to a more stringent version of the triviality bound, which is to demand that λ remains altogether perturbative ($< 4\pi$) till Λ . However, if the discovered scalar of mass around 125 GeV has couplings exactly coinciding with those of the SM Higgs, then the perturbativity of the theory is assured till as high as the Planck scale itself. Therefore in the post Higgs discovery era, the bound from triviality is rendered redundant.

A combined bound on M_h from both vacuum stability and triviality can be read from Fig.2.3.

2.3 Bound from unitarity

As outlined in the previous chapter, the longitudinal components of the massive gauge bosons in a spontaneously broken gauge theory bear a one-to-one mapping with the corresponding Goldstone bosons. This apparent connection enables one to impose vital constraints on the scalar sector by using scattering amplitudes involving the longitudinal gauge bosons. This possibility was first explored in [75,76]. For instance, in the SM, the amplitude corresponding to $W_L^+ W_L^- \rightarrow W_L^+ W_L^-$ increases with the centre-of-mass energy of the scattering process.

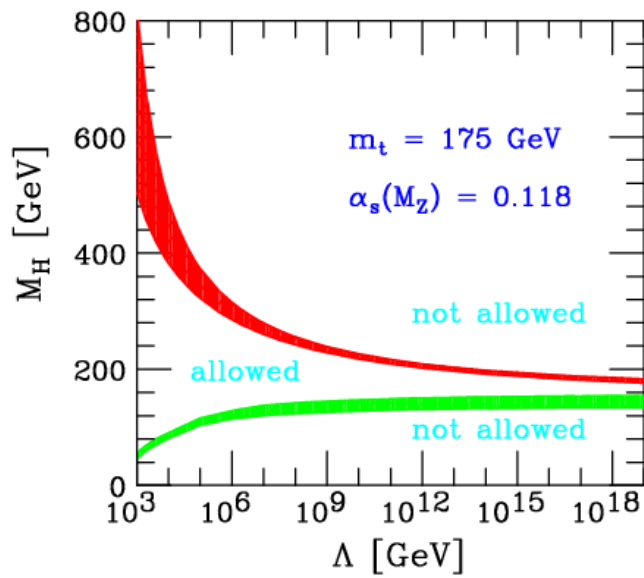


Figure 2.3: The allowed range of the Higgs mass in the SM versus the cutoff scale. Plot taken from [72].

In particular, we note

$$\mathcal{M}_{s \gg M_W^2}(W_L^+ W_L^- \longrightarrow W_L^+ W_L^-) = \frac{1}{v} \left[s + t - \frac{s^2}{s - M_h^2} - \frac{t^2}{t - M_h^2} \right], \quad (2.3.1)$$

where s, t are the Mandelstam variables. Neglecting $\mathcal{O}(\frac{M_h^2}{s})$ terms, the corresponding amplitude involving the Goldstone particles is⁴

$$\mathcal{M}_{s \gg M_h^2}(w^+ w^- \longrightarrow w^+ w^-) = -\frac{2M_h^2}{v^2}. \quad (2.3.2)$$

The amplitude is decomposed into partial waves in angular momentum l , and subsequently the scattering cross section is computed by carrying out the angular integral in the following.

$$\mathcal{M} = 16\pi \sum_{l=0}^{\infty} (2l+1) a_l P_l(\cos\theta), \quad (2.3.3a)$$

$$\sigma = \frac{16\pi}{s} \sum_{l=0}^{\infty} (2l+1)^2 |a_l|^2. \quad (2.3.3b)$$

The optical theorem equates the imaginary part of the forward-scattering amplitude to the cross section as

$$|a_l|^2 = \text{Im}(a_l) \quad (2.3.4)$$

$$|\text{Im}(a_l)| < \frac{1}{2} \quad (2.3.5)$$

In actual scattering processes, the strongest dependence on s comes from the $l=0$ terms. For $l=0$ therefore, we get

$$|\text{Im}(a_0)| < \frac{1}{2} \quad (2.3.6)$$

In other words, the corresponding amplitude $\mathcal{M}_{l=0}$ must now be bounded above at 8π as seen from eqn.(2.3.3a) Hence, using the optical theorem for the amplitude in eqn.(2.3.2) predicts an upper bound on the Higgs mass. That is,

$$M_h \leq 870 \text{ GeV}. \quad (2.3.7)$$

The above discussion captures the essence of how perturbative unitarity leads to upper bound on the mass of a scalar in a spontaneously broken theory. Of course a more sophisticated treatise is to couple $w^+ w^-$ scattering with other possible channels. That is, one must compute amplitudes amongst the states $\{w^+ w^-, w^+ h, w^+ z, z z, h h, z h\}$ and construct an amplitude matrix accordingly. In that case, a stronger bound of $M_h < 710$ GeV is obtained by demanding that each eigenvalue of the aforementioned matrix does not exceed 8π .

⁴ w^\pm, z denote the Goldstone bosons.

2.4 Need for an extended Higgs sector

This chapter emphasises that, in absence of dynamics beyond the SM, the EW vacuum can be stabilised till the Planck scale if and only if the t -quark mass is at the lower edge of its uncertainty limit. More precise measurements of the same could rule out any hope of salvaging the vacuum till the Planck scale. In such circumstances, one way to ameliorate this problem is to introduce additional bosonic degrees of freedom into the theory, preferably by extending the SM Higgs sector. With additional bosons also come additional quartic couplings. These bosonic fields modify the RG evolution trajectories of the quartic couplings by generating positive contributions in the beta functions (see for instance [77–79] and the references therein).

The extensions of the Higgs sector as discussed in the previous chapter could be potential candidates in this context. However in the process, one faces the following possibilities. First, a plurality of scalar fields opens up a higher number of directions in field space. In that case the vacuum has to be stabilised in each of these directions. Second, the bosonic contribution could get enhanced to such an extent so as to make the quartic couplings non-perturbative somewhere below the SM instability scale. This would defeat the very cause of invoking additional scalars. Balancing between these two issues calls for identifying specific allowed regions in the parameter space of the the Higgs sector. One thus derives important results by demanding that the theory remains perturbative and offers a stable vacuum till the Planck scale (or some high scale). We present such analyses for a few extended Higgs scenarios in the subsequent chapters.

Chapter 3

High-scale validity of a two-Higgs-doublet scenario: a study including LHC data

3.1 Introduction

The Higgs sector of the electroweak standard model continues to appear enigmatic from several angles. The existence of such a sector, comprising at least one scalar doublet, and driving the spontaneous symmetry breakdown $SU(2)_L \times U(1)_Y \rightarrow U(1)_Q$ is almost impossible to deny now. It is also widely agreed that the Large Hadron Collider (LHC) has found [80, 81] a neutral boson with mass around 125 GeV, which is almost certainly of spin zero [82] and dominantly a CP -even field [83–86]. However, despite the properties of the boson being *consistent* with that of the SM Higgs, rather persistent enquiries are on, to find out whether the electroweak symmetry breaking sector also contains some signature of physics beyond the standard model. The LHC data till date leaves room for such new physics.

Two sets of standpoints are noticed in such enquiries. First of all, with spin-1/2 fermions showing family replication, it is not obvious why the part of the matter sector containing spin-zero particles should also not have similar repetition. With this in view, multi-doublet scenarios are under regular scrutiny, the most widely investigated models being those with two Higgs doublets [28, 87] (as emphasised in **Chapter 1**). An extended electroweak symmetry breaking sector entails a rich phenomenology, including additional sources of CP -violation [88]. Of course, scalars belonging to higher representations of $SU(2)$ have also

attracted attention, especially triplets which can play a role in the so-called Type-II mechanism of neutrino mass generation [35]. Secondly, even with just one doublet (leading to a single physical scalar), the Higgs mass is not stable under quadratically divergent radiative corrections [25], and it is somewhat artificial (or ‘fine-tuned’) to have a 125 GeV Higgs if the cutoff for the SM is much higher than a TeV or so. Furthermore, it is also not clear that the SM scalar potential retains a finite and stable minimum at high scales. As discussed in **Chapter 2**, the next-to-next-to-leading order (NNLO) study [62, 65] finds that absolute stability up to the Planck scale requires [62]

$$M_h > 129.6 \text{ GeV} + 2.0(M_t - 173.34 \text{ GeV}) - 0.5 \text{ GeV} \frac{(\alpha_s(M_Z) - 0.1184)}{0.0007} \pm 0.3_{\text{th}} \text{ GeV}. \quad (3.1.1)$$

Thus, for the yet uncertain measurement of the top quark mass, which is crucial in governing the evolution of the Higgs self-coupling via Yukawa interactions, we may be doomed to live in an unstable vacuum if no new physics intervenes within the scale 10^{8-10} GeV [65], [89], [62], [56], [90], [91]. Therefore, the ultraviolet incompleteness of the current scheme of electroweak symmetry breaking looms up as a distinct possibility, even if one disregards the somewhat philosophical issue of naturalness.

In this chapter¹, we follow these two standpoints in tandem. We take up a two-Higgs doublet scenario as the minimal extension of the standard electroweak theory, assessing its viability as well as sufficiency modulo all available constraints. The motivation for the study is that the proportionality constant between the top quark mass and its coupling to the 125 GeV scalar is different from its SM value when more than one doublet is taken. Consequently, the dependence of the vacuum stability limit on the top quark mass is expected to be different. However, one can make precise and quantitative statements on the matter only when one takes cognizance of the exact scenario, and includes the complete set of renormalisation group equations appropriate for it. This is precisely what we aim to do here, using a two-Higgs doublet scenario at various levels of generality.

The desired suppression of flavour-changing Yukawa interactions is best implemented by imposing a discrete symmetry on such models, thus preventing both the doublets from coupling with $T_3 = +1/2$ and $-1/2$ fermions simultaneously. It is possible to go beyond such imposition and examine two Higgs doublets in a ‘basis-independent’ formulation [93–95]. However, we feel that our central issue, namely, the evolution of the Higgs self-interaction(s), is amenable to a more transparent study if one adheres to a specific Yukawa scheme. With

¹based on [92]

this in view, we adopt the so-called Type-II scenario for our study [87], to illustrate our point.

We begin by examining the situation when the discrete symmetry is exact, and derive the constraints on the low-energy values of the parameters of this scenario. The lighter neutral scalar mass being around 125 GeV is of course the prime requirement here, and constraints from rare processes such as $b \rightarrow s\gamma$ are also included. In addition, the constraints from perturbativity of all scalar quartic couplings are considered, together with those from vacuum stability. The parameter space thus validated is further examined in the light of the perturbativity and vacuum stability conditions at high scales. Thus we identify the parameter regions that keep a two-Higgs doublet scenario valid up to different levels of high scales: an exercise that reveals rather severe limits. The same investigation is carried out for cases where the discrete symmetry is broken by soft (dimension-2) and hard (dimension-4) terms in turn, with the Yukawa coupling assignment remaining (for simplicity) the same as in the case with unbroken symmetry. The effect of a CP -violating phase is also demonstrated. Finally, the regions found to be allowed from all the above considerations, at both low- and high-scales, are pitted against the existing data from the LHC in different channels. Thus we identify parameter regions that are consistent with the measured signal strengths in different channels. This entire chapter is aimed at indicating how far a two-Higgs doublet model can remain valid, not only at the LHC energy but also up to various high scales without further intervention of new physics.

Although a number of recent studies have addressed some similar questions [96–98], the present analysis has gone beyond them on the following points:

- It is revealed in this chapter that the high scale validity of the theory is less sensitive to the precise value of the top quark mass than in the SM. Regions in the parameter space are identified, for which the theory has no cutoff till the Planck scale, even though the top quark mass can be at the upper edge of the allowed band. Similarly, the high scale validity of the model is insensitive to $\alpha_s(M_Z)$.
- We find that it is rather difficult to retain the validity of a two-Higgs doublet scenario well above a TeV with the discrete symmetry intact. Also, large values of $\tan\beta$, the ratio of the vacuum expectation values (VEV) of the two doublets, are mostly disfavoured in this case.
- With the discrete symmetry broken, the theory can circumvent ultraviolet cutoffs. .

- We examine the constraints on the model including a CP -violating phase [99–102]. In fact, since the existence of a phase is a natural consequence of relaxing the discrete symmetry, the high-scale validity of a two Higgs doublet model may be argued to be contingent on the possibility of CP -violation in the scalar potential.
- We have performed a detailed examination of the validity of the scenario at both low and high scales, *including dimension-4 discrete symmetry breaking terms in our analysis*. The LHC constraints are also imposed in this situation.

3.2 The two-Higgs-doublet scenario and the scalar potential: basic features

In this chapter, we consider the most general renormalisable scalar potential for two doublets Φ_1 and Φ_2 , each having hypercharge (+1) (see eqn.(1.7.3) of **Chapter 1**),

$$\begin{aligned}
V(\Phi_1, \Phi_2) = & m_{11}^2 \Phi_1^\dagger \Phi_1 + m_{22}^2 \Phi_2^\dagger \Phi_2 - m_{12}^2 \left(\Phi_1^\dagger \Phi_2 + \Phi_2^\dagger \Phi_1 \right) + \frac{\lambda_1}{2} \left(\Phi_1^\dagger \Phi_1 \right)^2 + \frac{\lambda_2}{2} \left(\Phi_2^\dagger \Phi_2 \right)^2 \\
& + \lambda_3 \Phi_1^\dagger \Phi_1 \Phi_2^\dagger \Phi_2 + \lambda_4 \Phi_1^\dagger \Phi_2 \Phi_2^\dagger \Phi_1 + \frac{\lambda_5}{2} \left[\left(\Phi_1^\dagger \Phi_2 \right)^2 + \left(\Phi_2^\dagger \Phi_1 \right)^2 \right] \\
& + \lambda_6 \Phi_1^\dagger \Phi_1 \left(\Phi_1^\dagger \Phi_2 + \Phi_2^\dagger \Phi_1 \right) + \lambda_7 \Phi_2^\dagger \Phi_2 \left(\Phi_1^\dagger \Phi_2 + \Phi_2^\dagger \Phi_1 \right). \tag{3.2.1}
\end{aligned}$$

The parameters m_{12} , λ_5 , λ_6 and λ_7 could be complex in general, although the phase in *one* of them can be removed by redefinition of the relative phase between Φ_1 and Φ_2 . Thus this scenario in general has the possibility of CP -violation in the scalar sector.

In a general two-Higgs-doublet model (2HDM), a particular fermion can couple to both Φ_1 and Φ_2 (see eqn.(1.7.8) in **Chapter 1**). However this would lead to the flavour changing neutral currents (FCNC) at the tree level [103–106]². As outlined in **Chapter 1**, one way to avoid such FCNC is to impose a \mathbb{Z}_2 symmetry, such as one that demands invariance under $\Phi_1 \rightarrow -\Phi_1$ and $\Phi_2 \rightarrow \Phi_2$. This type of symmetry puts restrictions on the scalar potential. The \mathbb{Z}_2 symmetry is *exact* as long as m_{12} , λ_6 and λ_7 vanish, when the scalar sector also becomes CP -conserving. The symmetry is said to be broken *softly* if it is violated in the quadratic terms only, i.e., in the limit where λ_6 and λ_7 vanish but m_{12} does not. Finally, a *hard* breaking of the \mathbb{Z}_2 symmetry is realised when it is broken by the quartic terms as well. Thus in this case, m_{12} , λ_6 and λ_7 all are non-vanishing in general.

²In context of a typical flavour changing scenario, it has been shown in [107, 108] that the FCNCs are stable under RG evolution to a fairly large degree.

As mentioned in **Chapter 1**, we focus on a specific scheme of coupling fermions to the doublets. This scheme is referred to in the literature as the *Type-II* 2HDM, where the down type quarks and the charged leptons couple to Φ_1 and the up type quarks, to Φ_2 [109]. This can be ensured through the discrete symmetry $\Phi_1 \rightarrow -\Phi_1$ and $\psi_R^i \rightarrow -\psi_R^i$, where ψ is charged leptons or down type quarks and i represents the generation index. Although we start by analysing the high-scale validity of the model with $m_{12} = \lambda_6 = \lambda_7 = 0$, we subsequently include the effects of both soft and hard breaking of \mathbb{Z}_2 in turn, which bring back these parameters. The two simplifications that we still make are as follows: (a) the phases of λ_6 and λ_7 are neglected though that of m_{12} is considered, and (b) the Yukawa couplings of Φ_1 and Φ_2 are left unchanged.

Minimisation of the scalar potential in eqn.(3.2.1) yields

$$\langle \Phi_1 \rangle = \begin{pmatrix} 0 \\ \frac{v_1}{\sqrt{2}} \end{pmatrix}, \quad \langle \Phi_2 \rangle = \begin{pmatrix} 0 \\ \frac{v_2}{\sqrt{2}} \end{pmatrix}, \quad (3.2.2)$$

where the VEVs are often expressed in terms of the ratio

$$\tan \beta = \frac{v_2}{v_1}. \quad (3.2.3)$$

We parametrise the doublets in the following fashion,

$$\Phi_i = \frac{1}{\sqrt{2}} \begin{pmatrix} \sqrt{2}w_i^+ \\ v_i + h_i + iz_i \end{pmatrix} \text{ for } i = 1, 2. \quad (3.2.4)$$

Since the basis used in $V(\Phi_1, \Phi_2)$ allows mixing between the two doublets, one diagonalises the charged and neutral scalar mass matrices to obtain the physical states. There are altogether eight mass eigenstates, three of which become the longitudinal components of the W^\pm and Z gauge bosons. Of the remaining five, there is a mutually conjugate pair of charged scalars (H^\pm), two neutral scalars (H, h) and a neutral pseudoscalar (A), when there is no CP -violation. Otherwise, a further mixing occurs between (H, h) and A . The compositions of the mass eigenstates H and h depend on the mixing angle α .

In the absence of CP -violation, the squared masses of these physical scalars and the mixing angle α can be expressed as [110],

$$m_A^2 = \frac{m_{12}^2}{s_\beta c_\beta} - \frac{1}{2}v^2 \left(2\lambda_5 + \frac{\lambda_6}{t_\beta} + \lambda_7 t_\beta \right), \quad (3.2.5a)$$

$$m_{H^\pm}^2 = m_A^2 + \frac{1}{2}v^2 (\lambda_5 - \lambda_4), \quad (3.2.5b)$$

$$m_h^2 = \frac{1}{2} \left[(A + B) - \sqrt{(A - B)^2 + 4C^2} \right], \quad (3.2.5c)$$

$$m_H^2 = \frac{1}{2} \left[(A + B) + \sqrt{(A - B)^2 + 4C^2} \right], \quad (3.2.5d)$$

$$\tan 2\alpha = \frac{2C}{A - B}, \quad (3.2.5e)$$

where we have defined,

$$A = m_A^2 s_\beta^2 + v^2 (\lambda_1 c_\beta^2 + \lambda_5 s_\beta^2 + 2\lambda_6 s_\beta c_\beta), \quad (3.2.6a)$$

$$B = m_A^2 c_\beta^2 + v^2 (\lambda_2 s_\beta^2 + \lambda_5 c_\beta^2 + 2\lambda_7 s_\beta c_\beta), \quad (3.2.6b)$$

$$C = -m_A^2 s_\beta c_\beta + v^2 [(\lambda_3 + \lambda_4) s_\beta c_\beta + \lambda_6 c_\beta^2 + \lambda_7 s_\beta^2]. \quad (3.2.6c)$$

Furthermore, the interactions of the various charged and neutral scalars to the up- and down-type fermions are functions of α and β . Their detailed forms in different 2HDM scenarios, including the Type-II model adopted here for illustration, can be found in the literature [28].

3.3 Theoretical and experimental constraints

Next, we subject the Type-II 2HDM using various theoretical and experimental constraints (though the most binding ones are often irrespective of the specific type of 2HDM). It should be remembered at the outset that the most general \mathbb{Z}_2 violating 2HDM has seven quartic couplings, namely, λ_i ($i = 1, \dots, 7$), in addition to $\tan\beta$ and m_{12} , totalling to nine free parameters. Though such a nine-dimensional parameter is *prima facie* large enough to accommodate any phenomenology, the set of constraints under consideration below can ultimately become quite restrictive.

We discuss the theoretical constraints in subsection 3.3.1, and take up the experimental/phenomenological ones in the subsequent subsections. It should be noted that the parameter space is being constrained in two distinct ways. Subsections 3.3.2, 3.3.3 and 3.3.4 list essentially *low-energy* constraints which apply at the energy scale of the subprocesses leading to Higgs production. The various masses and couplings get restricted by the requirement of satisfying them. However, while such a strategy is valid for the discussion of subsection 3.3.1 as well, we additionally require the conditions laid down there to hold at various high scales, too. This not only restricts the low-energy parameters more severely, but also addresses the main issue asked in this chapter, namely, to what extent the 2HDM can be deemed ‘ultraviolet complete’.

3.3.1 Perturbativity, unitarity and vacuum stability

For the 2HDM to behave as a perturbative quantum field theory at any given scale, one must impose the conditions $|\lambda_i| \leq 4\pi$ ($i = 1, \dots, 7$) and $|y_i| \leq \sqrt{4\pi}$ ($i = t, b, \tau$) at that scale³. On applying such conditions, one implies upper bounds on the values of the couplings at low as well as high scales.

Next, we impose the more stringent condition of unitarity on the tree-level scattering amplitudes involving the scalar degrees of freedom. In a model with an extended scalar sector, the scattering amplitudes are taken between various two-particle states constituted out of the fields w_i^\pm , h_i and z_i corresponding to the parametrisation of eqn.(3.2.4). Maintaining this, there will be neutral two-particle states (e.g., $w_i^+ w_j^-$, $h_i h_j$, $z_i z_j$, $h_i z_j$) as well as singly charged two-particle states (e.g., $w_i^\pm h_j$, $w_i^\pm z_j$). The various two particle initial and final states give rise to a $2 \rightarrow 2$ *scattering matrix* whose elements are the lowest order partial wave expansion coefficients in the corresponding amplitudes. The method used by Lee, Quigg and Thacker (LQT) [111] prompts us to consider the eigenvalues of this two-particle scattering matrix [97,112,113]⁴. These eigenvalues, labelled as a_i , should satisfy the condition $|a_i| \leq 8\pi$. Again, these conditions apply to high scales as well, if we expect perturbativity to hold.

When the quartic part of the scalar potential preserves CP [114,115] and \mathbb{Z}_2 symmetries, the LQT eigenvalues are discussed in [116–118]. For $\lambda_6, \lambda_7 = 0$, we follow the procedure and notation of [116] and [118]. However, the matrices for coupled-channel analysis including λ_6 and λ_7 are derived by us (see \mathcal{M}_{NC} and \mathcal{M}_{CC} in **Appendix A.3**). The general formulae including λ_6, λ_7 , are given in **Appendix A.3**.

The condition to be taken up next is that of vacuum stability. For the scalar potential of a theory to be stable, it must be bounded from below in all directions. This condition is threatened if the quartic part of the scalar potential, which is responsible for its behaviour at large field values, turns negative. Avoiding such a possibility up to any given scale ensures vacuum stability up to that scale. The issue of vacuum stability in context of a 2HDM has been discussed in detail in [77,96,98,119,120]

The 2HDM potential has eight real scalar fields. By studying the behaviour of the quartic part of its scalar potential along different field directions, one arrives at the following

³The conditions are slightly different for the two types of couplings. The reason becomes clear if we note that the perturbative expansion parameter for $2 \rightarrow 2$ processes driven by the quartic couplings is λ_i . The corresponding parameter for Yukawa-driven scattering processes is $|y_i|^2$

⁴See **Chapter 2**

conditions [28, 121],

$$\text{vsc1} : \quad \lambda_1 > 0, \quad (3.3.1a)$$

$$\text{vsc2} : \quad \lambda_2 > 0, \quad (3.3.1b)$$

$$\text{vsc3} : \quad \lambda_3 + \sqrt{\lambda_1 \lambda_2} > 0, \quad (3.3.1c)$$

$$\text{vsc4} : \quad \lambda_3 + \lambda_4 - |\lambda_5| + \sqrt{\lambda_1 \lambda_2} > 0, \quad (3.3.1d)$$

$$\text{vsc5} : \quad \frac{1}{2}(\lambda_1 + \lambda_2) + \lambda_3 + \lambda_4 + \lambda_5 - 2|\lambda_6 + \lambda_7| > 0. \quad (3.3.1e)$$

The reader is reminded that the above conditions indicate a stable electroweak vacuum and not a metastable one. The couplings in the general \mathbb{Z}_2 violating Type-II 2HDM evolve from a low scale to a high scale according to a set of renormalisation group (RG) equations listed in **Appendix A.1**. If one proposes the UV cutoff scale of the model to be some Λ_{UV} , it might so happen that the couplings grow with the energy scale and hit the Landau pole before Λ_{UV} . A *second*, still unacceptable, possibility is that of the LQT eigenvalues crossing their unitarity limits. The RG evolution of the 2HDM couplings has been recently studied in [122, 123]. Finally, the stability conditions can get violated below Λ_{UV} , making the scalar potential unbounded from below. All these problems are avoided if one postulates that all of the conditions laid down above are valid up to Λ_{UV} , which marks the maximum energy up to which the 2HDM can be valid without the intervention of any additional physics.

3.3.2 Higgs mass constraints

The spectrum of a generic 2HDM consists of a charged scalar, a CP -odd neutral scalar and two CP -even neutral scalars. Since the LHC has observed a CP -even neutral boson around 125 GeV, we allow only those regions in the parameter space for which h , the lighter neutral scalar, lies in the mass range 124.53 - 126.18 GeV which is within 2σ error limits following [124]. In addition, the charged scalar is required to have a mass greater than 315 GeV due to low energy constraints, coming mainly from $b \rightarrow s\gamma$ [125, 126]. The benchmark points used by us are also consistent with $B \rightarrow \tau\nu_\tau$, $B_s \rightarrow \mu^+\mu^-$ and $B^0\text{-}\overline{B}^0$ mixing [126, 127].

3.3.3 Oblique parameter constraints

The presence of an additional $SU(2)$ doublet having a hypercharge $Y = 1$ modifies the electroweak oblique parameters [128]. It is to be noted that since the couplings of the fermions

to gauge bosons remain unaltered even after the introduction of the second doublet, all the additional contributions come from the scalar sector of the 2HDM. The oblique parameters can be decomposed as,

$$S = S_{SM} + \Delta S \tag{3.3.2a}$$

$$T = T_{SM} + \Delta T, \tag{3.3.2b}$$

where S_{SM} and T_{SM} denote the Standard Model (SM) contributions and ΔS and ΔT denote any new physics effect. The central value is the contribution coming from the standard model with the reference values $m_{h,\text{ref}} = 125.0$ GeV and $M_{t,\text{ref}} = 173.1$ GeV where M_t denotes the pole mass of the top quark. The expressions for ΔS and ΔT for a general 2HDM can be found in [95, 129–131]. The corresponding bounds have been collected from [132]. The splitting amongst the scalar masses affects the T parameter, which is linked to the custodial $SU(2)$ symmetry. Typically for $m_{12} = 0$, T prevents large mutual splitting among states other than the lightest neutral scalar. For $m_{12} \neq 0$, the scalars other than the light neutral one have masses $\sim m_{12}$. As m_{12} is increased, the masses approach the decoupling limit, and in that case, the oblique electroweak constraints are naturally satisfied, as the 2HDM approaches the SM in that case. The consistency with these parameters has nevertheless been explicitly ensured at each allowed point of the parameter space.

3.3.4 Collider constraints

Apart from the theoretical constraints discussed above, we also strive to find the region of parameter space of a 2HDM allowed by the recent Higgs data. The ATLAS [133–135] and CMS collaborations have measured the production cross section for a ~ 125 GeV Higgs multiplied by its branching ratios to various possible channels. In our case, since the underlying theory is a 2HDM, all the cross sections and decay widths get modified compared to the corresponding SM values. For example, the production cross section of the light neutral Higgs through gluon fusion will get rescaled in the case of a 2HDM due to the fact that the fermionic couplings of the 125 GeV Higgs are now changed with respect to the SM values by appropriate multiplicative factors. Similarly, the loop induced decay $h \rightarrow \gamma\gamma$ will now draw an additional contribution from the charged scalars. Some recent investigations in this area can be found in [136–148]. Also, model-independent analysis of the data, which impose constraints on non-SM couplings of the scalar discovered, have to allow such contributions [149–154]. In order to check the consistency of a 2HDM with the measured rates in various channels, we theoretically compute the signal strength μ^i for the i -th channel using

the relation:

$$\mu^i = \frac{R_{\text{prod}} \times R_{\text{decay}}^i}{R_{\text{width}}} . \quad (3.3.3)$$

Here R_{prod} , R_{decay}^i and R_{width} denote respectively the ratios of the theoretically calculated production cross section, the decay rate to the i -th channel and the total decay width for a ~ 125 GeV Higgs to their corresponding SM counterparts. Thus, our analysis strategy is to generate a region in parameter space allowed by the constraints coming from vacuum stability, perturbative unitarity and electroweak precision data. We subsequently compute μ^i for each point in that allowed region and compare them to the experimentally measured signal strengths, $\hat{\mu}^i$, supplied by the LHC. This exercise carves out a sub-region, which is allowed by the recent Higgs data, from the previously obtained parameter space. We have implemented the Runge-Kutta algorithm to solve the RG equations through our own code. The oblique parameters and the signal strengths to various channels have been computed using standard formulae available in the literature. Moreover, the consistency of the obtained results have been checked using the public code 2HDMC [155] at various parameter points.

For our numerical analysis, we have taken gluon fusion to be the dominant production mode for the SM-like Higgs.⁵ As for the subsequent decays of h , we have considered all the decay channels mentioned in Table 3.1. We use 1σ allowed ranges of $\hat{\mu}^i$.

3.4 Results with exact discrete symmetry

In this section, we set out to obtain the allowed parameter space of a Type-II 2HDM having an *exact* \mathbb{Z}_2 symmetry consistent with the various theoretical and collider constraints described above. In this particular case, one naturally has $m_{12} = 0$, $\lambda_6, \lambda_7 = 0$. Thus, we scan over the quartic couplings λ_i ($i = 1, \dots, 5$) within their perturbative limits ($\lambda_{1,2} \in [0, 4\pi]$ and $\lambda_{3,4,5} \in [-4\pi, 4\pi]$) and allow them to evolve from a low scale to a higher scale, designated by Λ_{UV} . The RG equations for the evolution of all the Type-II 2HDM couplings are listed in **Appendix A.1**. In our analysis, the scale from which the evolution starts, has been chosen to be the top quark pole mass $M_t = 173.1$ GeV. This pins down the values of the Yukawa couplings at that scale through the relations $y_t(M_t) = \sqrt{2}m_t(M_t)/v_2$ and $y_i(M_t) = \sqrt{2}m_i(M_t)/v_1$ for $i = b$ and τ . Here $m_j(M_t)$ refers to the *running* mass of

⁵While other channels such as vector boson fusion (VBF) and associated Higgs production with W/Z (VH) have yielded data in the 8 TeV run, the best fit signal strengths are still dominated by the gluon fusion channel. Here our primary task is to check the high scale validity of the 2HDM. In that approximation, the K-factors in σ and σ_{SM} are taken to be the same.

Channel	Experiment	$\hat{\mu}$	Energy in TeV (Luminosity in fb ⁻¹)
$h \rightarrow \gamma\gamma$	ATLAS	$1.55^{+0.33}_{-0.28}$	7 (4.8) + 8 (20.7)
$h \rightarrow \gamma\gamma$	CMS	$1.13^{+0.24}_{-0.24}$	7 (5.1) + 8 (19.6)
$h \xrightarrow{ZZ^*} 4l$	ATLAS	$1.43^{+0.40}_{-0.35}$	7 (4.6) + 8 (20.7)
$h \xrightarrow{ZZ^*} 4l$	CMS	$1.00^{+0.29}_{-0.29}$	7 (5.1) + 8 (19.7)
$h \xrightarrow{WW^*} 2l2\nu$	ATLAS	$0.99^{+0.31}_{-0.28}$	7 (4.6) + 8 (20.7)
$h \xrightarrow{WW^*} 2l2\nu$	CMS	$0.83^{+0.21}_{-0.21}$	7 (4.9) + 8 (19.4)
$h \rightarrow b\bar{b}$	ATLAS	$0.20^{+0.70}_{-0.60}$	7 (4.7) + 8 (20.3)
$h \rightarrow b\bar{b}$	CMS	$0.91^{+0.49}_{-0.49}$	7 (5.1) + 8 (18.9)
$h \rightarrow \tau\bar{\tau}$	ATLAS	$1.4^{+0.50}_{-0.40}$	8 (20.3)
$h \rightarrow \tau\bar{\tau}$	CMS	$0.91^{+0.27}_{-0.27}$	7 (4.9) + 8 (19.7)

Table 3.1: The signal strengths in various channels with their 1σ uncertainties.

the j -th fermion at the scale M_t in \overline{MS} scheme [156], [157]. In particular, we have used $m_t(M_t) = M_t(1 - \frac{4}{3\pi}\alpha_s(M_t))$ ⁶.

We obtain the allowed values of $\lambda_i(M_t)$ ($i = 1, \dots, 5$) which, in course of evolution towards Λ_{UV} , satisfy all the constraints of perturbativity, unitarity and vacuum stability at all intermediate scales. We choose $\Lambda_{UV} = 1$ TeV and $\tan\beta = 2$ as an appropriate benchmark.

We display our scan results as allowed regions of parameter space in $m_H - m_A$ plane as well in the $m_{H^\pm} - \alpha$ plane as shown in Fig.3.1. The oblique parameters play a role in restricting the splitting between the masses. Moreover, demanding perturbative unitarity and vacuum stability up to the TeV scale causes the allowed region to shrink further. In other words, for any value of the masses not within the allowed region, the quartic couplings are such that, if they are used as initial conditions in the RG equations, they would violate perturbative unitarity or vacuum stability below the TeV scale. For example, vacuum stability up to the TeV scale puts an upper bound on $|\lambda_5|$ which in turn translates into an upper bound on m_A (see eqns.(3.2.5a) and (3.3.1d)). The mixing angle α gets further constrained by the recent Higgs data. Since, values of m_H and m_A chosen do not play a role in modifying the Higgs signal strengths, we choose a benchmark $m_H = 200$ GeV and $m_A = 300$ GeV and project

⁶Unlike the SM, threshold corrections to the Yukawa couplings in a 2HDM are not available. So we only retained the one-loop QCD correction which is the same as in SM.

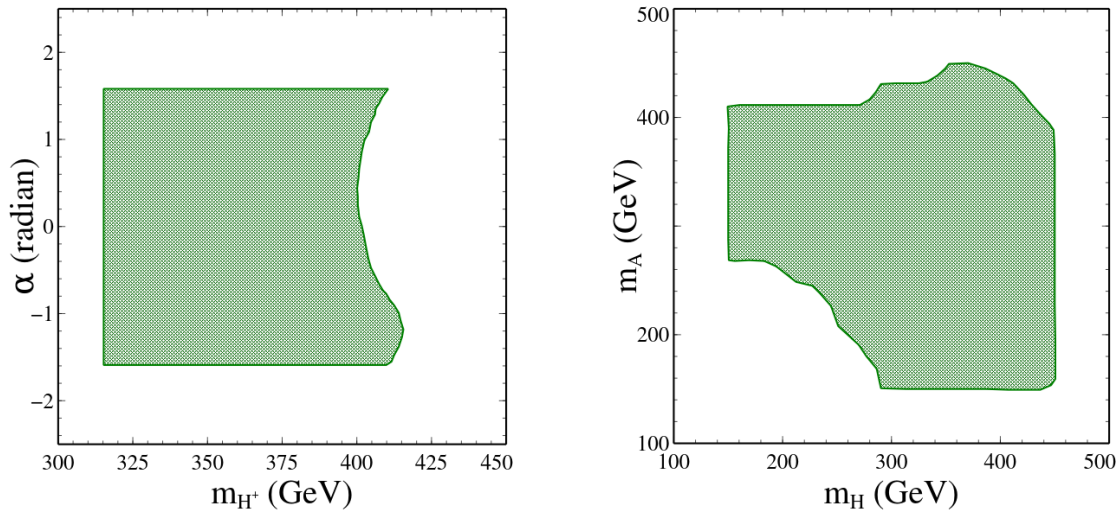


Figure 3.1: Theoretically allowed parameter spaces at $\Lambda_{UV} = 1$ TeV, $\tan\beta = 2$ and $m_{12} = 0$ GeV for $M_t = 173.1$ GeV. The region in the figure on the left is allowed concomitantly with that in the figure on the right. Note that the allowed region shown will expand further if $\tan\beta$ too is allowed to vary.

the allowed region in the $m_{H^\pm} - \alpha$ plane, shown in Fig.3.2.

Recent data indicate that M_t the top quark pole mass is $[173.07 \pm 0.52 \pm 0.72]$ GeV [127]⁷. Different values for M_t (within the allowed band) necessarily alter the running masses as well. However, choosing different values of the top quark mass does not cause any noticeable change to the allowed region in the parameter space of scalar masses and mixing angle. Since in this case, the RG running of the quartic couplings takes place over a relatively shorter length of energy scale, i.e., from the electroweak scale to 10 TeV, the evolution trajectories corresponding to different values of the top mass do not diverge apart from each other. For example, it has been checked that the allowed space in terms of masses, where we have used $M_t = 173.1$ GeV, remains almost identical if M_t takes any value between 171.0 and 175.2 GeV.

We thus can say that, in case of exact \mathbb{Z}_2 symmetry, the uncertainty in the top quark mass measurement has almost no bearing on the allowed region of the parameter space. This result alerts us to a more important one that we obtain in the next sections, namely, the high scale validity of the 2HDM irrespective of the measured value of the top quark mass.

⁷We have used the allowed range of the top quark pole mass as given in the above reference. The allowed range changes slightly, according to the most recent result [158]

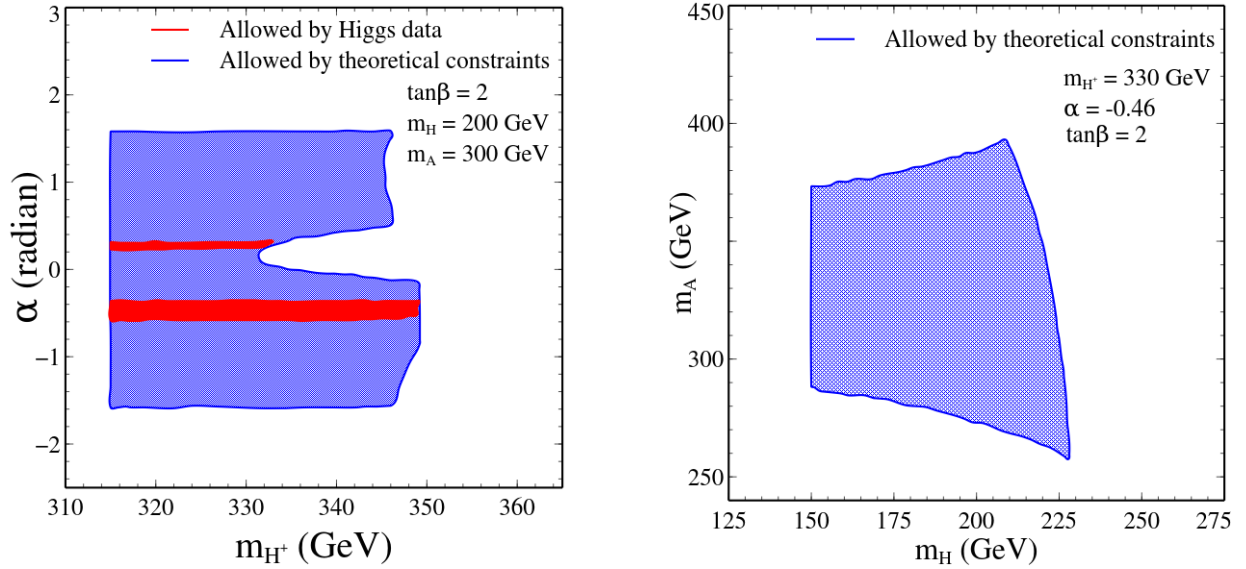


Figure 3.2: Region allowed in the $m_{H^\pm} - \alpha$ and $m_H - m_A$ planes, by the theoretical constraints and the recent Higgs data. In each case, the chosen benchmark values of the two other parameters are given in the legend.

For $\beta - \alpha = \pi/2$, the 2HDM couplings of the 125 GeV Higgs to fermions and gauge bosons are the same as the SM ones. In that case, the Higgs signal strengths to various channels should match with the corresponding SM ones. Fig. 3.2 shows an allowed band around $\alpha = \beta - \pi/2 = -0.46$ thus validating this observation. Over the entire region marked with red in Fig. 3.2, $\cos(\beta - \alpha)$ is very small. As a result, $m_H = 200$ GeV is not ruled out by the LHC data, since the ZZ and WW decay modes of H are suppressed.

To illustrate the RG running of the various couplings, the vacuum stability conditions and the LQT eigenvalues, we choose the following initial conditions,

$$\lambda_1(M_t) = 1.33, \quad \lambda_2(M_t) = 0.90, \quad \lambda_3(M_t) = 4.08, \quad \lambda_4(M_t) = -2.13, \quad \text{and} \quad \lambda_5(M_t) = -1.79 . \quad (3.4.1)$$

This choice of boundary conditions for our illustration is aimed at keeping λ_1 as low as possible, with m_h in the right range. We want to show that even with such a choice, the theory violates perturbativity and unitarity below 10 TeV. Thus the impossibility of this 2HDM with $m_{12} = 0$ at high scale gets established. Fig. 3.3 describes the RG running of λ_i with the aforementioned low values as boundary conditions. These values correspond to,

$$m_h = 125.44 \text{ GeV}, \quad m_H = 210.00 \text{ GeV}, \quad m_{H^\pm} = 345.00 \text{ GeV}, \\ m_A = 330.00 \text{ GeV}, \quad \alpha = 0.95 \text{ radian} . \quad (3.4.2)$$

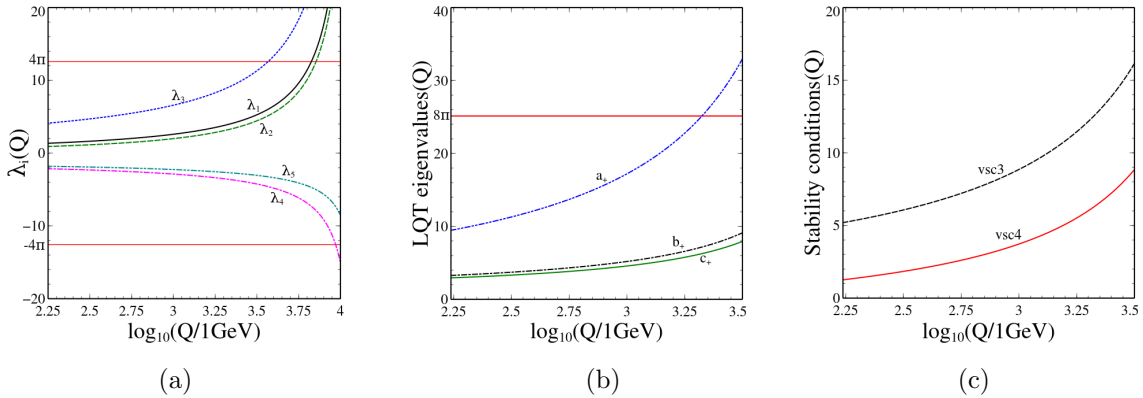


Figure 3.3: RG running of λ_i , the LQT eigenvalues and the stability conditions with the energy scale for $\tan \beta = 2$ and $m_{12} = 0$. The horizontal lines in the leftmost figure (Fig.3.3a) denote the perturbative limit and unitarity limit in the second figure (Fig.3.3b). Also a_+ , b_+ and c_+ in the second figure (Fig.3.3b) are the LQT eigenvalues explained in **Appendix A.3**. In the rightmost figure (Fig.3.3c), $vsc3$ and $vsc4$ represent the two stability conditions that are defined in eqns.(3.3.1a)-(3.3.1e).

which is an allowed point in the parameter space, as shown in Fig. 3.2. Since λ_1 starts evolving from rather large a value, it rises steeply with the energy scale. For the value of $\tan \beta$ taken here, y_b and y_τ have small initial values, and hence, they do not slow the evolution curve down to any appreciable extent (see eqn. (A.1.2a) in **Appendix A.1**). On the other hand, y_t , being the dominant Yukawa coupling in this case, prevents λ_2 to rise as sharply as λ_1 . The LQT eigenvalues (see eqn.(A.3.3) in **Appendix A.1**) a_+ , b_+ and c_+ evolve in a manner as shown in Fig.3.3b. Also, the stability conditions remain positive during the course of evolution, as shown in Fig.3.3c. A different initial condition which has a higher value of $\lambda_1(M_t)$ for instance, would lead to steeper evolution trajectories for the couplings. Hence, the overall conclusions regarding high-scale validity of this scenario would not alter.

This leads to the observation that the various λ_i become non-perturbative below a scale of 10 TeV. Also, it is seen that the LQT eigenvalue a_+ hits the unitarity limit faster than the quartic couplings hit their perturbative limits. Thus, this example illustrates the interplay among *perturbativity* and *unitarity* in determining the UV fate of this scenario and it appears that unitarity often proves stronger as a constraint than perturbativity. It should also be noted that all plots in Figs.3.1 and 3.2 use $\tan \beta = 2$. This is because the quartic couplings cannot be kept in their perturbative limits for $\tan \beta \geq 3$. A wider scan over the parameter

space corresponds to this observation. Also, one can generally conclude that in order to push the UV limit of 2HDM to higher scales, one must look beyond the *exact* \mathbb{Z}_2 symmetric case.

3.5 Results with softly broken discrete symmetry

This section illustrates the effects of the various constraints imposed on the model with non-zero m_{12} , i.e., in presence of a *soft* \mathbb{Z}_2 symmetry violating term. The RG runnings of the various couplings in the model are just like the ones in *exact* \mathbb{Z}_2 symmetric case, the only differences being in the expressions for the scalar masses as evident from eqn.(3.2.5). We scan the model parameter space and look for points which satisfy all the theoretical constraints up to $\Lambda_{UV} = 10^3, 10^{11}, 10^{16}, 10^{19}$ GeV in Figs. 3.4, and 3.6. Validity of the model up to the TeV scale, Grand Unification scale, Planck scale as well as $\sqrt{M_{\text{Pl}}M_{\text{TeV}}}$ is addressed in this manner⁸ The results in the figure show that as we go higher in Λ_{UV} , the allowed parameter space shrinks. The splitting amongst the scalar masses becomes the narrowest at the Planck scale, albeit being dependent on the values of $\tan\beta$ and m_{12} .

An inspection of the results so obtained shows that as Λ_{UV} is pushed towards higher scales, the allowed parameter space shrinks, and finally at the Planck scale, it is most constrained. For example, for $\tan\beta = 10$, $m_{12} = 200$ GeV and $\Lambda_{UV} = 10^{19}$ GeV, the masses (in GeV) are observed to lie in the following range,

$$m_H \in [635, 636], \quad m_{H^\pm} \in [619, 652], \quad m_A \in [618, 653] . \quad (3.5.1)$$

We note here that though m_{12} does not appear in the RG equations themselves, it indirectly puts constraints on λ_i through the mass constraints.

Since $\tan\beta$ determines the initial conditions for the Yukawa couplings, it does affect the RG running of λ_i . Although $m_b(M_t)$ and $m_\tau(M_t)$ are small compared to $m_t(M_t)$, for a high $\tan\beta$, $y_b(M_t)$ could be comparable to $y_t(M_t)$. This is the main motivation behind our choosing $\tan\beta = 20$. A change in the top quark mass is expected to modify the obtained

⁸Here M_{Pl} and M_{TeV} represents the Planck scale and TeV scale respectively. The benchmarks chosen are $\tan\beta = 2, 10, 20$ and $m_{12} = 200, 1000$ GeV, which represent the electroweak and TeV scales. This also keeps the 2HDM spectrum within the ultimate reach of the LHC. Having $\tan\beta$ higher than in the previous section is possible in this case, so long as m_{12} is correspondingly large, thus generating an acceptable m_h . For $\Lambda_{UV} = 10^{11}, 10^{16}, 10^{19}$ GeV, we project our allowed results as two dimensional contour plots in the $m_H - m_A$ and $m_{H^\pm} - \alpha$ planes. In each row, the plots in the left- and right-hand sides represent concomitantly allowed regions. This choice pins down the 2HDM parameter space in terms of the physically measurable observables.

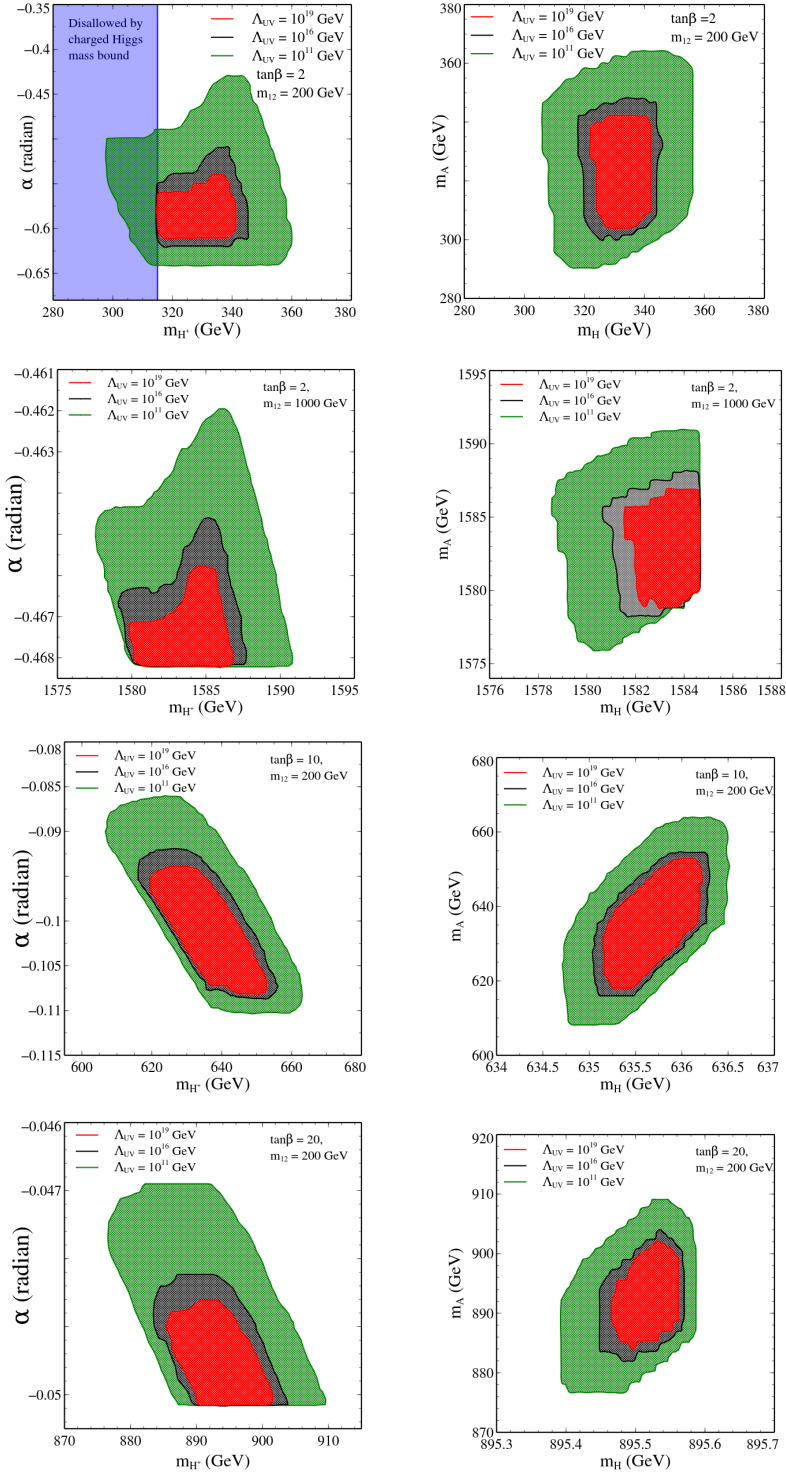


Figure 3.4: The allowed parameter spaces in the soft \mathbb{Z}_2 breaking case for $\Lambda_{UV} = 10^{11}$ (green), 10^{16} (grey) and 10^{19} GeV (red). The $\tan\beta$ and m_{12} values are shown in the plots. The shaded region (blue) in the top left figure denotes the exclusion coming from flavour constraints.

parameter space to a considerable extent. This fact is illustrated in Fig.3.5 where we choose $M_t = 171.0, 175.2$ GeV and highlight the difference in the parameter spaces so obtained. In the subsequent sections, we keep $M_t = 173.1$ GeV. It may be argued that in determining the high scale validity of the model, the relatively less crucial role played here by the top quark mass is just due to the larger number of free parameters in the 2HDM scenario. While this is true in a sense, the analysis reported in Fig.3.5 was still required for the following reason. To counter the downward evolution of λ_2 due to the top quark Yukawa coupling (see eqn.(A.1.2b) in **Appendix A.1**), the participation of the other λ_i plays a role. However, large values of these parameters may again violate perturbative unitarity, and in turn prevent one from extending the theory to high energy scales. The lesson to learn from Fig.3.5 is that valid regions in the parameter space can be found, which survive the above tug-of-war. Consequently, a Type-II 2HDM may hold true till the Planck scale without any additional new physics, even for high-end values of the top quark mass.

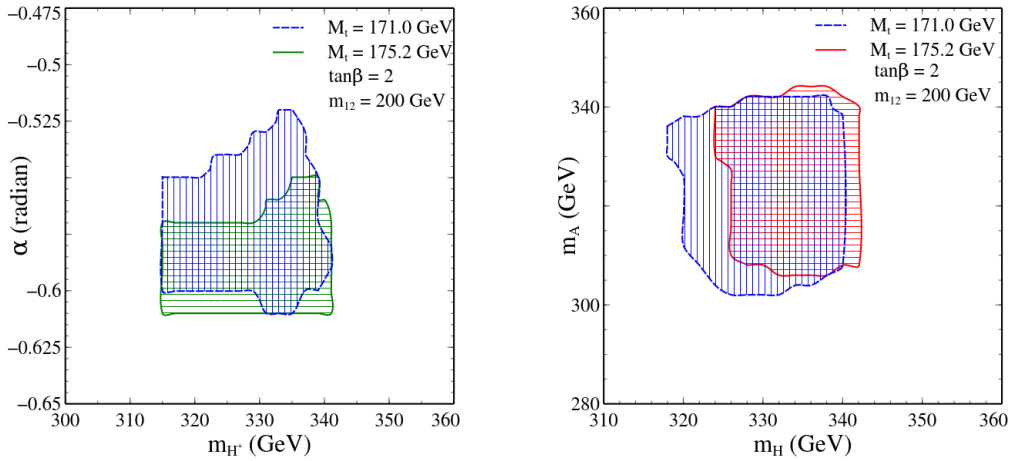


Figure 3.5: A comparison of the allowed parameter spaces at $\Lambda_{UV} = 10^{19}$ GeV, $\tan\beta = 2$ and $m_{12} = 1000$ GeV for two values of M_t , in the soft \mathbb{Z}_2 breaking case.

The impact of the recent LHC data on the parameter space already allowed by the theoretical constraints is shown in Fig.3.6. In this case, we pick up benchmark values of m_H and m_A suitably to avoid the direct search constraints. In addition, these benchmarks are chosen from a region satisfying the theoretical constraints up to the Planck scale. The 2HDM decay widths are sensitive to the mixing angles and the charged scalar mass and the collider constraints carve out a subregion in the $m_{H^\pm} - \alpha$ plane.

The figure shows allowed bands around $\alpha = \beta - \pi/2$ in each case. Note that for scalar masses ~ 1 TeV or more, the entire region allowed by the theoretical constraints is favoured

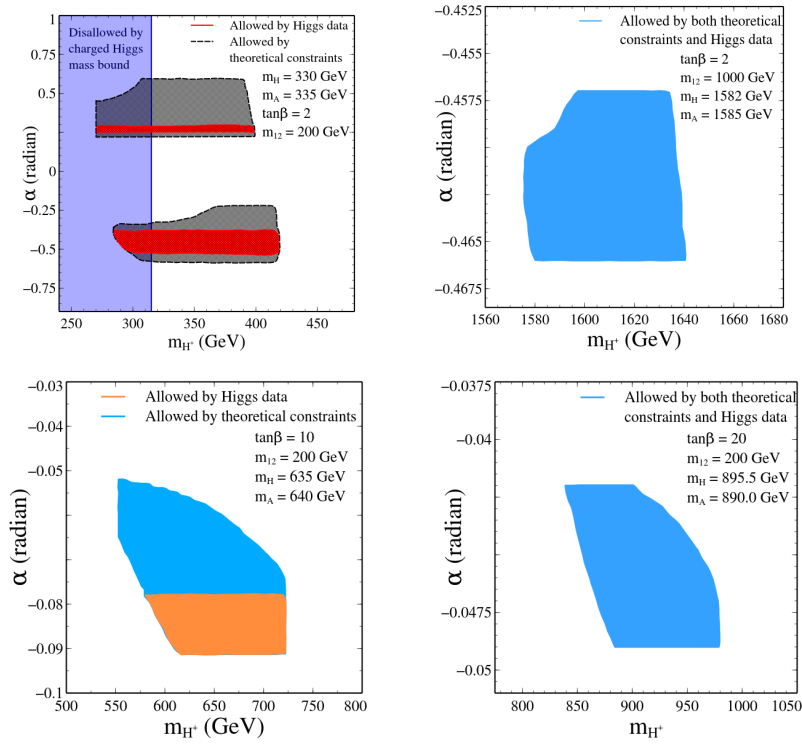


Figure 3.6: Regions in the m_{H^\pm} - α plane allowed by the Higgs data in the soft \mathbb{Z}_2 breaking case.

by the Higgs data. This is precisely due to the decoupling of the heavier degrees of freedom from the theory.

A small enough initial value of λ_2 causes $\lambda_2(Q)$ to turn negative at some scale affecting the vacuum stability of the theory thereby. To illustrate the point better, we choose an initial condition,

$$\lambda_1(M_t) = 0.03, \lambda_2(M_t) = 0.39, \lambda_3(M_t) = 0.49, \lambda_4(M_t) = -0.50 \text{ and } \lambda_5(M_t) = 0.03, \quad (3.5.2)$$

for the quartic couplings at $\tan\beta = 2$ and $m_{12} = 1000$ GeV, out of the allowed set of couplings which obey all the imposed constraints up to the $\Lambda_{UV} = 10^{19}$ GeV. These quartic couplings expressed in terms of the masses and the mixing angle become,

$$\begin{aligned} m_h &= 124.78 \text{ GeV}, \quad m_H = 1582.31 \text{ GeV}, \quad m_{H^\pm} = 1585.64 \text{ GeV}, \\ m_A &= 1580.56 \text{ GeV}, \quad \alpha = -0.466 \text{ radian}. \end{aligned} \quad (3.5.3)$$

We display the RG running of the λ_i , the stability conditions and the LQT eigenvalues in Fig.3.7. This choice of sample boundary conditions here is guided by a consideration complimentary to that of Fig.3.3. Here we show that it is possible to identify points in the parameter space, which correspond to the quartic couplings avoiding any perturbativity, unitarity or vacuum stability constraints all the way up to the Planck scale.

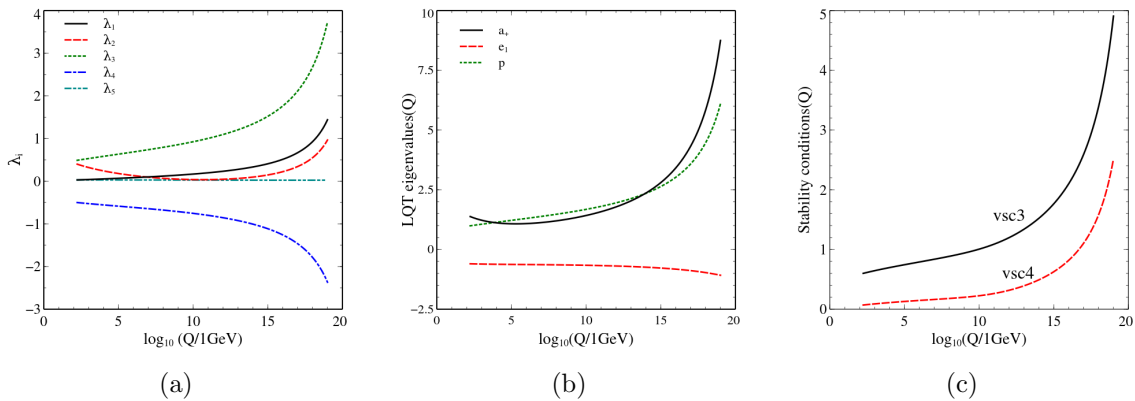


Figure 3.7: RG running of λ_i , the LQT eigenvalues and the stability conditions with the energy scale for $\tan\beta = 2$ and $m_{12} = 1000$ GeV in the soft \mathbb{Z}_2 breaking case.

As indicated in Fig.3.7b, $a_+(Q)$ grows most sharply amongst the other LQT eigenvalues and hence violates unitarity just after crossing the Planck scale in this case. Thus it turns

out that $|a_+(Q)| \leq 8\pi$ proves to be the strongest constraint in determining an upper bound on $|\lambda_i|$. Evolution of λ_i and the stability conditions are shown in Figs.3.7a and 3.7c.

The most important observation that emerges from this part of the chapter is that *the 2HDM can be valid all the way up to the Grand unification theory (GUT) scale or even the Planck scale without the intervention of any new physics. This is true even if the top quark mass is at the upper end of the currently allowed range.* The additional quartic couplings can counterbalance the effect of the Yukawa coupling threatening vacuum stability, while still remaining acceptable from the standpoint of perturbativity. It is seen that we get allowed parameter space for $\Lambda_{UV} = 10^{19}$ GeV corresponding to several values of $\tan \beta$ and m_{12} . For too large an m_{12} , the contribution of the extra scalars decouples from the theory. In that case, the RG running of the couplings below that m_{12} is governed by the SM beta functions. In that case, the stability of the electroweak vacuum is again more sensitive to the value chosen for M_t . This has been explicitly checked, for example with $m_{12} = 10^5$ GeV.

The strong coupling constant affects our analysis by determining the initial condition for g_3 . Current measurements yield a value 0.1184 ± 0.0007 for $\alpha_s(M_Z)$. In our analysis, we have used $\alpha_s(M_Z) = 0.1184$ throughout. However, we demonstrate the effect of a 3σ variation of $\alpha_s(M_Z)$ on the running of λ_2 , the quartic coupling where the effect is expected to be more pronounced compared to the other ones.

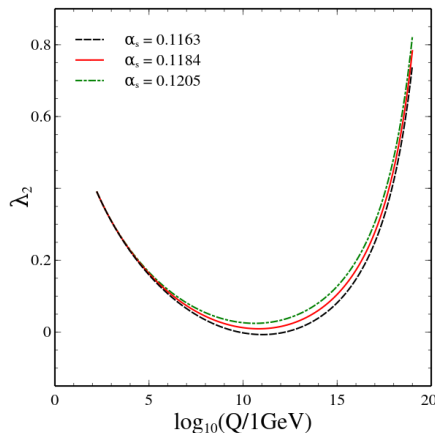


Figure 3.8: Running of λ_2 for three different values for $\alpha_s(M_Z)$ in the soft \mathbb{Z}_2 breaking case.

We took $\lambda_2(M_t) = 0.39$ in Fig.3.8. It is seen that the RG running is not significantly altered even by a 3σ variation of $\alpha_s(M_Z)$. Hence, for any value of $\alpha_s(M_Z)$ within this band, the parameter spaces will not change in a major fashion, and whatever constraints apply to $\lambda_2(M_t)$ will continue to be valid rather insensitively to $\alpha_s(M_Z)$.

The implication of having a complex m_{12} in the scalar potential [114, 115] is also investigated here. We rewrite the quadratic part of the scalar potential as

$$V_{quad}(\Phi_1, \Phi_2) = m_{11}^2 \Phi_1^\dagger \Phi_1 + m_{22}^2 \Phi_2^\dagger \Phi_2 - |m_{12}^2| \left(e^{i\delta} \Phi_1^\dagger \Phi_2 + e^{-i\delta} \Phi_2^\dagger \Phi_1 \right). \quad (3.5.4)$$

The quartic couplings are kept real as in the previous case. The presence of an arbitrary phase δ in m_{12}^2 , leads to a charged scalar H^+ , three neutral scalars H_1 , H_2 and H_3 which are not eigenstates of CP , and of course the charged and neutral Goldstone bosons. The masses of the neutral scalars can not be obtained in closed form in this case, rather, the corresponding mass matrix has to be diagonalised numerically. In the process of doing that, we choose the lightest neutral scalar, say H_3 to be around 125 GeV and the charged scalar to have a mass higher than 315 GeV. The quartic couplings satisfying these conditions are selected and are further constrained by the imposition of the theoretical constraints under RG.

We have chosen the values $\delta = \frac{\pi}{4}$, $|m_{12}| = 200$ GeV and $\tan \beta = 2$ as benchmark. This choice is illustrative. Constraints on the phase from, say, the electron dipole moment requires full evaluation at each point in the parameter space. For more discussions, we refer the reader to [159]. Scatter plots in mass planes are presented in Fig.3.9. For higher Λ_{UV} , the bounds on the scalar masses become tighter. To make the effect of the added phase in changing the scalar masses, we also show the mass bounds in the situation with $\delta = 0$. We would like to emphasise that it is not our purpose here to scan the allowed range of δ for different values of the mass parameters and quartic couplings. The point that we make is that the validity of this 2HDM up to high scales holds even with a CP -violating phase in the potential. $\delta = \frac{\pi}{4}$ is chosen as a benchmark for this demonstration. A detailed study of the δ dependence of the allowed parameter space and its phenomenological implications is the subject of a separate project.

Our observation therefore is that the regions in the parameter space of a 2HDM, consistent with UV- completion at the GUT/Planck scale, are dependent on the phase of the complex parameter(s) of the scalar potential. Together with the less crucial role played by the top mass uncertainty, this is the other important lesson to take home from this section.

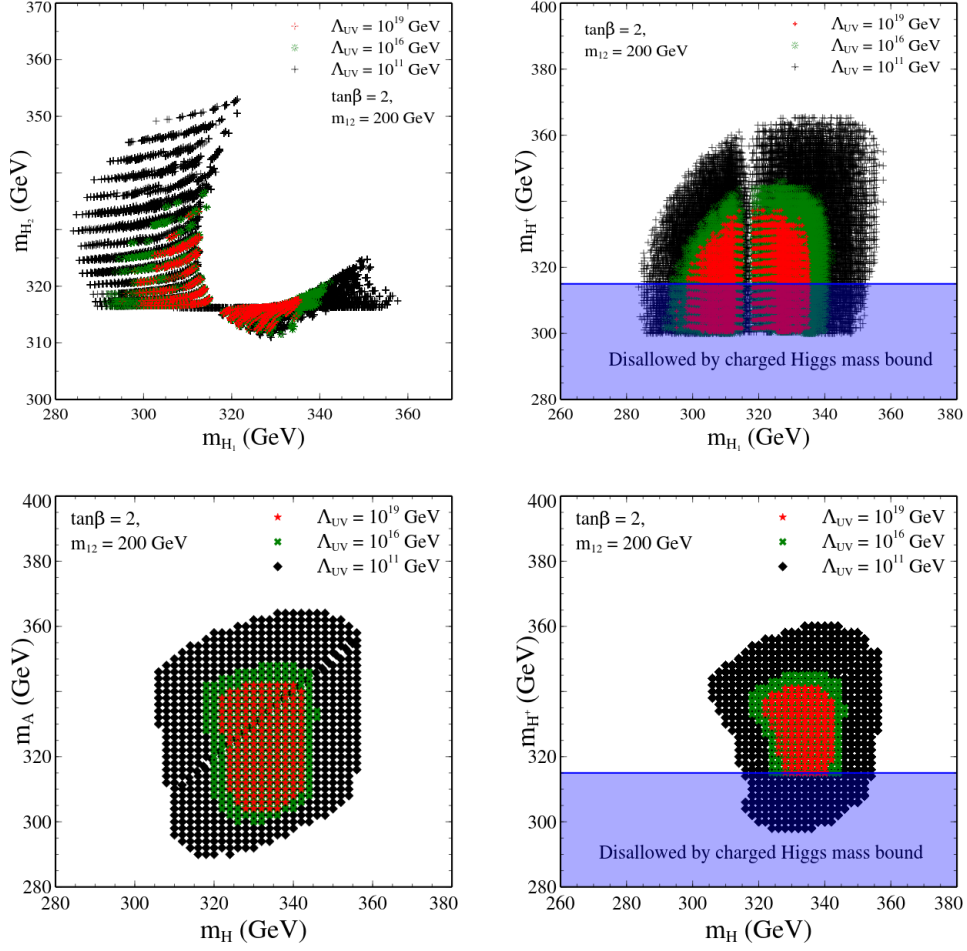


Figure 3.9: The allowed regions in mass plane as a function of Λ_{UV} in the soft \mathbb{Z}_2 breaking case. The upper and lower two plots correspond to $\delta = \frac{\pi}{4}$ and $\delta = 0$ respectively.

3.6 Results with quartic terms breaking the discrete symmetry

We now come to the last part of the chapter where the \mathbb{Z}_2 symmetry is broken both at the *soft* and *hard* level (i.e., $m_{12}, \lambda_6, \lambda_7 \neq 0$). In this case however, the RG running of the various couplings in the theory is different with respect to the *soft* breaking case, owing to the introduction of λ_6 and λ_7 (see [Appendix A.1](#) for the complete set of RG equations). While scanning the λ_i parameter space, we try to reduce the number of free parameters so that the analysis does not become unwieldy. We therefore fix some parameters studied earlier within their allowed ranges. In this spirit, we choose $\lambda_1(M_t) = 0.02$ and $\lambda_6(M_t) = \lambda_7(M_t)$ for computational convenience. $\lambda_1(M_t)$ has been deliberately chosen to be small so that it respects perturbative unitarity even up to the Planck scale. As in the plots shown previously, we present the allowed regions in the $m_H - m_A$ and $m_{H^\pm} - \alpha$ planes which satisfy all the conditions up to $\Lambda_{UV} = 10^3, 10^{11}, 10^{16}, 10^{19}$ GeV. The benchmarks are $\tan \beta = 2, 10, 20$ and $m_{12} = 200, 1000$ GeV. The results of the scans are shown in [Fig.3.10](#).

The range over which the scalar masses are distributed can be seen in [Fig.3.10](#). We note that for $m_{12} = 1$ TeV, the resulting scalar spectrum is almost degenerate. This is precisely due to the fact that the theoretical constraints pin down the allowed values of λ_i to a rather constricted range which also constrains the scalar masses and also the mixing angle in turn.

In the case where $\Lambda_{UV} = 10^3$ GeV, we show the subregions in the parameter spaces which are also allowed by the recent Higgs data. Similar to the previous sections, the results have been given in terms of allowed regions in the $m_{H^\pm} - \alpha$ plane for specific benchmark values of m_H and m_A . The major constraint, however, comes from the signal strength corresponding to $h \rightarrow \gamma\gamma$. It is clearly seen in [Fig.3.11](#) that $m_{12} = 1000$ GeV allows for a bigger region in the parameter space that is allowed by the Higgs data at 1σ level, compared to what $m_{12} = 200$ GeV does. This is obviously expected, given the fact that a high value of m_{12} takes the theory towards the decoupling limit, and thus the 125 GeV Higgs becomes SM-like. Hence, the bounds predicted on the scalar masses and the mixing angle together by the theoretical and collider constraints could be well tested in the next run of the LHC.

We demonstrate the UV-completion of the *hard* \mathbb{Z}_2 violating case by showing the RG evolution of the various quartic couplings and stability conditions up to $\Lambda_{UV} = 10^{19}$ GeV. We choose the following initial conditions for the quartic couplings at $\tan \beta = 2$ and $m_{12} = 1000$ GeV,

$$\lambda_1(M_t) = 0.02, \quad \lambda_2(M_t) = 0.48, \quad \lambda_3(M_t) = 0.40, \quad \lambda_4(M_t) = -0.30,$$

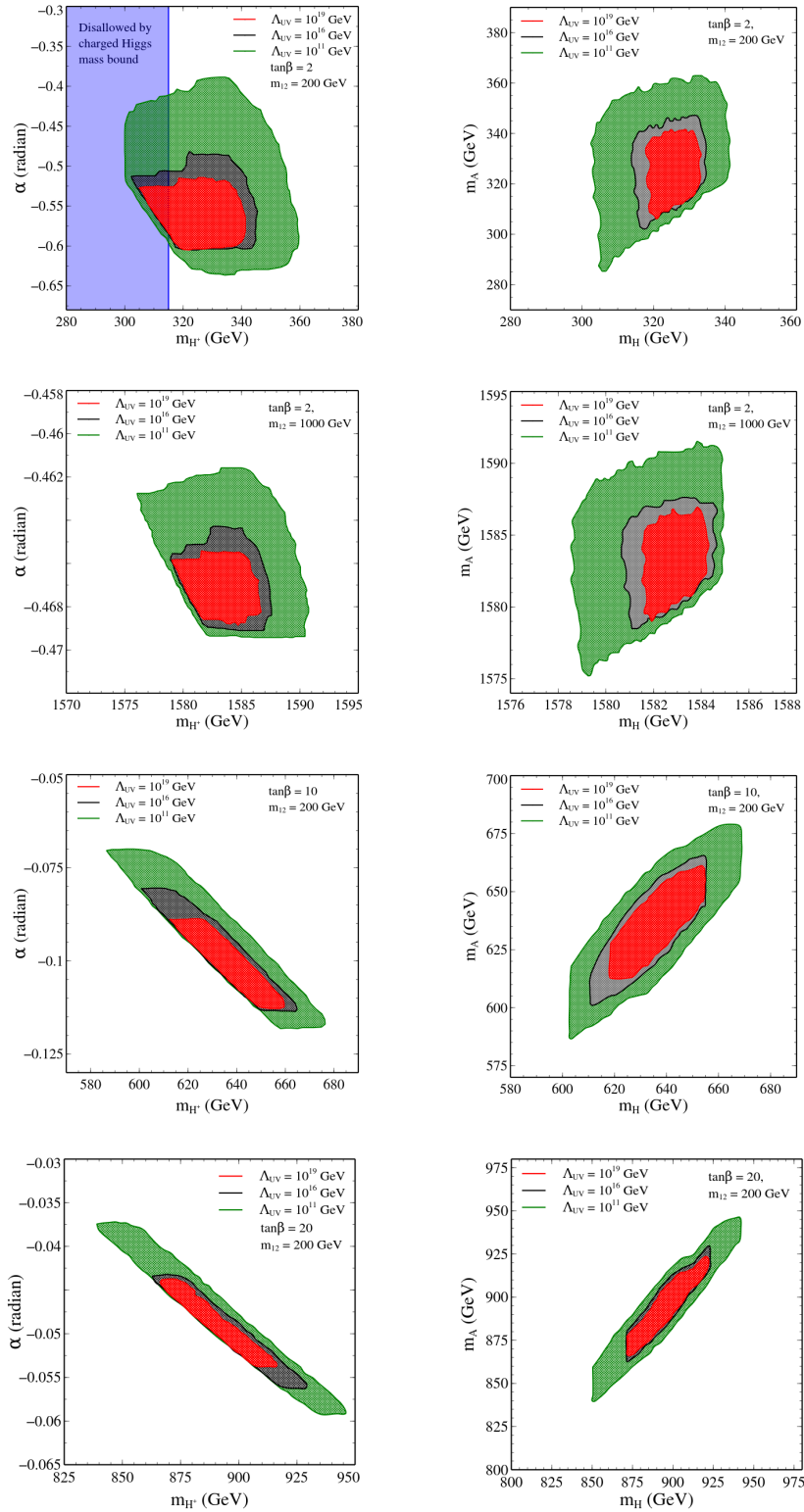


Figure 3.10: The allowed parameter spaces for $\Lambda_{UV} = 10^{11}$ (green), 10^{16} (grey) and 10^{19} GeV (red), in the $\lambda_6, \lambda_7 \neq 0$ case. The $\tan\beta$ and m_{12} values are shown in the plots.

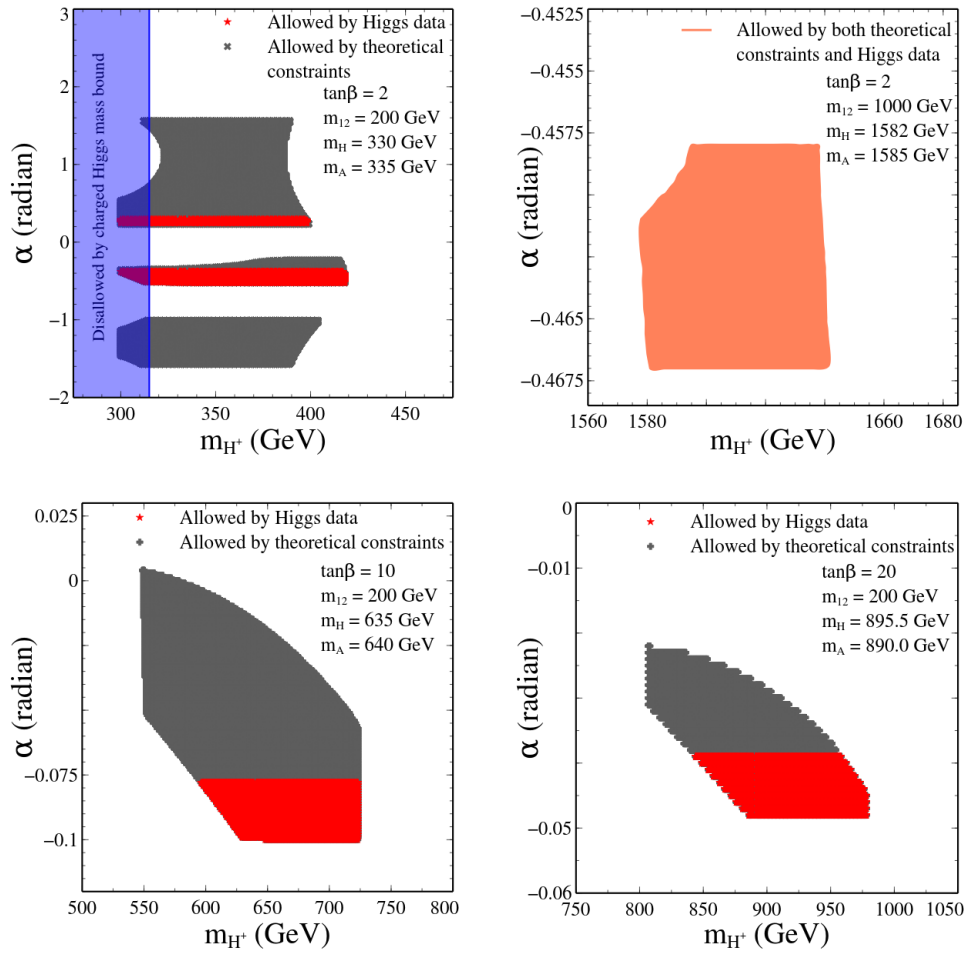


Figure 3.11: Results for $\Lambda_{UV} = 1$ TeV, in the $\lambda_6, \lambda_7 \neq 0$ case. The regions in red denote the part of the parameter space allowed by the Higgs data.

$$\lambda_5(M_t) = -0.01, \lambda_6(M_t) = -0.05 \text{ and } \lambda_7(M_t) = -0.05 . \quad (3.6.1)$$

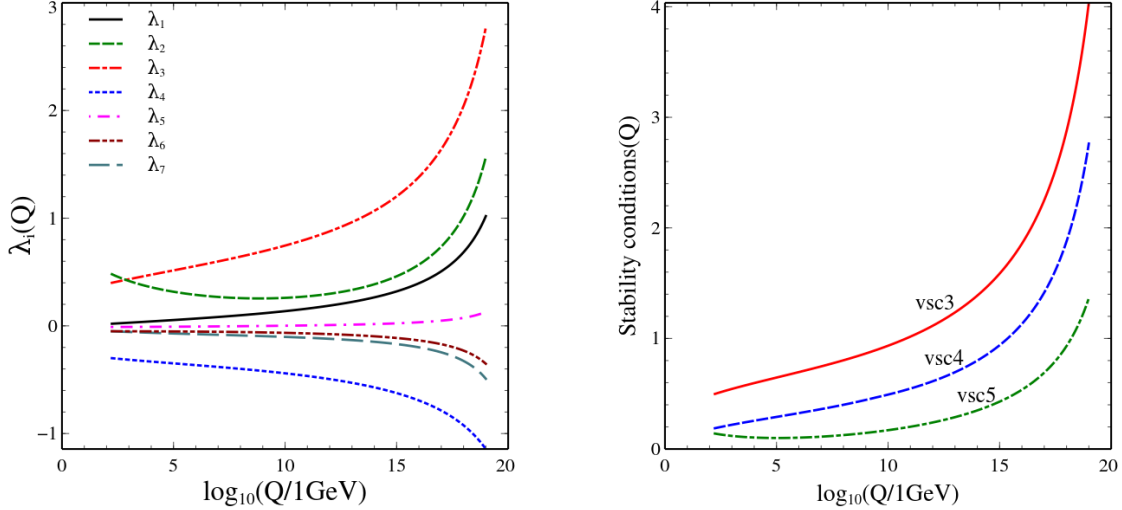


Figure 3.12: RG running of λ_i and the stability conditions with the energy scale for $\tan \beta = 2$ and $m_{12} = 1000$ GeV, in the $\lambda_6, \lambda_7 \neq 0$ case.

These particular initial conditions correspond to,

$$\begin{aligned} m_h &= 124.62 \text{ GeV}, \quad m_H = 1583.33 \text{ GeV}, \quad m_{H^\pm} = 1585.30 \text{ GeV}, \\ m_A &= 1582.52 \text{ GeV}, \quad \alpha = -0.467 \text{ radian} , \end{aligned} \quad (3.6.2)$$

and is an allowed point in the parameter space corresponding to the benchmark $m_{12} = 1000$ GeV, $\tan \beta = 2$ and $\Lambda_{UV} = 10^{19}$ GeV. As explained just after eqn.(3.4.1), the low-energy boundary values in are just illustrative. In all our scans (shown in Figs.3.1, 3.2, 3.4, 3.5, 3.6, 3.9, 3.10 and 3.11) to determine high-scale validity, a wide range of such boundary conditions are employed. Thus there is nothing fine-tuned about eqns.(3.4.1),(3.5.2) and (3.6.1). As shown in Fig.3.12, λ_3 increases most sharply whereas λ_2 first plunges down due to the effect of the $\mathcal{O}(y_t^4)$ term in the RG equation (see eqn.(A.1.2b) in **Appendix A.1**) and then starts increasing. Choosing same initial conditions for λ_6 and λ_7 causes their evolutions to become fairly similar. In this section, it should be noted that the allowed parameter spaces found are not expected to be exhaustive as we have not scanned over all $\lambda_i(M_t)$ independently, rather, have put $\lambda_1(M_t) = 0.02$ and $\lambda_6(M_t) = \lambda_7(M_t)$ while doing so. However, given the similar structure of the 1-loop beta functions of λ_6 and λ_7 (see eqns.(A.1.2f) and (A.1.2g) in **Appendix A.1**), the bounds obtained on them would have not substantially changed even if an independent scanning would have been done.

3.7 Summary and conclusions

We set out to investigate the high-scale behaviour of a 2HDM. The results are illustrated in the context of a Type-II scenario. We have used the theoretical constraints of perturbativity, unitarity and vacuum stability to constrain the parameter space of the model. The relatively less stringent constraints from oblique parameters, and also the LHC constraints on the signal strength in each decay channel of a Higgs around 125 GeV have also been taken into account.

We find that a 2HDM with a discrete \mathbb{Z}_2 symmetry (thereby forbidding some cross-terms in the two doublets in the potential) cannot be valid beyond 10 TeV, since otherwise the requirement of keeping one neutral scalar mass around 125 GeV cannot be met. With the discrete symmetry broken, on the other hand, it is possible to fulfil all the constraints over a much larger region of the parameter space. Thus the theory with a 2HDM can distinctly be valid up to energies as high as 10^{16} GeV or even the Planck scale, without the intervention of any additional physics. This feature holds irrespectively of the uncertainty in the measured value of the top quark mass, which is in contrast to what is expected in the standard model with a single Higgs doublet. In addition, high-scale validity of this scenario is not affected by the uncertainty in the strong coupling $\alpha_s(M_Z)$. The effect of a CP -violating phase in the potential is also considered, it is found that one can find regions in the parameter space valid up to high scales for at least one illustrative value (viz. $\frac{\pi}{4}$) of the phase. The allowed regions of the parameter space, in terms of the various quartic couplings as well as the scalar mass eigenvalues are presented by us in detail, in the light of theoretical as well as collider bounds. The inclusion of \mathbb{Z}_2 -breaking quartic couplings, too, is found to retain the high-scale validity of the theory over a large region.

Though we analysed in detail the Type-II 2HDM, many of the results obtained here are expected to hold for a more general 2HDM as well. A situation where some departure can take place is, for example one where the Yukawa coupling of the bottom quark becomes comparable to, or more than, that of the top quark. One possibility to explore in such a case is to look for those regions where the large number of quartic couplings can rescue the scenario from an unstable vacuum. The results presented here are based on one-loop RG equations, in consonance with most similar studies in the context of 2HDM.

It should also be noted that we call those regions in the parameter space as *allowed*, where the vacuum is strictly *stable*. The inclusion of a metastable vacuum, with lifetime greater than the age of the universe, will lead to larger allowed regions.

On the whole, our conclusion is that it is possible to validate a 2HDM till scales as high as the Planck mass without any additional physics. While the issue of naturalness

remains unaddressed in this statement, it is interesting to see that no current experimental measurement or theoretical restriction can affect high-scale validity, which is not the case for the SM.

Chapter 4

High-scale validity of a two-Higgs-doublet scenario: metastability included

4.1 Introduction

Chapter 3 established a connection between the parameter space of a Type-II 2HDM, and a stable EW vacuum till the Planck scale. Much of it is attributed to the presence of additional bosonic degrees of freedom in such a case compared to the SM. To elucidate the previous statement, the additional bosonic fields can offset the fermionic drag in the RG evolution through introducing additional terms in the beta functions of the quartic couplings. Although the results in the preceding chapter are for the Type-II 2HDM only, the qualitative conclusions regarding restoration of vacuum stability remain similar even switching over to the other Yukawa alignments.

It should, however, be remembered that the EW vacuum in the SM is acceptable over a substantial region of the parameter space by being not stable but *metastable* [65]. It is therefore of interest to investigate if the inclusion of a metastable vacuum also expands the allowed parameter space of a 2HDM. With this view, we take up the following studies in this chapter¹.

- But is there a possible metastable vacuum in a 2HDM? Can such a balance between

¹based on [160]

the bosonic and fermionic effects be struck that indeed leads to an additional minimum of the scalar potential, while prolonging the lifetime of the EW vacuum to a safe level?

- Studies on the high-scale validity of a 2HDM in the past were mostly confined to investigating absolute stability [92, 161–166]. Some studies connecting higher dimensional operators to Higgs metastability have occurred in the past [167, 168]. Moreover, a recent study on metastable vacua was done in a rather specialised kinds of 2HDM, which is the well known inert doublet model [169]. There, the SM-like doublet faces no alteration in its interaction strengths. It would be not only more interesting but also phenomenologically more important to identify regions with metastable vacua in a 2HDM where electroweak symmetry breaking (EWSB) is triggered when both the doublets receive vacuum expectation values (VEV) [170]. Two possibilities thus open up: (a) The scalar potential could furnish additional neutral minima around the TeV scale in the slice spanned by the neutral fields in the two doublets, and, (b) Additional minimum can appear when the scalar potential is improved by RG effects. Studies related to metastability in types (a) or (b) above have been reported with, for example, higher power terms in the potential. However, a thorough investigation of the parameter space of say, a Type-II 2HDM, is not there yet. We wish to fill this void in this chapter.
- As has already been substantiated in the previous chapter, a 2HDM (of, say Type-II) allows enough of parameter space with a *stable vacuum*, without any new physics all the way up to the Planck scale, even if the top mass is at its upper limit. The investigation in this direction becomes complete only after checking *whether and how the allowed region expands, once the possibility of a metastable electroweak vacuum is also taken into account*. We aim to complete the picture with the studies in this chapter.

The chapter has the following plan. In section 4.2, we review the salient features of the 2HDMs. Section 4.3 is dedicated to a discussion on how a metastable vacuum can arise. We also present an outline of the tunnelling probability computation in the same. Section 4.4 presents an overall strategy on how to look for a metastable vacua, and, also an account of the various experimental and theoretical constraints taken while doing so. The numerical results are highlighted in section 4.5 and finally the study is concluded in section 4.6. Important formulae used in the analysis are given in Appendices A.1 and A.3.

4.2 Model features.

The 2HDM scalar potential is the same as the one in **Chapter 1** and **Chapter 3** and we also assume both the doublets receive VEVs through EWSB. We choose a real m_{12} , and in addition, the terms proportional to λ_6 and λ_7 have been neglected in this chapter. We adhere to the Type-II 2HDM like what was done in the previous chapter. The quadratic parameters m_{11} and m_{22} can be traded off using the following EWSB conditions.

$$m_{11}^2 v_1 = m_{12}^2 v_2 - \frac{1}{2} \lambda_1 v_1^3 - \frac{1}{2} (\lambda_3 + \lambda_4 + \lambda_5) v_1 v_2^2, \quad (4.2.1a)$$

$$m_{22}^2 v_2 = m_{12}^2 v_1 - \frac{1}{2} \lambda_2 v_2^3 - \frac{1}{2} (\lambda_3 + \lambda_4 + \lambda_5) v_2 v_1^2. \quad (4.2.1b)$$

Defining $\tan\beta = \frac{v_2}{v_1}$ as in chapter 1, the parameter space can be described using the basis $\{m_{12}, \tan\beta, \lambda_1, \lambda_2, \lambda_3, \lambda_4, \lambda_5\}$, or equivalently, in terms of $\{m_{12}, \tan\beta, m_h, m_H, m_A, m_{H^+}, c_{\beta-\alpha}\}$. We choose the latter for the analysis in this chapter and use the following equations to convert to the former.

$$\lambda_1 = \frac{1}{v^2 c_\beta^2} \left(c_\alpha^2 m_H^2 + v^2 s_\alpha^2 m_h^2 - m_{12}^2 \frac{s_\beta}{c_\beta} \right), \quad (4.2.2a)$$

$$\lambda_2 = \frac{1}{v^2 s_\beta^2} \left(s_\alpha^2 m_H^2 + v^2 c_\alpha^2 m_h^2 - m_{12}^2 \frac{c_\beta}{s_\beta} \right), \quad (4.2.2b)$$

$$\lambda_3 = \frac{2m_{H^+}^2}{v^2} + \frac{s_{2\alpha}}{v^2 s_{2\beta}} (m_H^2 - m_h^2) - \frac{m_{12}^2}{v^2 s_\beta c_\beta}, \quad (4.2.2c)$$

$$\lambda_4 = \frac{1}{v^2} (m_A^2 - 2m_{H^+}^2) + \frac{m_{12}^2}{v^2 s_\beta c_\beta}, \quad (4.2.2d)$$

$$\lambda_5 = \frac{m_{12}^2}{v^2 s_\beta c_\beta} - \frac{m_A^2}{v^2}. \quad (4.2.2e)$$

In eqns.(4.2.2a)-(4.2.2e), s_θ and c_θ are shorthands for $\sin\theta$ and $\cos\theta$ respectively.

4.3 The computation of tunnelling probability.

The existence of a large number of scalar degrees of freedom makes the vacuum landscape of a 2HDM more elaborate and intriguing compared to the SM. Here we are confining ourselves to the situation when the vacuum breaks neither electric charge nor CP . Under such circumstances, the EWSB conditions in eqns.(4.2.1a) and (4.2.1b) can lead to several solutions, and at most two non-degenerate minima. In other words, apart from the EW minimum in which the universe currently resides ($v_1^2 + v_2^2 = (246 \text{ GeV})^2$, named N), there

exists another minimum somewhere around $((v'_1)^2 + (v'_2)^2 \neq (246 \text{ GeV})^2$, named N'). [96] finds the difference of depths of the tree level scalar potential at the two minima to be,

$$V_{N'} - V_N = \frac{m_{12}^2}{4v_1v_2} \left(1 - \frac{v_1v_2}{v'_1v'_2}\right)^2 (v_1v'_2 - v_2v'_1)^2. \quad (4.3.1)$$

Thus there exists the tantalizing possibility that the 2HDM offers such parameter points for which a neighbouring vacuum could actually be deeper than the one which corresponds to the observed W - and Z - boson masses. The EW minimum then loses its status as the global minimum and has been termed the *panic vacuum* in [96]. In those cases, computing the lifetime of tunnelling to the non-EW minimum from the EW one becomes the pertinent task. If the tunnelling lifetime turn out to be higher than the age of the universe, the non-EW minimum cannot be ruled out. However, thanks to the data from the LHC on Higgs signal strengths, the model points admitting $V_{N'} - V_N < 0$ are more or less ruled out [96,171]. However, a new landscape of vacua can still open up if one investigates the RG-*improved* effective potential in place of the bare tree-level one. In the context of the SM, it can be understood as follows: The SM quartic coupling turns negative at some energy scale 10^{8-11} GeV (exact location of the scale depends on the choice of the initial conditions), after which it again starts rising owing to the bosonic effects counterbalancing the negative top-Yukawa drag. The fallout of this is the emergence of a new minimum beyond the scale where the quartic coupling first becomes negative.

In a 2HDM, on the other hand, one has to handle the additional complication of having a higher number of field directions. In addition, the effects of the various interaction terms make it imperative to incorporate the effects of radiative corrections induced by the 2HDM. Therefore, we choose to analyse the one-loop corrected effective potential [172] in place of the tree level potential. One thus writes

$$V_{\text{eff}}(h_1, h_2) = V_{\text{tree}}(h_1, h_2) + V_{\text{1loop}}(h_1, h_2). \quad (4.3.2)$$

Here, $V_{\text{tree}}(h_1, h_2)$ and $V_{\text{1loop}}(h_1, h_2)$ denote the tree level and 1-loop parts of the effective potential, calculated along the $h_1 - h_2$ subspace.

For example, , the tree level potential reads

$$\begin{aligned} V_{\text{tree}}(h_1, h_2) &= \frac{1}{2}m_{11}^2h_1^2 + \frac{1}{2}m_{22}^2h_2^2 + m_{12}^2h_1h_2 + \frac{\lambda_1}{8}h_1^4 + \frac{\lambda_2}{8}h_2^4 \\ &\quad + \frac{\lambda_3 + \lambda_4 + \lambda_5}{4}h_1^2h_2^2. \end{aligned} \quad (4.3.3)$$

In the (h_1, h_2) plane, it has the following expression [173],

$$V_{\text{1loop}}(h_1, h_2) = \frac{1}{64\pi^2} \sum_i n_i M_i^4(h_1, h_2) \left[\ln\left(\frac{M_i^4(h_1, h_2)}{\mu^2}\right) - c_i \right]. \quad (4.3.4)$$

Where n_i refers to the number of degrees of freedom for the i th field and c_i are constants whose values depend on the regularization scheme adopted. To list the constants explicitly, $n_W = 6$, $n_Z = 3$, $n_t = -12$, $n_h = 1$; and $c_W = \frac{5}{6}$, $c_Z = \frac{5}{6}$, $c_t = \frac{3}{2}$, $c_h = \frac{3}{2}$. Moreover μ refers to the renormalisation scale emerging as an artefact of dimensional regularisation. $M_i^2(h_1, h_2)$ represent the field dependent mass squared.

The main theme of this work is to investigate possible high scale vacua in the context of 2HDM using the general prescription suggested by Coleman. $V_{\text{eff}}(h_1, h_2)$ depends on two variables, and hence, determining a classical solution interpolating the two vacua, even numerically, becomes an extremely challenging task. Furthermore, a generic classical path may not qualify as a "bounce" [68, 69], i.e, it might not pass through the top of a barrier separating two vacua. Coleman's prescription does not apply in such a case. However, one can always choose to look for additional minima along a particular ray in the $h_1 - h_2$ plane. Under this approximation, the effective potential is reduced to a function of a single variable again(that particular linear combination of h_1 and h_2). In models such as Type-I or Type-II 2HDM, the \mathbb{Z}_2 symmetry of the Yukawa interactions implies that the top quark always couples to Φ_2 . Thus it is the coupling λ_2 that experiences the maximum downward pull due to the Yukawa interactions and can consequently turn negative at high scales in spite of starting with a positive value at the input scale. It therefore makes sense to look for additional minima in the h_2 direction only. This approach is similar to what [169] opts in context of an inert doublet model.

We study the behaviour of the $V_{\text{eff}}(h_1, h_2)$ in the limit where $h_1 \simeq v$ and $h_2 \gg h_1, m_{12}$. In this limit, the squared masses have the following simplified expressions.

$$m_{H_1}^2(h_2) \simeq \frac{1}{2}(\lambda_3 + \lambda_4 + \lambda_5)h_2^2, \quad (4.3.5)$$

$$m_{H_2}^2(h_2) \simeq \frac{3}{2}\lambda_2 h_2^2, \quad (4.3.6)$$

$$m_{A_1}^2(h_2) \simeq \frac{1}{2}(\lambda_3 + \lambda_4 - \lambda_5)h_2^2, \quad (4.3.7)$$

$$m_{A_2}^2(h_2) \simeq \frac{1}{2}\lambda_2 h_2^2, \quad (4.3.8)$$

$$m_{H_1^+}^2(h_2) \simeq \frac{1}{2}\lambda_3 h_2^2, \quad (4.3.9)$$

$$m_{H_2^+}^2(h_2) \simeq \frac{1}{2}\lambda_2 h_2^2, \quad (4.3.10)$$

$$m_t^2(h_2) \simeq \frac{1}{2}y_t^2 h_2^2, \quad (4.3.11)$$

$$m_W^2(h_2) \simeq \frac{1}{4}g_2^2 h_2^2, \quad (4.3.12)$$

$$m_Z^2(h_2) \simeq \frac{1}{4}(g_1^2 + g_2^2)h_2^2. \quad (4.3.13)$$

Eqns.(4.3.5)-(4.3.10) express the field dependent squared masses for the scalar degrees of freedom that come from Φ_1 and Φ_2 . The corresponding ones for t, W, Z are shown in eqns.(4.3.11)-(4.3.13). All running couplings are evaluated at the scale $\mu \simeq h_2$. Under all these approximations, the real part of one-loop corrected potential takes the form

$$V_{\text{eff}}(h_2) \simeq \frac{\lambda_2^{\text{eff}}}{8}h_2^4. \quad (4.3.14)$$

where,

$$\begin{aligned} \lambda_2^{\text{eff}}(h_2) \simeq & \lambda_2(h_2) + \frac{1}{64\pi^2} \left[2(\lambda_3 + \lambda_4 + \lambda_5)^2 \left(\ln \frac{\lambda_3 + \lambda_4 + \lambda_5}{2} - \frac{3}{2} \right) + 18\lambda_2^2 \left(\ln \frac{3\lambda_2}{2} - \frac{3}{2} \right) + \right. \\ & 2(\lambda_3 + \lambda_4 - \lambda_5)^2 \left(\ln \frac{\lambda_3 + \lambda_4 - \lambda_5}{2} - \frac{3}{2} \right) + 2\lambda_3^2 \left(\ln \frac{\lambda_3}{2} - \frac{3}{2} \right) + 6\lambda_2^2 \left(\ln \frac{\lambda_3}{2} - \frac{3}{2} \right) + \\ & \left. 3g_2^4 \left(\ln \frac{g_2^2}{4} - \frac{5}{6} \right) + \frac{3}{2}(g_1^2 + g_2^2)^2 \left(\ln \frac{g_1^2 + g_2^2}{4} - \frac{5}{6} \right) - 24y_t^4 \left(\ln \frac{y_t^2}{2} - \frac{3}{2} \right) \right]. \quad (4.3.15) \end{aligned}$$

Where in eqn.(4.3.15), the term in square brackets refers to the finite correction generated by the Coleman Weinberg mechanism. We find that highly sub-dominant in our calculations.

In this limit, the probability of tunnelling to the deeper vacuum is given by [70]

$$p = T_U^4 \mu^4 e^{-\frac{8\pi^2}{3|\lambda_2^{\text{eff}}|}}. \quad (4.3.16)$$

Here one fixes μ to the scale where the probability is maximised, and, it turns out that $\frac{d\lambda_2}{d\log(Q)} = 0$ at $Q = \mu$. Using $T_U \simeq 10^{10}$ yr and requiring that the vacuum tunnelling lifetime is always higher than the lifetime of the universe is tantamount to having the following condition [70]:

$$\lambda_2^{\text{eff}}(h_2) \geq \frac{-0.065}{1 - 0.01 \ln(v/\mu)}. \quad (4.3.17)$$

It may be noted that we have accepted λ_2^{eff} turning negative in the h_2 direction as the sole condition for the loss of stability of the EW vacuum. There is in general an extended set of conditions for stability in a 2HDM [28] (see subsection 3.3.1 in **Chapter 1**). However, one can easily verify that the remaining conditions for stability in a 2HDM are violated, if at all, at low scale itself. Such violation, on the other hand, leads to the disappearance of the EW minimum as a whole. This cannot be a situation appropriate for metastability, and therefore the conditions other than $\lambda_2 < 0$ need not be used as signs for loss of stability.

4.4 A metastable vacuum and the 2HDM parameter space.

4.4.1 Analysis strategy.

As has already been emphasised in the previous chapter, a look-out for an additional vacuum at high scales requires one to study the evolution of the various couplings under RG equations. The values of the quartic couplings at the electroweak scale are, of course, connected with the masses and mixing angles in the scalar sector. A careful measurement of the signal strengths of the 125 GeV at the LHC has revealed that the resonance has couplings strikingly similar to the SM ones. These observations have their ramifications on the 2HDM parameter space. Thus, together with the requirement of having $m_h \simeq 125$ GeV, we also arrange for $\beta - \alpha = \frac{\pi}{2}$, in order to comply with these results from the LHC ($\beta - \alpha = \frac{\pi}{2}$ is the well known *alignment limit* [174, 175] in a 2HDM, in which the couplings of h to fermions and gauge bosons become exactly equal to the SM ones). In addition to these, similar to what was done in **Chapter 3** we also apply the constraints of perturbativity, unitarity and vacuum stability throughout the course of RG evolution (see subsection 3.3.1 in **Chapter 1**).

For a 'near-aligned' 2HDM, i.e. that has $(\beta - \alpha) \simeq \frac{\pi}{2}$, signal strengths of h to the fermionic and VV (Here $V = W, Z$) final states [176] nearly coincide with the corresponding SM values [140, 147]. What can still deviate, is the strength of the $h\gamma\gamma$ interaction. This is attributed to the participation of the charged Higgs in the loop [28, 177–179]. The corresponding decay width is given by

$$\Gamma^{2HDM}(h \rightarrow \gamma\gamma) = \frac{\alpha^2 g_2^2}{2^{10} \pi^3} \frac{m_h^3}{M_W^2} \left| \sin(\beta - \alpha) F_W + \left(\frac{\cos \alpha}{\sin \beta} \right) \frac{4}{3} F_t + \kappa F_{H^+} \right|^2. \quad (4.4.1)$$

Here g_2 denotes the $SU(2)_L$ gauge coupling. Also, κ is a dimensionless parameter that quantifies the strength of the coupling of h to a pair of charged Higgses. More clearly,

$$g_{hH^+H^-} = \kappa \frac{g_2 m_{H^+}^2}{m_W}. \quad (4.4.2)$$

Where $g_{hH^+H^-}$ denotes the above mentioned trilinear coupling. The functions F_W , F_t and F_{i+} encapsulate the effects of a W -boson, a t -quark and a charged scalar running in the loop and shall be defined as,

$$F_W = 2 + 3\tau_W + 3\tau_W(2 - \tau_W)f(\tau_W), \quad (4.4.3a)$$

$$F_t = -2\tau_t[1 + (1 - \tau_t)f(\tau_t)], \quad (4.4.3b)$$

$$F_{H^+} = -\tau_{i^+} [1 - \tau_{i^+} f(\tau_{i^+})]. \quad (4.4.3c)$$

Where,

$$f(\tau) = \left[\sin^{-1} \left(\sqrt{1/\tau} \right) \right]^2. \quad (4.4.4)$$

$$\text{with, } \tau = \frac{4m_a^2}{m_h^2}. \quad (4.4.5)$$

Here, $a = t, W$ and H^+ .

We assume h is dominantly produced through gluon fusion. In such a case, the signal strength for the diphoton final state is approximately given by,

$$\mu_{\gamma\gamma} = \frac{\Gamma^{2HDM}(h \rightarrow \gamma\gamma)}{\Gamma^{SM}(h \rightarrow \gamma\gamma)}. \quad (4.4.6)$$

In order to respect the 2σ bound on $\mu_{\gamma\gamma}$, from a combined measurement of ATLAS and CMS, we discard model points that violate $\mu_{\gamma\gamma} \in [1.04, 1.37]$ [180]. In addition, we also impose the T -parameter constraint and $m_{H^+} > 315$ GeV as illustrated in **Chapter 1**.

4.5 Results and discussions.

Model points that successfully negotiate all the aforesaid constraints are allowed to evolve under RG, till some scale Λ (say). Λ can be interpreted as the scale up to which no physics over and above the extended Higgs sector is required. If there is an additional, lower vacuum before Λ , the time scale for tunnelling from the EW vacua to the new one must therefore be larger than the age of the universe. It is intuitively expected that higher is Λ , tighter becomes the parameter space that is allowed at the EW scale. This is indeed confirmed by the findings reported in [92, 164]. Of course, the points leading to a metastable EW vacuum are identified through a detailed scan of the parameter space. However, the fate of a particular model point at high scales is sensitive to the value of the t -quark mass taken². With this in view, we propose the following benchmarks listed in Table 4.1.

In each case, we plot the evolution of λ_2^{eff} in Fig.4.1. The chosen benchmarks differ in their perturbative behaviour at high scales, although all of them have the common feature that the EW vacuum turns metastable, or even unstable for $M_t = 175$ GeV. In other words, the Type-II 2HDM may turn non-perturbative beyond a scale Λ , even though a vacuum deeper

²The Yukawa couplings at the EW scale have been evaluated in the same way as was done in section 3.4 of **Chapter 1**

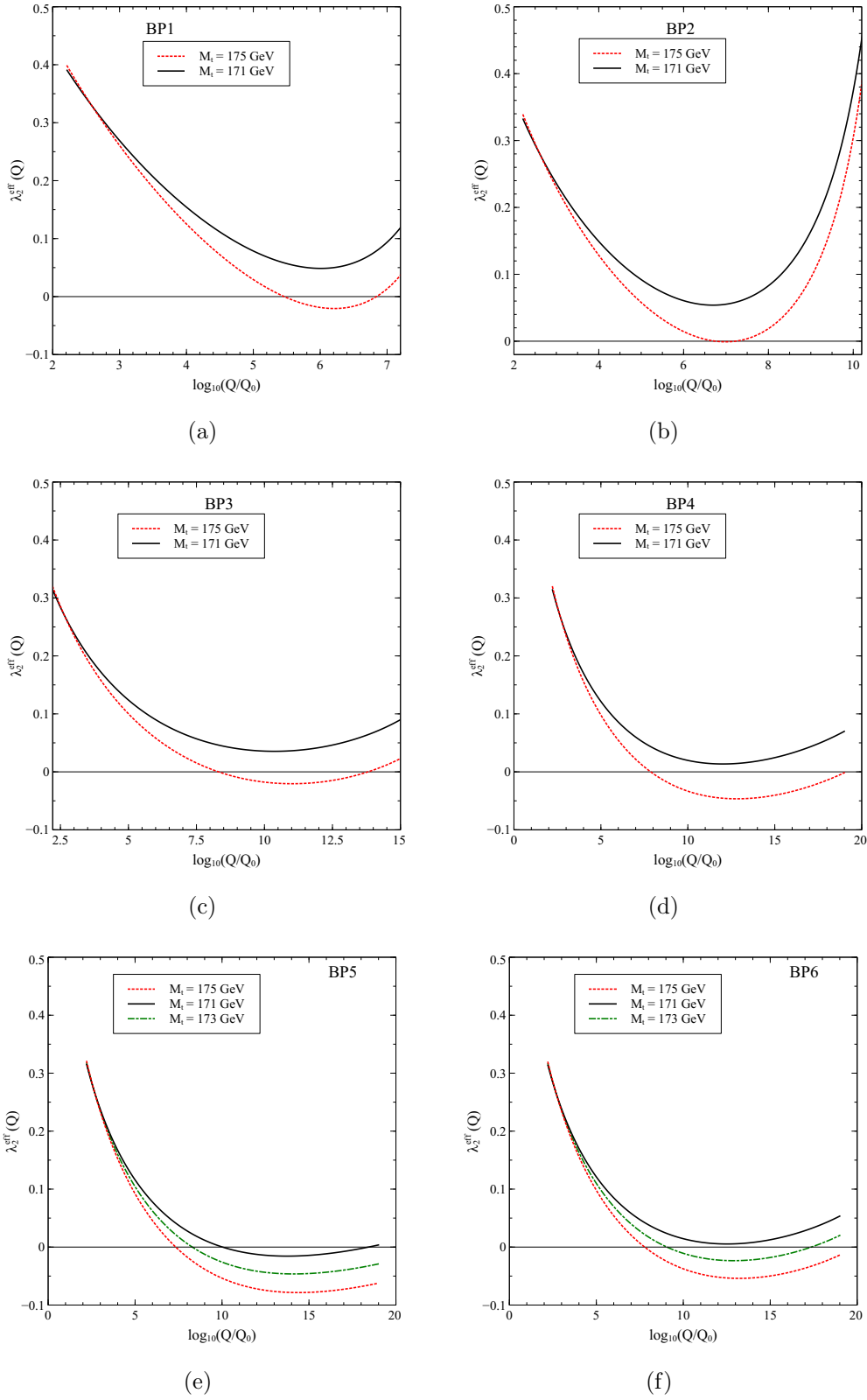


Figure 4.1: RG evolution of λ_2^{eff} for the benchmarks listed in Table 4.1, for more than one value of M_t . The colour coding is explained in the legends.

Benchmark	$\tan\beta$	$m_H(\text{GeV})$	$m_A(\text{GeV})$	$m_{H^+}(\text{GeV})$	$m_{12}(\text{GeV})$	Perturbative till
BP1	1.78	354	380	341	222	$\sim 10^7$ GeV
BP2	2.50	489	506	486	286	$\sim 10^{11}$ GeV
BP3	7.28	320	297	324	117	$\sim 10^{16}$ GeV
BP4	8.28	500	500	500	172	$\sim 10^{19}$ GeV
BP5	6.90	501	499	500	189	$\sim 10^{19}$ GeV
BP6	10.94	1499	1500	1498	451	$\sim 10^{19}$ GeV

Table 4.1: Benchmark points chosen to illustrate the behaviour under renormalisation group equations (RGE). Λ denotes the maximum extrapolation scale up to which perturbativity remains intact. The stability/metastability of the EW vacuum corresponding to these benchmarks is dictated by the value of M_t taken.

than the EW one might be encountered some place intermediate between the electroweak scale and Λ . Besides, although it is worth identifying those parameter points that keep the EW vacuum metastable all the way till the GUT or Planck scales, we also include for completeness in the benchmarks, two points where a 2HDM loses its perturbativity at a much lower scale. For instance in BP1(Fig.4.1a), at $M_t = 175$ GeV, λ_2^{eff} turns negative and, $\frac{d\lambda_2^{\text{eff}}}{dt} = 0$ occurs around 6.2×10^6 GeV (The scale at which the tunnelling probability gets maximised). An inspection of Fig.4.1a thus indicates that this particular benchmark leads to metastability. The same parameter point offers absolute stability for $M_t = 171$ GeV though. BP2(Fig.4.1b) describes a similar qualitative feature as seen in BP1, it also remains perturbative till 10^{11} GeV.

BP3(Fig.4.1c) is a more conservative benchmark in the sense that, it keeps the 2HDM perturbative till the GUT scale and also prevents an *unstable* EW vacuum even in the worst case scenario with $M_t = 175$ GeV. We remind the reader that the strength of the t -quark Yukawa coupling depends not only on the pole mass, but also on $\tan\beta$. This becomes crucial in deciding the fate of the EW vacuum at high scales. For instance, BP5(Fig.4.1e) experiences a higher t -quark negative pull compared to BP4(Fig.4.1d) owing to a lower value of $\tan\beta$ in BP5, even though the quartic couplings at the input scale are at the same ball-park for the two cases. BP6(Fig.4.1f) is a fine-tuned parameter point that is perturbative till the Planck scale, and for which the EW vacuum is stable, metastable or unstable for $M_t = 171$ GeV, 173 GeV and 175 GeV respectively. For the sake of completeness, we display the behaviour

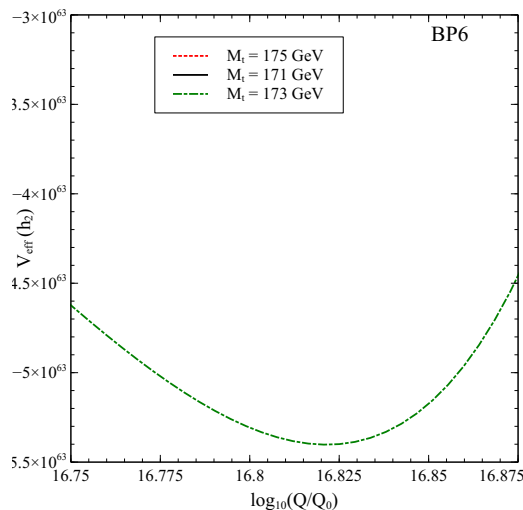


Figure 4.2: Behaviour of $V_{\text{eff}}(h_2)$ in BP6 for $M_t = 173$ GeV.

of $V_{\text{eff}}(h_2)$ for the BP6 benchmark with $M_t = 173$ GeV in Fig.4.2.

Model points are randomly sampled in the following specified ranges,

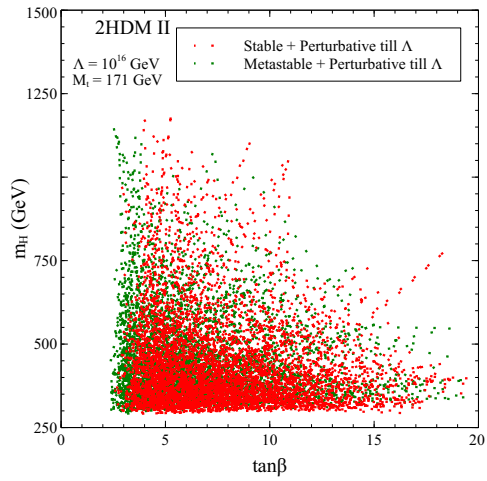
$$\begin{aligned} \tan \beta &\in [0.1, 20.0], \\ m_H, m_A, m_{H^+}, m_{12} &\in [0, 1200 \text{ GeV}]. \end{aligned} \quad (4.5.1)$$

A condition forbidding the loss of perturbativity/unitarity at scale Λ is imposed throughout the scan. The following broad features emerge from Figs. 4.3, 4.4 and 4.5. The results are shown using two representative values of Λ , namely 10^{16} GeV (Fig.4.3) and $\Lambda = 10^{19}$ GeV (Fig.4.4).

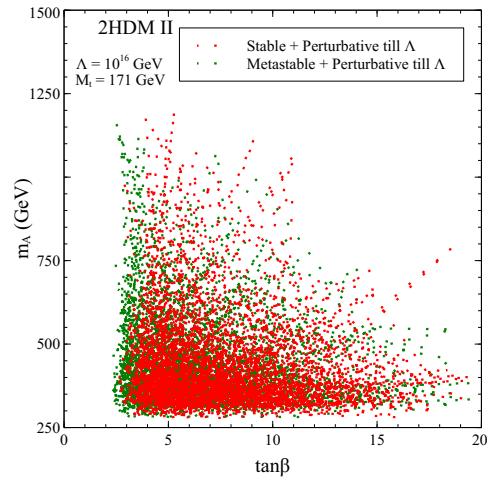
(i) Perturbativity puts stringent constraints on the splitting amongst the masses. In fact, for $\Lambda = 10^{19}$ GeV the masses are near-degenerate (see Fig.4.5). This effect can be attributed to the fact that for a large mass splitting, the λ_i are already large at the electroweak scale, leading to a blow-up soon after. In fact, a parameter point ensuring perturbative behaviour till the Planck scale does not tolerate a mass splitting more than $\simeq 10$ GeV. This constraint is considerably stronger than that from the T -parameter alone ($\simeq 50$ GeV). In other words, as far as the extended scalar potential is concerned, the T -parameter constraint is thus rendered redundant by the requirement of perturbativity till the GUT or the Planck scale.

(ii) As we mostly confine ourselves to a conservatively perturbative regime ($|\lambda_i| < 1$), the results obtained using two-loop evolution were found to differ only slightly from the corresponding one-loop ones. Thus, the overall conclusions continue to remain the same.

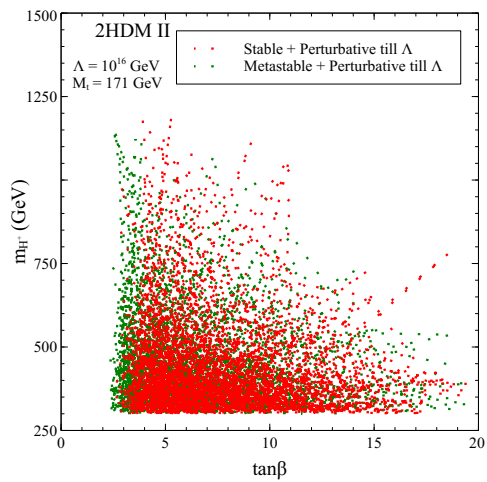
(iii) A smaller $\tan\beta$ for the same M_t implies an enhanced fermionic contribution to



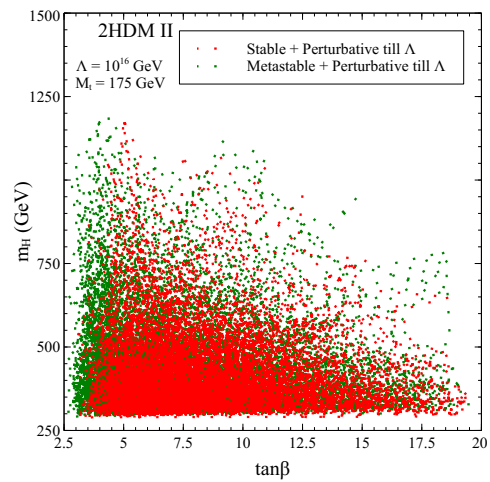
(a)



(b)



(c)



(d)

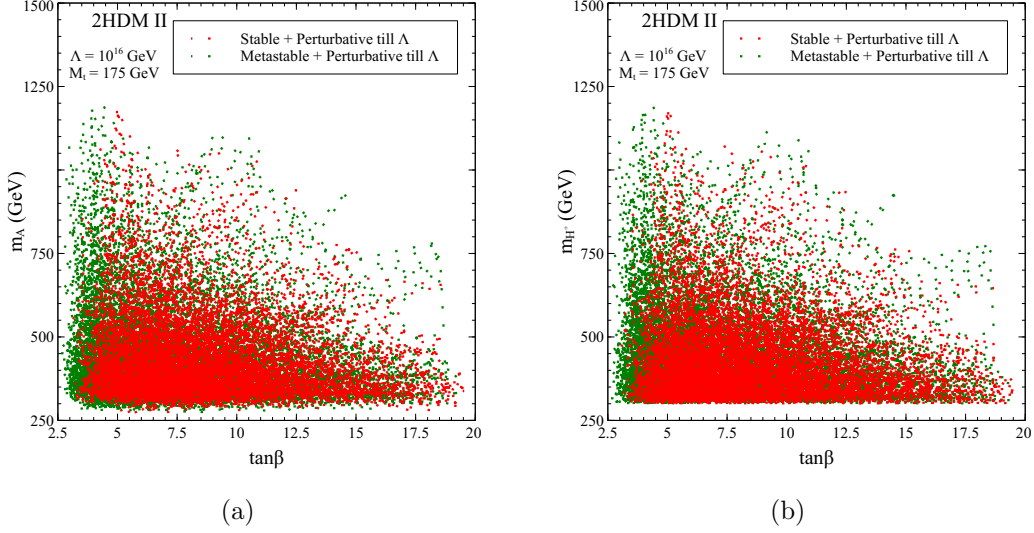
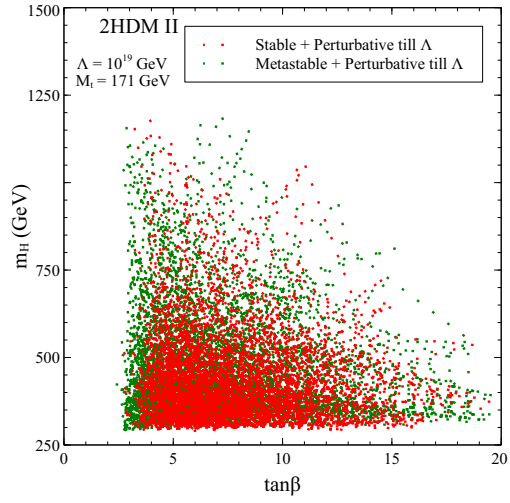


Figure 4.3: Distribution of points in the parameter space perturbative till 10^{16} GeV that lead to an either stable or metastable EW vacuum. The upper (lower) plots correspond to $M_t = 171$ (175) GeV. The colour coding is explained in the legends. 2HDM II refers to a Type-II 2HDM.

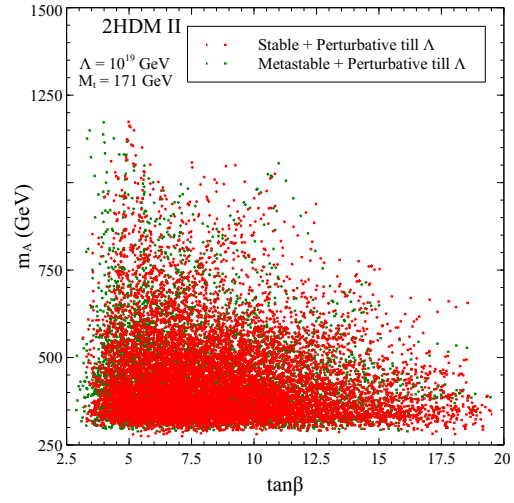
the evolution of λ_2 , and hence it favours a metastable vacuum over an absolutely stable one. Consequently, $\tan\beta$ is bounded from below in order to prevent tunnelling to the lower vacuum. Moreover, one would apprehend that the bound obtained by demanding absolute stability of the EW vacuum to be the stronger than the one obtained when one allows for a metastable scenario. For instance, for $M_t = 171$ GeV, the lower bounds read $\simeq 2.1$ and $\simeq 2.5$ for the two cases³.

(iv) The lower bound on $\tan\beta$ of course depends on the choice of M_t . For instance the parameter point parametrised in terms of the masses and $\tan\beta$ indeed shall have different evolution trajectories for two different values of M_t . This is reflected in the plots of Fig.4.3, where the lower bound is tighter for $M_t = 175$ GeV compared to what it is for $M_t = 171$ GeV, for both the "stable" as well as "metastable" models. Of course, in this case too, absolute stability yields a stronger bound than metastability. For $M_t = 175$ GeV, any model with $\tan\beta < 2.6$ yields a tunnelling lifetime lower than the age of the universe.

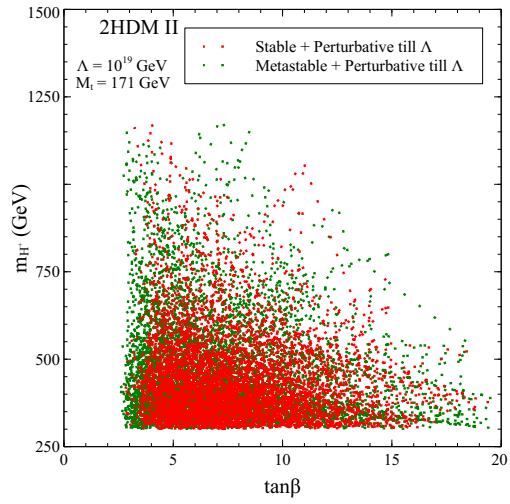
³The lower bound on $\tan\beta$ from absolute stability appears to be more stringent in this case compared to what was seen in **Chapter 1**. This is due to the tighter ranges taken for m_h and $c_{\beta-\alpha}$ in the present chapter.



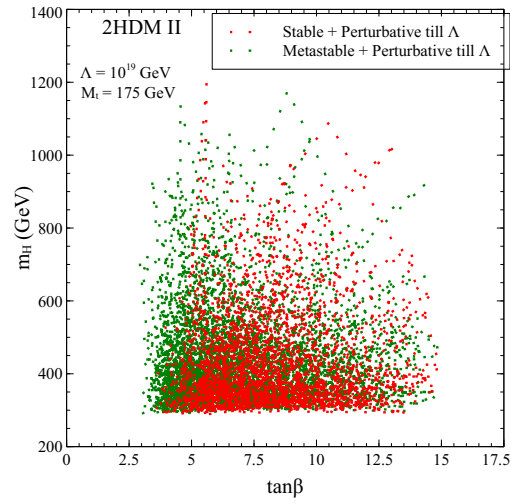
(a)



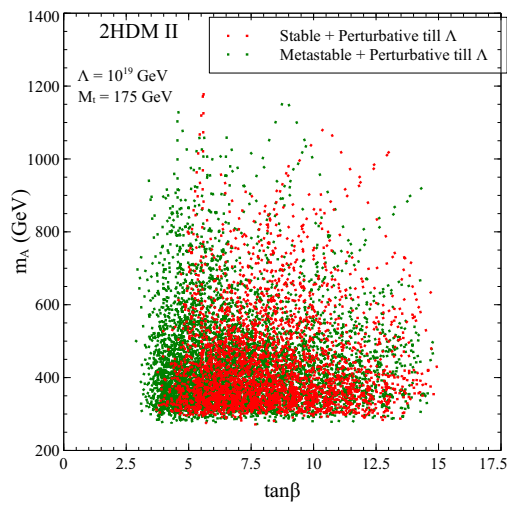
(b)



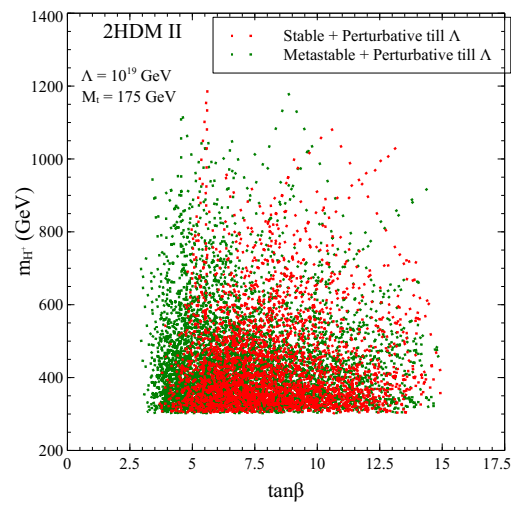
(c)



(d)



(a)



(b)

Figure 4.4: Distribution of points in the parameter space perturbative till 10^{19} GeV that lead to an either stable or metastable EW vacuum. The upper (lower) plots correspond to $M_t = 171$ (175) GeV. The colour coding is explained in the legends. 2HDM II refers to a Type-II 2HDM.

(v) Although the lower bound on $\tan\beta$ should also depend on the Λ chosen, it hardly changes with respect to the 10^{16} GeV value for $\Lambda = 10^{19}$ GeV. Only the number of allowed points shrinks to some extent, other essential features are unchanged.

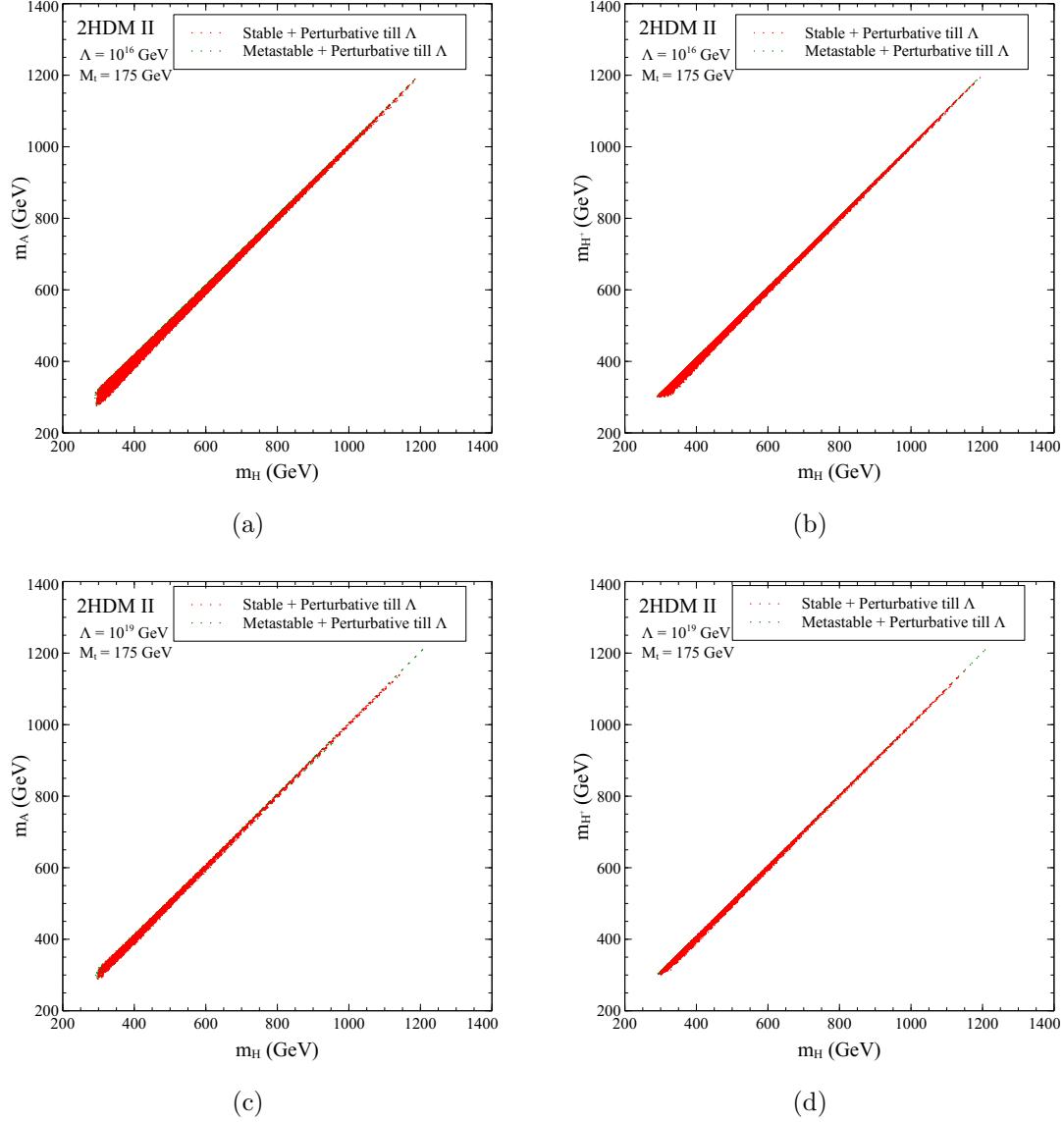


Figure 4.5: Distribution of parameter space points in the $m_H - m_A$ ($m_H - m_{H^+}$) plane as shown in the left (right) plots, for $M_t = 175$ GeV. The upper (lower) plots correspond to perturbativity till 10^{16} (10^{19}) GeV.

In the plane of $\tan\beta$ versus masses, it is expected that a particular parameter point responsible for a metastable EW vacuum can always be found in the vicinity of a point

that leads to absolute stability for $\tan\beta \geq 3.0$. This gets confirmed by an inspection of Fig.4.4. This can be understood from the fact that any enhanced fermionic contribution due to a higher $\tan\beta$ can always be cancelled by an appropriately increased bosonic contribution through a slight tweak in the masses. Of course, one also has to keep the couplings perturbative in doing so. Such a "fine-tuned" existence of a metastable EW vacuum is not a surprise and is always expected in the case of an extended Higgs sector (where the Yukawa interactions can be stronger *w.r.t* the SM), such as the Type-II 2HDM.

We take another approach where different scalar masses are fixed within specific narrow ranges, and allow $\tan\beta$ to vary. This approach turns useful in demarcating the "stable" region from the "metastable". We thus propose two central values of 500 GeV and 1000 GeV and allow only a 2 GeV split about that. Fig.4.6 presents the results for this choice.

For masses around 500 GeV and $M_t = 171$ GeV, the metastable points mostly cluster in the low $\tan\beta$ region. They get largely disfavoured at larger $\tan\beta$. Since the bosonic contribution to RG evolution is now restrained, absolute stability demands $\tan\beta \geq 3.0$. For $M_t = 175$ GeV however, lower bound on $\tan\beta$ for both stability as well as metastability goes up, stability is completely ruled out for $\tan\beta \leq 5.0$ for instance. Thus, for $M_t = 175$ GeV, the proportion of metastable model points is higher compared to what is seen for $M_t = 175$ GeV. The robustness of this claim is verified by the plots for masses $\simeq 1000$ GeV, which depict the same qualitative behaviour. Having pointed out the crucial role played by the parameter $\tan\beta$, we close this section here.

4.6 Summary and conclusions.

This chapter highlights the possibility of a metastable EW vacuum in a popular 2HDM framework. We have already noted in section 4.3 that the LHC data on the 125 GeV Higgs disfavours the occurrence of a panic vacuum at low energy. However, once the parameters occurring in the scalar potential are subjected to RG evolution, additional global minima may indeed occur at high scales. This can render the electroweak vacuum unstable or metastable. This is found to happen in the direction of the scalar field h_2 , because λ_2 can be driven to negative values by the top-Yukawa coupling, at high scales. Thus, along with a parameter space that leads to absolute stability, there exists also a parameter space that gives rise to metastability.

The analysis has been done for the Type-II case. We remark that, it is the relative strengths of the fermionic and bosonic contributions in the RG improved potential that seals

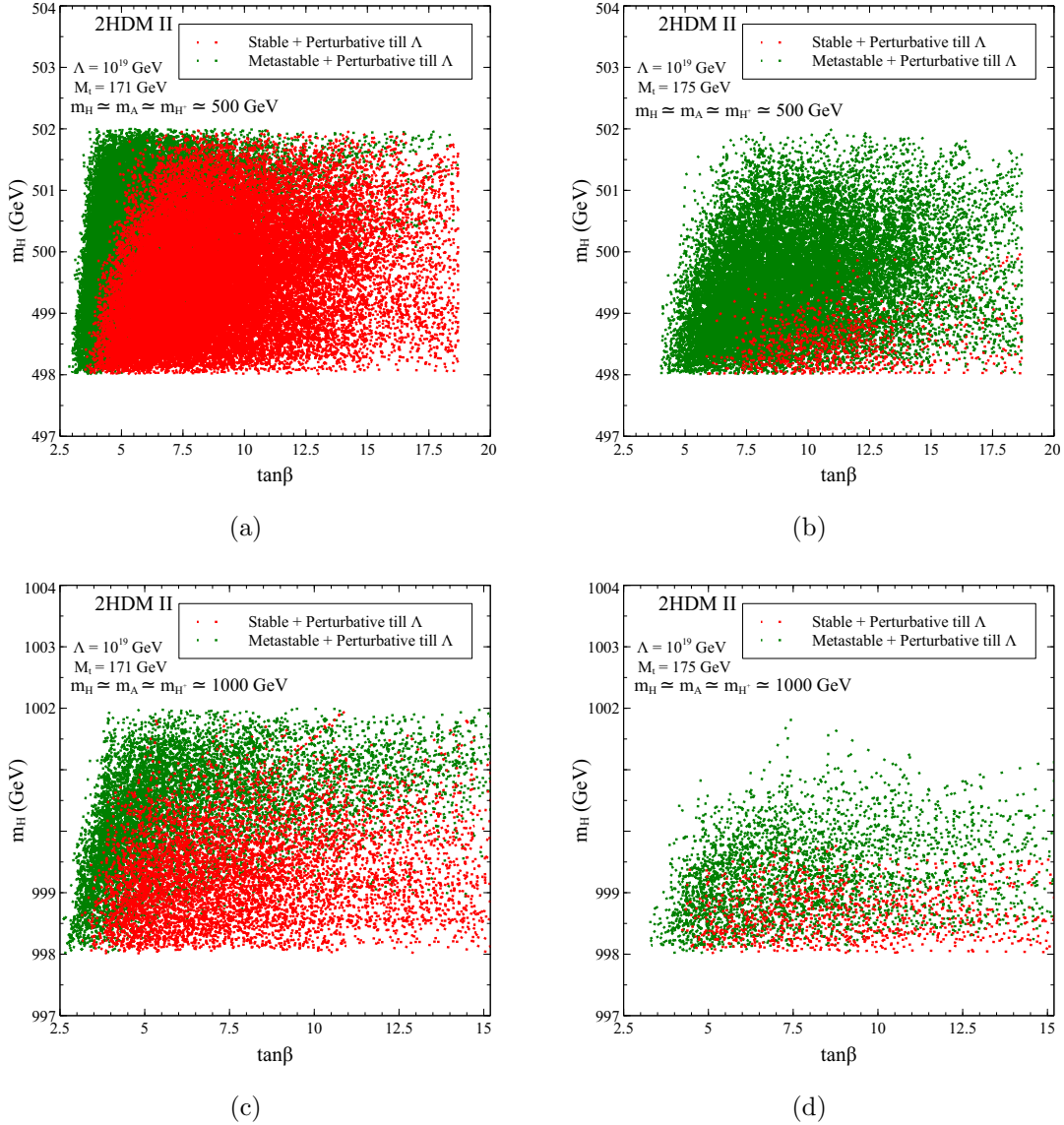


Figure 4.6: Distribution of points in the parameter space in the m_H - $\tan\beta$ plane that are perturbative till 10^{19} GeV and lead to an either stable or metastable EW vacuum. The mass splitting amongst the non-standard scalars is forced to stay within 2 GeV during these scans. The upper (lower) plots correspond to $M_t = 171$ (175) GeV. The colour coding is explained in the legends. 2HDM II refers to a Type-II 2HDM.

the fate of the EW vacuum where we currently reside. The introduction of additional bosonic degrees of freedom further introduces a tension between vacuum stability on the one hand, and, high-scale perturbativity on the other. This tension can be responsible for substantial constraints on the parameter space.

In a 2HDM, the strength of the fermionic contribution is controlled by not only the top quark pole mass, but also $\tan\beta$. Based on the results of this work, one would always expect a metastable model point in the vicinity of a point allowing for absolute stability. However, $\tan\beta$ picks up a lower bound from the requirement of metastability, which is tightened when one demands absolute stability of the EW vacuum. The sensitivity of the results to the top pole mass has also been emphasised.

Side by side with the issue of stability or metastability of the EW vacuum, a crucial role is played by perturbativity and unitarity. A demand of these, for example, all the way to the Planck scale results in the prediction of closely degenerate states H , A and H^+ . We find that this requirement cannot be compromised, even though a larger area of the 2HDM parameter space opens up, on allowing a metastable EW vacuum.

A pertinent extension would be to include finite temperature corrections to the 2HDM scalar potential and, study its impact on vacuum stability.

Chapter 5

High-scale validity of a two Higgs doublet scenario: predicting collider signals

5.1 Introduction

In the preceding chapters, it was elaborated how the challenge of vacuum instability in the SM can be overcome by switching over to two Higgs doublet scenarios. It was found that even with a minimal choice of the additional bosonic parameters (with $\lambda_6 = \lambda_7 = 0$ for example), the quartic couplings can become non-perturbative while evolving under RG. Moreover, this can happen at an energy scale lower than the vacuum instability scale. A balance between these two extremes is struck through judicious boundary conditions, which in turn leads to strong constraints on the masses and mixing angles. One can thus have a consistent and perturbative theory, with just one additional scalar doublet, up to the Planck scale even on the top quark mass being on the high side. Two important points emerge from such studies. First, the spectrum of the non-standard scalars allows for only a small splitting. Secondly, the couplings of the 125 GeV Higgs with gauge bosons should have rather small deviation from the SM values. On the other hand, the gauge interactions of the non-standard scalars become suppressed.

In this chapter¹, we aim to investigate the observability of a 2HDM at the present

¹based on [181]

[159, 182–189] and upcoming colliders [190, 191] within the parameter region that allows for high-scale validity (including both vacuum stability and perturbativity). This could turn challenging since the search prospects could be severely inhibited by the constraints. For instance, to discern a 2HDM from the SM background through resonances, fully reconstructible final states need to be looked at. The corresponding event rates tend to be small, owing to the constraints on the interaction strengths that come from demanding the dual requirement of high scale vacuum stability and perturbative unitarity. Moreover, removal of the backgrounds requires event selection criteria which further lower the signal strength.

To be more specific, the CP -even heavier neutral Higgs could lead to a four-lepton cascade at the LHC via the ZZ state. Side by side, the CP -odd scalar leaves its signature in the completely reconstructible channel hZ where h denotes the SM-like Higgs. The two final states mentioned above are indicative of the opposite CP -properties of the decaying Higgses, which from our requirement, are destined to have closely spaced masses. We adopt a cut-based analysis to calculate the statistical significance in the respective signals. We perform this analysis for both Type-I and Type-II 2HDMs. The allowed parameter space for the latter scenario is obtained via extensive investigation in reference [92]. For the former, though an analysis is found in [164], for the sake of completeness, we present a set of results here that go beyond what has been reported. It is found that the constraints from flavour changing neutral current (FCNC) phenomena put a strong lower limit on the Type-II 2HDM charged scalar mass (and, via the correlation demanded by high-scale validity, on the heavy neutral scalar and pseudoscalar masses as well). Thus while obtaining LHC signals, the region of the parameter space in the Type-II case is relatively more restricted. Keeping this in mind, we also present a brief discussion on the prospects at other types of colliders. In particular, we find that muon colliders can be useful in this respect.

This chapter comprises of the following parts. In section 5.2, we briefly survey the candidature of a 2HDM as a UV-complete scenario. Section 5.3 highlights the intrinsic features of the parameter space that permits high-scale stability. The search prospects at the LHC, and, future leptonic colliders are elaborated in sections 5.4 and 5.5 respectively. We summarise our findings and conclude in section 5.6.

5.2 2HDM and high scale validity.

Relevant details on the 2HDM scalar potential can be found in **Chapter 1** and **Chapter 3**. For the present study, we analyse the the celebrated Type-I and Type-II models [28] that

were discussed in **Chapter 1**. While the primary motivation such a choice is to suppress flavour changing neutral currents (FCNC) [192–194], it also reduces the number of free parameters in the Yukawa sector.² This in turn, simplifies the expressions for the one-loop beta functions. Note that one could introduce \mathbb{Z}_2 violation in the scalar potential only. This would ultimately lead to FCNC, however which would be radiatively suppressed. In this chapter, we consider both the cases of a 2HDM: one that *softly* violates \mathbb{Z}_2 , and, one that violates it through non-zero λ_6 and λ_7 .

We choose $\{\tan\beta, m_h, m_H, m_A, m_{H^+}, m_{12}, c_{\beta-\alpha}, \lambda_6, \lambda_7\}$ as the set of independent input parameters³. The rest of the quartic couplings are expressed in terms of which for convenience. With $v = 246$ GeV and writing $c_\alpha = \cos\alpha$, $s_\alpha = \sin\alpha$, the remaining couplings can be expressed as

$$\lambda_1 = \frac{1}{v^2 c_\beta^2} \left(c_\alpha^2 m_H^2 + v^2 s_\alpha^2 m_h^2 - m_{12}^2 \frac{s_\beta}{c_\beta} - \frac{3}{2} \lambda_6 v^2 s_\beta c_\beta - \frac{1}{2} \lambda_7 v^2 \frac{s_\beta^3}{c_\beta} \right), \quad (5.2.1a)$$

$$\lambda_2 = \frac{1}{v^2 s_\beta^2} \left(s_\alpha^2 m_H^2 + v^2 c_\alpha^2 m_h^2 - m_{12}^2 \frac{c_\beta}{s_\beta} - \frac{3}{2} \lambda_7 v^2 s_\beta c_\beta - \frac{1}{2} \lambda_6 v^2 \frac{c_\beta^3}{s_\beta} \right), \quad (5.2.1b)$$

$$\lambda_4 = \frac{1}{v^2} (m_A^2 - 2m_{H^+}^2) + \frac{m_{12}^2}{v^2 s_\beta c_\beta} - \frac{1}{2t_\beta} \lambda_6 - \frac{1}{2} t_\beta \lambda_7, \quad (5.2.1c)$$

$$\lambda_5 = \frac{m_{12}^2}{v^2 s_\beta c_\beta} - \frac{m_A^2}{v^2} - \frac{1}{2t_\beta} \lambda_6 - \frac{1}{2} t_\beta \lambda_7, \quad (5.2.1d)$$

$$\lambda_3 = \frac{1}{v^2 s_\beta c_\beta} ((m_H^2 - m_h^2) s_\alpha c_\alpha + m_A^2 s_\beta c_\beta - \lambda_6 v^2 c_\beta^2 - \lambda_7 v^2 s_\beta^2) - \lambda_4. \quad (5.2.1e)$$

The mass parameters m_{11} and m_{22} in the scalar potential are traded off using the EWSB conditions (eqns.(4.2.1a) and (4.2.1b) in **Chapter 1**). A given set of input parameters serves as boundary conditions for λ_i for the analysis using RG equations⁴. While carrying out the analysis, several constraints coming from both theory and experiments must be satisfied. Though, some of these have also been discussed in **Chapter 3** and **Chapter 4**, we outline them in the present chapter too for completeness.

5.2.1 Perturbativity, unitarity and vacuum stability

For the 2HDM to remain a perturbative theory at a given energy scale, one requires $|\lambda_i| \leq 4\pi$ ($i = 1, \dots, 5$) and $|y_i| \leq \sqrt{4\pi}$ ($i = t, b, \tau$) at that scale. This translates into upper bounds on the model parameters at low as well as high energy scales.

²It was reported in [195] that the FCNCs are stable under RG.

³ c_θ and s_θ are shorthands for $\cos\theta$ and $\sin\theta$ respectively.

⁴See section 3.4 in **Chapter 1** for a discussion on the Yukawa-couplings at the input scale.

The matrix containing 2→2 scattering amplitudes of longitudinal gauge bosons can be mapped to a corresponding matrix for the scattering of the Goldstone bosons [112, 117, 118, 196], by virtue of the EW equivalence theorem. The theory is deemed unitary if each eigenvalue of the aforementioned amplitude matrix does not exceed 8π . The expressions for the eigenvalues are given below.

$$a_{\pm} = \frac{3}{2}(\lambda_1 + \lambda_2) \pm \sqrt{\frac{9}{4}(\lambda_1 - \lambda_2)^2 + (2\lambda_3 + \lambda_4)^2}, \quad (5.2.2a)$$

$$b_{\pm} = \frac{1}{2}(\lambda_1 + \lambda_2) \pm \sqrt{\frac{1}{4}(\lambda_1 - \lambda_2)^2 + \lambda_4^2}, \quad (5.2.2b)$$

$$c_{\pm} = d_{\pm} = \frac{1}{2}(\lambda_1 + \lambda_2) \pm \sqrt{\frac{1}{4}(\lambda_1 - \lambda_2)^2 + \lambda_5^2}, \quad (5.2.2c)$$

$$e_1 = (\lambda_3 + 2\lambda_4 - 3\lambda_5), \quad (5.2.2d)$$

$$e_2 = (\lambda_3 - \lambda_5), \quad (5.2.2e)$$

$$f_1 = f_2 = (\lambda_3 + \lambda_4), \quad (5.2.2f)$$

$$f_+ = (\lambda_3 + 2\lambda_4 + 3\lambda_5), \quad (5.2.2g)$$

$$f_- = (\lambda_3 + \lambda_5). \quad (5.2.2h)$$

When the quartic part of the scalar potential preserves CP and \mathbb{Z}_2 symmetries, the aforementioned eigenvalues are discussed in [116–118]⁵.

Demanding high-scale positivity of the 2HDM potential along various directions in the field space leads to the following conditions on the scalar potential [28, 121, 199, 200]:

$$\text{vsc1} : \quad \lambda_1 > 0, \quad (5.2.3a)$$

$$\text{vsc2} : \quad \lambda_2 > 0, \quad (5.2.3b)$$

$$\text{vsc3} : \quad \lambda_3 + \sqrt{\lambda_1 \lambda_2} > 0, \quad (5.2.3c)$$

$$\text{vsc4} : \quad \lambda_3 + \lambda_4 - |\lambda_5| + \sqrt{\lambda_1 \lambda_2} > 0. \quad (5.2.3d)$$

Meeting the above positivity criteria at each scale of evolution effectively rules out deeper vacua at high energy scales.

In addition to the above, the splitting amongst the scalar masses is restricted by invoking the T -parameter constraint. We have used $\Delta T = 0.05 \pm 0.12$ following [132], where ΔT measures departure from the SM contribution. We have filtered all points in our parameter space through the above constraints and retained only those points that negotiate it

⁵NLO corrections to the unitarity bounds for a 2HDM are carried out in [197, 198]. However, for the typical values of the quartic couplings that are in consonance with high scale perturbativity, the results would not change upon including the NLO corrections.

successfully. Measurement of the rate for $b \rightarrow s\gamma$ leads to $m_{H^+} \geq 480$ GeV in case of the Type-II 2HDM [125, 201]⁶. In case of Type-I, there is no such lower bound. The constraint $m_{H^+} \geq 80$ GeV originating from direct searches however still persists.

5.3 Type-I 2HDM: Allowed parameter space for stable vacuum

We start by completing the existing studies [92, 161, 164, 165] on the parameter space allowing for high scale vacuum stability and perturbativity for a Type-I 2HDM⁷. A corresponding discussion for the Type-II 2HDM can be seen in [92]. We fix $m_h = 125$ GeV and $M_t = 175$ GeV, the rest of the parameters are generated randomly in the following ranges.

$$\tan\beta \in [1, 20], m_H \in [200, 1000], m_A \in [200, 1000], m_{H^+} \in [200, 1000],$$

$$\cos(\beta - \alpha) \in [-0.4, 0.4], \lambda_6 \in [-1, 1], \lambda_7 \in [-1, 1].$$

The generated values of the masses and mixing angles are translated to the basis of the quartic couplings using eqns.(5.2.1a)-(5.2.1e). The strong correlation among the masses, namely $m_H \simeq m_A \simeq m_{H^+}$, is revealed from Fig.5.1. This itself can be traced back to eqns. (5.2.1a)-(5.2.1e). Any large mass gap results in giving large values for λ_i at the EWSB scale itself, such that they turn non-perturbative rather early in the course of evolution. This feature is also corroborated in [164]. It is important to note that the mass-splitting depends, albeit weakly, on the chosen value of $\tan\beta$. For instance, in case of $\tan\beta = 2$, the maximum splitting allowed is $\simeq 15$ GeV for $\Lambda = 10^{19}$ GeV. This goes down to $\simeq 10$ GeV in case of $\tan\beta = 10$ for the same value of Λ . It should be noted here that the bound on mass splitting that comes from the requirement of perturbativity till high scales is much more stringent than what is obtained by the imposition of the T -parameter constraint alone.

Also important is the ensuing constraint on $\cos(\beta - \alpha)$ which decides the interaction strengths between W, Z and the non-standard scalars. The more suppressed is $\cos(\beta - \alpha)$, closer are the h -interactions to the corresponding SM values. Thus, measurement of signal strengths of h leads to constraint on this parameter [140, 174, 202]. Models valid up to 10^{19} GeV could allow for $|\cos(\beta - \alpha)| \leq 0.15$ and $|\cos(\beta - \alpha)| \leq 0.05$ for $\tan\beta = 2$ and $\tan\beta = 10$ respectively. This bound can be amply relaxed by choosing a lower Λ , for example

⁶This bound is stronger compared to $m_{H^+} \geq 315$ GeV, which is what was used in the analyses of

Chapter 3 and **Chapter 4**.

⁷The RG equations for the Type-I 2HDM are listed in **Appendix A.2**

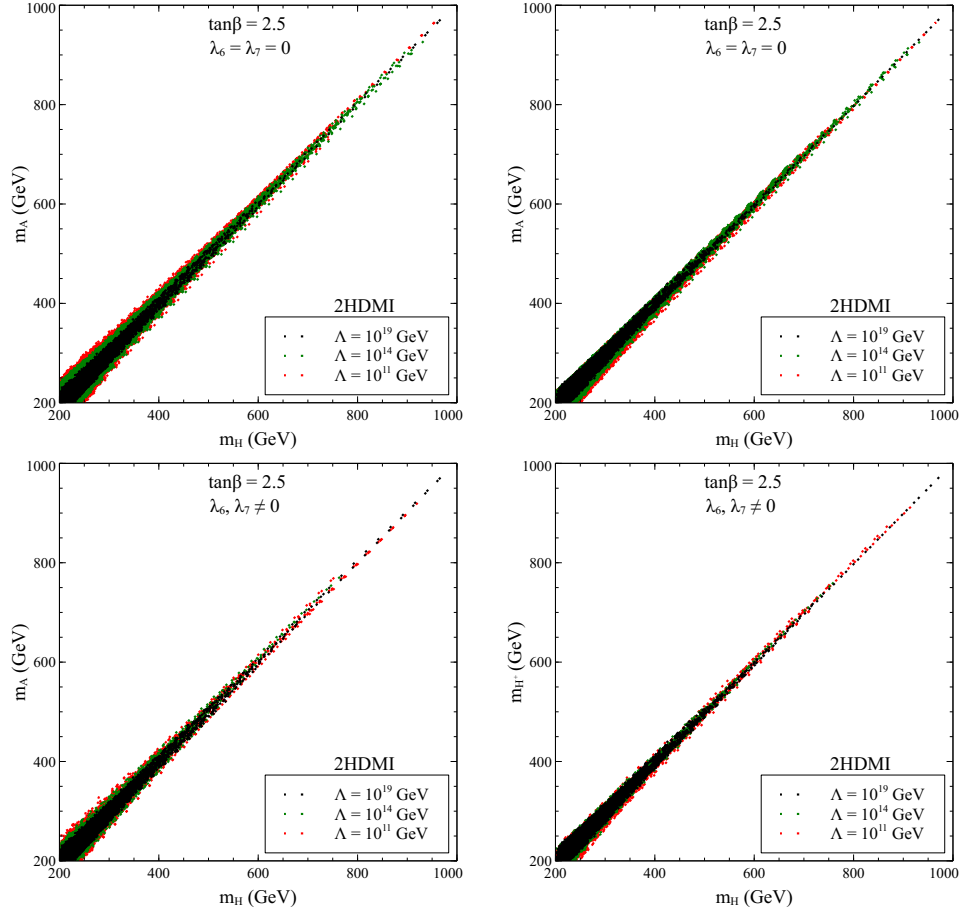


Figure 5.1: Distribution of the parameter points valid till Λ in the $m_H - m_A$ (left) and $m_H - m_{H^+}$ (right) planes for the Type-I 2HDM. The colour coding can be read from the legends. We fix $\tan\beta = 2.5$ as a benchmark. The upper(lower) plots correspond to $\lambda_6 = \lambda_7 = 0$ ($\lambda_6, \lambda_7 \neq 0$). We have varied λ_6, λ_7 in the interval $[-1, 1]$ for the lower plots.

one finds $|\cos(\beta - \alpha)| \leq 0.14$ in case of $\tan\beta = 10$ if one demands validity up to 10^{19} GeV. This apparent correlation between the UV cutoff scale and the maximum allowed value of $\cos(\beta - \alpha)$ [203], could lead us to predict the maximal extrapolation scale up to which such a 2HDM could be probed at the colliders. Of course, such a correlation can be noticed for the Type-II scenario as well. The additional result presented here, over and above what is found in the literature, is the establishment of the mass correlations for $\lambda_6, \lambda_7 \neq 0$, as shown in Fig.5.1.

5.4 Signals at the LHC: Types I and II.

The previous section illustrates that higher the UV cutoff of a 2HDM is, tighter become the mass-splitting and the bound on $|\cos(\beta - \alpha)|$. Such a constrained scenario makes its observability at the LHC a rather challenging task, as also emphasised in section 5.1. In particular, if we probe H and A via their decays into reconstructible final states, then the invariant mass distributions of the decay products would coincide. However, probing H and A in reconstructible but distinct final states could enable one to tag the CP of the decaying boson. Given that, we propose the following signals:

- (i) $pp \longrightarrow H \longrightarrow ZZ \longrightarrow 4l$,
- (ii) $pp \longrightarrow A \longrightarrow hZ \longrightarrow l^+l^-b\bar{b}$,

where, $l = e, \mu$. We have implemented the model using `FeynRules` [204]. The generated Universal FeynRules Output (UFO) files are then fed to the Monte-Carlo (MC) event generator `MadGraph` [205] for generation of event samples. The parton-showering and hadronisation is carried out in the `PYTHIA-6` [206] framework. We simulated H and A production through the gluon-gluon fusion (ggF) channel using the CTEQ6L1 parton distribution functions. This is because ggF offers higher rates compared to other channels. The renormalisation and factorisation scales have been set at m_H and m_A for the first and second signals respectively. We mention in this context that detector simulation and analysis of the events were done using `Delphes` [207].

For simulating the proposed final states, we hold m_H and m_A fixed and scan over the remaining input quantities. From the randomly generated parameter sets, we select an illustrative assortment of benchmark points (Table 5.1) to highlight the main findings of the analysis.

The benchmarks are distinct from another *vis-a-vis* RG evolution patterns. While choosing them, it was ensured that the UV cutoff of a given benchmark does not change upon

Benchmark	$m_H(\text{GeV})$	$m_A(\text{GeV})$	$m_{12}(\text{GeV})$	$\cos(\beta - \alpha)$
BP1a	350	351	200	-0.18
BP1b	350	351	200	-0.12
BP2a	400	401	230	-0.15
BP2b	400	401	230	-0.10
BP3a	500	501	280	-0.095
BP3b	500	501	280	-0.070
BP3c	500	501	280	-0.050
BP4a	550	551	320	-0.075
BP4b	550	551	320	-0.060
BP4c	550	551	320	-0.050
BP5a	600	601	350	-0.050
BP5b	600	601	350	-0.035
BP5c	600	601	350	-0.025

Table 5.1: Benchmarks chosen for simulating the proposed channels. We have taken $m_h = 125$ GeV and $\tan\beta = 2.5$ throughout. Any higher $\tan\beta$ would lead to a lower ggF rate and so was not chosen.

switching between the Type-I and Type-II models. For instance, in the case where $\lambda_6 = \lambda_7 = 0$, BP1b, BP1b, BP3c, BP4c and BP5c are conservative input sets ensuring a stable vacuum and a perturbative model till $\sim 10^{19}$ GeV. This can be read from the small values of $|\cos(\beta - \alpha)|$ characterizing them. The other benchmarks are however not that conservative, but still they manage to stabilise the vacuum till at least 10^{11} GeV. Likewise, BP3b and BP4b are included to estimate the statistical significance of scenarios valid till 10^{14} GeV. For a given set of couplings, elevating the masses of H and A progressively diminishes the intensity of the signals, and, also narrows the allowed band of $|\cos(\beta - \alpha)|$. The choice of the benchmarks is thus guided by the aim to understand the maximum m_H, m_A as well as the highest UV cutoff up to which the scenario can be experimentally observed.

5.4.1 $pp \rightarrow H \rightarrow ZZ \rightarrow 4l$

H is produced through gluon fusion and decays to two on-shell Z bosons. We look for a final state where the Z bosons subsequently decay into four leptons [208]. The dominant background for this process comes from $ZZ^{(*)}$ production. Taking into account subleading contributions from the $Z\gamma$ and $\gamma\gamma$ channels and multiplying by appropriate next-to-leading order (NLO) K-factors [205], the total background cross section is $\simeq 42$ fb. Some basic cuts, as listed below, were applied during event generation.

Basic-cuts:

- All leptons have a minimum transverse momentum of 10 GeV, $p_T^l \geq 10$ GeV.
- Pseudorapidity of the leptons must lie within the window $|\eta^l| \leq 2.5$.
- All possible lepton-pairs are resolved using $\Delta R_{ll} > 0.3$.

We multiply the ggF cross sections of H production by an NLO K factor of 1.5. The following selection cuts SC_H listed below were further imposed⁸

Selection cuts:

- $SC1_H$: The invariant mass of the final state leptons lie within the window $m_H - 15 \text{ GeV} \leq m_{4l} \leq m_H + 15 \text{ GeV}$.
- $SC2_H$: The transverse momenta of the leptons lie above the thresholds $p_T^{l_1} > p_{T,\min}^{l_1}$, $p_T^{l_2} > p_{T,\min}^{l_2}$, $p_T^{l_3} > 30 \text{ GeV}$, $p_T^{l_4} > 20 \text{ GeV}$.
- $SC3_H$: Transverse momenta of the reconstructed Z -bosons satisfy $p_T^{Z_1} > p_{T,\min}^{Z_1}$, $p_T^{Z_2} > p_{T,\min}^{Z_2}$.

We take $p_{T,\min}^{Z_1/Z_2} = 20, 20, 40, 50, 70$ GeV and $\{p_{T,\min}^{l_1}, p_{T,\min}^{l_2}\} = \{50 \text{ GeV}, 30 \text{ GeV}\}$, $\{50 \text{ GeV}, 30 \text{ GeV}\}$, $\{80 \text{ GeV}, 50 \text{ GeV}\}$, $\{90 \text{ GeV}, 70 \text{ GeV}\}$, $\{100 \text{ GeV}, 70 \text{ GeV}\}$ for BP1, BP2, BP3, BP4, BP5 respectively, the decisive factor in this choice of $p_{T,\min}^{Z_1/Z_2}$ being m_H , for any benchmark point.

For $m_H > 500$ GeV, the leading and the subleading leptons are strongly boosted, thus having a good probability of surviving the strong p_T -cuts. In addition, appropriate cuts on

⁸ p_T , η and ϕ respectively denote the transverse momentum, pseudorapidity and azimuthal angle of a particle. For two particles having pseudorapidity and azimuthal angle separations $\Delta\eta$ and $\Delta\phi$, one defines $\Delta R = \sqrt{\Delta\eta^2 + \Delta\phi^2}$. For details, see the reviews [209], [210, 211].

the p_T of the Z-bosons also contributes towards improving the signal-to-background ratio. Here, σ_S^{SC} and σ_B^{SC} respectively refer to the signal and background cross sections after the selection cuts. Denoting the number of signal and background events as \mathcal{N}_S and \mathcal{N}_B at a given integrated luminosity (\mathcal{L}), the statistical significance or the confidence limit (CL) is defined as $CL = \frac{\mathcal{N}_S}{\sqrt{\mathcal{N}_S + \mathcal{N}_B}}$.

Benchmark	σ_S^{SC} (fb)	σ_B^{SC} (fb)	\mathcal{N}_S^{100}	\mathcal{N}_B^{100}	\mathcal{N}_S^{3000}	\mathcal{N}_B^{3000}	CL ₁₀₀	CL ₃₀₀₀
BP1a	0.173	0.334	17.36	33.40	520.94	1002.18	2.43	13.34
BP1b	0.145	0.334	14.54	33.40	436.31	1002.18	2.10	11.50
BP2a	0.104	0.194	10.42	19.46	312.73	584.00	1.90	10.44
BP2b	0.071	0.194	7.11	19.46	213.38	584.00	1.37	7.55
BP3a	0.026	0.064	2.59	6.48	77.99	194.60	0.86	4.72
BP3b	0.016	0.064	1.68	6.48	50.52	194.60	0.58	3.22
BP3c	0.009	0.064	0.97	6.48	29.37	194.60	0.35	1.96
BP4a	0.011	0.041	1.13	4.16	34.06	124.91	0.49	2.70
BP4b	0.008	0.041	0.81	4.16	24.52	124.91	0.36	2.00
BP4c	0.006	0.041	0.61	4.16	18.33	124.91	0.27	1.53
BP5a	0.004	0.029	0.41	2.96	12.32	89.090347	0.22	1.22
BP5b	0.002	0.029	0.22	2.96	6.70	89.090347	0.12	0.68
BP5c	0.001	0.029	0.12	2.96	3.61	89.090347	0.06	0.37

Table 5.2: A record of the number of surviving events in the $H \rightarrow 4l$ channel after the selection cuts at the $\sqrt{s} = 14$ TeV LHC for a Type-I 2HDM. Here $\mathcal{N}_S^{100(3000)}$ and $\mathcal{N}_B^{100(3000)}$ respectively denote the number of signal and background events at $\mathcal{L} = 100(3000) \text{ fb}^{-1}$. Besides, $CL_{100(3000)}$ denotes the confidence level at $\mathcal{L} = 100(3000) \text{ fb}^{-1}$.

Tables 5.2 and 5.3 contain the estimated CL for all the benchmarks. The following features thus emerge:

(i) The statistical significance diminishes as m_H is increased. This is due to two reasons. First, the ggF cross section for a single H drops. Secondly, the higher is m_H , the smaller is the upper limit on $|\cos(\beta - \alpha)|$ consistent with high scale stability, and hence, the lower is the $H \rightarrow ZZ$ branching ratio.

(ii) Type-I 2HDM offers a marginally higher significance as compared with Type-II. This

Benchmark	σ_S^{SC} (fb)	σ_B^{SC} (fb)	\mathcal{N}_S^{100}	\mathcal{N}_B^{100}	\mathcal{N}_S^{3000}	\mathcal{N}_B^{3000}	CL ₁₀₀	CL ₃₀₀₀
BP3a	0.025	0.064	2.56	6.48	76.99	194.60	0.85	4.67
BP3b	0.016	0.064	1.65	6.48	49.65	194.60	0.58	3.17
BP3c	0.009	0.064	0.95	6.48	28.73	194.60	0.35	1.92
BP4a	0.011	0.041	1.12	4.16	33.64	124.91	0.48	2.67
BP4b	0.008	0.041	0.80	4.16	24.15	124.91	0.36	1.97
BP4c	0.006	0.041	0.60	4.16	18.02	124.91	0.27	1.50
BP5a	0.004	0.029	0.40	2.96	12.148	89.09	0.22	1.20
BP5b	0.002	0.029	0.21	2.96	6.58	89.09	0.124	0.67
BP5c	0.001	0.029	0.11	2.96	3.54	89.09	0.06	0.36

Table 5.3: A record of the number of surviving events in the $H \rightarrow 4l$ channel after the selection cuts at the $\sqrt{s} = 14$ TeV LHC for a Type-II 2HDM. Here $\mathcal{N}_S^{100(3000)}$ and $\mathcal{N}_B^{100(3000)}$ respectively denote the number of signal and background events at $\mathcal{L} = 100(3000) \text{ fb}^{-1}$. Besides, $\text{CL}_{100(3000)}$ denotes the confidence level at $\mathcal{L} = 100(3000) \text{ fb}^{-1}$.

is entirely attributed to the persistence of a slightly higher $H \rightarrow ZZ$ branching ratio in Type-I.

(iii) For $m_H \simeq 350$ GeV, an integrated luminosity of 100 fb^{-1} is sufficient to yield a 3σ significance.

(iv) To observe an H of mass around $\simeq 500$ GeV that originates from a 2HDM valid till 10^{19} GeV with a minimum of 3σ confidence level, one needs to gather 3000 fb^{-1} of data at the LHC. The statistical significance decreases for higher masses. In short, the observability of a given H can be improved by either lowering m_H and holding the UV cutoff fixed or vice versa. This interplay is illustrated in Fig.5.2 and Fig.5.3.

Fig.5.2 corroborates the previous observation that an H with $m_H = 500$ GeV can lead to a 3σ signal at the LHC, consistently with perturbativity as well as a stable vacuum till 10^{19} GeV. This is true for both Type-I and Type-II 2HDM. Note that the parameter space relaxes upon the introduction of non-vanishing λ_6 and λ_7 . This marginally helps in elevating the UV cutoff without compromising on the strength of the signal. For $m_H = 550$ GeV, on the other hand, a 2HDM (of either Type-I or Type-II) cannot be extrapolated beyond 10^{11} GeV if a 3σ statistical significance has to be maintained. This is confirmed by an inspection

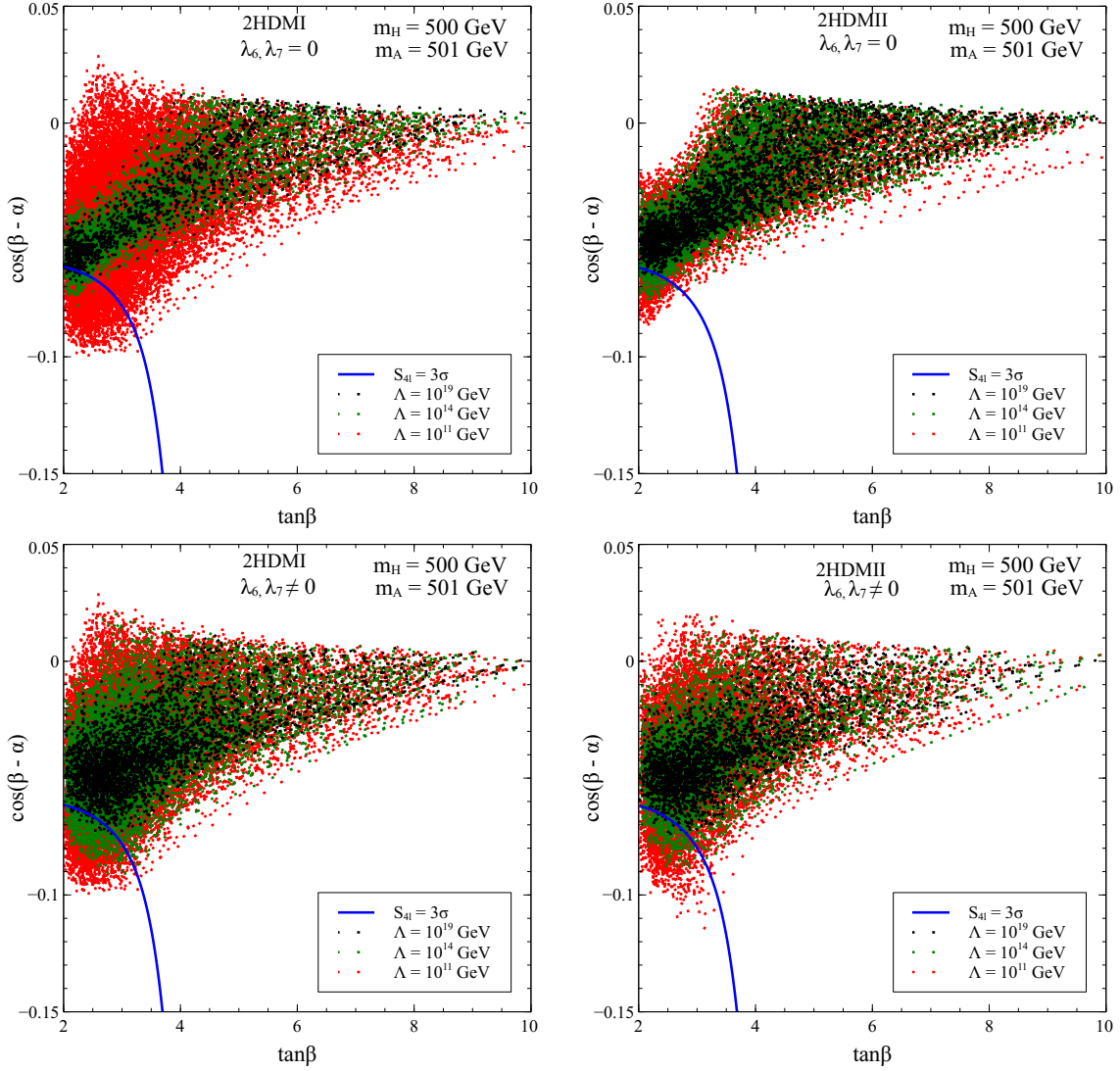


Figure 5.2: The parameter space in the $\tan\beta$ vs. $c_{\beta-\alpha}$ plane for $m_H = 500$ GeV and $m_A = 501$ GeV that allows for validity till 10^{11} GeV (red), 10^{14} GeV (green) and 10^{19} GeV (black). The region inside the blue curve corresponds to a signal significance greater than or equal to 3σ . The upper and lower plots are for $\lambda_6 = \lambda_7 = 0$ and $\lambda_6, \lambda_7 \neq 0$ respectively.

of Fig.5.3.

We examine the prospects of reconstructing A through the proposed $l^+l^-b\bar{b}$ final state in the following section.

5.4.2 $pp \longrightarrow A \longrightarrow hZ \longrightarrow l^+l^-b\bar{b}$

In the absence of CP -violation (as assumed here), the hZ pair production points towards a CP -odd parent particle [212], and a peak in the invariant mass close to the afore mentioned ZZ peak should be the smoking gun signal of the near degeneracy of a scalar and a pseudoscalar. However, $pp \longrightarrow t\bar{t}$ generates the dominant background for this final state. Subleading contributions come from the production of ZWW and $Zb\bar{b}$. Similar to the previous analysis, we adopt a K -factor = 1.5 for pseudoscalar production for all the benchmarks. The following cuts are applied during event-generation.

Basic cuts:

- $p_T^l \geq 10$ GeV, $p_T^b \geq 20$ GeV,
- $|\eta^l| \leq 2.5$, $|\eta^b| \leq 2.5$,
- $\Delta R_{ll} > 0.3$, $\Delta R_{lb} > 0.4$, $\Delta R_{bb} > 0.4$.

On applying the above cuts, the NLO background cross section turns out to be $\simeq 32$ pb. The following selection cuts (SC_A) are imposed for an efficient background rejection.

Selection cuts:

- $SC1_A$: The invariant mass of the leptons satisfy $85.0 \text{ GeV} \leq m_{ll} \leq 100 \text{ GeV}$.
- $SC2_A$: The invariant mass of the b-jets satisfy $95.0 \text{ GeV} \leq m_{bb} \leq 155 \text{ GeV}$.
- $SC3_A$: The scalar sum of the transverse momenta of the leptons and b-jets satisfies $\sum_{l,b} p_T > (\sum_{l,b} p_T)_{\min}$.
- $SC4_A$: An upper bound on the missing transverse momenta, $\cancel{E}_T \leq 30 \text{ GeV}$.
- $SC5_A$: The invariant mass of the $2l - 2b$ system lies within the range $m_A - 30 \text{ GeV} \leq m_{llbb} \leq m_A + 30 \text{ GeV}$.
- $SC6_A$: p_T of the reconstructed Z -boson satisfies $p_T^Z > 120 \text{ GeV}$ for BP5, and, $> 100 \text{ GeV}$ for the rest

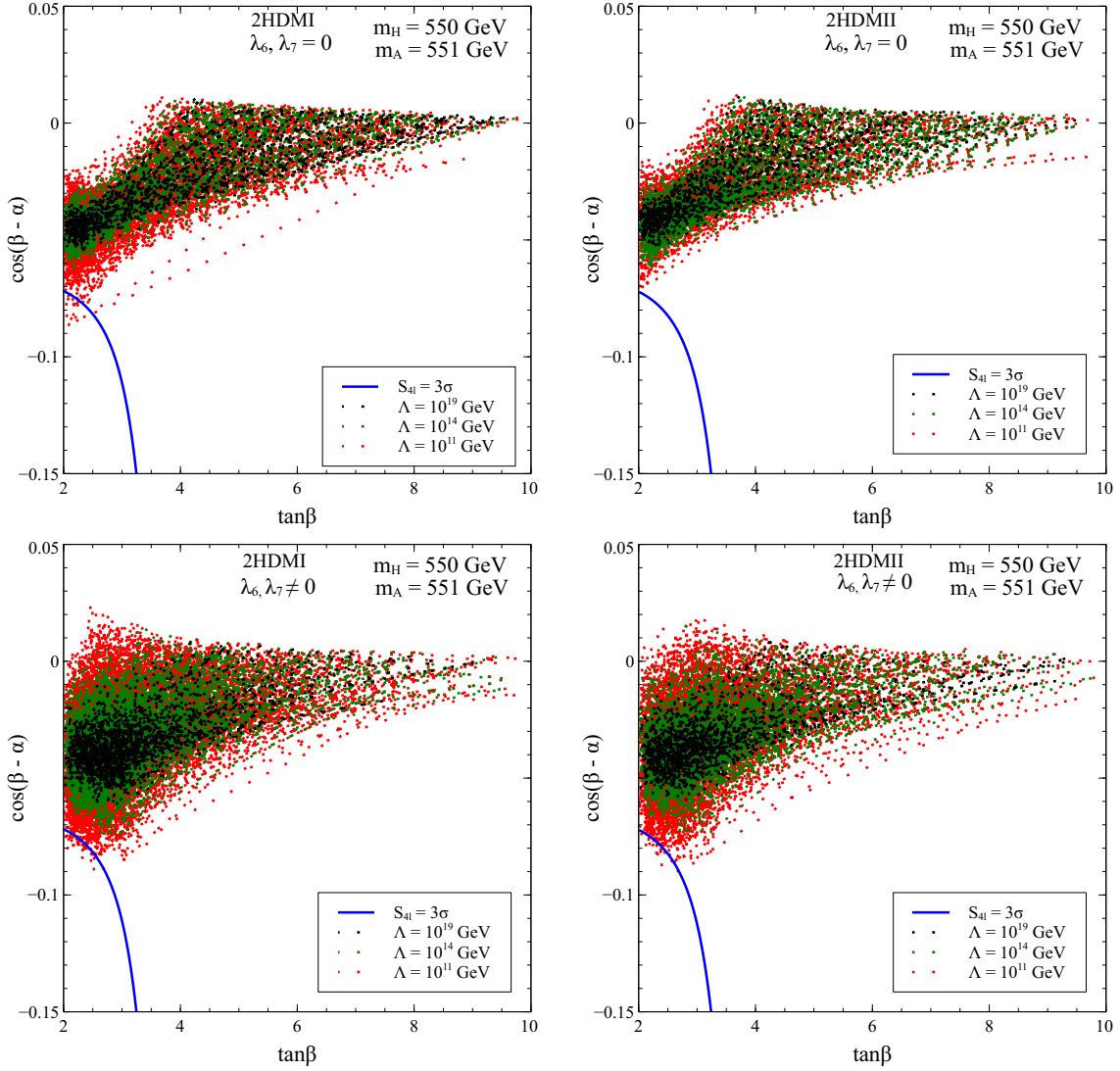


Figure 5.3: The parameter space in the $\tan\beta$ vs. $c_{\beta-\alpha}$ plane for $m_H = 550$ GeV and $m_A = 551$ GeV that allows for validity till 10^{11} GeV (red), 10^{14} GeV (green) and 10^{19} GeV (black). The region inside the blue curve corresponds to a signal significance greater than or equal to 3σ . The upper and lower plots are for $\lambda_6 = \lambda_7 = 0$ and $\lambda_6, \lambda_7 \neq 0$ respectively.

- $SC7_A$: Upper bounds on the p_T of the b-jets, $p_T^{b_1} > p_{T,\min}^{b_1}$.

The cuts on the p_T of leading b-jet as well as on scalar the sum of the p_T of the b -jets and leptons are appropriately strengthened with increase in m_A . We opt for $\{(\sum_{l,b} p_T)_{\min}, p_{T,\min}^{b_1}\} = \{270 \text{ GeV}, 40 \text{ GeV}\}$ for BP1, $\{320 \text{ GeV}, 40 \text{ GeV}\}$ for BP2, $\{350 \text{ GeV}, 50 \text{ GeV}\}$ for BP3 and BP4, and, $\{380 \text{ GeV}, 70 \text{ GeV}\}$ for BP5. The selection cuts involve reconstructing the invariant masses of not only the decaying A , but also of the Z and the h , appropriately in each case. A lower limit on the scalar sum of the p_T of the leptons and the b -hadrons also aids in increasing the significance. All the \cancel{E}_T in the signal is generated from mismeasurement of the momenta of the visible particles, thus generating a soft missing \cancel{E}_T distribution. On the other hand, the corresponding background has a harder p_T spectrum since the $t\bar{t}$ and ZWW channels always lead to neutrinos in the final state. Therefore, a suitable upper bound on the missing transverse energy reduces a portion of these backgrounds.

Tables 5.4 and 5.5 contain the statistical significances for this signal for Type-I and Type-II respectively. In this channel, too, Type-I fares slightly better than Type-II, much due to the same reason outlined in preceding discussion. In this channel, The statistical significance of BP1-5 is also enhanced *w.r.t* the $4l$ case, albeit marginally. The confidence level corresponding to $m_A = 500 \text{ GeV}$ looms around 3σ , for both Type-I and Type-II.

A clearer picture regarding the observability of an A of masses 500 GeV and 550 GeV emerge upon inspection of Fig.5.4 and Fig.5.5 respectively. We display the 5σ contour as well in case of the $l^+l^-b\bar{b}$ channel. For $m_A = 550 \text{ GeV}$ with non-zero λ_6 and λ_7 , the $l^+l^-b\bar{b}$ channel offers sensitivity at the level of 3σ for a scenario valid till 10^{14} GeV or even higher. On the contrary, the corresponding cutoff cannot be pushed above 10^{11} GeV if one demands similar observability in case of the $4l$ final state from H -decay. Overall, a violation of the \mathbb{Z}_2 symmetry via λ_6 and λ_7 aids to the effort of observing a 2HDM valid up to high cutoff scales.

It is mentioned that the analysis for this channel is subject to uncertainties, albeit small, that are introduced while estimating the background cross section. Upon considering the errors in the $t\bar{t}$ production rates and the background NLO K-factors [205], the total background cross section can deviate up to $\simeq \pm 20\%$. This, however, does not modify the overall conclusions made in this section.

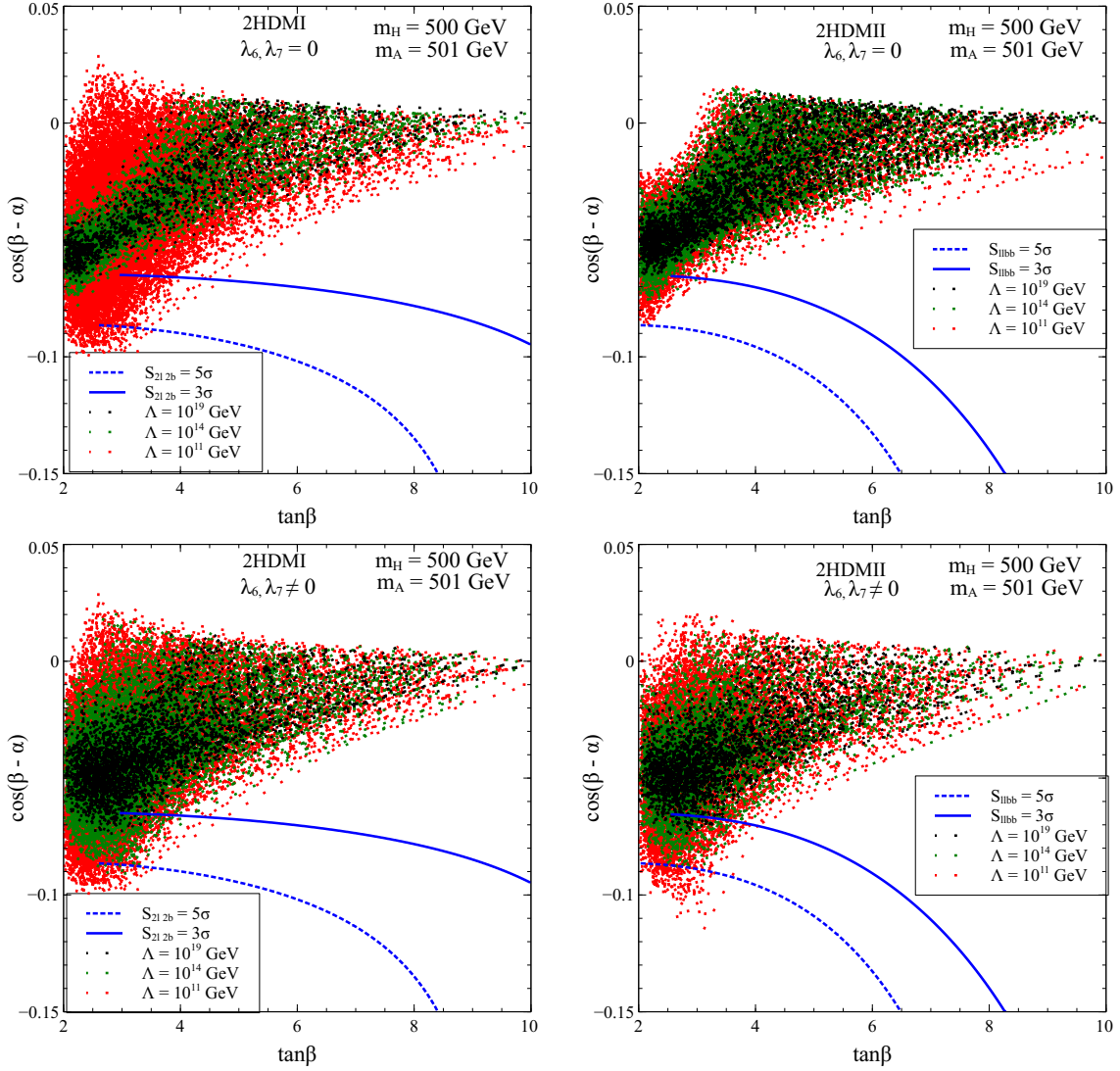


Figure 5.4: The parameter space in the $\tan\beta$ vs. $c_{\beta-\alpha}$ plane for $m_H = 500$ GeV and $m_A = 501$ GeV that allows for validity till 10^{11} GeV (red), 10^{14} GeV (green) and 10^{19} GeV (black). The region inside the solid (broken) blue curve corresponds to a signal significance greater than or equal to $3(5)\sigma$. The upper and lower plots are for $\lambda_6 = \lambda_7 = 0$ and $\lambda_6, \lambda_7 \neq 0$ respectively.

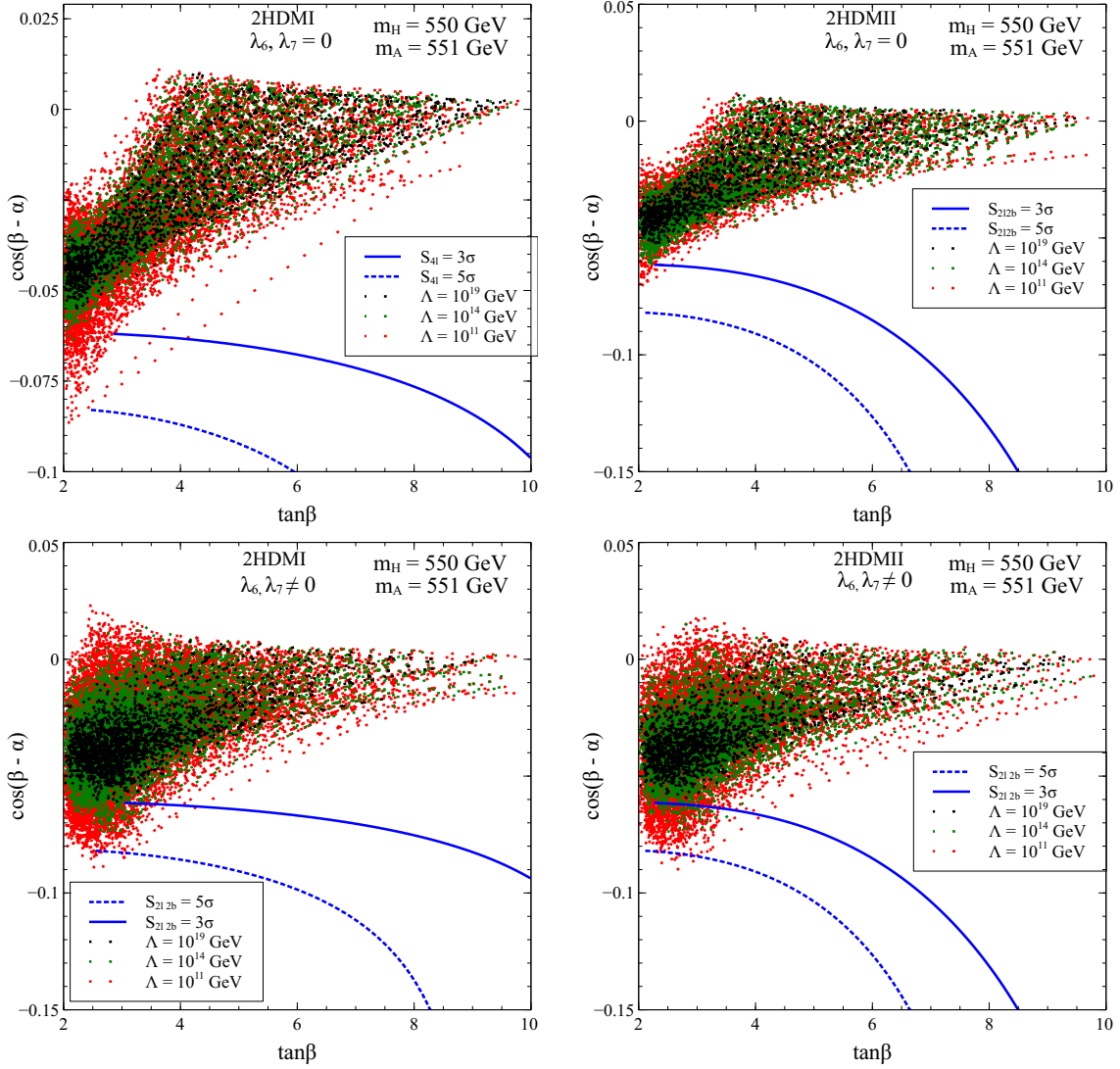


Figure 5.5: The parameter space in the $\tan\beta$ vs. $c_{\beta-\alpha}$ plane for $m_H = 550$ GeV and $m_A = 551$ GeV that allows for validity till 10^{11} GeV (red), 10^{14} GeV (green) and 10^{19} GeV (black). The region inside the solid (broken) blue curve corresponds to a signal significance greater than or equal to $3(5)\sigma$. The upper and lower plots are for $\lambda_6 = \lambda_7 = 0$ and $\lambda_6, \lambda_7 \neq 0$ respectively.

Benchmark	σ_S^{SC} (fb)	σ_B^{SC} (fb)	\mathcal{N}_S^{300}	\mathcal{N}_B^{100}	\mathcal{N}_S^{3000}	\mathcal{N}_B^{3000}	CL ₁₀₀	CL ₃₀₀₀
BP1a	1.65	10.94	164.60	1094.05	4938.02	32821.48	4.64	25.41
BP1b	0.90	10.94	89.55	1094.05	2686.45	32821.48	2.60	14.26
BP2a	0.55	4.30	55.22	430.24	1656.63	12907.32	2.51	13.73
BP2b	0.28	4.30	27.92	430.24	837.64	12907.32	1.30	7.14
BP3a	0.132	1.387	13.24	138.73	397.11	4161.95	1.07	5.88
BP3b	0.076	1.387	7.63	138.73	228.91	4161.95	0.63	3.45
BP3c	0.041	1.387	4.05	138.73	121.52	4161.95	0.34	1.86
BP4a	0.066	0.632	6.56	63.22	196.86	1896.59	0.79	4.30
BP4b	0.044	0.632	4.35	63.22	130.50	1896.59	0.53	2.90
BP4c	0.031	0.632	3.08	63.22	92.53	1896.59	0.38	2.07
BP5a	0.021	0.334	2.07	33.37	62.19	1000.98	0.35	1.91
BP5b	0.010	0.334	1.05	33.37	31.38	1000.98	0.18	0.98
BP5c	0.005	0.334	0.54	33.37	16.27	1000.98	0.09	0.51

Table 5.4: A record of the number of surviving events in the $A \rightarrow l^+l^-b\bar{b}$ channel after the selection cuts at the $\sqrt{s} = 14$ TeV LHC for a Type-I 2HDM. Here $\mathcal{N}_S^{100(3000)}$ and $\mathcal{N}_B^{100(3000)}$ and respectively denote the number of signal and background events with $\mathcal{L} = 100(3000)$ fb⁻¹. Besides, CL₁₀₀₍₃₀₀₀₎ denotes the confidence level for $\mathcal{L} = 100(3000)$ fb⁻¹.

5.5 Prospects at other colliders

With the prospects of observing non-standard scalars with masses above the 500 GeV range at the LHC turning bleak, we resort to future lepton colliders for better observability. These include not only the e^+e^- colliders, but also a muon collider [191].

The principal heavy Higgs production channels at the e^+e^- machine are those of associated production (VH) and Vector-Boson-Fusion (VBF) [213]. The production rate in both of these modes is controlled by the value of $\cos(\beta - \alpha)$. As elaborated in the previous sections, $\cos(\beta - \alpha)$ is tightly bounded by the requirement of a stable vacuum till the Planck scale. In addition, the maximum \sqrt{s} proposed for the ILC is 1 TeV [214] which hinders a probe of heavy scalars due to kinematical limitations. For instance, the VH production cross section for an H of mass 600 GeV could be at most $\simeq 0.01$ fb in a ILC with $\sqrt{s} = 1$ TeV. This does

Benchmark	σ_S^{SC} (fb)	σ_B^{SC} (fb)	\mathcal{N}_S^{300}	\mathcal{N}_B^{100}	\mathcal{N}_S^{3000}	\mathcal{N}_B^{3000}	CL ₁₀₀	CL ₃₀₀₀
BP3a	0.130	1.387	13.01	138.73	390.23	4161.95	1.06	5.78
BP3b	0.075	1.387	7.49	138.73	224.80	4161.95	0.62	3.39
BP3c	0.040	1.387	3.98	138.73	119.30	4161.95	0.33	1.82
BP4a	0.065	0.632	6.45	63.22	193.61	1896.59	0.77	4.23
BP4b	0.043	0.632	4.28	63.22	128.30	1896.59	0.52	2.85
BP4c	0.030	0.632	3.03	63.22	90.95	1896.59	0.37	2.04
BP5a	0.020	0.334	2.04	33.37	61.18	1000.98	0.34	1.88
BP5b	0.010	0.334	1.03	33.37	30.87	1000.98	0.18	0.96
BP5c	0.005	0.334	0.53	33.37	16.00	1000.98	0.09	0.50

Table 5.5: A record of the number of surviving events in the $A \rightarrow l^+l^-b\bar{b}$ channel after the selection cuts at the $\sqrt{s} = 14$ TeV LHC for a Type-II 2HDM. Here $\mathcal{N}_S^{100(3000)}$ and $\mathcal{N}_B^{100(3000)}$ respectively denote the number of signal and background events with $\mathcal{L} = 100(3000) \text{ fb}^{-1}$. Besides, $\text{CL}_{100(3000)}$ denotes the confidence level at for $\mathcal{L} = 100(3000) \text{ fb}^{-1}$.

not result in the requisite signal significance when the backgrounds are estimated and the cut efficiencies are folded in.

5.5.1 $\mu^+\mu^-$ collisions and radiative return

A particularly interesting process in a muon collider is one of radiative return (RR) [215], where one does not need to know the mass of the resonantly produced scalar precisely. In our context, the processes under consideration are

$$\mu^+\mu^- \longrightarrow H \gamma, A \gamma. \quad (5.5.1)$$

Note here that H/A can be produced in association with a γ in t -channel $\mu^+\mu^-$ annihilations. When the center of mass energy of the muon collider is above the heavy resonance, the photon emission from the initial state provides an opportunity to reconstruct the mass of the heavy scalar or pseudoscalar. For this, one need not know the mass of the (unknown) heavy resonance. The final state then consists of a soft photon and other visible products exhibiting an invariant mass peak. The closer is the mass of the heavy scalar to the centre-of-mass (COM) energy of $\mu^+\mu^-$ collisions, the higher the cross section.

Thus tagging a heavy scalar state from invariant mass peak of its decay product can help us in reducing the background and increasing the statistical significance. Moreover, in order to obtain information on the CP of the heavy resonance, the CP -even and the CP -odd states must be allowed to decay in different final states following their production through RR. We can propose $H \rightarrow ZZ \rightarrow 4l$ and $A \rightarrow hZ \rightarrow l^+l^-b\bar{b}$, which resemble the signals studied in the previous sections, and distinguish the CP -even scalar from the CP -odd one. In order to study the observability of the benchmarks BP3a - BP5c in RR, we choose the COM energy of the $\mu^+\mu^-$ collisions to be just 10 GeV above m_H , in each case. For BP3a, the RR cross section for H production is $\simeq 1.3$ fb for a Type-II 2HDM. Upon multiplying by the branching ratios corresponding to $H \rightarrow ZZ$ and $Z \rightarrow ll$, the corresponding cross section for the $4l + \gamma$ final state turns out to be $\mathcal{O}(10^{-4})$ (fb). The cross section for the $l^+l^-b\bar{b} + \gamma$ final state could still be $\mathcal{O}(10^{-3})$ (fb). However, it will ultimately get reduced when kinematical cuts are applied. In a Type-II 2HDM, though the $\mu\mu H$ coupling is proportional to $\tan\beta$, opting for a higher value of $\tan\beta$ does not help in this regard, since in that case, the allowed value of $|\cos(\beta - \alpha)|$ decreases owing to the demand of validity till high scales. This diminishes the $H \rightarrow ZZ$ and $A \rightarrow hZ$ branching ratios, and ultimately, leads to further lower rates. The other BPs too predict negligibly small RR rates for both Type-I and Type-II. With such meagre RR rates in $4l + \gamma$ as well as $l^+l^-b\bar{b} + \gamma$ channels, chances of observing the heavy resonances are obliterated.

Still promising could be the fermionic decay channels of H/A in this regard. For instance, the $b\bar{b}A$ coupling in a Type-(I)II 2HDM is proportional to $\cot\beta(\tan\beta)$ and for sufficiently small $|\cos(\beta - \alpha)|$, the fermionic couplings of H and A are nearly equal. The advantage of a muon collider over the LHC is that the $b\bar{b}$ final state can rise above the background more effectively. As we shall see below, this enhances the mass reach.

One can thus probe the observability of the heavy scalars in the $\mu^+\mu^- \rightarrow H/A\gamma \rightarrow b\bar{b}\gamma$ ⁹. It is readily seen that for $\tan\beta > 1$, Type-II has higher production rates of H/A through RR compared to Type-I. This could give a handle in distinguishing between Type-I and Type-II. Therefore, to test the potency of RR in the $H/A \rightarrow b\bar{b}$ mode, we tabulate two additional benchmarks, as shown in Table 5.6.

The values of the other 2HDM parameters have been fixed appropriately so as to ensure vacuum stability and perturbative unitarity till the Planck scale. For instance, we chose

⁹In view of the high t -Yukawa coupling, one could also look at $\mu^+\mu^- \rightarrow H/A\gamma \rightarrow t\bar{t}\gamma$ in principle. However that channel will ultimately lead to lesser rates compared to the $b\bar{b}$ mode owing to the smaller $t\bar{t}$ branching fraction.

Benchmark	\sqrt{s} (GeV)	$\tan\beta$	m_H (GeV)	m_A (GeV)
BP6	500	12	492	493
BP7	1000	12	992	993

Table 5.6: The values of m_H , m_A and $\tan\beta$ chosen to probe the radiative return channel. The values of \sqrt{s} are also shown.

$m_{12} = 150$, $c_{\beta-\alpha} = 0.01$ and $m_{12} = 500$, $c_{\beta-\alpha} = 0.001$ for BP6 and BP7 respectively. We take 500 GeV and 1 TeV to be COM energy for these two cases. Accordingly, $\sqrt{s} - m_{H/A}$ is maintained around ~ 7 GeV to maximise the efficiency of the radiative return mechanism. In addition, we have purposefully chosen a somewhat large value for $\tan\beta$ to elevate the H/A production rate to the order of 10 fb. Moreover, we also get a sizeable branching ratio for the $H/A \rightarrow b\bar{b}$ channel for both BP6 and BP7 ($> 70\%$).

The SM background comes from the processes $\mu^+\mu^- \rightarrow b\bar{b}$ and $\mu^+\mu^- \rightarrow b\bar{b}\gamma$. The cut, $m_H - 30 \text{ GeV} < m_{bb} < m_H + 30 \text{ GeV}$ on the invariant mass of the b -pair is imposed. The softness of the photon in the case of RR can be exploited to reduce the background by putting an upper bound on the photon p_T , which we take to be 30 GeV. Effects arising out of smearing the photon-energy are small, so we keep the photon-energy same as the simulated value. The confidence levels obtained for BP6 and BP7 are listed in Table 5.7.

Benchmark	σ_S^{SC} (fb)	σ_B^{SC} (fb)	\mathcal{N}_S^{500}	\mathcal{N}_B^{500}	\mathcal{N}_S^{1000}	\mathcal{N}_B^{1000}	CL ₅₀₀	CL ₁₀₀₀
BP6	2.13	32.22	1067.83	16110.05	2135.65	32220.08	8.14	11.12
BP7	0.29	2.52	146.55	1264.28	293.10	2528.57	3.90	5.51

Table 5.7: Number of signal and background surviving events in the radiative return process at the muon collider. Here $\mathcal{N}_S^{500(1000)}$ and $\mathcal{N}_B^{500(1000)}$ and respectively denote the number of signal and background events $\mathcal{L} = 500(1000) \text{ fb}^{-1}$. Besides, CL₅₀₀₍₁₀₀₀₎ denotes the confidence level at $\mathcal{L} = 500(1000) \text{ fb}^{-1}$.

Table 5.7 shows that it is possible to experimentally observe an H as heavy as 1 TeV through radiative return. The corresponding signal rates are almost identical for a near degenerate A decaying to $b\bar{b}$, and thus, are not separately shown. Thus, radiative return in the $b\bar{b}$ channel does succeed in predicting abundant signal events in case of heavy scalars. This is reflected by a sizeable statistical significance of $\sim 5\sigma$ that can be obtained in case

of a scalar of mass 1 TeV when the $\mu^+\mu^-$ machine is operated at an integrated luminosity of 1000 fb^{-1} . More importantly, this is found to be in perfect agreement with high-scale stability and perturbativity up to M_{Pl} . However in this channel, one faces the difficulty in distinguishing between a $b\bar{b}$ resonance that comes from an H and one coming from A . This is in sharp contrast with the results obtained in case of the 14 TeV LHC. Over there, though the CP of the scalar can be tagged, its observability does not exceed 3σ in terms of confidence level for masses beyond 500 GeV.

5.6 Summary and conclusions.

By virtue of the additional bosonic fields, a 2HDM ensures the stability of the EW vacuum till a cutoff scale all the way up to the Planck scale. This holds true even after switching between the Type-I and Type-II cases. However stringent constraints apply on the parameter space in the process. This is especially true when vacuum stability and perturbative unitarity are demanded up to the Planck scale. Then, the couplings of the non-standard scalars to other bosonic states become very small because of suppressed $\cos(\beta - \alpha)$. In addition, the mass spectrum of the non-standard scalar bosons becomes quasi-degenerate. These constraints limit the observability of such a 2HDM at colliders.

We have studied in detail the interplay between high-scale validity and the discernibility of the scenario at the LHC and at a future muon collider. In the LHC, signatures of the CP -even boson H and CP -odd boson A are studied through their decays into the $4l$ and $l^+l^-b\bar{b}$ channel respectively. The search turns challenging due to the stringent upper bound on $\cos(\beta - \alpha)$. A sizeable signal significance demands an upper bound on $\tan\beta$, contrary to high scale validity constraints, where no such bound is predicted. An analysis at the 14 TeV LHC including detector effects reveals that H and A of masses around 500 GeV can be simultaneously observed in their respective channels with at least 3σ confidence when the integrated luminosity is 3000 fb^{-1} . The observability improves upon de-escalating the cutoff scale, attaining 5σ statistical significance becomes possible when the cutoff is near 10^{11} GeV .

Radiative return at the muon collider yields sizeable production rates of H or A . We have studied the observation their prospects through their subsequent decay to the $b\bar{b}$ final state. Contrary to the results obtained for the LHC, the $\mu^+\mu^-$ machine can lead to a 5σ statistical significance even if the scalar mass is 1 TeV. Thus a certain complementarity of roles between the LHC and a muon collider is noticed. The former has relatively lower mass reach but clearly differentiates the H -peak from the A -peak, while the latter loses this

distinction by being forced to look at the $b\bar{b}$ decay mode, though up to higher (pseudo)scalar masses.

Chapter 6

Particle dark matter: An introduction

6.1 What is dark matter?

One of the most compelling reasons for expecting fundamental physics beyond the ambit of the SM is the presence of dark matter in the universe. A great majority of matter in the universe is unseen, since visible stars and gas inside galaxies and clusters account for only a small fraction of the matter contribution to the energy density of the universe. The rest of the contribution is believed to be coming from invisible matter, termed as "dark matter". The term was coined by the astronomer F. Zwicky in 1933 when he postulated its existence based on his observations on the COMA galaxy cluster [216]. According to the space observatory PLANCK [217,218], the universe consists of $4.82 \pm 0.05\%$ ordinary matter, $25.8 \pm 0.4\%$ dark matter and $69 \pm 1\%$ dark energy.

The Λ CDM model [219] is a cosmological model which describes the universe in terms of a cosmological constant (Λ), dark energy and cold dark matter (CDM). It is deemed to be the standard model of Big Bang cosmology. The inclusion of dark matter in the Λ CDM paradigm provides a reasonable account of the structure of the cosmic microwave background (CMB) [220, 221] and the large-scale structure in the distribution of galaxies. These hypotheses have been supported by various astrophysical evidences of dark matter, the principal examples of which include the observations on the galaxy rotation curves, gravitational lensing and the anisotropies observed in the CMB. The PLANCK satellite mission has published precise measurements of the CMB, which are in complete agreement with the predictions of Λ CDM model. Therefore, all these lines of evidence suggest that galaxies, galaxy clusters, and the universe as a whole contain far more matter than that

which can be observed via electromagnetic signals.

Despite such concrete astrophysical evidences, the nature of dark matter is still unknown. An immediate hypothesis is that dark matter is made up of elementary particles, which are mostly believed not to be the SM ones. In such a case, when dark matter becomes a part of the paradigm of particle physics many new questions arise. They are, for instance, *Is dark matter made up of only one kind of particle, or, do they involve many? What could be the mass of the constituent particle(s)? How does dark matter interact with the SM fields and with itself? Is a dark matter particle absolutely stable or does it exhibit late decays?* Although such issues can be addressed using particle physics models, more definitive statements on the origin of particle dark matter is expected to emerge through experiments only.

This thesis aims to probe some aspects of particle dark matter. However, the following comment is in order. Given the absence of conclusive signals of particle dark matter as yet, astrophysicists have also argued for various modifications of general relativity, such as Modified Newtonian Dynamics (MOND) [222], that attempt to explain the observations without invoking additional matter.

We discuss a few evidences of dark matter in the subsequent section.

6.2 Some evidences for dark matter

- ***Rotation curves of spiral galaxies:*** In a spiral galaxy, most of its mass is concentrated near a central bulge. A rotational curve of a galaxy is defined to be the orbital speed of the stars in the galaxy as a function of their radial distance from the galactic center. For a star of mass m moving at a distance r from the galactic center with a circular velocity $v(r)$, the following holds

$$\frac{mv^2(r)}{r} = \frac{GmM}{r^2}, \quad (6.2.1)$$

where, M denotes the mass of the galactic matter within the radius r . Be the star outside the dense central hub of the galaxy, M can be taken to be constant. In that case, one expects $v(r) \propto \frac{1}{\sqrt{r}}$ using eqn.(6.2.1). On the contrary, observational measurements of rotation curves for several spiral galaxies show $v(r) = \text{constant}$ for large r . For instance, In our galaxy, $v \simeq 240$ km/s at the location of our solar system, with little change up to the largest observable radius.

The discrepancy can be explained by assuming $M \propto r$, that is, by hypothesizing the existence of a substantial amount of undetected matter permeating the galaxy.

- **Mass-to-luminosity ratio in galaxy clusters:** The virial theorem relates the time-averaged kinetic energy to the time-averaged potential energy of a system of interacting non-relativistic particles in dynamic equilibrium. Referring to the kinetic and potential energies of the system as T and V respectively, the virial theorem states

$$V + 2T = 0. \quad (6.2.2)$$

For a galaxy cluster of mass M and radius R , and where v_{rms} is the root mean square speed of each galaxy, one writes

$$V = -\frac{3}{5} \frac{GM^2}{R}, \quad (6.2.3a)$$

$$T = \frac{3}{2} M v_{rms}^2. \quad (6.2.3b)$$

Therefore, the gravitational mass M of such a galaxy cluster can now be estimated from eqns.(6.2.2),(6.2.3a) and (6.2.3b) if R and v_{rms} are known from measurements. Zwicky found that the estimated mass-to-luminosity ratio in the Coma cluster is around 50 times as large as that of any individual galaxy. This is indicative of the presence of large proportions of gravitating mass in galaxy clusters. These observations were corroborated by more sophisticated techniques in the recent times.

- **Bullet clusters:** One of the most energetic events after the big bang was the collision of two giant galaxy clusters at a distance of around 4 billion light years from the Earth. Analyses of the X-ray spectra have revealed that the collision was massive enough to cause the baryonic matter (normal matter) in each colliding cluster to displace from its respective dark matter halo [223–225]. On the contrary, the dark matter halos as surmised from gravitational lensing effects [226] around the tails of the cluster (where the baryon density is palpably low), show that they passed through each other undistorted. This particular phenomenon has led to the understanding that dark matter is collisionless, i.e., it interacts with luminous matter as well as with itself very weakly. The 'non-baryonic' massive particle interpretation thus gains ground.
- **The cosmic microwave background:** The cosmic microwave background (CMB) is the electromagnetic radiation left over from the time of recombination in Big Bang cosmology, with a radiation density around $\simeq 0.25 \text{ eV/cm}^3$. It has essentially established the Big Bang Theory as the standard model of cosmology. The CMB spectrum resembles closely to a perfect blackbody, but contains certain anisotropies [221,227,228]. These anisotropies can be decomposed into a power spectrum, whose peaks constrain

cosmological parameters. The first peak mostly shows the density of baryonic matter, while the third peak relates mostly to the density of dark matter, measuring the density of matter and the density of atoms. The spectrum was first observed by WMAP [229–231], and the results support the Λ CDM model.

6.3 Some properties of dark matter

The miscellaneous evidences discussed above do point out towards some important properties that dark matter must necessarily have, an understanding of which helps to build particle physics models of dark matter. We therefore enlist them below.

- Dark matter is non-luminous, that is, it does not interact with the photon. Otherwise, it would have led to a CMB spectrum different *w.r.t* what is observed today. Dark matter particles are therefore electrically neutral.
- The dark matter in the universe is all pervading, and, it aids the formation of large-scale structures such as galaxy clusters by aggregating gravitating mass.
- Dark matter particles are stable on a cosmological time scale. That is, even if they decay, the corresponding lifetime must exceed the age of the universe.
- Weak interactions of dark matter, that is to say, interactions with W^+ and Z are permitted. However, they must be in consonance with the non-observation of dark matter in the recent direct detection experiments. Interactions with other SM matter particles are expected to be more suppressed. It is also worthwhile to comment on dark matter self-interactions in this context. For hard-sphere elastic scattering, a constraints applies on the self-interaction cross section per unit dark matter mass, i.e., $\frac{\sigma}{m} < 1 \text{ cm}^2/g$. This bound stems from observations on the structure of galaxy clusters.
- The known fundamental particles (Standard Model particles) like leptons and quarks do not qualify as dark matter candidates as they are electrically charged. The only exceptions are neutrinos, which are neutral particles. But the relic density of neutrinos falls far too short of the observed relic density of dark matter [232, 233]. Moreover, neutrinos contribute to hot dark matter, whereas according to CMB studies, dark matter is overwhelmingly cold or warm.

6.4 Types of dark matter

Dark matter can be classified based on their thermal history, their baryonic content, and, their mass. Below is a discussion of the various classification schemes.

6.4.1 From thermal history

Dark matter can be classified on the basis of whether it was produced thermally or non-thermally in the early Universe. Thermal dark matter is produced via the collision of cosmic plasma in radiation-dominated era. That is, the dark matter particles were in thermal and chemical equilibrium with the thermal plasma in the early universe. They were produced through annihilation of the SM particles, and the reverse of it would also occur concurrently. The dark matter particles decoupled from the thermal soup when the interaction rate diminished compared to the rate of Hubble expansion. This caused the comoving number density of the dark matter particles to become constant that time onwards. This phenomenon, where the annihilation rate exactly equalled the expansion rate is known as "freeze-out" and the temperature at which the freeze-out occurred is known as the freeze-out temperature for that DM species. In this context, the case of a Weakly Interacting Massive Particles (WIMP) as candidate for dark matter is particularly interesting. On the other hand, non-thermal production refers to processes taking place outside of the thermal equilibrium. In such a case, the dark matter relic density generated by the out-of-equilibrium decays of heavier states, or, through annihilation of other particles [234]. Examples of non-thermal dark matter candidates include super-light particles such as axions and super-heavy particles such as WIMPzillas [235] which are produced by gravitational effects.

6.4.2 From particle content

The particle nature of dark matter is yet not verified. However, that the proportion of visible matter in the universe is somewhat lesser than the baryonic matter, a small room is indeed left for dark matter to have a baryonic nature. Baryonic dark matter can be present in the gas of intergalactic medium (Lyman alpha), floating stars in a cluster of galaxies etc. The amount of baryonic dark matter can be inferred from models of Big Bang nucleosynthesis [236–238]. It should be however remembered that dark matter is believed to be dominantly non-baryonic since its proportion by far exceeds the same for baryons. Since non-baryonic dark matter has little or no interactions with ordinary matter, it is harder to

detect compared to its baryonic counterpart.

6.4.3 From mass and speed

Dark matter particles with masses around ~ 1 keV have relativistic speeds during freeze-out. Such are categorised as hot dark matter. These are characterized by $x_f = \frac{m}{T_f} < 3$, with m and T respectively denoting the dark matter mass and its freeze-out temperature. If on the other hand, one has $x_f > 3$, then the corresponding dark matter is referred to as cold dark matter (CDM). Such particles generally have masses $\sim \mathcal{O}(10)\text{GeV} - 1\text{TeV}$ and are non-relativistic at freeze-out epoch. Weakly interacting massive particles (WIMPs) are hypothetical particles that are thought to constitute CDM [239, 240].

There is an important difference between these two types from the perspective of structure formation. Simulations of a universe dominated by cold dark matter produce galaxy distributions that are roughly similar to what is observed. In contrast, a relativistic entity such as the hot dark matter would smear out the large-scale structure of galaxies and hence would not be viable [241]. There is also an intermediate kind called warm dark matter [242], which is however still not ruled out. In this thesis, we have considered scenarios of cold dark matter based on extended scalar sectors.

6.5 Some popular models for dark matter

In this section, we discuss some popular dark matter scenarios.

- ***The lightest supersymmetric particle***: Supersymmetric models not only pose an attractive solution to the naturalness problem, but also DM promising candidates. In most supersymmetric scenarios, the proton is rendered stable by the action of a particular discrete symmetry called R -parity. This is defined to be $R = (-1)^{3(B-L)+2S}$, with B, L and S respectively denoting the baryon number, lepton number and spin of the particle. A fallout of R -parity conservation is that all SM particles carry $R = 1$ and their superpartners carry $R = -1$. Consequently, the lightest superpartner becomes a stable particle. Within the framework of the Minimal Supersymmetric Standard Model (MSSM) [243, 244], an example of such a stable entity is the lightest neutralino. That is, admixtures of the $s = 1/2$ partners of the Higgs fields, the B and the W_3 bosons lead to four Majorana fermions known as neutralinos. As highlighted before, the lightest neutralino therefore becomes a promising dark matter candidate [245–248]. However,

in scenarios beyond the MSSM, alternative dark matter candidates can be predicted. These include gravitinos [249–251] and right-handed sneutrinos [252–254] for instance.

- ***Kaluza Klein dark matter***: In extra dimensional models, the SM is postulated to be embedded in five spacetime dimensions ($d = 5$), where the fifth dimension is compactified. As a result, an infinite number of states, called KK-tower, emerge corresponding to each SM field. In a KK tower, the various states are designated by the quantum number n . For instance, an SM particle is the $n = 1$ state and $n = 2, 3, \dots$ are the corresponding KK excitations. Now, in Universal Extra Dimensions (UED) [255], an analogue of the R -parity emerges, known as the KK parity, which also leads to stable particles that could be possible dark matter candidates [256–265]. One example of such is the first KK-excitation of the $U(1)_Y$ gauge boson, denoted as $B_\mu^{(1)}$.
- ***The axion***: The axion is one of the leading non- baryonic cold DM candidates. The axion, a light pseudoscalar boson, was proposed to address the strong CP problem [266–270]. A number of astrophysical observations and laboratory experiments have put the bound on axion mass to be $\simeq 0.53$ eV [271]. In spite of having this tiny a mass, they can still be cold [272, 273] if they are produced through non-thermal means.
- ***Scalar dark matter***: A scalar dark matter candidate is usually modelled by extending the SM scalar sector. Two popular examples of which are the scalar singlet, and the inert doublet dark matter. In either case, the additional scalars are prevented from receiving vacuum expectation values, and, this is achieved by demanding them to be odd under some discrete symmetry such as \mathbb{Z}_2 . This symmetry, whose action is similar to that of R -parity in supersymmetry, is responsible for the stability of the dark matter particle. The former scenario employs an $SU(2)_L$ singlet scalar that couples only to the SM Higgs through the scalar potential [274]. Therefore, annihilation to SM states proceeds via an s -channel Higgs exchange. Therefore, such classes of models are also referred to as 'Higgs portal' scenarios. On the other hand, in the latter scenario, an additional $SU(2)_L$ scalar doublet, commonly called an 'inert doublet', is used [275]. In this case, apart from h -mediated annihilations, possibilities of coannihilation amongst the inert scalars also open up.

6.6 Calculation of relic abundance

In the thermal soup, a dark matter particle (χ) and its antiparticle ($\bar{\chi}$) are produced by the annihilation $X_{SM}X_{SM} \rightarrow \chi\bar{\chi}$, where X_{SM} is an SM particle. The reverse reaction $X_{SM}X_{SM} \rightarrow \chi\bar{\chi}$ also takes place, and, a simultaneous occurrence of the two maintains the dark matter particle in thermal equilibrium. However, as the annihilation rate depreciates with respect to the rate of expansion of the universe, the interactions maintaining the thermal equilibrium freeze out. Since χ does not decay, its abundance becomes fixed and does not change as the universe evolves. Hence, the dark matter abundance is more commonly termed as the relic abundance/density. The relic density is denoted by Ωh^2 , and is more formally defined as $\Omega h^2 = \frac{\rho_\chi}{\rho_c}$. Here, ρ_χ and ρ_c respectively refer to the dark matter density and the critical density in the universe. In this section, we outline the procedure of calculating the relic density in the framework of Friedmann Robertson Walker (FRW) cosmology. More detailed discussions are to be found in [276–278].

The relic abundance of thermally produced DM particles is computed by solving the Boltzmann equation given by

$$\dot{n} + 3Hn = -\langle \sigma v \rangle (n^2 - n_{\text{eq}}^2). \quad (6.6.1)$$

where $n \rightarrow$ Number density of the DM particle,

$n_{\text{eq}} \rightarrow$ Equilibrium number density,

$H = \frac{\dot{a}}{a} \rightarrow$ Hubble constant, a being the scale factor of the FRW metric,

$\langle \sigma v \rangle \rightarrow$ Thermal average of the product of the annihilation cross section and the relative velocity v of the two annihilating particles.

Details of calculating $\langle \sigma v \rangle$ can be found in [279, 280] For a DM particle of mass m and with number of internal degrees of freedom $= g$, the equilibrium number density in the limit $T \ll m$, is given by

$$n_{\text{eq}} = g \int \frac{d^3p}{(2\pi)^3} e^{-\frac{E}{T}}, \quad (6.6.2)$$

$$\simeq g \int \frac{d^3p}{(2\pi)^3} e^{-(m + \frac{p^2}{2m})/T}. \quad (6.6.3)$$

Denoting s to be the total entropy density in the universe, we introduce the comoving number density (Y) as the ratio of the number density to the entropy density, i.e., $Y = \frac{n}{s}$. eqn.(6.6.1) is then recasted as

$$\dot{Y} = -s \langle \sigma v \rangle (Y^2 - Y_{\text{eq}}^2) \quad (6.6.4)$$

Next, we define $x = \frac{m}{T}$ where m and T respectively denote the DM mass and the temperature of the thermal soup. Using the fact that $H \propto \frac{1}{t}$ in the radiation dominated era and considering Y to be a function of x , eqn.(6.6.4) becomes

$$\frac{dY}{dx} = \frac{1}{3H} \frac{ds}{dx} \langle \sigma v \rangle (Y^2 - Y_{\text{eq}}^2) \quad (6.6.5)$$

In the framework of FRW cosmology, the Hubble constant is expressible in terms of the total energy density (ρ) and the gravitational constant (G). In turn ρ depends on the temperature and the number of relativistic degrees of freedom contributing to it ($g_{\text{eff}}(T)$). Therefore the following relations

$$H = \left(\frac{8}{3} \pi G \rho \right)^{\frac{1}{2}}, \quad (6.6.6a)$$

$$\rho = g_{\text{eff}}(T) \frac{\pi^2 T^4}{30}, \quad (6.6.6b)$$

$$s = h_{\text{eff}}(T) \frac{2\pi^2 T^3}{45}, \quad (6.6.6c)$$

upon used in eqn.(6.6.5), ultimately lead to the following,

$$\frac{dY}{dx} = - \left(\frac{45}{\pi} G \right)^{-1/2} \frac{g_*^{1/2} m}{x^2} \langle \sigma v \rangle (Y^2 - Y_{\text{eq}}^2) \quad (6.6.7)$$

Where, in eqn.(6.6.7),

$$g_*^{1/2} = \frac{h_{\text{eff}}}{g_{\text{eff}}^{1/2}} \left(1 + \frac{T}{3h_{\text{eff}}} \frac{dh_{\text{eff}}}{dT} \right). \quad (6.6.8)$$

Before freeze-out occurs at a temperature T_f , Y obeys the equilibrium number density. That is, for $T > T_f$, $Y \simeq Y_{\text{eq}}$. At freeze-out, one takes $Y = (1 + \delta)Y_{\text{eq}}$ with $\delta \simeq 1.5$. Another important input in this context is the analytical form $Y_{\text{eq}}(x) = \frac{45g}{4\pi^4} \frac{x^2 K_2(x)}{h_{\text{eff}}(m/x)}$. Here $K_n(x)$ refers to the modified Bessel's function. Upon substituting these in eqn.(6.6.7), we obtain the condition of freeze-out as under:

$$\begin{aligned} \left(\frac{45G}{\pi} \right)^{-1/2} \frac{45g}{4\pi^4} \frac{K_2(x)}{h_{\text{eff}}} g_*^{1/2} m \langle \sigma v \rangle \delta(\delta + 2) = \\ \frac{K_1(x)}{K_2(x)} - \frac{3}{x} \left(\frac{g_*^{1/2}(T) g_{\text{eff}}^{1/2}(T)}{h_{\text{eff}}(T)} - 1 \right). \end{aligned} \quad (6.6.9)$$

The value of x at freeze-out, $x_f = \frac{T_f}{m}$ is obtained by solving eqn.(6.6.9) numerically. Once x_f gets known, the comoving number density at the present epoch (Y_0) is straightforwardly determined by integrating eqn.(6.6.7)¹. The relic density can then expressed in terms of the

¹Generally one observes $Y \gg Y_{\text{eq}}$, in which case eqn.(6.6.7) can even be solved analytically. However, it is customary to opt for an exact numerical solution for a more precise prediction for the relic.

same as

$$\Omega h^2 = 2.755 \times 10^8 \frac{m}{\text{GeV}} Y_0. \quad (6.6.10)$$

At the freeze out temperature the annihilation cross section can be expanded as follows.

$$\langle \sigma v \rangle = a + bv^2. \quad (6.6.11)$$

In terms of the coefficients a and b , and denoting the Planck mass as M_{Pl} ,

$$\Omega h^2 \simeq \frac{1.04 \times 10^9 / \text{GeV}}{M_{Pl}} \frac{x_f}{\sqrt{g_*(x_f)}} \frac{1}{a + \frac{3b}{x_f}}. \quad (6.6.12)$$

A couple of statements are now in order. First, eqn.(6.6.12) indicates that the dark matter particle freezes-out earlier if its annihilation cross section is on the higher side ². Correspondingly its relic abundance will be less. Second, obtaining the correct abundance of dark matter today via thermal production requires a self-annihilation cross section of $\langle \sigma v \rangle \simeq 10^{-26} \text{cm}^2$, which is roughly what is expected for a new particle in the 100 GeV mass range interacting via the electroweak force. This naturally fits WIMPs as successful candidates for CDM. This observation is known as the "WIMP miracle".

It is pointed out here that there are three important exceptions to the validity of the above formalism [281]. Such situations are encountered whenever there is an annihilation near a mass threshold, a coannihilation [282], or, a resonance in the annihilation cross section.

6.7 Search for dark matter

One of the most exciting areas in modern day astroparticle physics is searching dark matter through various experiments. Although there is yet no definitive evidence in favour of dark matter, the quest is still on, and, can be broadly divided into three categories: direct searches, indirect searches and collider searches. Direct searches are aimed at obtaining dark matter signals through various terrestrial detectors. Indirect methods employ space-based instruments to search for signals from products of WIMP annihilation, such as γ -rays or antiprotons. In addition to these, observation of signals with an excess of missing transverse energy at the colliders could also hint at presence of dark matter along with its fundamental interactions. We present below a brief outline of the various search techniques.

² h in this equation refers to the Planck constant and should not be confused with the Higgs boson.

6.7.1 Direct search

Whenever a dark matter particle strikes a terrestrial detector, it will scatter off the nucleus of the detector material, as a result of which the detector nucleus should experience a recoil. The magnitude of this recoil would be feeble owing to the tiny interaction strength. A dark matter direct detection experiment therefore seeks to measure this low recoil energy (\sim KeV). The experimental set up must be placed in the deep underground to eliminate backgrounds from the cosmic-rays.

The detection rate is defined to be the number of particles detected in a detector per unit time per unit recoil energy. The differential detection rate of WIMP per unit detector mass is given by [278].

$$\frac{dR}{dE} = N_T \Phi \int_{v_{min}}^{\infty} \frac{d\sigma}{dq^2} f(v) dv \quad (6.7.1)$$

In eqn.(6.7.1), Φ is the dark matter flux and N_T is the number of target nuclei per unit mass. The dark matter velocity v is measured in the Earth's reference frame with $f(v)$ as the velocity distribution function. Besides, the term $\frac{d\sigma}{dq^2}$ refers to the differential scattering cross section with q^2 denoting the momentum transferred to the recoiling nucleus. Further, v_{min} is the minimum velocity the dark matter particle must have in order to scatter off a nucleus (of mass m_{nuc}) with a recoil energy E_R . If μ stands for the reduced mass of the dark matter-nucleon system, it is noted that

$$v_{min} = \left(\frac{m_{nuc} E_R}{2\mu^2} \right)^{1/2}. \quad (6.7.2)$$

Computing $\frac{dR}{dE}$ requires inputs from particle physics, nuclear physics as well as astrophysics, as is evident from eqn.(6.7.1). To elucidate, the interaction at the fundamental level is guided by the coupling of the dark matter with quarks (and gluons) inside the nucleon. This coupling therefore is dependent on the particular particle physics model taken. Once the scattering cross-section at this level is obtained, it is translated to the nucleonic level using appropriate hadronic matrix elements (matrix elements of quark and gluon operators in nucleonic state). Also needed are distribution functions of the quarks inside the nucleons. In addition to these, astrophysical inputs, such as the knowledge of the form of $f(v)$ also make their way into the calculation of the nuclear recoil rate.

Dark matter detections are of two types: spin-dependent and spin-independent. In the spin-independent case, the scattering cross section is proportional to the square of the atomic mass A , whereas the cross sections for spin-dependent scattering are proportional to $J(J+1)$,

where J is the spin of the target nucleus. The experimental sensitivity of spin-dependent cross section is far below than that of spin-independent cross sections. In this thesis, as a neutral scalar particle is considered as a viable WIMP dark matter, only the spin-independent cross sections are considered. The spin-independent cross section of the nuclear recoil for a nucleus of mass m_N and atomic number Z is given by

$$\sigma = \frac{4m^2m_N^2}{\pi(m+m_N)^2} [Zf_p + (A-Z)f_n]^2. \quad (6.7.3)$$

Here, f_p and f_n are the form factors for the proton and the neutron respectively. Presently, non-observation of dark matter in direct detections from experiments like XENON, LUX have set a limit on WIMP-nucleon scattering cross section for a given dark matter mass [283–285]. In fact, the most stringent bound has come from the LUX experiment. These experiments have also ruled out the previous claim made by the experiments like DAMA/LIBRA, Co-GeNT, CDMS etc [286–288] of having detected signature of dark matter of mass around $\simeq 10$ GeV .

6.7.2 Indirect search

Indirect search techniques [289] are focussed at looking for dark matter signatures through their annihilation to various SM final states, such as, to $q\bar{q}, ZZ, W^+W^-$ and $\gamma\gamma$. These primary particles eventually decay into positrons, electrons, anti-protons, protons, neutrinos and γ -rays, which can be observed by suitable detectors. Another example in this category would be the rise in the fraction of positrons in the total e^+e^- -flux for energies above $\simeq 5$ GeV, which could possibly have an explanation in terms of dark matter annihilation. Although this thesis does not seek to explain any of the indirect signatures using extended Higgs sectors, we present below a brief account for completeness.

- **Gamma ray signals:** Prompt gamma ray signals can arise due to dark matter annihilations, and, detection of such signals, particularly in the direction of the galactic centre, can possibly be a handy way to predict the dark matter mass. However, such gamma rays need not have the exactly same origin. For instance, whenever two dark matter particles annihilate and directly produce $\gamma\gamma$ or γZ , the resultant photon spectrum is monochromatic, something which cannot be mimicked by an astrophysical process (which produces a continuous spectrum). On the other hand, photons can also be given rise to by the fragmentation and decay of fermions and gauge boson pairs, that are in turn produced through dark matter annihilations. Therefore, contrary to

a line signal, this process leads to a continuous photon spectrum. In addition, e^+e^- pairs produced by dark matter annihilations can undergo inverse Compton scattering in the galactic radiation field resulting in photons.

The Fermi-LAT is an imaging large-area gamma ray telescope aimed at looking for gamma rays from astrophysical sources, such as galactic centres and dwarf spheroidal galaxies. The telescope is sensitive to the gamma energy range of 20 MeV - 300 GeV. For instance, The Fermi-LAT experiment had claimed to have seen a line spectrum for gamma rays from the direction of the galactic center around $\simeq 130$ GeV. This led to its possible explanation through annihilation of two dark matter particles with masses $\simeq 130$ GeV [290–294]. However, not all astrophysical gamma ray backgrounds have been understood properly till date. As a result, more definitive explanations to the origins of these excesses have not emerged.

- ***Positron and antiproton excesses:*** Payload for Antimatter Matter Exploration and Light-nuclei Astrophysics (PAMELA) is an operational cosmic ray research module attached to an Earth orbiting satellite, dedicated towards detecting cosmic rays with a focus on their antimatter component in the form of antiprotons and positrons. Preliminary results had indicated an excess of positrons in the energy range 10-60 GeV. Similarly, the Alpha Magnetic Spectrometer-02 [AMS-02], placed at the International Space Station, had reported a rise in the positron fraction starting at ~ 10 GeV and extending at least to 350 GeV [295]. In addition, AMS-02 had also reported a deviation of the antiproton fraction from secondary astrophysical sources of cosmic ray collisions for the antiproton kinetic energy between 50 to 500 GeV [296]. Although this observation was not backed up by similar findings by PAMELA, these excesses were interpreted to be originating from annihilation of WIMPs with masses in the ~ 100 GeV ballpark. In fact, the antiproton spectrum provided a stringent constraint on the corresponding annihilation rate. Theorists also looked whether such excesses in the positron and antiproton spectra could corroborate the observed gamma ray excesses in the galactic centre. However, several inaccuracies in the experimental set ups of both PAMELA and AMS-02 were later found out, and hence, these observations were no longer deemed concrete later.

6.7.3 Collider search

An alternative approach to the detection of dark matter is to produce them in a laboratory. The Large Hadron Collider (LHC) may be able to detect dark matter particles produced in collisions of the proton beams. Since dark matter should have negligible interactions with normal visible matter, it may be detected indirectly as an excess of missing transverse energy over and above what is expected from the SM. Constraints on dark matter were also put in the Large Electron Positron (LEP) experiment using similar principles.

As a dark matter particle χ would entirely evade a detector, a generic approach to its detection is to pair produce $\bar{\chi}\chi$ in association with a visible particle X_{SM} . Till now, the collider searches using mono-jets or mono-photons [297, 298] in association with missing transverse energy have not reported of significant excesses. Even if some smoking gun signal is reported someday, it is crucial to reinforce the observation by corresponding observations in the indirect or direct detection sectors. This will pin down on the exact nature of the dark matter particle.

6.8 Summary

In all, dark matter continues to be as enigmatic as it was when it got postulated. In this chapter, we have reviewed some of its key aspects. Starting with the experimental evidences favouring dark matter, we have discussed the dark matter types and also some relevant particle physics models for the same. The calculation of the relic density is presented in a sketchy manner. In addition, various techniques of dark matter detection have also been reviewed.

In the remaining part of this thesis, we have studied the compatibility of high scale vacuum stability and perturbative unitarity of some extended Higgs models, in conjunction with with dark matter phenomenology, particularly in context of the inert Higgs doublet(s). A model with one inert Higgs doublet augmented by right handed neutrinos is what is investigated in the next chapter. In addition, in the last chapter, we have studied a scenario with two inert doublets in a similar spirit.

Chapter 7

Dark matter, neutrino masses and high scale validity of an inert Higgs doublet model

7.1 Introduction

The previous chapters have led to the important conclusion that the EW vacuum can be stabilised till the Planck scale by switching over to the 2HDMs. Moreover this can be ensured while keeping the theory perturbative throughout the course of RG evolution. We also observed that the conclusion regarding the high scale validity of the model depends on the presence (or absence) of certain discrete symmetries. We investigated the consequences of turning on a \mathbb{Z}_2 symmetry and also violating it through quadratic terms, in this context.

Side by side, it is worthwhile to remember two rather pressing issues which prompt one to look beyond the Standard Model (BSM). These are the non-zero mass and mixing of neutrinos and the likely existence of Weakly Interacting Massive Particles (WIMP), contributing to Cold Dark Matter (CDM)¹. Given this, it is an attractive idea to look for a theory that can simultaneously address all of the aforesaid problems in one framework. Here we consider one such scenario based on a 2HDM.

In this chapter², we investigate a scenario, first proposed in reference [299], that extends the SM with an extra Higgs doublet and three right handed neutrinos with a \mathbb{Z}_2 symmetry,

¹A more detailed discussion on dark matter is presented in **Chapter 6**

²based on [166]

under which all SM particles are even while this additional scalar doublet and the right-handed neutrinos are odd. This symmetry prevents the additional doublet from having a vacuum expectation value (VEV) thus vetoing the tree-level neutrino mass generation. Moreover, there exists a stable scalar particle in the form of the lightest neutral mass eigenstate of the additional doublet, which yields an eligible DM candidate. The extra doublet is essentially an *inert* doublet. Although a lot of study has already taken place on minimal inert doublet models [170, 275, 300–316], the extra appeal of this model lies in the radiative generation of neutrino mass. Though various aspects of this scenario have already been investigated [317–328], the present chapter includes the following points which have not been emphasised before.

- We investigate the vacuum stability of this model at various scales, and identify the regions of its parameter space, which keeps the model valid all the way up to the Planck scale. The contribution of additional scalar fields as well as the right-handed neutrinos to the renormalisation group (RG) equations [given in **Appendix B**] has been taken into account here. Using these modified RG equations we evaluate the scalar quartic couplings at different scales. During the evolution of the quartic couplings we demand not only vacuum stability but also perturbativity of the couplings as well as unitarity of the $2 \rightarrow 2$ scattering matrix at each scale.
- The heavy right-handed neutrinos introduce a new mass scale (M) to the theory and the neutrino Yukawa couplings contribute to the RG evolution this scale onwards only. This brings out greater implications on the parameter space that distinguishes this model from a minimal inert doublet model. In this chapter, we will show the salient features of the model that emerges from the above fact.
- This model also contributes to leptogenesis due to the presence of heavy right-handed fermions. The values of the right-handed neutrino mass scale used in the high-scale analysis are taken to be commensurate with leptogenesis constraints. Thus the part of the model space consistent up to the Planck scale is also supportive of leptogenesis.
- We also examine the candidature of the lightest \mathbb{Z}_2 -odd particle as DM candidate, and identify the allowed values of the couplings yield the right relic abundance. We ensure that the dark matter candidate is consistent with the recent result of direct detection experiments. We identify a substantial region of the parameter space, which simultaneously satisfy the vacuum stability, perturbativity and unitarity requirements and accommodate the dark matter candidate with the correct relic density.

- Finally, we examine the 125 GeV scalar and make sure that the signal strengths in the observed channels (such as the $h \rightarrow \gamma\gamma$ channel) are consistent with data from the Large Hadron Collider (LHC).

We organise the paper as follows. In section 7.2, we briefly describe the model and its various features. In section 7.3, we explain all the theoretical constraints and collider constraints that we use in the RG running of different quartic couplings. Next, in section 7.4, we discuss the DM aspects of this model. After explaining our analysis strategy in section 7.5, we present our results related to high-scale validity in section 7.6. Finally in section 7.7, we summarise our results. Relevant formulae are given in **Appendix B** and **Appendix A.3**.

7.2 The Radiative Neutrino Mass Model with an inert doublet

In addition to the SM fields, the radiative neutrino mass model with an inert doublet [299], contains a Higgs doublet (Φ_2) and three right handed (RH) neutrinos (N^i) with an unbroken \mathbb{Z}_2 symmetry, under which the doublet and the right handed neutrinos are odd while all other SM particles are even. Being odd under the symmetry, Φ_2 does not acquire any vacuum expectation value (VEV) and has no tree-level couplings to fermions.

The relevant Yukawa and mass terms are

$$-\mathcal{L}_Y = y_{ij}\bar{N}^i\tilde{\Phi}_2^\dagger L_L^j + h.c + \frac{M_i}{2}(\bar{N}^i N^i + h.c), (i, j = 1, 2, 3) \quad (7.2.1)$$

Here L_L^j are the SM lepton doublets and M_i are the Majorana masses for the heavy right-handed neutrinos N^i . The scalar potential is

$$\begin{aligned} V = & \frac{1}{2}\lambda_1(\Phi_1^\dagger\Phi_1)^2 + \frac{1}{2}\lambda_2(\Phi_2^\dagger\Phi_2)^2 + \lambda_3(\Phi_1^\dagger\Phi_1)(\Phi_2^\dagger\Phi_2) + \lambda_4(\Phi_2^\dagger\Phi_1)(\Phi_1^\dagger\Phi_2) \\ & + \left[\frac{\lambda_5}{2}(\Phi_1^\dagger\Phi_2)^2 + h.c. \right] + m_{\Phi_1}^2\Phi_1^\dagger\Phi_1 + m_{\Phi_2}^2\Phi_2^\dagger\Phi_2. \end{aligned} \quad (7.2.2)$$

where all parameters are real, and Φ_1 is the SM Higgs doublet.

The two scalar doublets can be written as

$$\Phi_1 = \begin{pmatrix} G^+ \\ \frac{1}{\sqrt{2}}(v + h + iG^0) \end{pmatrix} \quad \text{and} \quad \Phi_2 = \begin{pmatrix} H^+ \\ \frac{1}{\sqrt{2}}(H + iA) \end{pmatrix}. \quad (7.2.3)$$

where, $v = 246$ GeV, is the electroweak vacuum expectation value (VEV). One thus has five physical states (h, H, A, H^\pm) and three Goldstone bosons (G^0, G^\pm). While h corresponds

to the physical SM-like Higgs field, the inert doublet components are one CP -even neutral scalar (H), one CP -odd neutral scalar (A) and a pair of charged scalars (H^\pm). The physical masses are given by

$$\begin{aligned} M_{H^\pm}^2 &= m_{\Phi_2}^2 + \frac{1}{2}\lambda_3 v^2, \\ M_H^2 &= m_{\Phi_2}^2 + \lambda_L v^2, \\ M_A^2 &= m_{\Phi_2}^2 + \lambda_A v^2. \end{aligned} \tag{7.2.4}$$

where $\lambda_{L/A} = \frac{1}{2}(\lambda_3 + \lambda_4 \pm \lambda_5)$. The value of λ_1 is determined using $M_h = 125$ GeV³. Majorana masses for the light neutrinos are generated radiatively through one-loop exchange of the \mathbb{Z}_2 -odd neutral scalars. The general expression for the loop-induced contributions to the light neutrino mass matrix [299] is

$$\mathcal{M}_{ij}^\nu = \sum_{k=1}^3 \frac{y_{ik}y_{jk}M_k}{16\pi^2} \left[\frac{M_H^2}{M_H^2 - M_k^2} \ln \frac{M_H^2}{M_k^2} - \frac{M_A^2}{M_A^2 - M_k^2} \ln \frac{M_A^2}{M_k^2} \right]. \tag{7.2.5}$$

Thus, the neutrino masses and mixing are determined by the inert scalar masses and the right-handed neutrino masses M_i . These masses represent the scale of lepton number violation and hence that of leptogenesis [329, 330] in this model. Some studies have already been done in this context [304, 323, 325, 326, 331]. Our choice of the right-handed neutrino (Majorana) mass scales made the present study automatically compatible with leptogenesis. To satisfy the necessary constraints in the low DM mass region where $M_{DM} < M_W$ (M_{DM} denotes the dark matter mass), one must take the lightest of the Majorana masses to be $M \geq 110$ TeV, where as in the high DM mass region ($M_{DM} > 500$ GeV) the bound is only 1 TeV [304]. Hence, to be consistent in both cases, we use two values of M , (a) $M = 110$ TeV and (b) $M = 10^9$ TeV. While, in one hand, choice of (a) is motivated by the idea of having the lowest possible leptogenesis scale, we choose to work with (b) which have interesting consequences on the RG running. We will show in later sections, how the mass scale (b) of M affects the stability of the vacuum mainly in the high DM mass region and eventually explain the physical reasons behind it.

Along with the above restrictions we also demand $M_\nu \sim \mathcal{O}(0.1$ eV) to be consistent with neutrino oscillation data for some fixed M and other exotic scalar masses. However, for simplicity, we consider only one diagonal Yukawa coupling (y_ν) and do not look into the hierarchical details of the Yukawa matrix. At this point, it is to be noted that a more rigorous

³We have used upper cased M to designate the scalar masses in this chapter, contrary to **Chapter 3**, **Chapter 4**, **Chapter 5** and **Chapter 8**, where lower case was used.

study with the intricate flavour structure of the neutrino Yukawa matrix can highlight the region of the model space that fits the observed pattern of neutrino mixing [328]. However, we would like to emphasise that the broad conclusions on the high-scale validity of this scenario *vis-a-vis* the DM constraints remain unchanged. Finally, we should mention that the lighter state between H and A is the DM candidate. We present our illustrative results for cases where H plays this role.

7.3 Constraints from perturbativity, unitarity, vacuum stability and collider data

In this section, we briefly describe the constraints that are imposed on the model parameters and how exactly they shape the results so obtained⁴.

7.3.1 Vacuum stability

The scalar potential is considered bounded from below, if it does not turn negative for large field values along all possible field directions. In this model, stability of the electroweak vacuum is ensured up to some specified energy scale if the following conditions are satisfied for all scales Q up to that scale:

$$\text{vsc1} : \quad \lambda_1(Q) > 0, \quad (7.3.1a)$$

$$\text{vsc2} : \quad \lambda_2(Q) > 0, \quad (7.3.1b)$$

$$\text{vsc3} : \quad \lambda_3(Q) + \sqrt{\lambda_1(Q)\lambda_2(Q)} > 0, \quad (7.3.1c)$$

$$\text{vsc4} : \quad \lambda_3(Q) + \lambda_4(Q) - |\lambda_5(Q)| + \sqrt{\lambda_1(Q)\lambda_2(Q)} > 0. \quad (7.3.1d)$$

Such conditions have been elaborately discussed in literature [28, 77, 119, 121]. One should make a note that these conditions ensure *absolute* stability of the electroweak vacuum. For metastability, the conditions are somewhat less stringent, they have been discussed at length in **Chapter 3** and **Chapter 4**.

⁴Although the conditions of vacuum stability, perturbativity and unitarity for the inert doublet case are same as the corresponding conditions in case of a Type-II 2HDM, they are nonetheless discussed here for completeness.

7.3.2 Perturbativity

For the scalar quartic coupling $\lambda_i (i = 1 - 5)$, the criterion for perturbativity is

$$\lambda_i(Q) < 4\pi. \quad (7.3.2)$$

The corresponding constraints for the Yukawa and gauge interactions are

$$y_i(Q), g_i(Q) < \sqrt{4\pi}. \quad (7.3.3)$$

where, Q represents the energy scale at which they are being computed. We demand that the criteria in eqn.(7.3.2) be obeyed at all energy scales up to the cutoff of this model.

7.3.3 Unitarity

A further set of conditions come on demanding unitarity of the scattering matrix comprising all $2 \rightarrow 2$ channels involving, by the optical theorem [92, 97, 112, 113]. In our context, this translates into the condition that the absolute value of each distinct eigenvalue of the aforementioned amplitude matrix be bounded above at 8π (after factoring out $\frac{1}{16\pi}$ from the matrix). These eigenvalues are

$$\begin{aligned} a_{\pm} &= \frac{3}{2}(\lambda_1 + \lambda_2) \pm \sqrt{\frac{9}{2}(\lambda_1 - \lambda_2)^2 + (2\lambda_3 + \lambda_4)^2}, \\ b_{\pm} &= \frac{1}{2}(\lambda_1 + \lambda_2) \pm \sqrt{\frac{1}{4}(\lambda_1 - \lambda_2)^2 + \lambda_5^2}, \\ c_{\pm} &= d_{\pm} = \frac{1}{2}(\lambda_1 + \lambda_2) \pm \sqrt{\frac{1}{4}(\lambda_1 - \lambda_2)^2 + \lambda_5^2}, \\ e_1 &= (\lambda_3 + 2\lambda_4 - 3\lambda_5), \\ e_2 &= (\lambda_3 - \lambda_5), \\ f_1 &= f_2 = (\lambda_3 + \lambda_4), \\ f_+ &= (\lambda_3 + 2\lambda_4 + 3\lambda_5), \\ f_- &= (\lambda_3 + \lambda_5). \end{aligned} \quad (7.3.4)$$

7.3.4 Collider data

In addition to the theoretical constraints discussed above, important bounds on scalar mass parameters come from collider data.

- In order to identify h with the SM-like Higgs as observed by the ATLAS and CMS collaborations, one requires $M_h \simeq 125$ GeV.
- To be consistent with the LEP bounds, one must have

$$M_H + M_A > M_Z, \quad (7.3.5)$$

$$M_{H^\pm} + M_{A/H} > M_W.$$

Moreover, for neutralino as in the supersymmetric context, LEP-II searches limit pseudo-scalar mass (M_A) to 100 GeV when $M_H < M_A$ [301, 332]. Similarly, chargino search data, properly extrapolated, imply $M_{H^\pm} > 70$ GeV [333].

- Though all the tree-level couplings of h are identical to those of the SM Higgs, the charged scalar H^\pm potentially modifies the loop induced couplings $h\gamma\gamma$ and $hZ\gamma$ via loop contributions [177, 334–337]. We theoretically compute the signal strength $\mu_{\gamma\gamma}$ for h decaying to the diphoton channel as the ratio of the decay width in the ‘*model*’ to that in the SM. Its experimental value reported by the ATLAS and CMS collaborations stand at 1.17 ± 0.27 and 1.13 ± 0.24 respectively [180, 338]. Demanding the signal strength to be within 2σ limits of the experimentally quoted values puts further constraints on the model. We use the limit on $\mu_{\gamma\gamma}$ weighted as below:

$$\frac{1}{\sigma^2} = \left(\frac{1}{\sigma^2}\right)_{ATLAS} + \left(\frac{1}{\sigma^2}\right)_{CMS}, \quad (7.3.6)$$

$$\frac{\mu_{\gamma\gamma}}{\sigma^2} = \left(\frac{\mu_{\gamma\gamma}}{\sigma^2}\right)_{ATLAS} + \left(\frac{\mu_{\gamma\gamma}}{\sigma^2}\right)_{CMS}. \quad (7.3.7)$$

where, the numerators on the right hand side denotes the central values of the respective experimental results and $\sigma_{ATLAS/CMS}$ are the corresponding uncertainties. The resultant uncertainty is σ .

7.4 Dark Matter Issues

As stated earlier, we identify H as the DM candidate. For the complimentary choice, namely, A with the same mass as the DM candidate, we have checked that the contribution to the relic density is of similar magnitude. The relevant DM constraints to be considered are as follows:

- According to recent PLANCK experiment [339] the observed cold DM relic density is

$$\Omega_{DM}h^2 = 0.1199 \pm 0.0027. \quad (7.4.1)$$

We restrict our result up to 3σ deviation from the central value.

- Strong constraints come from direct DM searches. Recently, XENON100 [285] and LUX [283] experiments have put upper-bound on the DM-nucleon scattering cross section for a wide range of the DM mass. In our case, the direct detection cross section strategy is based on t -channel Higgs mediation. We choose to work in the region of the parameter space allowed by the LUX limit.
- For $M_H \leq M_h/2$, the decay mode of Higgs to two DM particle ($h \rightarrow HH$) will presumably contribute to the invisible decay width of the Higgs boson. We take into account the current constraint on the Higgs invisible branching ratio ($< 20\%$) from model independent Higgs precision analysis [149, 340].

7.4.1 Case-A: Low mass DM ($50 \text{ GeV} < M_H < 90 \text{ GeV}$)

In this mass region, the dominant annihilation channel for H are the DM self-annihilation processes through h mediation. This keeps the relic density at the right level. For both positive and negative values of DM-DM-Higgs couplings, the relic density remains within the allowed range as long as the $M_H < 90 \text{ GeV}$. The sub-dominant contribution to the relic density comes from the t -channel processes to vector boson final states mediated by A and H^\pm . A detailed discussion in this regard on a similar model can be found, for example in [304, 306, 315]. However, the coupling λ_2 has no effect in the relic density calculation. In the next section, we will discuss this results elaborately. One more notable point is that, annihilation processes that mediated by the heavy right-handed neutrinos give negligible contribution (less than 1%) to the relic density calculation. These processes are suppressed by the heavy mediator mass.

7.4.2 Case-B: High mass DM ($M_H > 500 \text{ GeV}$)

The interesting feature of this region is that, the correct relic abundance can be achieved if and only if H , A and H^\pm are almost degenerate, at most have a mass difference of the order of 10 GeV. This is mainly because at this high mass, the annihilation channels with vector boson final states can have direct quartic couplings ($HHVV, V = W^\pm, Z$) or can be mediated by any of the three scalars through t/u channels. These diagrams yield too large an annihilation cross section to match with the proper relic density. However, cancellation between direct quartic coupling diagrams and t/u channels diagram occurs for mass-degenerate H , A and

H^\pm , which in turn brings down the annihilation cross section to the desired range. Due to narrow mass differences among the inert scalars, coannihilation becomes inevitable.

7.5 Analysis strategy

The aim of this chapter is to probe the parameter space of an inert doublet model (IDM) augmented with heavy RH neutrinos compatible with various theoretical and experimental constraints elaborated in the previous sections. We carry out our investigation in the two separate mass regions. In each region, we scan over the relevant parameters, namely, the masses M_H , M_A and M_H^\pm , and the coupling λ_L . With M_h fixed at 125 GeV, λ_2 , λ_L , M_H , M_A and M_H^\pm fix all the remaining quartic interactions. At this point it is to be mentioned that the parameter λ_2 can not be constrained by any physical observable at least at tree level. However, λ_2 is bounded by the stability and perturbativity condition and we have explicitly checked that $0 < \lambda_2 < 0.36$ to satisfy the theoretical constraints. Rather than scanning over λ_2 , we have demonstrated our results with two benchmark values (0.1 and 0.001) for it, both of which are well within the above limit.

These quartic couplings are then used as the electroweak boundary conditions at $Q = M_t$ and their RG evolution to high scales is studied. Here M_t denotes the top quark pole mass. The reader is reminded that the effect of the RH neutrinos is turned on at a scale $Q = M$. Thus, for $M_t \leq Q \leq M$, we do not include the RH neutrino contributions to the one-loop RG equations. We include such conditions for $Q \geq M$ and use the RG equations listed in **Appendix B**. The scale up to which the scenario remains consistent is denoted by Λ_{UV} . For a generic parameter point $\lambda_i(Q = M_t)$, we check the aforementioned theoretical constraints at all intermediate scales up to Λ_{UV} . If the constraints are all satisfied, we tag $\lambda_i(Q = M_t)$ as an *allowed* point. This marks out an allowed region in the parameter space defined at the electroweak scale. Moreover, the effects of constraints stemming from the DM observables and collider searches are examined independently in this region. The finally allowed parameter regions are thus identified and presented for benchmark values of λ_2 and M . We use the publicly available package `micrOMEGAs-v3.6.9.2` [341] for DM analysis.

Amongst the SM fermions, only the top quark plays the dominant role in the evolution of the couplings. The boundary condition for its Yukawa interaction at the electroweak scale is fixed by $y_t(M_t) = \frac{\sqrt{2}M_t}{v}(1 - \frac{4}{3\pi}\alpha_s(M_t))$. We have used $M_t = 173.39$ GeV throughout our analysis.

7.6 Numerical results

7.6.1 Low mass DM region

We perform a detailed parameter space scan where $M_H < 100$ GeV. In this scan, we impose the LEP bounds as discussed in subsection 7.3.4.

$$\lambda_L : [-1.0, 1.0] \tag{7.6.1}$$

$$M_H : [50.0 \text{ GeV}, 90.0 \text{ GeV}] \tag{7.6.2}$$

$$M_A : [100.0 \text{ GeV}, 500.0 \text{ GeV}] \tag{7.6.3}$$

$$M_{H^+} : [100.0 \text{ GeV}, 500.0 \text{ GeV}] \tag{7.6.4}$$

We solve the RG equations for two values of M , 110 TeV and 10^9 TeV respectively. We then show the allowed parameter space in the $\lambda_L - M_H$ plane for different choices of Λ_{UV} in Fig 7.1 and 7.2. The regions denoted by A (red), B (cyan) and C (green) correspond to $\Lambda_{UV} = 10^6, 10^{16}$ and 10^{19} GeV respectively. We overlay the region allowed by the Higgs to diphoton signal strength within 2σ limits of the current data as grey region named D. As mentioned earlier, the full analysis is done for two values of λ_2 at the electroweak scale (0.1 and 0.001).

Let us briefly summarise the features that emerge from the figures and their possible explanations.

- From Fig.7.1, it can be seen that an IDM with RH neutrinos possesses stable vacuum even up to the Planck scale, but the higher the cutoff scale Λ_{UV} , less amount of parameter space become allowed. To understand this, one can recollect that the t -quark Yukawa coupling in the SM is responsible for the downward evolution of the scalar self-coupling, which poses a threat to the vacuum stability. The presence of the additional scalar quartic couplings (λ 's) in a model like this offsets such an effect; however, the boost thus provided to these couplings tend to violate the perturbativity and unitarity condition. This necessitates a tightrope walking, and the scale up to which it is possible is Λ_{UV} . Hence, it is natural that for higher Λ_{UV} , fewer combinations of parameters will achieve this fine balance, and consequently the allowed region shrinks.
- Fig.7.1 also shows that λ_L is bounded on both sides and the limits stay almost same for different right handed neutrino mass scale(M). This is of no surprise and can be easily understood. Since $\lambda_3 = \frac{2}{v^2}(M_{H^\pm}^2 - M_H^2 + \lambda_L v^2)$, the upper bound on λ_L is imposed by the requirement of perturbative unitarity. This is because a higher positive value

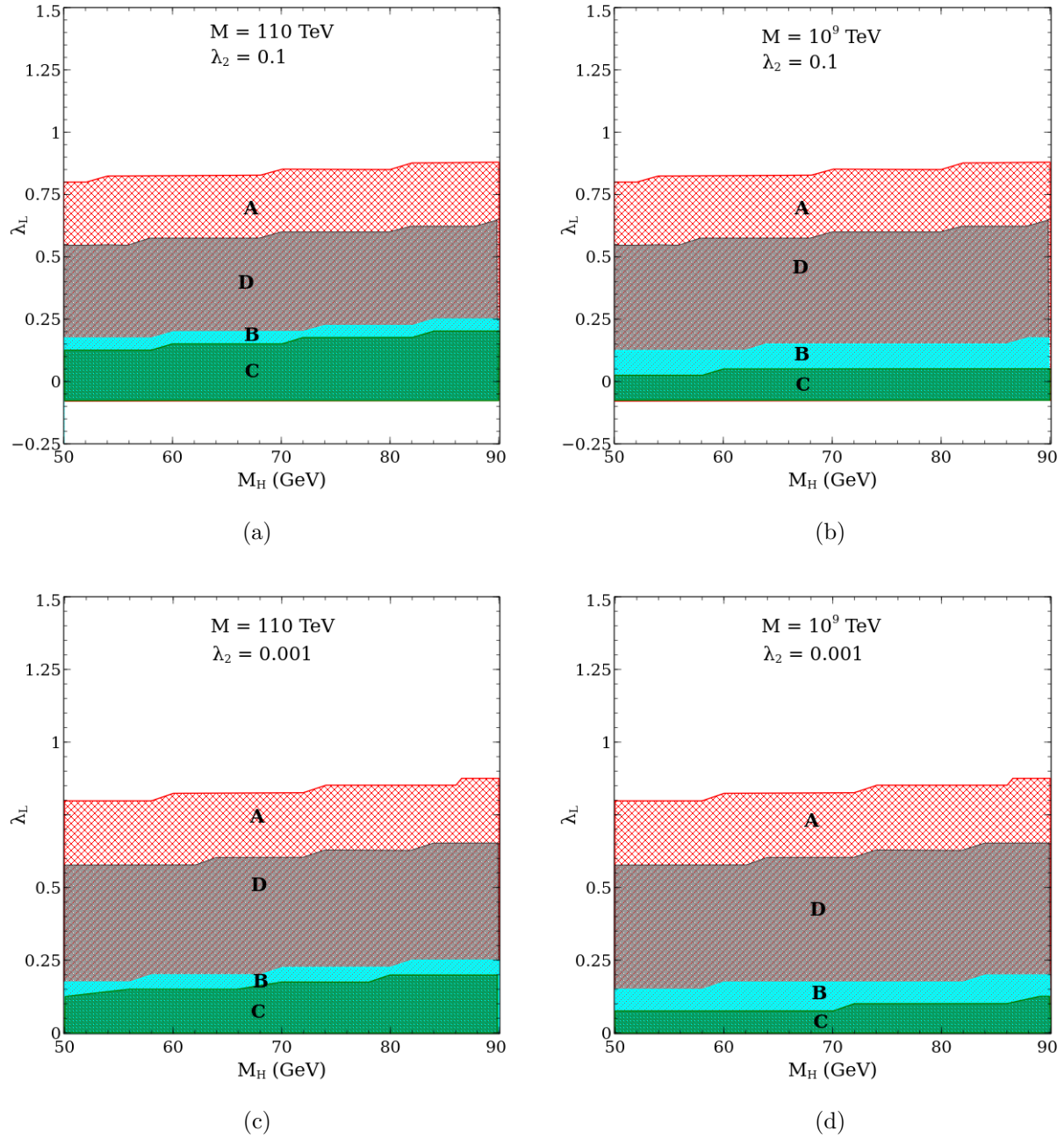


Figure 7.1: Regions compatible with the theoretical constraints for $M = 110$ TeV (left panel) and 10^9 TeV (right panel) with three different choices of Λ_{UV} and two values of λ_2 . The regions denoted by A (red), B (cyan) and C (green) obey these constraints up to $\Lambda_{UV} = 10^6$, 10^{16} and 10^{19} GeV respectively. The grey region denoted by D keeps the Higgs to diphoton signal strength within 2σ limits of the current data.

of λ_L makes λ_3 large at the electroweak scale which violates perturbative unitarity in course of its evolution under RG. On the other hand, a large negative value of λ_L induces a large negative value to λ_3 . As a consequence, the vacuum stability condition vsc4 of eqn.(7.3.1d) is violated even near the EW scale. This puts a lower limit on λ_L independent of M and Λ_{UV} , as evident from Fig.7.1. However, it must be noted that the lower limit of λ_L is not independent of λ_2 , which is another consequence of eqn.(7.3.1d) that requires the condition $\lambda_3 + \lambda_4 - |\lambda_5| > -\sqrt{\lambda_1\lambda_2}$ to be satisfied. With the decrease in the value of λ_2 the lower limit of the combination $\lambda_3 + \lambda_4 - |\lambda_5|$ enhances. This combination can be approximated to λ_L in the perturbative regime and hence lower values of λ_2 increases the lower bound of λ_L , as can be seen from the upper and lower panel of Fig.7.1 that corresponds to $\lambda_2 = 0.1$ and $\lambda_2 = 0.001$ respectively.

- To check the compatibility of the DM constraints with the theoretical ones, we look for the region allowed by the 3σ limits on $\Omega_{\text{DM}}h^2$ from PLANCK data and 90% CL limit on the spin-independent DM-nucleon scattering cross section from LUX data. In Fig. 7.2, we show the parameter space allowed by the entire set of DM constraints. An inspection of Fig. 7.1 and Fig. 7.2 shows that almost the full parameter space allowed by the DM constraints lies in the region which is also favoured by the vacuum stability condition all the way up to the Planck scale. However, the region corresponding to $\lambda_L \leq -0.1$ (shaded region in Fig. 7.2) does not lead to the stable vacuum.
- It should be noted that in Fig. 7.2 we keep M_H^\pm and M_A fixed at 200 GeV. For higher values of M_{H^\pm} and M_A , there is hardly any change in the annihilation cross section. However, for values of M_H^\pm and M_A less than 200 GeV, the allowed region of Fig. 7.2 gets slightly modified. For example, for $M_H \simeq 70$ GeV and $M_{H^\pm} = M_A = 200$ GeV, the DM-DM-Higgs coupling $\lambda_L \simeq 0.007$, but for $M_{H^\pm} = M_A = 100$ GeV, one needs $\lambda_L \simeq 0.009$ to satisfy the relic density constraint. It should be noted however that both of the above points in the parameter space are within the stability region as shown in Fig. 7.1.

Therefore, it is not possible to constrain M_H^\pm and M_A using DM constraints alone, theoretical constraints however predict strong upper bounds on these masses, as is evident from Fig. 7.3 and Fig. 7.4.

- In Fig. 7.3 and Fig. 7.4, we show the theoretically valid regions in the $\lambda_3 - M_H^\pm$ and $\lambda_L - M_A$ planes. As in previous cases, we exhibit the same for two different M and λ_2 values. Also, in each case, we overlay the parameter spaces allowed by the 2σ limit of

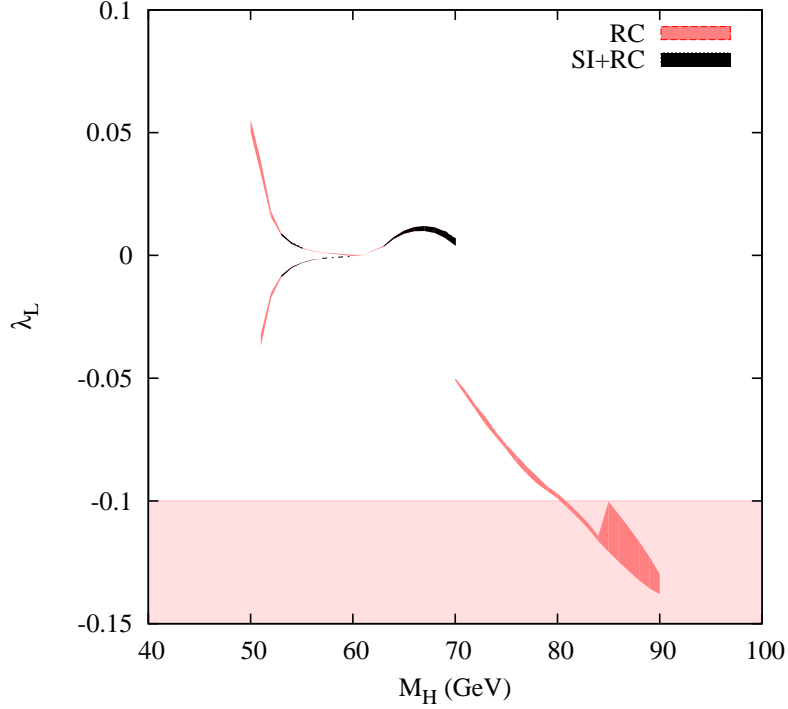


Figure 7.2: Region allowed by imposing the constraints on relic density(RC) and spin-independent cross section(SI) for DM-nucleon scattering. The red(gray) region is allowed only by the requirement of $\Omega_{\text{DM}}h^2$ being in the correct range. The black region is allowed by both the $\Omega_{\text{DM}}h^2$ and direct detection constraints. The shaded horizontal band below is disallowed by vacuum stability conditions. Here, $M_{H^\pm} = M_A = 200$ GeV.

Higgs to diphoton signal strength (region **D**). We observe that a tight upper bound of 160-170 GeV is realised on the masses M_{H^\pm} and M_A for the cutoff at the Planck scale and the couplings (λ_3, λ_L) are also bounded. The upper bounds on the masses M_{H^\pm} and M_A are imposed by the requirement of perturbativity and unitarity up to the desired cutoff. With M_H in the aforementioned range, large masses of the other \mathbb{Z}_2 -odd scalars imply high values of the quartic couplings at the electroweak scale which potentially violate perturbativity or unitarity at some high scale. On the other hand, the vacuum

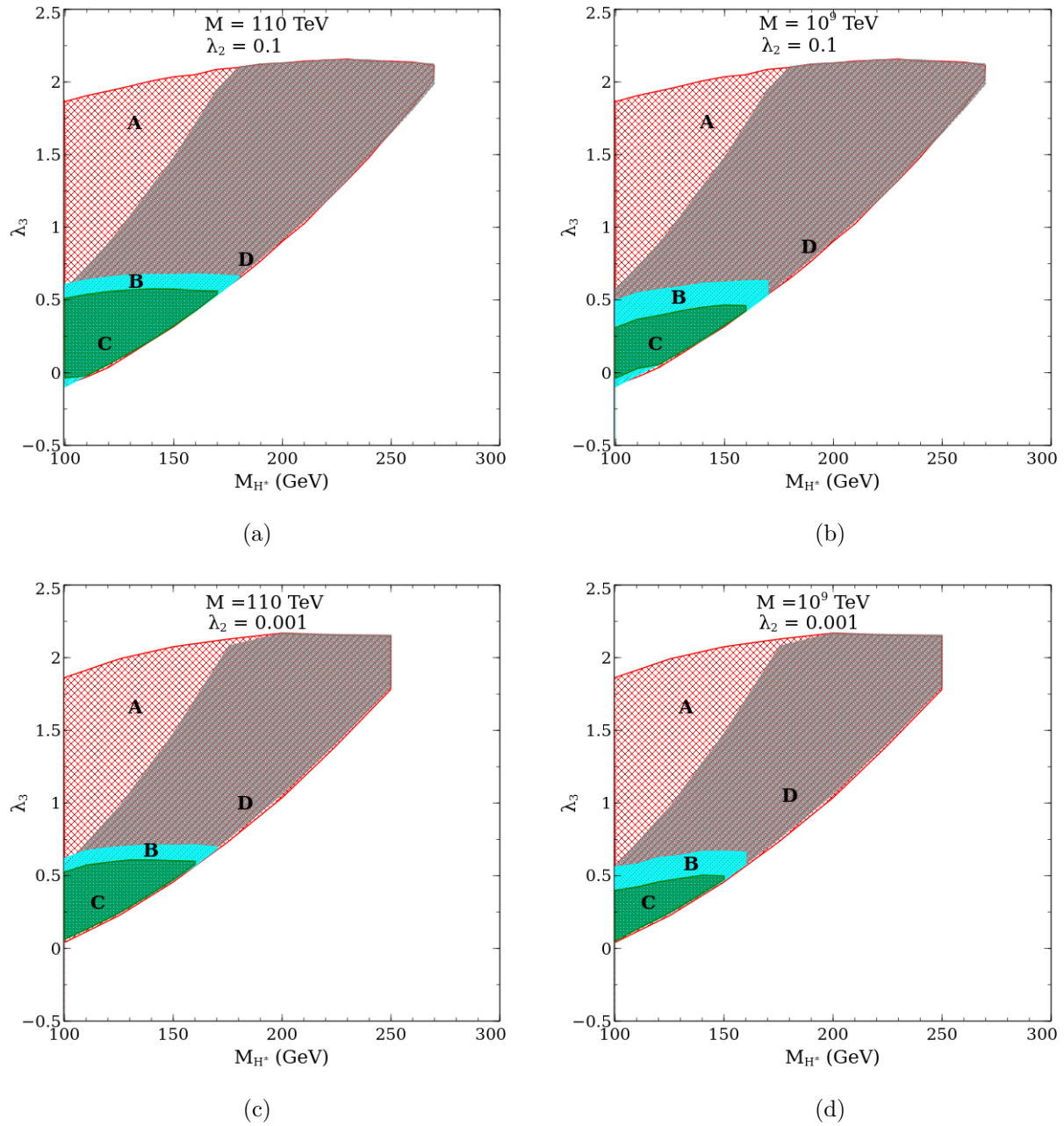


Figure 7.3: Regions allowed by the theoretical constraints projected in the $\lambda_L - M_A$ and $\lambda_3 - M_{H^\pm}$ planes. The regions denoted by A (red), B (cyan) and C (green) obey those constraints up to $\Lambda_{UV} = 10^6, 10^{16}$ and 10^{19} GeV respectively. The grey region denoted by D shows the 2σ allowed limit of the Higgs to diphoton signal strength.

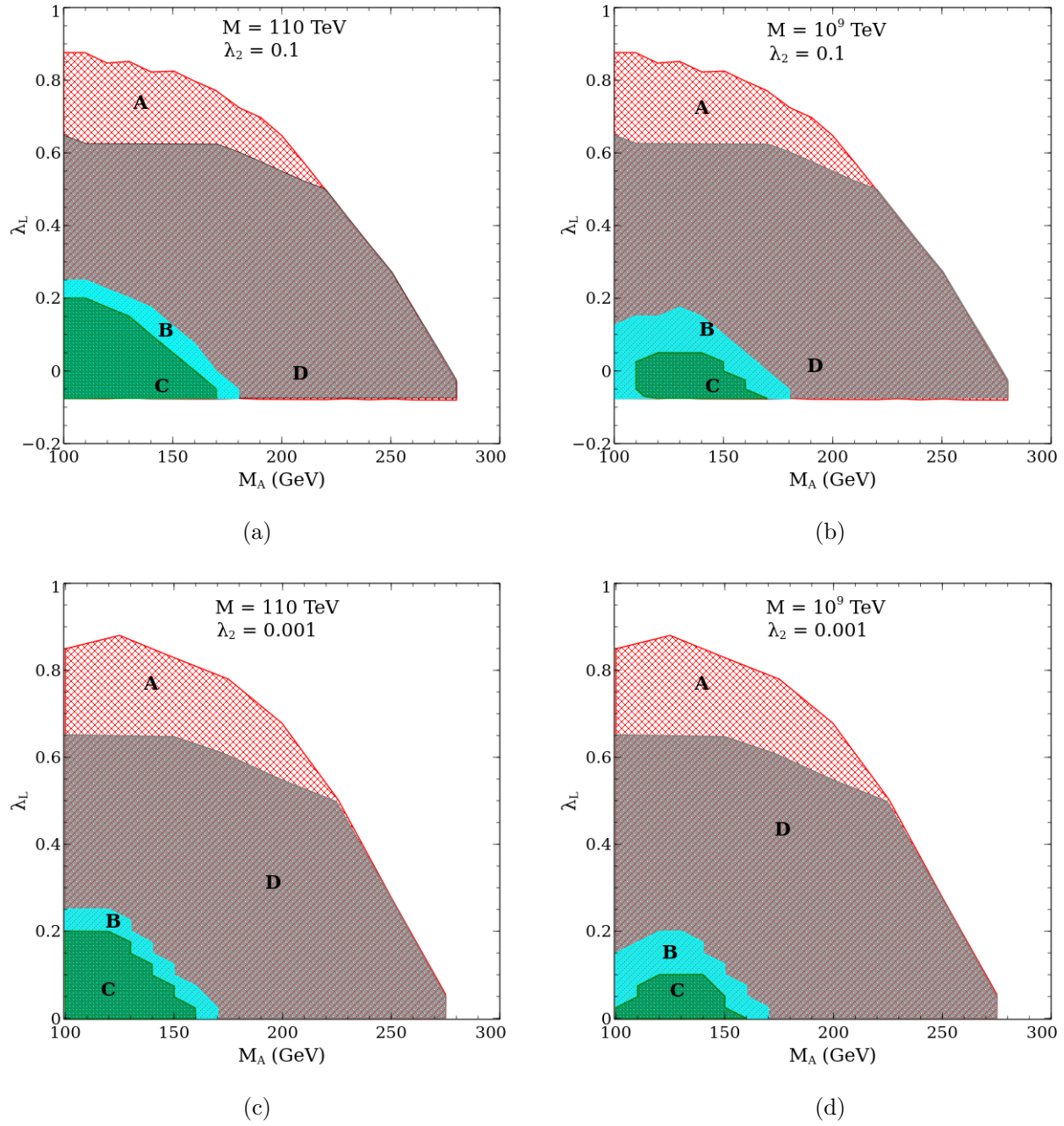


Figure 7.4: Regions allowed by the theoretical constraints projected in the $\lambda_L - M_A$ and $\lambda_3 - M_H^\pm$ planes. The regions denoted by A (red), B (cyan) and C (green) obey those constraints up to $\Lambda_{UV} = 10^6, 10^{16}$ and 10^{19} GeV respectively. The grey region denoted by D shows the 2σ allowed limit of the Higgs to diphoton signal strength.

stability condition $\lambda_3 + \sqrt{\lambda_1 \lambda_2} \geq 0$ forbids large negative values of λ_3 . The explanations of the limits of λ_L have already been mentioned above.

- The new physics contribution to the Higgs to diphoton decay channel comes from the charged Higgs loop which is a function of M_{H^\pm} and λ_3 . The fact that λ_3 can not be large negative results in a fall in the signal strength for diphoton channel. However, the parameter space for $\Lambda_{UV} = 10^{19}$ GeV is still allowed by the current limits on $\mu_{\gamma\gamma}$ defined in eqn.(7.3.7).

7.6.2 High mass DM region

This section demonstrates the high scale validity of our scenario in the limit of a high DM mass. As discussed earlier, one needs to tune the mass splitting amongst H , H^\pm and A and the coupling λ_L to an appropriate degree in order to achieve a relic density within the desired bounds. It is seen that the maximal allowed splitting (ΔM) amongst the masses of the \mathbb{Z}_2 odd scalars is 10 GeV. As previously mentioned, for each chosen values of λ_2 (0.1 and 0.001), one is thus motivated to scan the high DM mass region in the following ranges:

$$\lambda_L : [-1.0, 1.0] \tag{7.6.5}$$

$$M_H : [550.0 \text{ GeV}, 1000.0 \text{ GeV}] \tag{7.6.6}$$

$$M_A : [M_H, M_H + 10.0 \text{ GeV}] \tag{7.6.7}$$

$$M_{H^\pm} : [M_H, M_H + 10.0 \text{ GeV}] \tag{7.6.8}$$

Unlike the previous case, while the theoretical constraints ruled out a large portion of the parameter space, the DM constraints put a less stringent bound on it in this high DM mass region. Therefore, in Fig. 7.5 and Fig. 7.6, we demonstrate the parameter region allowed only by the DM constraints and then overlay the part which are further allowed by theoretical constraints. The full (pink) region denoted by **RC+ SI** shows the valid parameter space allowed by DM constraints. In accordance with previous notation, the regions denoted by A (red), B (cyan) and C (green) correspond to $\Lambda_{UV} = 10^6$, 10^{16} and 10^{19} GeV respectively.

Let us explain the various features of the model that emerges from the figures, in detail.

- (1) The interplay of the theoretical and experimental constraints is studied in the form of correlation plots in the $M_H - \lambda_L$ (Fig. 7.5) as well as $M_{H^\pm} - \lambda_3$ (Fig. 7.6) plane. As can be seen, a significant amount of parameter space is forbidden for the theory to be valid until the Planck scale.

(2) Similar to the previous section, the upper and lower bounds on λ_L are placed from the requirements of perturbative unitarity and vacuum stability conditions respectively, as shown in Fig. 7.5. In this region too the lower limit of λ_L has dependence on λ_2 . Same happens for λ_3 , as depicted in Fig. 7.6.

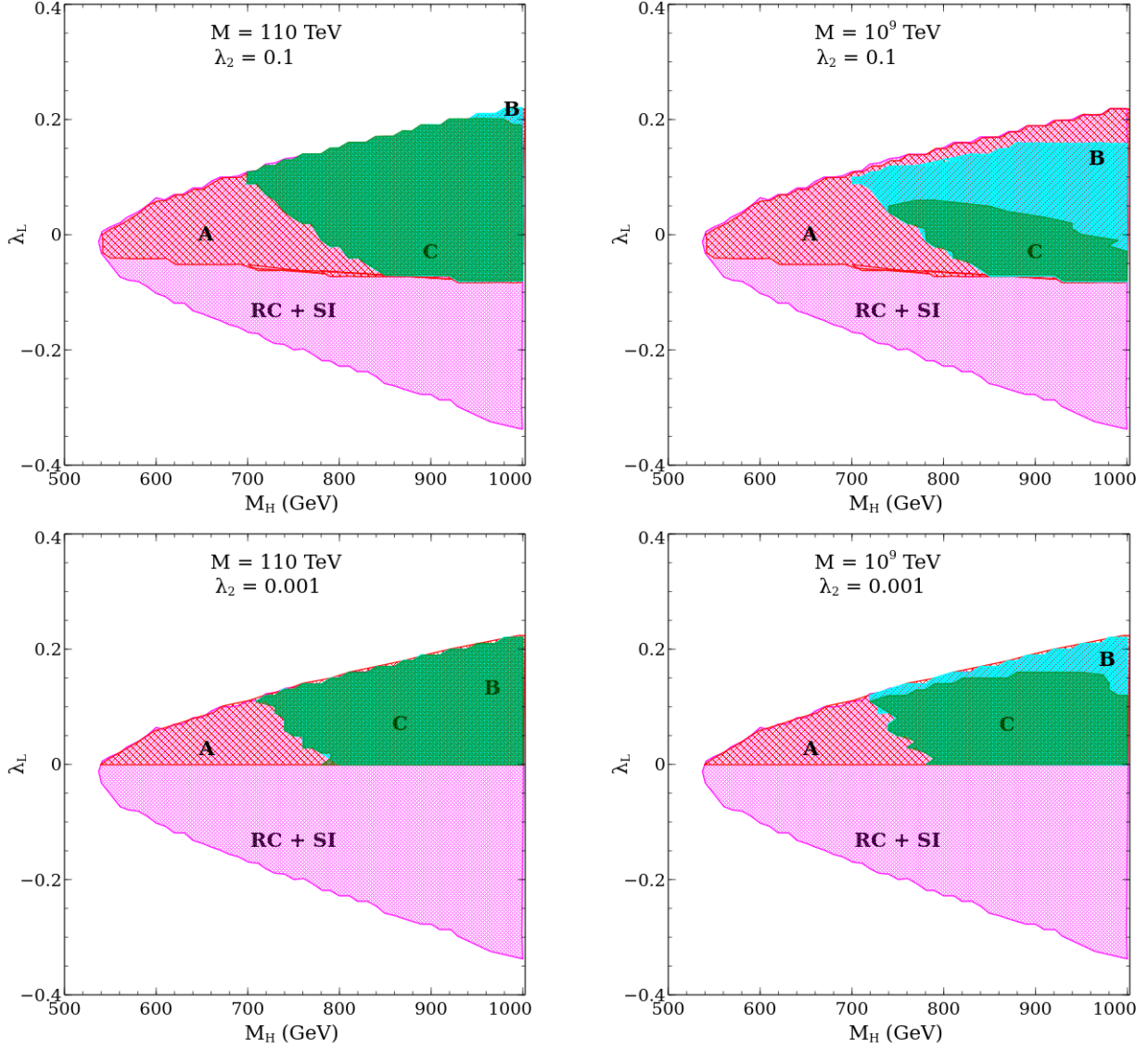


Figure 7.5: Region(s) allowed in the M_H - λ_L plane obeying the various constraints for $M = 10^4$ GeV (left panel) and $M = 10^{12}$ GeV (right panel). The full region (marked by ‘RC + SI’) (magenta) is allowed by the DM constraints alone. The overlapped regions labelled by **A** (red), **B** (cyan) and **C** (green) are consistent with the theoretical constraints up to $\Lambda_{UV} = 10^6, 10^{16}$ and 10^{19} GeV respectively.

- (3) It is to be noted that the theoretically allowed parameter space in this high DM mass region is fully consistent with the Higgs to diphoton LHC data. Since, a heavy H^\pm which naturally arises in this region, does not cause any significant deviation in diphoton signal strength for the SM-like scalar. This occurs even with a large positive λ_3 (within the bounds shown in Fig. 7.6). In principle, a large negative λ_3 could modify $\mu_{\gamma\gamma}$ unacceptably. However, as Fig. 7.6 shows, such values are inconsistent with the aforementioned theoretical constraints.
- (4) It is worth noting here that the parameter space valid until the Planck scale and corresponding to $M = 110$ TeV shrinks significantly for $M = 10^9$ TeV, as can be seen in Fig. 7.5 and Fig. 7.6. This is because, the significant part of the parameter space is discarded by the stability condition at large M where the neutrino Yukawa couplings becomes large $\mathcal{O}(0.1)$. Such large Yukawa coupling contributes to the beta function of λ_2 as shown in eqn.(B.1.2b) through the terms $+\lambda_2 y_\nu^2$ and $-y_\nu^4$ that either makes λ_2 perturbative in some cases or λ_2 negative and the vacuum unstable in other. We elaborately discuss this feature below with some benchmark points.

We have selected two benchmark points(BP1 and BP2) as samples out of the allowed regions consistent with the relic density constraints. These points demonstrate how the different theoretical constraints can truncate the scale of validity of this scenario for two different values of right-handed neutrino masses $M = 110$ TeV and $M = 10^9$ TeV respectively. The parameter values are listed in Table. 7.1.

BP	M_H	M_{H^\pm}	M_A	λ_L	λ_2
BP1	850.0 GeV	854.0 GeV	858.0 GeV	0.02	0.1
BP2	710.0 GeV	712.0 GeV	711.0 GeV	0.11	0.1

Table 7.1: Benchmark values (BP) of parameters affecting the RG evolution of the quartic couplings. For each BP, two values of M , namely, 110 TeV and 10^9 TeV, have been used.

BP1 and BP2 yield $\Omega_{\text{DM}} h^2 = 0.1151$ and 0.1207 respectively, which is within the allowed range of relic density. For $M = 110$ TeV, BP1 ensures a stable vacuum till the Planck scale (Fig. 7.7a). It is also consistent throughout with perturbativity and unitarity. However, one has $y_\nu = 0.168$ at $M = 10^9$ TeV. For this value, the term $\mathcal{O}(\lambda_2 y_\nu^2)$ has a dominant role in the RG evolution and λ_2 starts increasing rapidly from 10^9 TeV onwards (Fig. 7.7b).

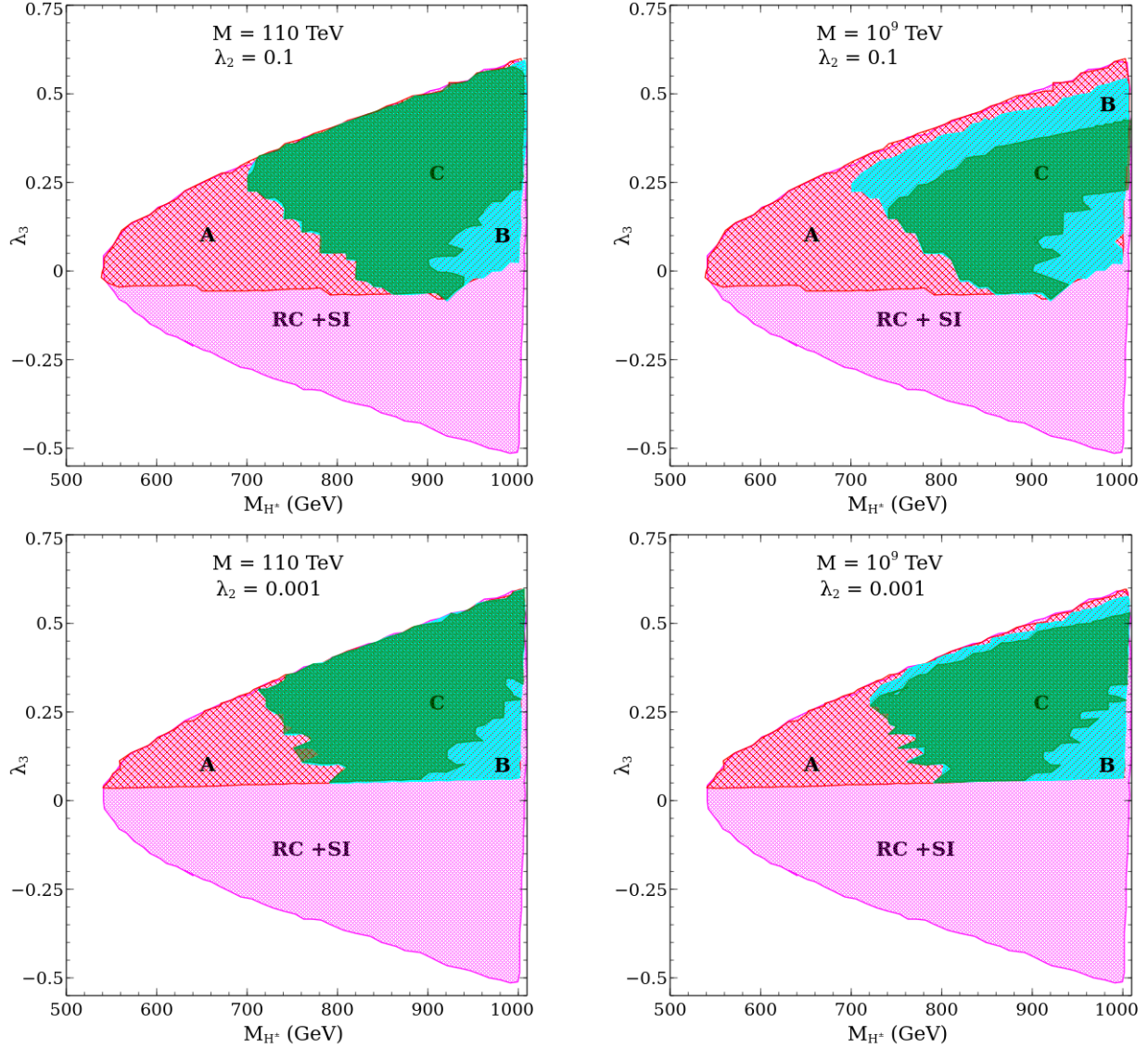


Figure 7.6: Region(s) allowed in the M_{H^\pm} - λ_3 plane obeying the various constraints. The full region (marked by ‘**RC + SI**’) (magenta) is allowed by the DM constraints alone. The overlapped regions labelled by **A** (red), **B** (cyan) and **C** (green) are consistent with the theoretical constraints up to $\Lambda_{UV} = 10^6, 10^{16}$ and 10^{19} GeV respectively.

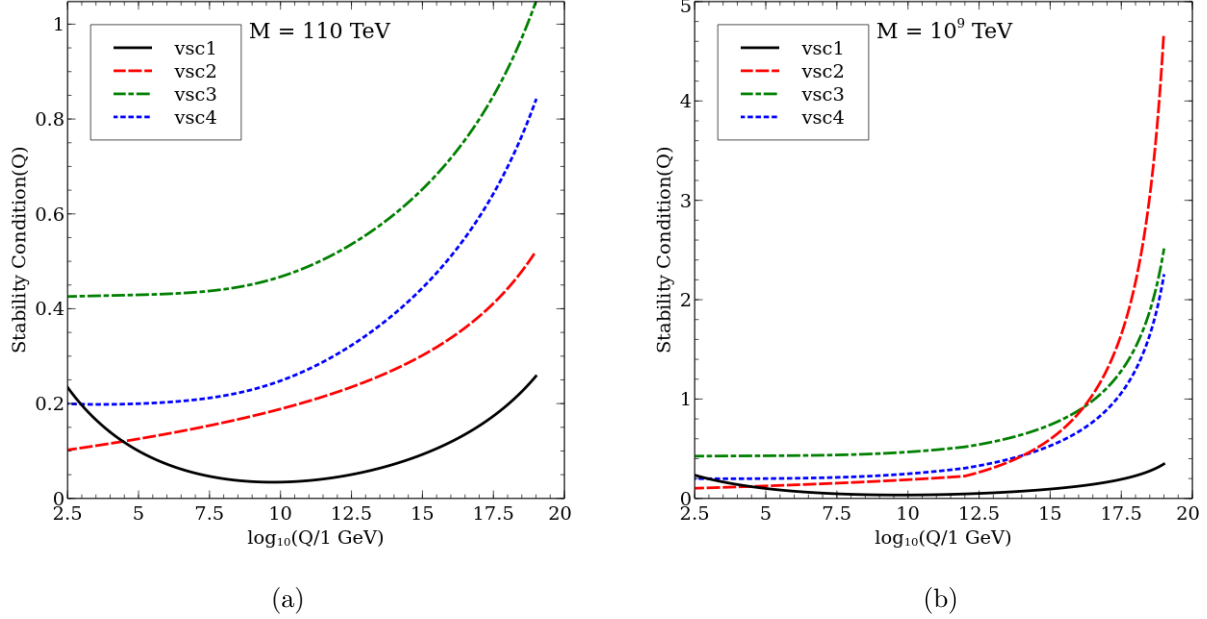


Figure 7.7: RG running of different scalar quartic couplings corresponding to BP1. The solid, dashed, dashed dotted and dotted lines denote the evolution curves of the stability conditions vsc1, vsc2, vsc3 and vsc4 respectively.

For $M = 110 \text{ TeV}$, BP2 exhibits similar features in the evolution trajectory as in BP1 (Fig. 7.8a). For $M = 10^9 \text{ TeV}$, the Yukawa coupling y_ν starts with an initial value around 0.51. This is accounted for by the very small mass splitting, of the order of a GeV, between H and A . Thus, the dominant contribution from the RH neutrinos comes from the $\mathcal{O}(y_\nu^4)$ term that causes λ_2 to drop sharply (Fig. 7.8b). Hence, in BP2, vacuum stability is destroyed shortly after 10^9 TeV as the condition $\lambda_2 > 0$ gets violated. This particular feature can only be witnessed in the case of closely spaced M_H and M_A , which is the primary requirement to satisfy the relic density constraints as discussed before. This completes the explanation of how the allowed area can shrink due to different theoretical constraints for $M = 10^9 \text{ TeV}$.

7.7 Summary and Conclusions

We have examined the high-scale validity of a scenario that (a) offers a scalar dark matter, (b) radiatively generates Majorana masses for neutrinos, and (c) is responsible for leptogenesis. For this, we extend the SM fields with one additional inert Higgs doublet field (Φ_2) and three

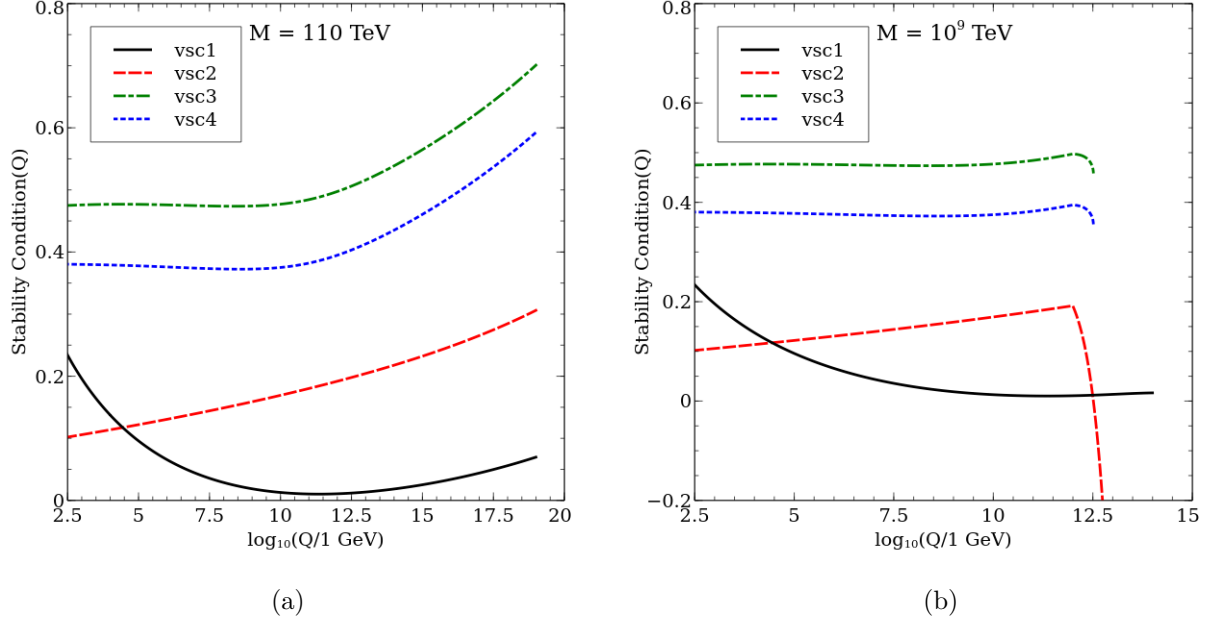


Figure 7.8: Same as Fig. 7.7 but for the benchmark point BP2.

right handed neutrinos (N^i). These new particles are odd under a discrete \mathbb{Z}_2 symmetry, while all the SM particles are even. Because of this discrete symmetry, Φ_2 does not acquire any VEV and has no tree-level couplings to fermions. In this scenario, one has five physical scalars (h, H, A, H^\pm), where, h is denoted as the SM like Higgs boson with a mass of 125 GeV. The lightest state between H and A is the dark matter candidate due to built in \mathbb{Z}_2 symmetry. In our analysis we have assumed H to be the dark matter candidate. Neutrino masses are generated at the one-loop level. The neutrino masses and mixing angles are determined in terms of Yukawa couplings (y_ν), new Higgs particle masses (M_H, M_A) and three heavy Majorana masses ($M_{1,2,3}$). In our numerical analysis we have assumed M_1 is mass of the lightest state and considered two values, namely, $M_1 \equiv M = 110 \text{ TeV}$ and 10^9 TeV . These two mass scales are consistent with leptogenesis. For simplicity, in our analysis, we have considered only one diagonal Yukawa coupling and to determine the value of this coupling we have scanned over M_H and M_A for a given value of M , by keeping $M_\nu \sim \mathcal{O}(0.1 \text{ eV})$.

The parameter space of this model is determined in terms of additional Higgs boson masses, M_H, M_A, M_{H^\pm} , one quartic coupling λ_2 and a set of quartic coupling combinations, λ_L . While scanning the parameter space of this model, we have imposed the LEP bound on scalar masses, M_H, M_A and M_{H^\pm} .

As far as the dark matter constraints are concerned, we have used the relic density limits obtained at 3σ uncertainty from the PLANCK experiment and the direct detection cross section limit from the LUX experiment. Finally, for $M_H < M_h/2$, which would lead to large invisible decay width of the SM like Higgs boson, we demanded that the corresponding branching ratio is less than 20% as obtained from the model independent Higgs precision analysis.

With these set of constraints in hand, we have then scanned the IDM parameter space for two different ranges of dark matter masses, $50 \text{ GeV} < M_H < 90 \text{ GeV}$ and $M_H > 500 \text{ GeV}$. It should be noted that with M_h fixed at 125 GeV, $\lambda_2, \lambda_L, M_H, M_A$ and $M_{H\pm}$ determined all the remaining quartic couplings. We have used these quartic couplings as the electroweak boundary condition by setting the starting RG running scale $Q = M_t$ and evolved these couplings up to the scale Λ_{UV} , where this scenario remained consistent. In the RG evolution of these quartic couplings, the neutrino Yukawa couplings started playing its role from the right handed neutrino mass scale $Q = M$ onwards. Following are the salient features of this model that our analysis brings out.

- Through the study in this chapter we have explicitly demonstrated that at the low DM mass region, the vacuum stability, perturbativity and unitarity constraints put stringent limits on the low-energy value of the coupling λ_L and the \mathbb{Z}_2 -odd scalar masses $M_{H\pm}, M_A$. These bounds strongly depend upon the scale up to which the theory is valid and the right-handed neutrino mass scale. It is interesting to note that all the parameter space allowed by the DM relic density and direct detection constraints lies well within the region allowed by the theoretical constraints valid up to the Planck scale. However, once we have imposed the condition that the Higgs to diphoton signal strength ($\mu_{\gamma\gamma}$) should lie within 2σ of the weighted average value of the ATLAS and CMS data, the allowed parameter space further squeezed.
- The scenario with high DM mass region ($M_H > 500 \text{ GeV}$) is significantly different from that of the low DM mass region. In the former case, the DM being very heavy, the constraint from direct detection is rather insignificant. On the other hand, the relic density constraint is ensured by a degenerate \mathbb{Z}_2 -odd scalars ($\Delta M \simeq 10 \text{ GeV}$). As a result of these, a large part of the parameter space in $\lambda_L - M_H$ and $\lambda_3 - M_{H\pm}$ planes remain unconstrained.
- However, the study of the high scale validity of high DM mass region has interesting consequences. The DM-allowed region reduces substantially after imposing the theo-

retical constraints and this reduction is strongly dependent on the cutoff scale (Λ_{UV}). The effect of neutrino Yukawa couplings in the RG evolution of the different quartic couplings are also prominent in this case. We have found that with the increase in the right handed neutrino mass scale M , the neutrino Yukawa coupling (y_ν) also increases, which in turn further reduces the allowed parameter space by either destabilising the vacuum or violating the perturbativity bound. There is nonetheless a clearly identifiable region of the parameter space, which keeps the model valid all the way up to the Planck scale. This scenario is consistent with the measured Higgs-to-diphoton rates as measured during the 8 TeV run of the LHC.

Chapter 8

High-scale validity of a model with Three-Higgs-doublets

8.1 Introduction

The previous chapters have endowed us with the understanding that a 2HDM could be deemed a "UV- complete" scenario that offers a stable EW vacuum as well a perturbative theory till the Planck scale. It was also emphasised that the conclusions that emerge are connected to the discrete symmetries of the 2HDM scalar potential and the alignment of the VEVs of the two doublets.

It is however not possible to predict the actual number of scalar doublets present in nature from fundamental principles. As hinted at in **Chapter 1** the discovered scalar resonance around 125 GeV [80, 342] could very well arise from an N-Higgs doublet scenario (NHDM) with the additional parameters arranged suitably to give to it, SM-like couplings to fermions and gauge bosons. Since discovery of extra scalars at the colliders is the only direct way to pin down on the exact scalar structure present, and given the LHC has not reported the existence of a spin-0 boson besides the 125 GeV scalar, an elaborate scalar spectrum such as the NHDM could be still a possibility.

In this chapter¹, we aim to probe a three-Higgs doublet model (3HDM), in particular, investigate how it fares in stabilising the Higgs potential as well as in keeping the theory perturbative till the Planck scale. As in the case of 2HDM, we would like to understand the role of discrete symmetries, and also of the pattern of EWSB in the process. The

¹based on [343]

primary reason to choose a 3HDM is that it is the next simplest example beyond 2HDMs, which has been exhaustively studied in the literature [32, 32, 33, 344–353]. In addition, all possible discrete symmetry groups corresponding to a 3HDM have been identified. Another important motivation behind choosing 3HDMs is that the existence of three scalar doublets, replicating the three fermion families, sheds light on the flavour problem. In other words, it is possible that the three families of quarks and leptons could be described by the same symmetries that describe the three scalar doublets. In such cases, this family symmetry could be spontaneously broken along with the electroweak symmetry, although some residual symmetry could survive, thereby stabilising a possible scalar DM candidate.

3HDMs have rather wide scalar spectrum. In fact, invariance under $SU(2)_L \times U(1)_Y$ tells us that there are four neutral scalars, and a pair of charged scalars obtainable from a generic 3HDM. It is reminded that 3HDMs come in various types, depending upon the global symmetry present. One of them is the 3HDM endowed with a global S_3 symmetry [354–359]. This S_3 symmetry is already important from the perspective of flavour, it reproduces the lepton masses and mixings accurately [360–365]. The scalar sector is also interesting since there is an economy of parameters compared to a more generic 3HDM. In fact, the eight dimensionless parameters in the scalar potential can be fully traded off in favour of the seven masses and one mixing angle. The S_3 -symmetric scalar sector has spurred some investigation in the past, and some standalone studies related to DM phenomenology have also occurred [366]. However, the present study is mainly directed towards analysing the Higgs sector, and, it includes the following features which have not been highlighted before.

- We derive the renormalisation group equations at one-loop for the dimensionless parameters in an S_3 symmetric Higgs potential. Using these, we probe high-scale behaviour of the scalar potential. That is, we evolve the scalar quartic couplings and require that the model remains perturbative and keeps vacuum stability intact at each intermediate energy scale. Through this exercise, we try to identify the parameter space at the input scale that keeps the model *valid* till very high scales.
- Electroweak Symmetry Breaking (EWSB) is triggered when one or more doublet receives a vacuum expectation value (VEV). While several such configurations of the VEVs can be there in principle, we consider two such cases which not only are more relevant from the phenomenological point of view, but also demonstrative of the high-scale validity of the S_3 potential. For instance, we analyse a 'two inert doublet' scenario where only one doublet gets a VEV, and which predicts existence of stable scalars

through some remnant symmetry. This scenario thus stands as a potential candidate for describing DM.

- The parameter space allowing for high-scale validity is also subject to various *low energy* constraints, i.e., the ones originating from the oblique S, T and U parameters, signal strength measurements for the 125 GeV Higgs, and also DM searches.

This chapter is organised as follows. In section 8.2, we briefly discuss the salient features of the model, particularly the scalar and Yukawa sectors. The various constraints applied are listed in section 8.3. The numerical results so obtained are detailed in section 8.4, and finally, we summarise in section 8.5. Relevant expressions and equations can be found in Appendix C.

8.2 The S_3 symmetric three-Higgs-doublet model (S_3 HDM) in brief.

8.2.1 Scalar sector.

The scalar sector consists of three scalar doublets ϕ_1 , ϕ_2 and ϕ_3 . Under the S_3 group, ϕ_1 and ϕ_2 transform as a doublet and ϕ_3 is a singlet. That is,

$$\begin{pmatrix} \phi_1 \\ \phi_2 \end{pmatrix} \longrightarrow M \begin{pmatrix} \phi_1 \\ \phi_2 \end{pmatrix}, \quad \phi_3 \longrightarrow \phi_3. \quad (8.2.1)$$

In eqn.(8.2.1), M refers to the doublet representation given by

$$M = \begin{pmatrix} \cos \theta & \sin \theta \\ -\sin \theta & \cos \theta \end{pmatrix}, \quad \begin{pmatrix} \cos \theta & \sin \theta \\ \sin \theta & -\cos \theta \end{pmatrix}, \quad \text{for } \left(\theta = 0, \pm \frac{2\pi}{3} \right). \quad (8.2.2)$$

The most general renormalisable scalar potential consistent with the gauge and S_3 symmetries can be cast as [367],

$$\begin{aligned} V(\phi) = & \mu_{11}^2(\phi_1^\dagger\phi_1 + \phi_2^\dagger\phi_2) + \mu_{33}^2\phi_3^\dagger\phi_3 \\ & + \lambda_1(\phi_1^\dagger\phi_1 + \phi_2^\dagger\phi_2)^2 + \lambda_2(\phi_1^\dagger\phi_2 - \phi_2^\dagger\phi_1)^2 + \lambda_3 \left\{ (\phi_1^\dagger\phi_2 + \phi_2^\dagger\phi_1)^2 + (\phi_1^\dagger\phi_1 - \phi_2^\dagger\phi_2)^2 \right\} \\ & + \lambda_4 \left\{ (\phi_3^\dagger\phi_1)(\phi_1^\dagger\phi_2 + \phi_2^\dagger\phi_1) + (\phi_3^\dagger\phi_2)(\phi_1^\dagger\phi_1 - \phi_2^\dagger\phi_2) + \text{h.c.} \right\} \\ & + \lambda_5(\phi_3^\dagger\phi_3)(\phi_1^\dagger\phi_1 + \phi_2^\dagger\phi_2) + \lambda_6 \left\{ (\phi_3^\dagger\phi_1)(\phi_1^\dagger\phi_3) + (\phi_3^\dagger\phi_2)(\phi_2^\dagger\phi_3) \right\} \end{aligned}$$

$$+\lambda_7 \left\{ (\phi_3^\dagger \phi_1)(\phi_3^\dagger \phi_1) + (\phi_3^\dagger \phi_2)(\phi_3^\dagger \phi_2) + \text{h.c.} \right\} + \lambda_8 (\phi_3^\dagger \phi_3)^2. \quad (8.2.3a)$$

A 3HDM is usually known to have CP -violating phases [368] in the scalar sector. For example a complex λ_4 and λ_7 in this case leads to non-conservation of CP , although the phases are severely constrained by measurements of Electric Dipole Moment of the Neutron (EDMN) [369]. The high-scale stability of a 2HDM is found intact regardless of the CP phase [92]. Thus, the overall conclusions regarding validity of the S_3 HDM at high scales is expected to remain unaffected by the introduction of CP phases. So we choose λ_4 and λ_7 to be real henceforth.

EWSB assigns (VEVs) v_1 , v_2 and v_3 to the doublets ϕ_1 , ϕ_2 and ϕ_3 respectively. They obey $v_1^2 + v_2^2 + v_3^2 = (246 \text{ GeV})^2$. Besides, S_3 -invariance forces additional relationships among them through the minimisation conditions below.

$$2\mu_{11}^2 = -2\lambda_1(v_1^2 + v_2^2) - 2\lambda_3(v_1^2 + v_2^2) - v_3\{6\lambda_4 v_2 + (\lambda_5 + \lambda_6 + 2\lambda_7)v_3\}, \quad (8.2.4a)$$

$$2\mu_{11}^2 = -2\lambda_1(v_1^2 + v_2^2) - 2\lambda_3(v_1^2 + v_2^2) - \frac{3v_3}{v_2}\lambda_4(v_1^2 - v_2^2) - (\lambda_5 + \lambda_6 + 2\lambda_7)v_3^2, \quad (8.2.4b)$$

$$2\mu_{33}^2 = \lambda_4 \frac{v_2}{v_3}(v_2^2 - v_1^2) - (\lambda_5 + \lambda_6 + 2\lambda_7)(v_1^2 + v_2^2) - 2\lambda_8 v_3^2. \quad (8.2.4c)$$

The self-consistency of eqns. (8.2.4a) and (8.2.4b) gives rise to the following possibilities,

$$\lambda_4 = 0, \quad (8.2.5a)$$

$$\text{or, } v_1 = \sqrt{3}v_2, \quad (8.2.5b)$$

$$\text{or, } v_1 = v_2 = 0, v_3 = 246 \text{ GeV}. \quad (8.2.5c)$$

The first case causes a physical scalar to turn massless as reported in [370]. This directs us towards the other two cases that we outline below.

The doublets are parametrised in the following fashion,

$$\phi_i = \frac{1}{\sqrt{2}} \begin{pmatrix} \sqrt{2}w_i^+ \\ v_i + h_i + iz_i \end{pmatrix}, \text{ for } i = 1, 2, 3. \quad (8.2.6)$$

The physical scalar spectrum of a generic CP -conserving 3HDM consists of three CP -even neutral scalars, H_1 , H_2 and h ; two CP -odd neutral scalars A_1 and A_2 ; and two charged scalars H_1^+ and H_2^+ . We define $\tan\beta = \frac{2v_2}{v_3}$ for Scenario A (eqn.8.2.5b). For this VEV-alignment, only two mixing angles α and β are sufficient to parametrise the transformation matrices connecting the $SU(2)$ eigen-basis to the physical basis, somewhat resembling a 2HDM. ² The model is more conveniently described in terms of physical quantities like

²A more detailed discussion regarding the transformation matrices can be found in [370].

masses and mixing angles. The eight λ_i can be traded for the seven masses and the mixing angle α (See [370] for definition.) using the following equations,

$$\lambda_1 = \frac{1}{2v^2 \sin^2 \beta} \left\{ (m_h^2 \cos^2 \alpha + m_{H_1}^2 \sin^2 \alpha) + \left(m_{H_1^+}^2 - m_{H_2^+}^2 \cos^2 \beta - \frac{1}{9} m_{H_2}^2 \right) \right\} \quad (8.2.7a)$$

$$\lambda_2 = \frac{1}{2v^2 \sin^2 \beta} \left\{ (m_{H_1^+}^2 - m_{A_1}^2) - (m_{H_2^+}^2 - m_{A_2}^2) \cos^2 \beta \right\}, \quad (8.2.7b)$$

$$\lambda_3 = \frac{1}{2v^2 \sin^2 \beta} \left(\frac{4}{9} m_{H_2}^2 + m_{H_2^+}^2 \cos^2 \beta - m_{H_1^+}^2 \right), \quad (8.2.7c)$$

$$\lambda_4 = -\frac{2 m_{H_2}^2}{9 v^2} \frac{1}{\sin \beta \cos \beta}, \quad (8.2.7d)$$

$$\lambda_5 = \frac{1}{v^2} \left\{ \frac{\sin \alpha \cos \alpha}{\sin \beta \cos \beta} (m_{H_1}^2 - m_h^2) + 2m_{H_2^+}^2 + \frac{1}{9} \frac{m_{H_2}^2}{\cos^2 \beta} \right\}, \quad (8.2.7e)$$

$$\lambda_6 = \frac{1}{v^2} \left(\frac{1}{9} \frac{m_{H_2}^2}{\cos^2 \beta} + m_{A_2}^2 - 2m_{H_2^+}^2 \right), \quad (8.2.7f)$$

$$\lambda_7 = \frac{1}{2v^2} \left(\frac{1}{9} \frac{m_{H_2}^2}{\cos^2 \beta} - m_{A_2}^2 \right), \quad (8.2.7g)$$

$$\lambda_8 = \frac{1}{2v^2 \cos^2 \beta} \left\{ (m_h^2 \sin^2 \alpha + m_{H_1}^2 \cos^2 \alpha) - \frac{1}{9} m_{H_2}^2 \tan^2 \beta \right\}. \quad (8.2.7h)$$

We also put forth the Scenario B (eqn.(8.2.5c)) as an alternate symmetry breaking pattern. In this case, ϕ_3 is the only active doublet, which is in fact a singlet under S_3 . Consequently, all the fermions couple to ϕ_3 alone and thus they too are S_3 -singlets. The remaining doublets ϕ_1 and ϕ_2 remain *inert*. A \mathbb{Z}_2 symmetry is found unbroken for $\lambda_4 = 0$, and it forbids mixing among scalars coming from different doublets thus enabling one to express the doublets directly in terms of the physical fields as

$$\phi_3 = \frac{1}{\sqrt{2}} \begin{pmatrix} \sqrt{2} w^+ \\ v + h + iz \end{pmatrix}, \quad (8.2.8)$$

$$\phi_i = \frac{1}{\sqrt{2}} \begin{pmatrix} \sqrt{2} H_i^+ \\ H_i + i A_i \end{pmatrix} \text{ for } , i = 1, 2. \quad (8.2.9)$$

With $m_h^2 = 2\lambda_8 v^2$ now, the S_3 symmetry leads to a mass degeneracy in the inert sector,

$$m_{H_1}^2 = m_{H_2}^2 = \mu_{11}^2 + \frac{1}{2} \lambda_L v^2, \quad (8.2.10a)$$

$$m_{A_1}^2 = m_{A_2}^2 = \mu_{11}^2 + \frac{1}{2} \lambda_A v^2, \quad (8.2.10b)$$

$$m_{H_1^+}^2 = m_{H_2^+}^2 = \mu_{11}^2 + \frac{1}{2} \lambda_5 v^2. \quad (8.2.10c)$$

Here $-\lambda_L v$ and $-\lambda_A v$ denote the H_1 - H_1 - h and A_1 - A_1 - h couplings respectively. This mass degeneracy can be lifted in this case, for example, by introducing an S_3 breaking quadratic term of the form $-\mu_{12}^2(\phi_1^\dagger\phi_2 + \phi_2^\dagger\phi_1)$ ³. However, implications of a broken S_3 symmetry are outside the scope of this study.

It is interesting to probe the parameter space arising out of such a VEV-alignment by proposing H_1 and H_2 as possible DM candidates. For the S_3 HDM to qualify as a good DM model, its predictions of relic density and direct detection rates must be matched against corresponding experimental data. We arrange for the hierarchy $m_{H_1} < m_{A_1}, m_{H_1^+}$ throughout our numerical analysis (H_1 and A_1 are similar to each other in terms of the masses and couplings, the only difference being the sign of λ_7 . Thus a flip in the sign of λ_7 would tantamount to interchanging H_1 and A_1 . In that case, A_1 would be the DM candidate and the hierarchy required would be $m_{A_1} \leq m_{H_1}, m_{H_1^+}$. The overall physics thus would remain unchanged.). LEP constraints on the direct search for charged and pseudoscalar Higgs bosons are evaded by taking $m_{H_i^+}$ and $m_{A_i} > 100$ GeV [371]. Similar to the previous case, we describe the model parameter space in terms of the physical parameters $\{ \lambda_1, \lambda_2, \lambda_3, m_{H_1}, m_{A_1}, m_{H_1^+}, \lambda_L \}$.

Our main motivation is to study the high-scale stability of the S_3 HDM for the two different VEV- assignments discussed above. In doing that we juxtapose the constraints coming from oblique parameters, Higgs signal strengths in the first case, and also the ones coming from relic density and direct detection in the second case. In principle there can be other such VEV-configurations as well, and our choice is not exhaustive in that sense. Nonetheless, this chapter takes into account two representative cases. The first one defines an *active* 3HDM scenario, i.e, when all three ϕ_1, ϕ_2 and ϕ_3 receive non-zero VEVs. The second one describes an *inert* scenario, where these inert scalars do not mix with the 125 GeV Higgs that comes from ϕ_3 .

³The degeneracy persists even after one-loop radiative effects are incorporated. This is because the \mathbb{Z}_2 symmetry that emerges unbroken after EWSB is an exact symmetry not only of the scalar potential, but of the entire Lagrangian. Thus, this not only leads to equal tree level masses, but also equal couplings for H_1 and H_2 . The two-point correlators for H_1 and H_2 , $\Pi_{H_1 H_1}(p)$ and $\Pi_{H_2 H_2}(p)$ (say) respectively, would have exactly the same expressions then. This would lead to equal one-loop corrected masses for H_1 and H_2 . In other words, the unbroken \mathbb{Z}_2 symmetry would protect the degeneracy at the one-loop level.

8.2.2 Yukawa Sector.

We take the first two fermion families in an S_3 -doublet and the third to be a singlet. The most general Yukawa Lagrangian consistent with the gauge and S_3 symmetries, for the up-type quarks is then given by

$$\begin{aligned}
- \mathcal{L}_Y^u &= y_1^u \left(\bar{Q}_{1L} \tilde{\phi}_3 u_{1R} + \bar{Q}_{2L} \tilde{\phi}_3 u_{2R} \right) + y_2^u \left\{ \left(\bar{Q}_{1L} \tilde{\phi}_2 + \bar{Q}_{2L} \tilde{\phi}_1 \right) u_{1R} + \left(\bar{Q}_{1L} \tilde{\phi}_1 - \bar{Q}_{2L} \tilde{\phi}_2 \right) u_{2R} \right\} \\
&\quad + y_3^u \bar{Q}_{3L} \tilde{\phi}_3 u_{3R} + y_4^u \bar{Q}_{3L} \left(\tilde{\phi}_1 u_{1R} + \tilde{\phi}_2 u_{2R} \right) \\
&\quad + y_5^u \left(\bar{Q}_{1L} \tilde{\phi}_1 + \bar{Q}_{2L} \tilde{\phi}_2 \right) u_{3R} + \text{h.c.} .
\end{aligned} \tag{8.2.11}$$

The lower component of the $SU(2)$ doublets of Higgs multiplets are uncharged in the convention we use. The standard definition $\tilde{\phi}_i = i\sigma_2 \phi_i^*$ was used in eqn.(8.2.11). The Yukawa couplings of the d_R quarks can be obtained by replacing u_{iR} by d_{iR} , y_i^u by y_i^d , and $\tilde{\phi}_i$ by ϕ_i in \mathcal{L}_Y^u and similarly for leptons. The Yukawa couplings are in general complex, which can be responsible for CP violation. More elaborate discussions on S_3 symmetric Yukawa textures can be found in [372–375].

After symmetry breaking, the mass matrix that arises in the up-type quark sector is the following, (In the $(u \ c \ t)$ basis):

$$\mathcal{M}_u = \begin{pmatrix} (y_1^u v_3 + y_2^u v_2)/\sqrt{2} & y_2^u v_1/\sqrt{2} & y_5^u v_1/\sqrt{2} \\ y_2^u v_1/\sqrt{2} & y_1^u v_3 - y_2^u v_2/\sqrt{2} & y_5^u v_2/\sqrt{2} \\ y_4^u v_1/\sqrt{2} & y_4^u v_2/\sqrt{2} & y_3^u v_3/\sqrt{2} \end{pmatrix}, \quad \text{with } v_1 = \sqrt{3}v_2. \tag{8.2.12}$$

The texture is of the same form for the down-type quarks and charged leptons. In principle, one can retain all the parameters in the Yukawa matrix and fine-tune them appropriately in order to reproduce the correct fermion masses and mixings. However that would make the analysis using RG complicated and unwieldy, and hence, we look for a simplification. Choosing $y_4^u, y_5^u = 0$ brings \mathcal{M}_u to a $2 \times 2 \oplus 1 \times 1$ block-diagonal form. The quark masses in the SM can be straightforwardly reproduced by diagonalising the remaining the 2×2 block and then tuning the parameters appropriately. For example, the choice $y_1^u < y_2^u < y_3^u$ reproduces the observed up-type quark mass hierarchy. The advantage of this choice is that only $y_3^u = \frac{v}{v_3} y_t^{SM}$ gets a value large enough to cast an impact on the RG evolution, where y_t^{SM} is the SM t -quark Yukawa coupling and, all other Yukawa couplings have a negligible bearing. In addition, even if we invoke a non-zero y_4^u and y_5^u , the observed quark-mixings will always render them small. Exactly this approximation is applied to the bottom quark and lepton sectors also. It is easy to see that then $y_3^u: y_3^b: y_3^l = m_t: m_b: m_\tau$, i.e, this particular approximation preserves the hierarchy of Yukawa couplings observed in the SM. Hence we

infer that only the t -quark can contribute significantly to the beta functions through the parameter y_3^u and the effect of all other fermions can be safely neglected in this context. Thus effectively with only one Yukawa coupling into the picture, as far as high-scale stability is concerned, it becomes easier to throw light on the scalar sector.

In the inert case, all the fermion generations are S_3 -singlets and hence couple only to ϕ_3 .

8.3 Constraints imposed.

We have maintained $m_h = 125$ GeV throughout. Parameter space of the scenario at hand is surveyed thoroughly by generating random model-points in the

$\{\tan\beta, m_{H_1^+}, m_{H_2^+}, m_{A_1}, m_{A_2}, m_{H_1}, m_{H_2}, c_{\beta-\alpha}\}$ basis in scenario A and, $\{\lambda_1, \lambda_2, \lambda_3, m_{H_1}, m_{A_1}, m_{H_1^+}, \lambda_L\}$ in scenario B. We discuss below the various theoretical and experimental constraints imposed to shape the results.

8.3.1 Theoretical constraints.

The S_3 HDM remains a calculable theory if the model parameters fulfil the respective perturbativity constraints, $|\lambda_i| \leq 4\pi$, $|y_t|, |g_1|, |g_2|, |g_3| \leq \sqrt{4\pi}$. A more stringent choice is to demand all of the couplings $\leq \sqrt{4\pi}$. We however stick to 4π , since this projects out the maximally allowed parameter space.

The $2 \rightarrow 2$ amplitude matrix corresponding to scattering of the longitudinal components of the gauge bosons can be mapped to a corresponding matrix for the scattering of the Goldstone bosons [76, 97, 117, 118]. The theory respects unitarity if each eigenvalue of the aforementioned amplitude matrix does not exceed 8π .

$$|a_i^\pm|, |b_i| \leq 8\pi, \text{ for } i = 1, 2, \dots, 6. \quad (8.3.1)$$

The expressions for the individual eigenvalues [370] in terms of quartic couplings are given below :

$$a^\pm = \left(\lambda_1 - \lambda_2 + \frac{\lambda_5 + \lambda_6}{2} \right) \pm \sqrt{\left(\lambda_1 - \lambda_2 + \frac{\lambda_5 + \lambda_6}{2} \right)^2 - 4 \left\{ (\lambda_1 - \lambda_2) \left(\frac{\lambda_5 + \lambda_6}{2} \right) - \lambda_4^2 \right\}}, \quad (8.3.2a)$$

$$b^\pm = (\lambda_1 + \lambda_2 + 2\lambda_3 + \lambda_8) \pm \sqrt{(\lambda_1 + \lambda_2 + 2\lambda_3 + \lambda_8)^2 - 4 \{ \lambda_8(\lambda_1 + \lambda_2 + 2\lambda_3) - 2\lambda_7^2 \}}, \quad (8.3.2b)$$

$$c^\pm = (\lambda_1 - \lambda_2 + 2\lambda_3 + \lambda_8) \pm \sqrt{(\lambda_1 - \lambda_2 + 2\lambda_3 + \lambda_8)^2 - 4 \left\{ \lambda_8(\lambda_1 - \lambda_2 + 2\lambda_3) - \frac{\lambda_6^2}{2} \right\}}, \quad (8.3.2c)$$

$$d^\pm = \left(\lambda_1 + \lambda_2 + \frac{\lambda_5}{2} + \lambda_7 \right) \pm \sqrt{\left(\lambda_1 + \lambda_2 + \frac{\lambda_5}{2} + \lambda_7 \right)^2 - 4 \left\{ (\lambda_1 + \lambda_2) \left(\frac{\lambda_5}{2} + \lambda_7 \right) - \lambda_4^2 \right\}}, \quad (8.3.2d)$$

$$e^\pm = (5\lambda_1 - \lambda_2 + 2\lambda_3 + 3\lambda_8) \pm \left[(5\lambda_1 - \lambda_2 + 2\lambda_3 + 3\lambda_8)^2 - 43\lambda_8(5\lambda_1 - \lambda_2 + 2\lambda_3) - \frac{1}{2}(2\lambda_5 + \lambda_6)^2 \right]^{1/2} \quad (8.3.2e)$$

$$f^\pm = \left(\lambda_1 + \lambda_2 + 4\lambda_3 + \frac{\lambda_5}{2} + \lambda_6 + 3\lambda_7 \right) \pm \left[\left(\lambda_1 + \lambda_2 + 4\lambda_3 + \frac{\lambda_5}{2} + \lambda_6 + 3\lambda_7 \right)^2 - 4 \left\{ (\lambda_1 + \lambda_2 + 4\lambda_3) \left(\frac{\lambda_5}{2} + \lambda_6 + 3\lambda_7 \right) - 9\lambda_4^2 \right\} \right]^{1/2}, \quad (8.3.2f)$$

$$h_1 = \lambda_5 + 2\lambda_6 - 6\lambda_7, \quad (8.3.2g)$$

$$h_2 = \lambda_5 - 2\lambda_7, \quad (8.3.2h)$$

$$h_3 = 2(\lambda_1 - 5\lambda_2 - 2\lambda_3), \quad (8.3.2i)$$

$$h_4 = 2(\lambda_1 - \lambda_2 - 2\lambda_3), \quad (8.3.2j)$$

$$h_5 = 2(\lambda_1 + \lambda_2 - 2\lambda_3), \quad (8.3.2k)$$

$$h_6 = \lambda_5 - \lambda_6. \quad (8.3.2l)$$

In addition to the above, the scalar potential must be bounded from below in order to render the electroweak vacuum stable. Demanding absolute *stability* of the vacuum leads to the following conditions [370],

$$\text{vsc1} : \lambda_1 > 0, \quad (8.3.3)$$

$$\text{vsc2} : \lambda_8 > 0, \quad (8.3.4)$$

$$\text{vsc3} : \lambda_1 + \lambda_3 > 0, \quad (8.3.5)$$

$$\text{vsc4} : 2\lambda_1 + (\lambda_3 - \lambda_2) > |\lambda_2 + \lambda_3|, \quad (8.3.6)$$

$$\text{vsc5} : \lambda_5 + 2\sqrt{\lambda_8(\lambda_1 + \lambda_3)} > 0, \quad (8.3.7)$$

$$\text{vsc6} : \lambda_5 + \lambda_6 + 2\sqrt{\lambda_8(\lambda_1 + \lambda_3)} > 2|\lambda_7|, \quad (8.3.8)$$

$$\text{vsc7} : \lambda_1 + \lambda_3 + \lambda_5 + \lambda_6 + 2\lambda_7 + \lambda_8 > 2|\lambda_4|. \quad (8.3.9)$$

These conditions can be arrived at by demanding the scalar potential remains positive along

various directions in the field space in the $\phi_i \rightarrow \infty$ limit. We do not consider *metastable* vacua configurations in this chapter [167, 168], which are expected to project a more relaxed parameter space in this context.

8.3.2 Oblique parameters.

The S_3 HDM induces modification in the S , T and U parameters through the additional scalars participating in the loops of the gauge-boson self energies. One discerns the 3HDM contribution from the SM as,

$$S = S_{SM} + \Delta S, \tag{8.3.10a}$$

$$T = T_{SM} + \Delta T, \tag{8.3.10b}$$

$$U = U_{SM} + \Delta U. \tag{8.3.10c}$$

Here ΔS , ΔT and ΔU denote the S_3 HDM contributions. These have been derived following the approach outlined in [130]. Relevant expressions can be found in the **Appendix C.2**. The central value is the contribution coming from the standard model with the reference values $m_{h,\text{ref}} = 125.0$ GeV and $M_{t,\text{ref}} = 173.1$ GeV where M_t denotes the pole mass of the top quark. We have used 1σ limits of S , T and U following [376].

8.3.3 Higgs Signal-strengths

The ATLAS and CMS collaborations have measured the production cross section for the 125 GeV Higgs multiplied by its branching ratios to various possible channels. The results so far are increasingly in favour of the SM predictions. An extended Higgs sector, such as the S_3 HDM although can very well contain a scalar with mass around 125 GeV, but yet can potentially modify the signal strength predictions through its modified Higgs-gauge boson and Higgs-fermion couplings. For example, the hVV and $hb\bar{b}$ couplings get scaled by $\sin(\beta - \alpha)$ and $\frac{\sin\alpha}{\cos\beta}$ w.r.t the SM, in the case with three non-zero VEVs. The loop induced decay widths to $\gamma\gamma$ and $Z\gamma$ final states are also modified. However, one can always arrange for $\alpha = \beta - \frac{\pi}{2}$ which reproduces exact SM couplings. This so called *alignment limit* is present in two-Higgs doublet models as well [110]. We explore a case where this limit is not strictly enforced, rather $\sin(\beta - \alpha) = 0.98$ is taken. The reader is reminded that the tree level couplings of h to fermions and gauge bosons remain identical to the SM in the presence of additional inert doublets.

In order to check the consistency of a 2HDM with the measured rates in various channels, we theoretically compute the signal strength μ^i for the i -th channel using the relation:

$$\mu^i = \frac{R_{\text{prod}} \times R_{\text{decay}}^i}{R_{\text{width}}} . \quad (8.3.11)$$

Here R_{prod} , R_{decay}^i and R_{width} denote respectively the ratios of the theoretically calculated production cross section, the decay rate to the i -th channel and the total decay width for a ~ 125 GeV Higgs to their corresponding SM counterparts. For our numerical analysis, we have taken gluon fusion to be the dominant production mode for the SM-like Higgs.⁴ The predicted signal-strengths to ZZ , WW , $b\bar{b}$ channels are in excellent agreement with the SM once the alignment limit is invoked. $\mu_{\gamma\gamma}$ still needs to be controlled since the charged scalars do not decouple from the theory in spite of an exact alignment (see **Appendix C.3**). In an exact-alignment scenario, the total width of h hardly deviates from its SM value and $\mu_{\gamma\gamma}$ settles approximately to $\frac{\Gamma_{h \rightarrow \gamma\gamma}^{S_3\text{HDM}}}{\Gamma_{h \rightarrow \gamma\gamma}^{\text{SM}}}$. Latest measurements from ATLAS and CMS give $\mu_{\gamma\gamma} = 1.17_{-0.27}^{+0.27}$ and $1.12_{-0.24}^{+0.24}$ respectively [180, 377]. We use the cited limits at 2σ .

We make the passing remark that in-house codes have been employed to carry out the computations related to oblique parameters and signal strengths. In particular, the RG equations have been numerically solved by implementing the Runge-Kutta (RK4) algorithm in the same.

8.3.4 Dark matter relic density and direct detection

In the one active + two inert doublet case, we impose that the relic density must be away by at most 3σ limits from the PLANCK [339] central value. That is,

$$0.1118 \leq \Omega h^2 \leq 0.1199. \quad (8.3.12)$$

A more relaxed requirement is to impose only the upper limit, in which case it implies that the S_3 inert scalars only partially account for the observed relic density. Relic density calculations in this chapter are done using the publicly available code `micrOMEGAs` [341].

Experiments like XENON100 [285], LUX [283] have placed upper limits on WIMP-nucleon scattering cross sections (σ^{SI}). We again use `micrOMEGAs` to compute the cross sections and adhere to the more stringent constraints by LUX. Given that WIMP-nucleon

⁴While other channels such as vector boson fusion (VBF) and associated Higgs production with W/Z (VH) have yielded data in the 8 TeV run, the best fit signal strengths are still dominated by the gluon fusion channel.

scattering in this model occurs only through a t-channel h exchange, the cross section computation is plagued by the uncertainty in the strange quark form factor. We have resorted to the `micrOMEGAs` default parameters in this regard. We have imposed an upper bound of 10^{-46} cm² on the spin-independent WIMP-nucleon cross section throughout our analysis.

8.3.5 Evolution under renormalisation group.

The main motivation behind this chapter is to study the behaviour of the S_3 HDM parameters under RG. The *strategy* adopted is, we select parameter points consistent with the constraints discussed above. The parameter space obtained in the process is allowed to evolve under RG. The one loop beta functions employed for this analysis are listed in **Appendix C.1**. They were derived by demanding scale-invariance of the one-loop corrected scalar potential following [120], and, cross checked by a standard Feynman diagrammatic calculation. Constraints stemming from perturbativity, unitarity and vacuum stability are demanded to be fulfilled throughout the course of evolution, up to some cutoff Λ . There is however, no natural choice for Λ , given the fact we assume that S_3 HDM is the only physics up to this scale. We aim to push Λ to as high as the GUT scale, or the Planck scale, and explore the consequences on our scenario. Incorporation of these constraints in the RG evolution tightens up the parameter space at the electroweak scale.

Discussion of the RG constraints is crucial in context of a non-minimal Higgs sector such as the S_3 HDM, owing to the fact that the additional scalars could ameliorate the vacuum instability problem in the SM [77]. However, due to the additional bosonic content, quartic couplings tend to rise fast and hit the *Landau pole* even though vacuum stability is preserved. To strike a balance between these extremes, the model parameters have to be judiciously tuned. This is precisely what we aim to do in context of an S_3 HDM.

8.4 Impact of the constraints on the parameter space.

8.4.1 Scenario A: $v_1 = \sqrt{3}v_2$.

Model points are sampled randomly through a scan of the parameter space within the specified ranges,

$$\begin{aligned} \tan\beta &\in [0.1, 50] \\ m_{H_1}, m_{H_2} &\in [125 \text{ GeV}, 1000 \text{ GeV}] \end{aligned}$$

$$m_{A_1}, m_{A_2} \in [100 \text{ GeV}, 1000 \text{ GeV}]$$

$$m_{H_1^+}, m_{H_2^+} \in [80 \text{ GeV}, 1000 \text{ GeV}]$$

Demanding perturbativity at the electroweak scale puts upper bounds on the scalar masses and $\tan\beta$. In particular, all the scalar masses lie below ~ 800 GeV and $\tan\beta \in [0.3, 13.6]$. The upper bounds on the masses and $\tan\beta$ settle at 1 TeV and 17.3 respectively upon relaxing the perturbativity constraint. In that case the bounds are put by unitarity alone, an observation in consonance with the findings in [370]. Any value of $\tan\beta$ outside the quoted limit is responsible for making the theory non-perturbative through the large values it gives to the quartic couplings in the process. This can be revealed through an inspection of eqns.(8.2.7a)-(8.2.7h).

The next part of the analysis involves evolution under RG. The key finding here is that this scenario is not valid beyond 10^7 GeV. This is attributed to the following two reasons: (i) Quartic couplings are large at the input scale itself, they hit the perturbative limit around the multi-TeV scale. This can be understood using the following logic, the quartic couplings at the input scale are typically $\sim \frac{m^2}{v^2}$ (see eqns.(8.2.7a)-(8.2.7h)), where m refers to any physical S_3 HDM mass. Thus for an m below the TeV scale, at least one quartic coupling becomes large enough to make the theory non-perturbative. (ii) $\tan\beta > 3$ in particular destabilises the vacuum by enhancing the t -Yukawa with respect to its SM value. It so happens that for many parameter points, the Yukawa coupling itself evolves to non-perturbative value below the instability scale, however this is a subleading effect. The T parameter constraint negates a large number of scan points, many of which otherwise clear the RG constraints up to the highest permissible cutoff 10^7 GeV. This we show in Fig.(8.2). ΔS mostly stays within its 1σ limit. We also prepare the following two benchmark models (Table 8.1) to reinforce our observation on a violated vacuum stability or unitarity.

Benchmark	$\tan\beta$	m_{A_1} (GeV)	m_{A_2} (GeV)	$m_{H_1^+}$ (GeV)	$m_{H_2^+}$ (GeV)	m_{H_1} (GeV)	m_{H_2} (GeV)
BP1	3.54	265.12	392.00	146.00	105.00	233.77	143.05
BP2	1.02	102.22	167.78	119.80	107.00	214.95	132.35

Table 8.1: Benchmark points chosen to illustrate the behaviour under RGE. Λ denotes the maximum extrapolation scale up to which vacuum stability and perturbativity are ensured.

BP1 leads to a destabilised vacuum through $\lambda_8 < 0$ occurring below the TeV scale. On the other hand, λ_1 in BP2 rises rapidly and quickly becomes non-perturbative just after crossing

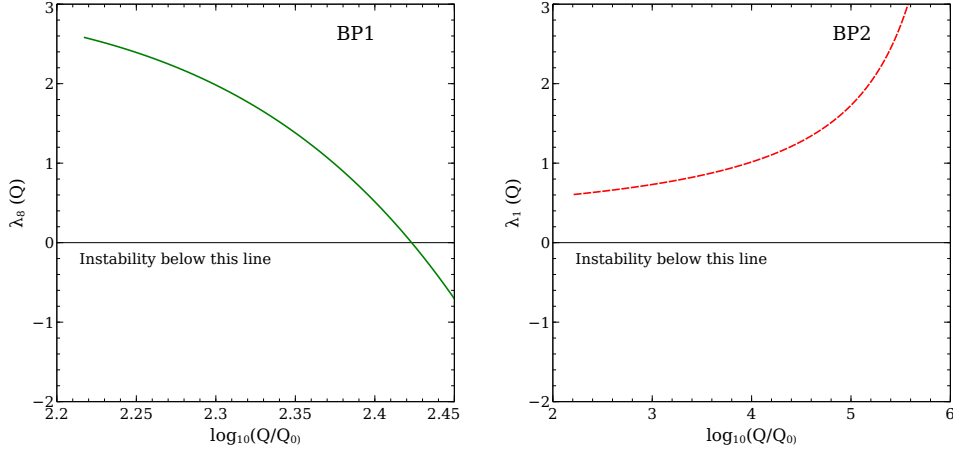


Figure 8.1: Running of λ_8 corresponding to BP1 (left) and λ_1 corresponding to BP2 (right). $m_h = 125$ GeV and an exact alignment $\sin(\beta - \alpha) = 1.0$ taken in both.

10^6 GeV. The running of λ_8 and λ_1 in the two cases is displayed in Fig.8.1. Also, the bounds finally obtained on λ_i , taking into account the oblique parameter and the diphoton constraints, are summarised in the Table 8.2.

The $h \rightarrow \gamma\gamma$ rate diminishes with respect to the SM throughout the parameter space, however only for a strict imposition of $\sin(\beta - \alpha) = 1$ [370]. We have projected the $\mu_{\gamma\gamma}$ values in the S_3 HDM versus $m_{H_1^+}$ and $m_{H_2^+}$ in Fig.8.3. The dimensionful $h - H_i^+ - H_i^-$ coupling denoted by $g_{hH_i^+H_i^-}$ is conveniently expressed through $g_{hH_i^+H_i^-} = \frac{2\kappa_i m_{H_i^+}^2}{v}$, where κ_i are dimensionless. Whenever $\alpha = \beta - \frac{\pi}{2}$, it is seen that $\kappa_i = -\left(1 + \frac{m_h^2}{2m_{H_i^+}^2}\right)$ [370] (exact expression given in **Appendix C.3**). A decrement in $\mu_{\gamma\gamma}$, in an exact alignment case thus becomes inevitable, since both κ_1 and κ_2 are always negative (see **Appendix C.3**). In fact, $\mu_{\gamma\gamma}$ never exceeds 0.82 for validity till 10^6 GeV, given that $|\kappa_1|, |\kappa_2| \geq 1.39$ in that case. Following a similar trend, the points valid till $\Lambda = 10^7$ GeV give $\mu_{\gamma\gamma} < 0.63$ and hence are not phenomenologically acceptable. The bounds put on λ_i translate into corresponding bounds on $\tan\beta$ and the non-standard scalar masses, as shown in Fig.8.4. We point out that while m_{H_2} could be up to 270 GeV for $\Lambda = 10^6$ GeV, the other masses do not exceed 210 GeV for most parameter points. It is to be noted that κ_1 and κ_2 can take either sign for departure from exact alignment, and hence an increment in the diphoton rate is possible there. (See Fig.8.3 for the case when $\sin(\beta - \alpha) = 0.98$.)

A generic feature in context of Scenario A is that, the mass parameters m_{11}^2 and m_{33}^2 get traded off through the tadpole conditions, making λ_i expressible in terms of the physical

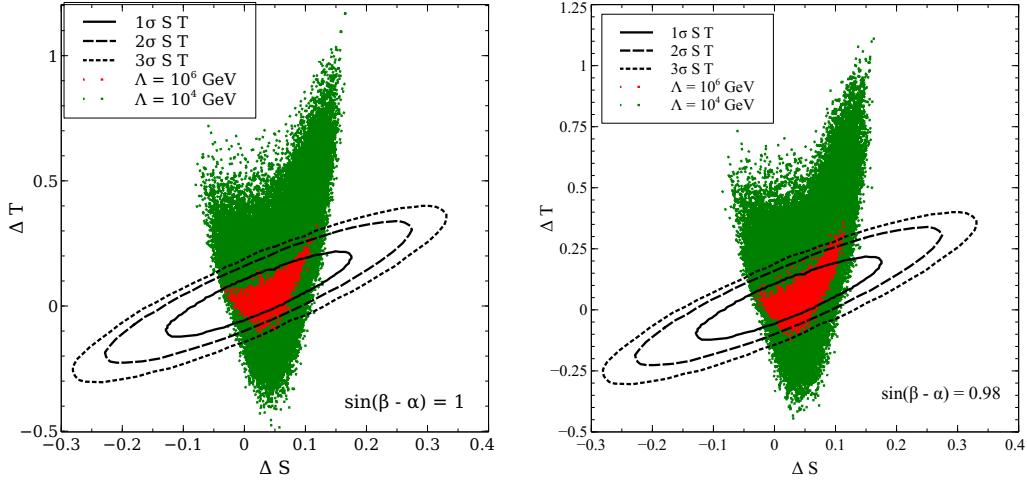


Figure 8.2: Contribution of the S_3 HDM scalars to the oblique parameters for $\sin(\beta - \alpha) = 1.0$ (Left) and $\sin(\beta - \alpha) = 0.98$ (Right). The ellipses denote the 1σ (solid), 2σ (dashed) and 3σ (dotted) limits. The green and red points indicate validity till 10^4 GeV and 10^6 GeV respectively. We notice that the oblique parameters do not change appreciably for a slight departure from exact alignment.

scalars only. Thus for physical scalars lurking below a 1 TeV mass, λ_i are already $\mathcal{O}(1)$ or even larger at the input scale. This does not lead to a model that is perturbative at a high scale. As a possible remedy, additional mass parameters in the equations relating λ_i to the physical masses could induce cancellations keeping λ_i further small at the EW scale. This could be achieved either through inclusion of quadratic terms violating S_3 , or through invoking an *inert* VEV structure where all of m_{11}^2 and m_{33}^2 do not get eliminated. These terms can elevate the non-standard masses to around ~ 1 TeV and can also lead to $\mu_{\gamma\gamma} > 1$. Since a broken S_3 group is beyond the ambit of the present study, we focus on the inert case (Scenario B) in the subsequent section.

8.4.2 Scenario B: $v_1 = v_2 = 0$, $v_3 = 246$ GeV.

One needs to put $\lambda_4 = 0$ in order to keep the DM stable through an unbroken \mathbb{Z}_2 symmetry. Correct relic density is obtained in the mass regimes $m_{H_1} < 80$ GeV and $m_{H_1} > 370$ GeV. We discuss below the phenomenology in detail.

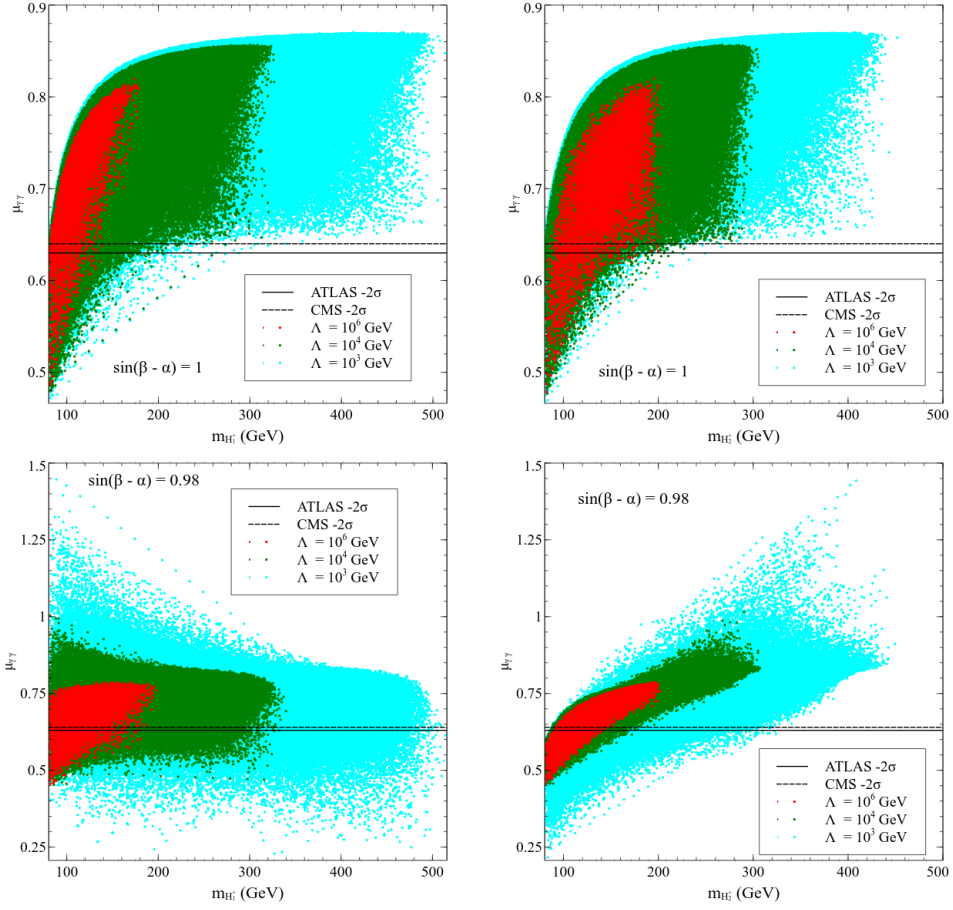


Figure 8.3: $h \rightarrow \gamma\gamma$ rates for an S_3 HDM valid till a cutoff Λ . The cyan, green and red points are respectively for $\Lambda = 10^3, 10^4$ and 10^6 GeV. The solid and dotted lines denote the 2σ limits below the central value given by ATLAS and CMS respectively .

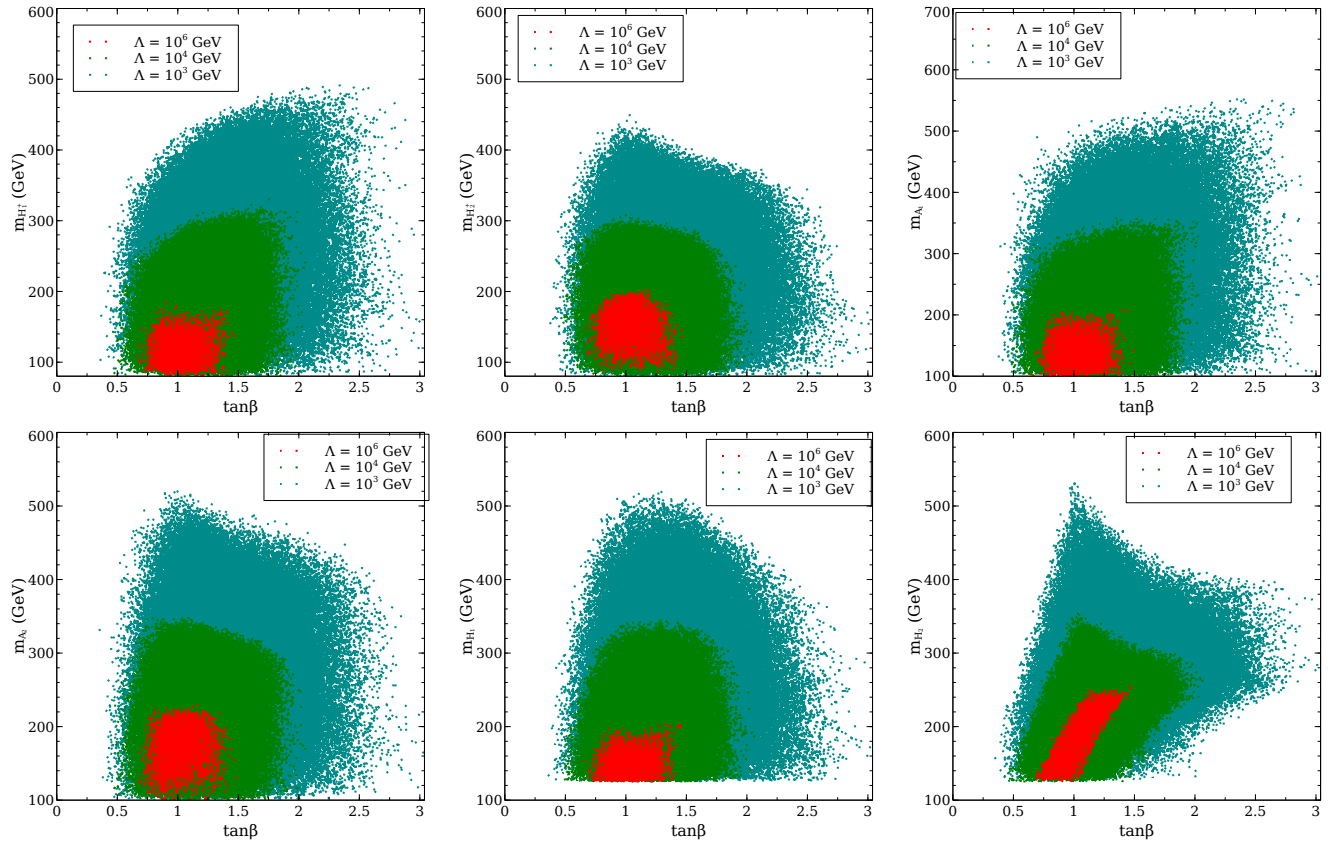


Figure 8.4: Regions consistent with the theoretical constraints up to a given cutoff. The cyan, green and red points are valid till 10^3 GeV, 10^4 GeV and 10^6 GeV respectively. Oblique parameter and diphoton constraints are also taken into account. Points valid till 10^7 GeV get disallowed by the diphoton constraint and are hence not displayed. An exact alignment is chosen and it has been checked that the bounds do not change for a small deviation from exact alignment.

Parameter	$\Lambda = 10^3$ GeV	$\Lambda = 10^4$ GeV	$\Lambda = 10^6$ GeV
$\lambda_1 \in$	[0, 2.7]	[0, 1.4]	[0, 0.7]
$\lambda_2 \in$	[-2.7, 2.5]	[-1.4, 1.3]	[-0.6, 0.6]
$\lambda_3 \in$	[-2.2, 2.6]	[-1.0, 1.3]	[-0.2, 0.6]
$\lambda_4 \in$	[-2.1, -0.1]	[-0.9, -0.1]	[-0.4, -0.1]
$\lambda_5 \in$	[-2.7, 5.5]	[-1.1, 3.0]	[-0.4, 1.5]
$\lambda_6 \in$	[-5.3, 4.0]	[-2.6, 1.9]	[-1.1, 0.7]
$\lambda_7 \in$	[-2.2, 0.9]	[-1.0, 0.3]	[-0.4, 0]
$\lambda_8 \in$	[0, 3.8]	[0, 1.9]	[0.1, 1.1]

Table 8.2: Bounds on the quartic couplings, for $\Lambda = 10^3, 10^4, 10^6$ GeV. Oblique parameter and diphoton constraints are also taken into account. We show the numbers up to the first decimal place.

$$m_{H_1} < 80 \text{ GeV}$$

DM particles dominantly annihilate to the $b\bar{b}$ final state through an h in the s-channel, in this mass regime. A sharp decline in relic abundance is noted for $m_{H_1} > 80$ GeV, when the VV (V denoting a vector boson.) modes open up. Maintaining appropriate mass gaps amongst H_1 , A_1 and H_1^+ turns advantageous in the two following ways. Firstly, the DM relic abundance does not deplete fast through coannihilations brought in by a narrow mass splitting. Secondly, it gives sizeable values to λ_5 , λ_6 and λ_7 which in turn aid to stabilise the vacuum far beyond the SM instability scale, even up to the Planck scale. Overall, the phenomenology in this mass regime is broadly similar to the case with a single inert doublet.

Benchmark	m_{H_1} (GeV)	m_{A_1} (GeV)	$m_{H_1^+}$ (GeV)	λ_L	Ωh^2	$\sigma^{SI}(cm^2)$	Λ (GeV)
BP3	57.00	102.00	120.00	0.0042	0.1170	4.63×10^{-47}	10^{19}

Table 8.3: Benchmark point illustrating the behaviour under RGE. Λ denotes the maximum extrapolation scale up to which vacuum stability and perturbativity are ensured.

The displayed benchmark BP3 (Table 8.3) keeps $\text{BR}(h \rightarrow \text{invisible}) < 19\%$ owing to the tiny λ_L . RG evolution corresponding to BP3 is shown in Fig.8.5. A perturbative theory at high scales requires m_{A_1} and $m_{H_1^+}$ to obey sharp upper bounds, a feature not reflected by

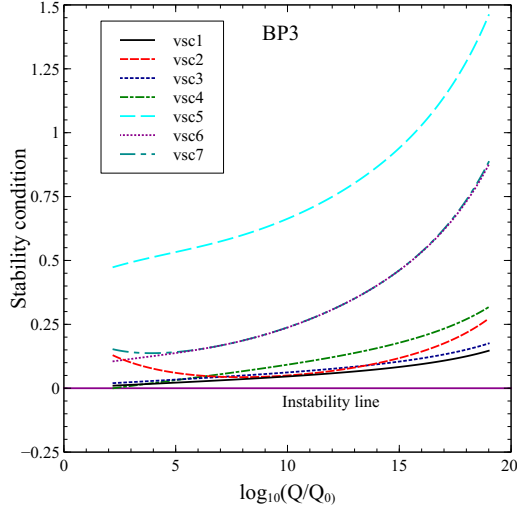


Figure 8.5: Evolution of BP3 under RG. Colour coding is explained in the legends and the vacuum instability line is highlighted.

the DM constraints alone. For instance, we need $m_{A_1}, m_{H_1^+} < 135$ GeV in order to salvage perturbativity till the GUT scale.

$m_{H_1} > 370$ GeV

In this region, dark matter relic density tends to diminish due to prohibitively large annihilation to VV final states. Annihilation amplitudes in this case are the interference of the $H_1 - H_1 - V - V$ four-point coupling diagrams and the t/u channel diagrams with H_1^+/A_1 in the propagator. However, a small splitting among the masses of the inert scalars induces cancellation between these two classes of diagrams thereby burgeoning relic density to the desired range. Larger is m_{H_1} , higher is the annihilation to the longitudinal gauge bosons and hence higher becomes λ_L . While a similar phenomenology occurs in case of a single inert doublet, apart from the DM mass < 80 GeV region, Ωh^2 is ~ 0.1 again only when the DM mass > 500 GeV. For example, for $m_{H_1} = 387.5$, $m_{A_1} = 390.5$, $m_{H_1^+} = 389.6$, $\lambda_L = 0.056$, the dominant annihilation channels are $H_1 H_1 \rightarrow WW$ 12%, $H_2 H_2 \rightarrow WW$ 12%, $H_1 H_1 \rightarrow ZZ$ 10%, $H_2 H_2 \rightarrow ZZ$ 10%, $H_1^+ H_1^- \rightarrow WW$ 6%, $H_2^+ H_2^- \rightarrow WW$ 6%, $H_1^+ H_1 \rightarrow \gamma W^+$ 6%, $H_2^+ H_2 \rightarrow \gamma W^+$ 6%. For a spectrum $m_{H_1} = 904.1$, $m_{A_1} = 912.1$, $m_{H_1^+} = 904.3$, the requisite λ_L for a correct relic increases to ~ 0.49 . One thus requires a small mass splitting and an appropriately adjusted λ_L to generate correct relic density.

To examine high-scale validity of this scenario, model points are generated in the following

range.

$$\lambda_L \in [-4\pi, 4\pi] \quad (8.4.1)$$

$$m_{H_1} \in [300.0 \text{ GeV}, 1000.0 \text{ GeV}] \quad (8.4.2)$$

$$m_{A_1} \in [m_{H_1}, m_{H_1} + 100.0 \text{ GeV}] \quad (8.4.3)$$

$$m_{H_1^\pm} \in [m_{H_1}, m_{H_1} + 100.0 \text{ GeV}] \quad (8.4.4)$$

We also fix $\lambda_1 = \lambda_2 = \lambda_3 = 0.01$ at the initial scale, since these couplings do not enter into the calculations of relic density and WIMP-nucleon cross sections. This choice is rather judicious, an higher value mostly makes the couplings non-perturbative at high scales. Fig.8.6 displays the variation of relic density corresponding to model points valid up to three different cutoffs $\Lambda = 10^3 \text{ GeV}$, 10^{16} GeV and 10^{19} GeV . Fig.8.7 projects spin-independent WIMP-nucleon cross section.

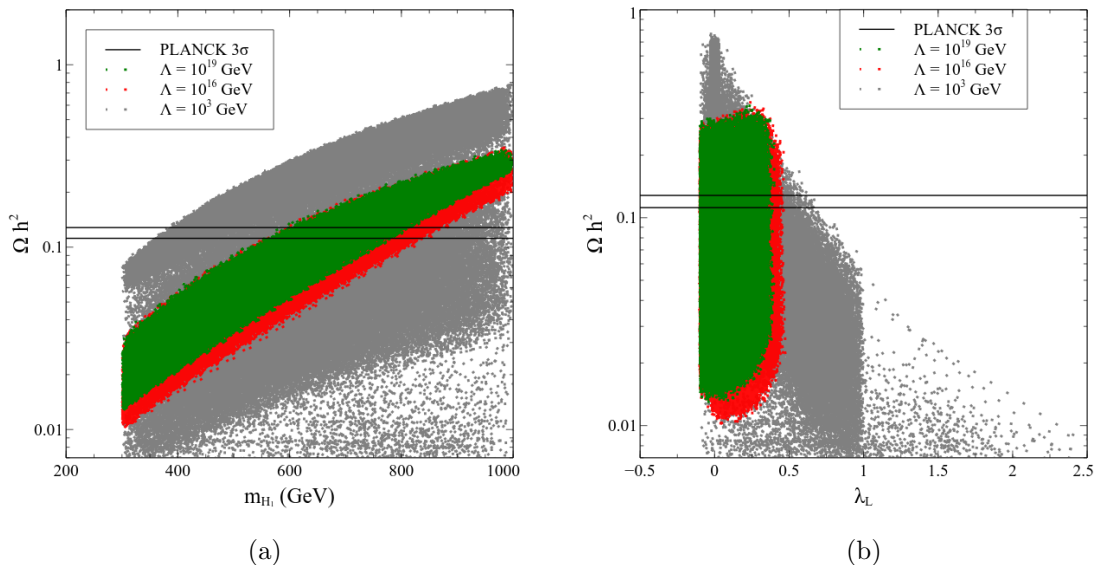


Figure 8.6: The dark matter relic density versus m_{H_1} (left) and the coupling of H_1 pair to the Higgs boson λ_L (right). The grey, green and red points preserve validity up to 1TeV, the GUT scale 10^{16} GeV and the Planck scale 10^{19} GeV respectively. The horizontal black lines denote the 3σ limits of the PLANCK data. .

An inspection of Fig.8.6 and Fig.8.7 points out that one can render the S_3 HDM stable up to GUT and Planck scales with initial conditions consistent with the constraints of relic density and direct detection. We highlight this fact as the most important conclusion in this

part. This, however happens only if $m_{H_1} > 580$ GeV. This result be understood as follows. The evolution of λ_8 and hence vacuum stability is crucially dictated by the values of λ_5 , λ_6 and λ_7 at the initial scale. They can be expressed in terms of the masses as

$$\lambda_5 = \lambda_L + \frac{2}{v^2}(m_{H_1^+}^2 - m_{H_1}^2), \quad (8.4.5)$$

$$\lambda_6 = \frac{1}{v^2}(m_{H_1}^2 + m_{A_1}^2 - 2m_{H_1^+}^2), \quad (8.4.6)$$

$$\lambda_7 = \frac{1}{2v^2}(m_{H_1}^2 - m_{A_1}^2). \quad (8.4.7)$$

We find that for an H_1 below 580 GeV, λ_5 , λ_6 and λ_7 are not sizeable enough to ensure $\lambda_8(Q) > 0$ up to the GUT scale. On the other hand, perturbative unitarity restricts the mass splitting to ~ 50 GeV which is automatically consistent with the T parameter constraint. While the stability condition $\lambda_5 + 2\sqrt{\lambda_8(\lambda_1 + \lambda_3)} > 0$ disfavors large negative values of λ_5 , tight upper bounds are imposed by perturbative unitarity. This translates into $-0.1 < \lambda_L < 0.4$ for a model valid up to M_{Pl} (see Fig.8.6).

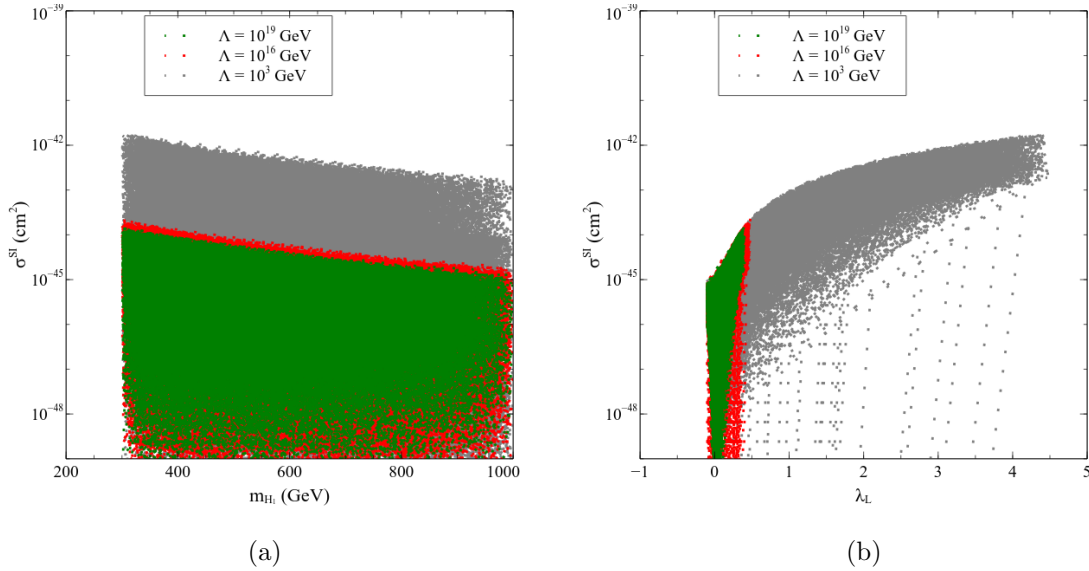


Figure 8.7: Spin-independent WIMP-nucleon scattering cross section vs m_{H_1} (left) and the coupling of H_1 pair to the Higgs boson λ_L (right). The grey, green and red points preserve validity up to 1 TeV, the GUT scale 10^{16} GeV and the Planck scale 10^{19} GeV respectively. Note that a large proportion of model points do obey the LUX upper bound while fulfilling stability requirements.

For a more comprehensive understanding, the parameter space negotiating all the im-

posed constraints successfully is displayed as correlation plots in Fig.8.8. Our demand of $\sigma^{\text{SI}} < 10^{-46} \text{ cm}^2$ throughout in Fig.8.8 automatically complies with the LUX results. The DM masses are strongly restricted by the requirements of DM searches, and high-scale validity till a given Λ . For instance we note $m_{H_1} \in [550 \text{ GeV}, 830 \text{ GeV}]$ and $[550 \text{ GeV}, 750 \text{ GeV}]$ for $\Lambda = M_{\text{GUT}}$ and $\Lambda = M_{\text{Pl}}$ respectively (see Fig.8.8).

A situation, where $\mu_{\gamma\gamma} < 1$ (Fig.8.9) for most part of the parameter space is attributed to a mostly non-negative λ_5 (or a very small negative value). With $\lambda_1 = \lambda_3 = 0.01$ at the input scale, λ_5 gets bounded from below at $\simeq -0.1$ by the vacuum stability condition $\lambda_5 > -2\sqrt{\lambda_8(\lambda_1 + \lambda_3)}$. One can get a deeper lower bound, and hence a $\mu_{\gamma\gamma}$ substantially larger than unity for larger values of λ_1 and λ_3 , but in that case one does not have a perturbative theory till 10^{19} GeV . Very low values of $\mu_{\gamma\gamma}$ seen in Fig.8.9 are possible for points valid only up to the TeV scale, where a positive λ_5 as large as ~ 6.5 is allowed without causing a breakdown of perturbativity below 1 TeV. Parameter points valid till the GUT and Planck scales rarely correspond to a diphoton signal strength less than 0.87. This indeed is within the 2σ limit from both the ATLAS and CMS central values. This very observation that validity till very high scales always predicts a depletion in the diphoton rate, but the rate can still be kept within the experimental bounds emerges as an important consequence in this regard. The diphoton rate thus bears fingerprints of an extended Higgs sector such as the $S_3\text{HDM}$, whose tree level couplings could mimic the corresponding SM ones. This calls for its accurate measurements in 13 TeV LHC for instance, or at the other upcoming colliders.

To sum up, DM phenomenology plays a vital role in deciding the fate of this scenario at high scales. The interplay of various effects involved is captured through the benchmarks in Table 8.4. The RG running of these benchmarks is shown in Fig.8.10. The first benchmark BP4 can possibly describe physics nearly up to the GUT scale, beyond which perturbativity breaks down. However, BP4 predicts a relic density below the observed limit. This is attributed to the relatively large mass splittings amongst the S_3 scalars, which generate such sizeable λ_5 , λ_6 and λ_7 at the initial scale that can ensure $\lambda_8(Q) > 0$ throughout. However we pay the price of a diminished coannihilation, and thereby a relic density below the desired range. A fall out of this relatively large λ_5 in this case is a suppressed $\mu_{\gamma\gamma}$. BP5 highlights the fact that correct relic density and direct detection rates are achievable in this model for a DM around 390 GeV, a feature not observed in the model with a single inert doublet. The maximal mass difference in such a case is restricted to $\sim 13 \text{ GeV}$. However, BP5 does not keep the EW vacuum stable beyond 10^8 GeV .

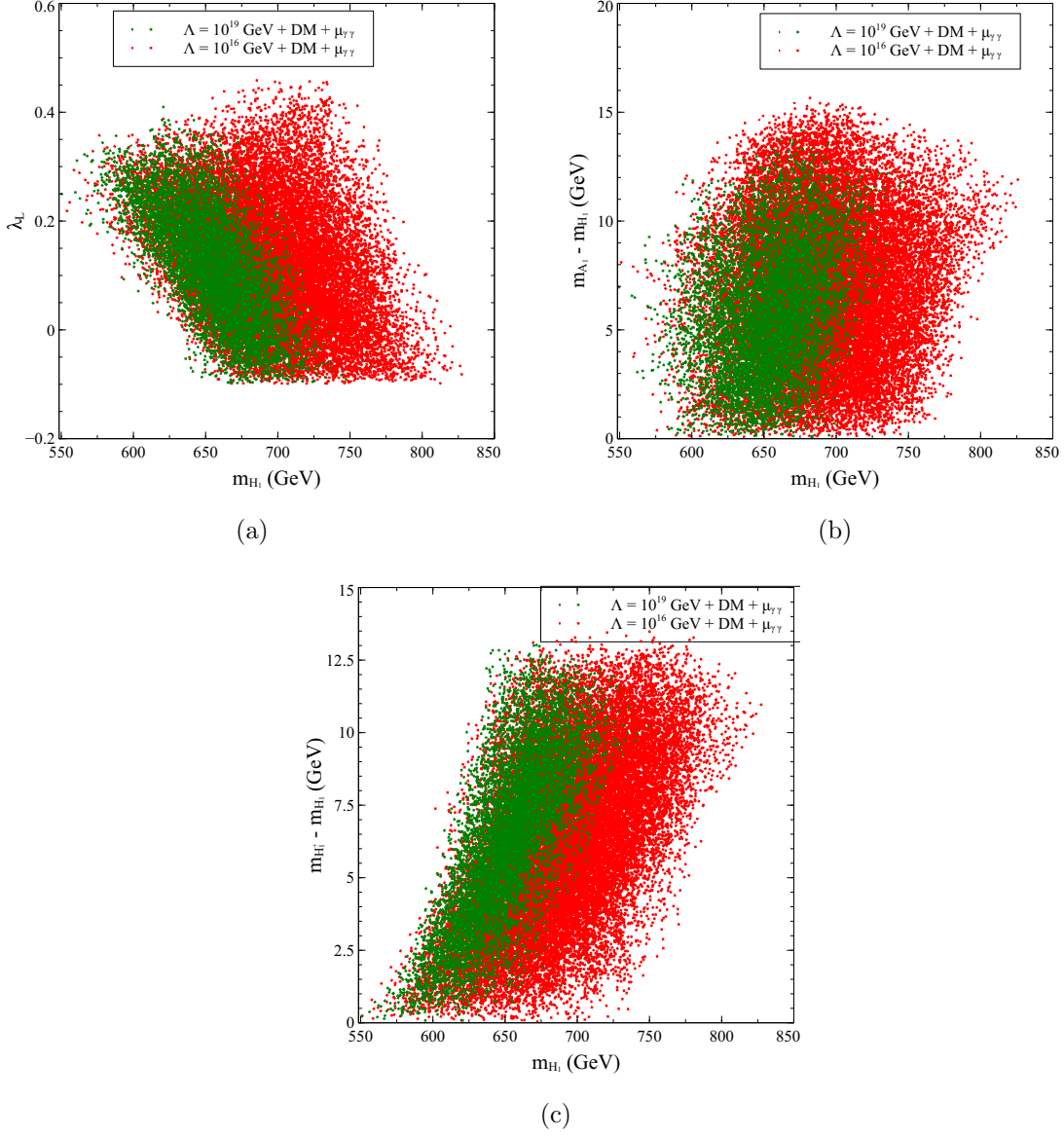
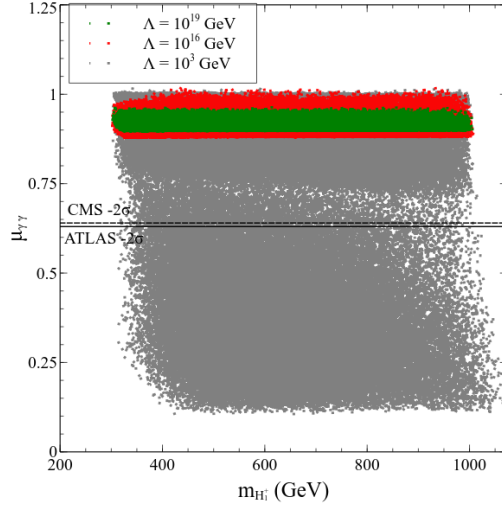


Figure 8.8: The viable S_3 HDM parameter space projected on the λ_L vs m_{H_1} (top left), $m_{A_1} - m_{H_1}$ vs m_{H_1} (top right), $m_{H_1^+} - m_{H_1}$ vs m_{H_1} (bottom) planes. " $\Lambda + \text{DM} + \mu_{\gamma\gamma}$ " in the legends refers to validity up to Λ as well as consistency with DM searches and diphoton signal strength. The green and red points correspond to $\Lambda = 10^{16}$ GeV and $\Lambda = 10^{19}$ GeV respectively.

BP6 and BP7 are conservative choices which predict relic density and direct detection rates in the correct ballpark, and also extrapolate the model to the GUT and Planck scales



(a)

Figure 8.9: Distribution of parameter points valid till 10^3 GeV (grey), 10^{16} (red) GeV and 10^{19} (green) GeV in the $\mu_{\gamma\gamma}$ vs $m_{H_1^+}$ plane. The solid and dotted lines denote the 2σ limits below the central value given by ATLAS and CMS respectively .

respectively. We note here that in BP4, BP6 and BP7, vsc1, vsc3, vsc4, vsc5, vsc6, vsc7 rise with Q , whereas in BP5, vsc5 and vsc6 go down. This observation has its root in the structure of the S_3 HDM beta functions (see Appendix C.1), which mostly guarantee vsc1, vsc3, vsc4, vsc5, vsc6, vsc7 > 0 throughout the evolution once they start with positive values at the EW scale. We remark here that BP6 and BP7 correspond to $\mu_{\gamma\gamma} = 0.935$ and 0.911 respectively, which are within the 2σ limit from the central value.

In the same connection, we have found that an $m_{H_1} > 1$ TeV can render the EW vacuum stable at least up to the SM instability scale. However that pushes μ_{11} to yet higher values, thereby introducing a so-called *intermediate* scale into the picture. It is then implied that the S_3 scalars are practically decoupled below μ_{11} , and that it would be more appropriate to solve the RG equations in a piecewise fashion, i.e., evolve from the EW scale to μ_{11} using the SM beta functions only, and then invoke S_3 HDM above the μ_{11} threshold. However we mostly encounter $\mu_{11} \lesssim 600$ GeV for S_3 masses < 1 TeV. We have checked that for such a μ_{11} , a piecewise evolution practically gives the same numerical results.

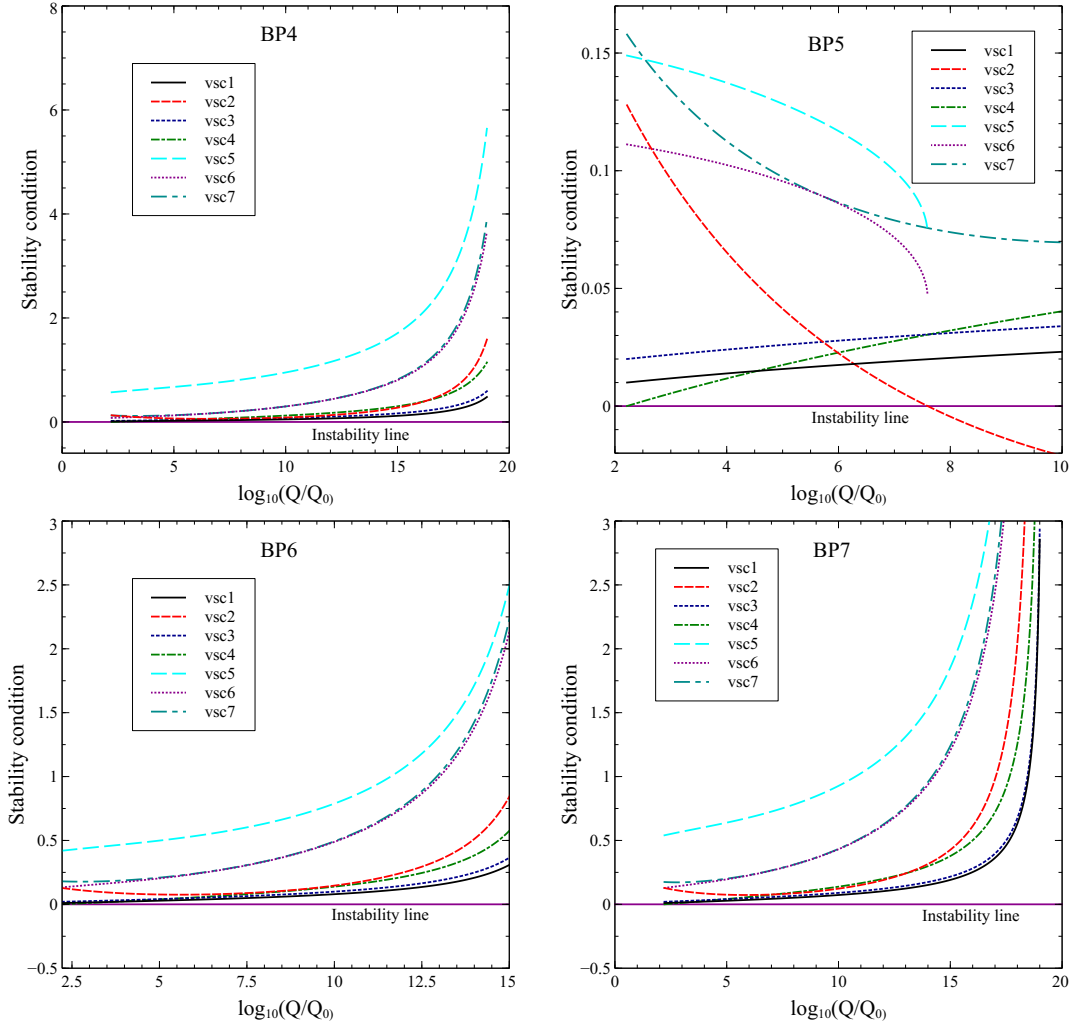


Figure 8.10: RG Evolution of BP4, BP5, BP6 and BP7. Colour coding is explained in the legends and the vacuum instability line is highlighted. Note that vsc5 and vsc6 are not defined whenever $\lambda_8 < 0$.

Benchmark	m_{H_1} (GeV)	m_{A_1} (GeV)	$m_{H_1^+}$ (GeV)	λ_L	Ωh^2	$\sigma^{SI}(cm^2)$	Λ (GeV)
BP4	479.200	480.475	494.525	-0.0236	0.0635	2.13×10^{-47}	10^{19}
BP5	390.000	391.000	392.000	0.0050	0.1200	1.44×10^{-48}	10^8
BP6	707.400	720.000	713.500	0.032	0.1214	1.80×10^{-47}	Just below 10^{16}
BP7	718.600	727.450	727.225	0.0268	0.1263	1.22×10^{-47}	10^{19}

Table 8.4: Benchmark points chosen to illustrate the behaviour under RGE. Λ denotes the maximum extrapolation scale up to which vacuum stability and perturbativity are ensured.

8.5 Conclusions and future work

3HDMs offer a rich scalar spectrum and can give rise to prominent signatures at the colliders [354, 355]. In this chapter, we have tried to investigate an S_3 -symmetric Higgs sector in the light of various theoretical as well as experimental constraints. Robust regimes of the model parameter space were surveyed using the latest data on the 125 GeV Higgs and oblique parameters. The high-scale behaviour was probed by evolving the model couplings under the RGEs, and this study in this chapter appears to be the first attempt in that direction in context of 3HDMs. A unitary and perturbative theory, along with a stable EW vacuum was ensured at each step of evolution. We have illustrated our findings in context of two specific alignment of the doublet VEVs. The salient features of the numerical results that emerge are highlighted below.

- In the first case, non-zero VEVs are assigned to all three of the doublets while maintaining $v_1 = \sqrt{3}v_2$. It is found that this scenario is not stable beyond 10^7 GeV, an effect brought about by an interplay of perturbative unitarity and vacuum stability. Stringent upper bounds are placed on the scalar masses and $\tan\beta$ in this case. In particular we note $\tan\beta < 1.3$ and the S_3 scalar masses lie below 270 GeV for $\Lambda = 10^6$ GeV, the maximum phenomenologically accepted scale.
- The second case is a scenario with two inert doublets. There lies an identifiable region in the parameter space in this case that extends validity of the model till the Planck scale. Moreover, this parameter space is robust enough to accommodate a successful candidate for dark matter. High-scale stability in this case manifests itself by placing upper bounds on the coupling of the DM to the 125 GeV Higgs, the DM mass, as well on the mass splitting amongst the inert scalars. The bounds get sharper when both the DM as well as high-scale stability constraints are imposed simultaneously. In a

word, a connection emerges between DM phenomenology at the *low* scale and a good UV behaviour at *high* scales. This finding is qualitatively similar to the model with a single inert doublet [312]. However, the addition of the extra inert doublet narrows down the gap between the *low* and *high* DM mass regions, with respect to what is observed in the single inert doublet case.

- Scenario B predicts a *decrement* in the diphoton decay width with respect to the SM value, so does Scenario A for an exact alignment. This particular feature of Scenario B is not seen by considering tree-level stability constraints alone and is an explicit consequence of renormalisation group evolution. The numerical predictions however can be made to lie within the current experimental limits without running into conflict with high-scale stability.

Altogether then, we conclude that the inert scenario fares much better than the non-inert one in terms of high-scale validity and signal strength measurements. It is thus safe to comment that the S_3 HDM can certainly alleviate the vacuum stability problem, however not for all permissible VEV-structures. Several extensions of the present study are possible. One could analyse a more general S_3 -symmetric Yukawa texture in a similar context, admittedly though such texture would give rise to Flavour-Changing Neutral Currents (FCNC) [365] at the tree level. It was shown in [378] that raising the S_3 masses to ~ 10 TeV suppresses the possible FCNCs. The requirement of such heavy scalars necessitates the inclusion of S_3 violating quadratic terms [357]. Another motivation of a broken S_3 symmetry is in the context of DM. In scenario B for instance, it will lead to a non-degenerate spectrum and hence a modified DM phenomenology, at least at the quantitative level. Indirect detection signatures of such a DM scenario could be of special importance in light of latest data. Adding further to it, the large number of bosonic degrees of freedom offered by the S_3 HDM could favour a *strong* first order electroweak phase transition, thereby making way for baryogenesis, something already looked at for a more generic 3HDM with two inert doublets. [379].

Chapter 9

Summary and conclusions

In the following, we summarise the work done in this thesis and highlight its major findings.

Chapter 1 contains an introduction to the SM and a brief discussion on its shortcomings. The fate of the electroweak vacuum in the SM is discussed in **Chapter 2**. In the same chapter, we have also discussed the possibility of stabilising the vacuum till the Planck scale by extending the SM Higgs sector.

In **Chapter 3**, we have considered the conditions for the validity of a Type-II two-Higgs doublet model up to high energy scales, together with all other low- and high-energy constraints. The constraints on the parameter space at low energy, including the measured value of the Higgs mass and the signal strengths in channels were juxtaposed with the conditions of vacuum stability, perturbativity and unitarity at various scales. We found that a scenario with an exact \mathbb{Z}_2 symmetry in the potential does not remain valid beyond $\simeq 10$ TeV without the intervention of additional physics. Whereas for a broken \mathbb{Z}_2 symmetry, the theory can be valid even up to the Planck scale without any new physics coming in. Most importantly, high-scale validity remains intact in spite of an uncertainty in the top quark mass as well as in $\alpha_s(M_Z)$, in contrast to the SM. It was also shown that the presence of a CP -violating phase is allowed when the \mathbb{Z}_2 symmetry is relaxed. The allowed regions in the parameter space were presented for each case.

Complementing the study in **Chapter 3**, we have made an attempt to identify regions in a Type-II two-Higgs Doublet Model, which correspond to a metastable electroweak vacuum, in **Chapter 4**. We analyse scenarios which retain perturbative unitarity up to Grand unification and Planck scales. Substantial regions of the parameter space were thus identified as corresponding to metastability, for top quark mass at the high as well as low end of its currently allowed range. It has been concluded that although the Type-II Two-Higgs

Doublet Model can stabilise the electroweak vacuum till the Planck scale, for an appropriate tuning of the parameter points, a metastable vacuum too is a possibility.

In **Chapter 5**, we investigate the collider signals of a Type-I and Type-II 2HDMs that allow for a stable vacuum till the Planck scale. In particular, the near degeneracy of the neutral heavy scalar and the pseudoscalar is a feature that was probed. It is revealed from the investigation that the LHC allows distinguishability of these two states, together with signal significance of at least 3σ , in its high-luminosity run. While e^+e^- colliders may have rather low event rates, muon colliders, cashing on the principle of radiative return, can probe 2HDM scenarios with (pseudo)scalar masses up to a TeV or so, though with the price of losing distinction between the CP -even and odd states.

Chapter 6 presents an introduction to various aspects of particle dark matter. In **Chapter 7**, a two-Higgs doublet scenario containing three $SU(2)_L$ singlet heavy neutrinos with Majorana masses is considered. While making the heavy neutrinos and one of the two scalar doublets odd under \mathbb{Z}_2 , this model not only generates Majorana masses for the light neutrinos radiatively, but also makes the lighter of the neutral \mathbb{Z}_2 -odd scalars an eligible dark matter candidate. Taking two representative values of a common mass scale of the heavy neutrinos, we identified the allowed regions of the parameter space of the model, which are consistent with all dark matter constraints, and, also with a stable vacuum and a perturbative theory till the Planck scale. Moreover, a part of the corresponding parameter space was observed to yield the correct signal strength in the diphoton channel for the scalar observed at the LHC.

Similar to what was done in **Chapter 3** and **Chapter 7**, we have studied high scale vacuum stability and perturbative unitarity in context of a model with three-Higgs doublets (3HDM) in **Chapter 8**. In particular, we have chosen a 3HDM endowed with a global S_3 symmetry. We took two viable alignments of vacuum expectation values (VEV) in our study. All three doublets receive non-zero vacuum expectation values in the first case, and in the second case, two of the doublets remain without VEV. The constraints on the parameter space at low energy, including the measured value of the Higgs mass and the signal strengths, oblique corrections and also measurements of relic density and direct detection rates were juxtaposed with the conditions of vacuum stability, perturbativity and unitarity at various scales. It was found that the scenario with three non-zero VEVs becomes non-perturbative beyond 10^7 GeV. On the contrary, the scenario with only one non-zero VEV turns out to be a successful model for cold dark matter phenomenology, and, valid up to the Planck scale at the same time. Stringent restrictions are obtained on the model parameter space in each

case. Thus, the S_3 symmetric scalar sector is deemed to be "ultraviolet-complete" through this study.

Appendices

Appendix A

Type-I and Type-II 2HDM

A.1 Renormalisation group (RG) equations for Type-II 2HDM

The RG equations for the gauge couplings, for this model, are given by [28],

$$16\pi^2 \frac{dg_3}{dt} = -7g_3^3, \quad (\text{A.1.1a})$$

$$16\pi^2 \frac{dg_2}{dt} = -3g_2^3, \quad (\text{A.1.1b})$$

$$16\pi^2 \frac{dg_1}{dt} = 7g_1^3. \quad (\text{A.1.1c})$$

Since we want to avoid CP -violation coming from the quartic sector of the Higgs potential, we choose to keep λ_i ($i = 1, \dots, 7$) real. In that case, the quartic couplings evolve according to,

$$16\pi^2 \frac{d\lambda_1}{dt} = 12\lambda_1^2 + 4\lambda_3^2 + 4\lambda_3\lambda_4 + 2\lambda_4^2 + 2\lambda_5^2 + 24\lambda_6^2 + \frac{3}{4}(3g_2^4 + g_1^4 + 2g_2^2g_1^2) - \lambda_1(9g_2^2 + 3g_1^2 - 12y_b^2 - 4y_\tau^2) - 12y_b^4 - 4y_\tau^4, \quad (\text{A.1.2a})$$

$$16\pi^2 \frac{d\lambda_2}{dt} = 12\lambda_2^2 + 4\lambda_3^2 + 4\lambda_3\lambda_4 + 2\lambda_4^2 + 2\lambda_5^2 + 24\lambda_7^2 + \frac{3}{4}(3g_2^4 + g_1^4 + 2g_2^2g_1^2) - 3\lambda_2(3g_2^2 + g_1^2 - 4y_t^2) - 12y_t^4, \quad (\text{A.1.2b})$$

$$16\pi^2 \frac{d\lambda_3}{dt} = (\lambda_1 + \lambda_2)(6\lambda_3 + 2\lambda_4) + 4\lambda_3^2 + 2\lambda_4^2 + 2\lambda_5^2 + 4(\lambda_6^2 + \lambda_7^2) + 16(\lambda_6\lambda_7) + \frac{3}{4}(3g_2^4 + g_1^4 - 2g_2^2g_1^2) - \lambda_3(9g_2^2 + 3g_1^2 - 6y_t^2 - 6y_b^2 - 2y_\tau^2) - 12y_t^2y_b^2, \quad (\text{A.1.2c})$$

$$16\pi^2 \frac{d\lambda_4}{dt} = 2(\lambda_1 + \lambda_2)\lambda_4 + 8\lambda_3\lambda_4 + 4\lambda_4^2 + 8\lambda_5^2 + 10(\lambda_6^2 + \lambda_7^2) + 4(\lambda_6\lambda_7) + 3g_2^2g_1^2 - \lambda_4(9g_2^2 + 3g_1^2 - 6y_t^2 - 6y_b^2 - 2y_\tau^2) + 12y_t^2y_b^2, \quad (\text{A.1.2d})$$

$$16\pi^2 \frac{d\lambda_5}{dt} = (2\lambda_1 + 2\lambda_2 + 8\lambda_3 + 12\lambda_4)\lambda_5 + 10(\lambda_6^2 + \lambda_7^2) + 4\lambda_6\lambda_7 - \lambda_5(9g_2^2 + 3g_1^2 - 6y_t^2 - 6y_b^2 - 2y_\tau^2), \quad (\text{A.1.2e})$$

$$16\pi^2 \frac{d\lambda_6}{dt} = (12\lambda_1 + 6\lambda_3 + 8\lambda_4)\lambda_6 + (6\lambda_3 + 4\lambda_4)\lambda_7 + 10\lambda_5\lambda_6 + 2\lambda_5\lambda_7 - \lambda_6(9g_2^2 + 3g_1^2 - 9y_b^2 - 3y_t^2 - 3y_\tau^2), \quad (\text{A.1.2f})$$

$$16\pi^2 \frac{d\lambda_7}{dt} = (12\lambda_2 + 6\lambda_3 + 8\lambda_4)\lambda_7 + (6\lambda_3 + 4\lambda_4)\lambda_6 + 10\lambda_5\lambda_7 + 2\lambda_5\lambda_6 - \lambda_7(9g_2^2 + 3g_1^2 - 9y_t^2 - 3y_b^2 - y_\tau^2). \quad (\text{A.1.2g})$$

For the Yukawa couplings the corresponding set of RG equations are,

$$16\pi^2 \frac{dy_b}{dt} = y_b \left(-8g_3^2 - \frac{9}{4}g_2^2 - \frac{5}{12}g_1^2 + \frac{9}{2}y_b^2 + y_\tau^2 + \frac{1}{2}y_t^2 \right), \quad (\text{A.1.3a})$$

$$16\pi^2 \frac{dy_t}{dt} = y_t \left(-8g_3^2 - \frac{9}{4}g_2^2 - \frac{17}{12}g_1^2 + \frac{9}{2}y_t^2 + \frac{1}{2}y_b^2 \right), \quad (\text{A.1.3b})$$

$$16\pi^2 \frac{dy_\tau}{dt} = y_\tau \left(-\frac{9}{4}g_2^2 - \frac{15}{4}g_1^2 + 3y_b^2 + \frac{5}{2}y_\tau^2 \right). \quad (\text{A.1.3c})$$

A.2 Renormalisation group (RG) equations for Type-I 2HDM

The beta functions for the gauge in this case are the same as Type-II. The ones for the quartic couplings are

$$16\pi^2 \frac{d\lambda_1}{dt} = 12\lambda_1^2 + 4\lambda_3^2 + 4\lambda_3\lambda_4 + 2\lambda_4^2 + 2\lambda_5^2 + 24\lambda_6^2 + \frac{3}{4}(3g_2^4 + g_1^4 + 2g_2^2g_1^2) - \lambda_1(9g_2^2 + 3g_1^2), \quad (\text{A.2.1a})$$

$$16\pi^2 \frac{d\lambda_2}{dt} = 12\lambda_2^2 + 4\lambda_3^2 + 4\lambda_3\lambda_4 + 2\lambda_4^2 + 2\lambda_5^2 + 24\lambda_7^2 + \frac{3}{4}(3g_2^4 + g_1^4 + 2g_2^2g_1^2) - 3\lambda_2(3g_2^2 + g_1^2 - 4y_t^2 - 4y_b^2 - y_\tau^2) - 12y_t^4 - 12y_b^4 - 4y_\tau^4, \quad (\text{A.2.1b})$$

$$16\pi^2 \frac{d\lambda_3}{dt} = (\lambda_1 + \lambda_2)(6\lambda_3 + 2\lambda_4) + 4\lambda_3^2 + 2\lambda_4^2 + 2\lambda_5^2 + 4(\lambda_6^2 + \lambda_7^2) + 16(\lambda_6\lambda_7) + \frac{3}{4}(3g_2^4 + g_1^4 - 2g_2^2g_1^2) - \lambda_3(9g_2^2 + 3g_1^2 - 6y_t^2 - 6y_b^2 - 2y_\tau^2) - 12y_t^2y_b^2, \quad (\text{A.2.1c})$$

$$16\pi^2 \frac{d\lambda_4}{dt} = 2(\lambda_1 + \lambda_2)\lambda_4 + 8\lambda_3\lambda_4 + 4\lambda_4^2 + 8\lambda_5^2 + 10(\lambda_6^2 + \lambda_7^2) + 4(\lambda_6\lambda_7) + 3g_2^2g_1^2 - \lambda_4(9g_2^2 + 3g_1^2 - 6y_t^2 - 6y_b^2 - 2y_\tau^2) + 12y_t^2y_b^2, \quad (\text{A.2.1d})$$

$$16\pi^2 \frac{d\lambda_5}{dt} = (2\lambda_1 + 2\lambda_2 + 8\lambda_3 + 12\lambda_4)\lambda_5 + 10(\lambda_6^2 + \lambda_7^2) + 4\lambda_6\lambda_7 - \lambda_5(9g_2^2 + 3g_1^2 - 6y_t^2 - 6y_b^2 - 2y_\tau^2), \quad (\text{A.2.1e})$$

$$16\pi^2 \frac{d\lambda_6}{dt} = (12\lambda_1 + 6\lambda_3 + 8\lambda_4)\lambda_6 + (6\lambda_3 + 4\lambda_4)\lambda_7 + 10\lambda_5\lambda_6 + 2\lambda_5\lambda_7 - \lambda_6(9g_2^2 + 3g_1^2 - 3y_b^2 - 3y_t^2 - y_\tau^2), \quad (\text{A.2.1f})$$

$$16\pi^2 \frac{d\lambda_7}{dt} = (12\lambda_2 + 6\lambda_3 + 8\lambda_4)\lambda_7 + (6\lambda_3 + 4\lambda_4)\lambda_6 + 10\lambda_5\lambda_7 + 2\lambda_5\lambda_6 - \lambda_7(9g_2^2 + 3g_1^2 - 9y_t^2 - 9y_b^2 - 3y_\tau^2). \quad (\text{A.2.1g})$$

The ones for the Yukawa couplings are,

$$16\pi^2 \frac{dy_b}{dt} = y_b \left(-8g_3^2 - \frac{9}{4}g_2^2 - \frac{5}{12}g_1^2 + \frac{9}{2}y_b^2 + y_\tau^2 + \frac{3}{2}y_t^2 \right), \quad (\text{A.2.2a})$$

$$16\pi^2 \frac{dy_t}{dt} = y_t \left(-8g_3^2 - \frac{9}{4}g_2^2 - \frac{17}{12}g_1^2 + \frac{9}{2}y_t^2 + \frac{3}{2}y_b^2 + y_\tau^2 \right), \quad (\text{A.2.2b})$$

$$16\pi^2 \frac{dy_\tau}{dt} = y_\tau \left(-\frac{9}{4}g_2^2 - \frac{15}{4}g_1^2 + 3y_b^2 + 3y_t^2 + \frac{5}{2}y_\tau^2 \right). \quad (\text{A.2.2c})$$

A.3 Unitarity bounds

We perform a coupled channel analysis of $2 \rightarrow 2$ scattering involving fields in the scalar sector, to the leading order. The basis of neutral two-particle states is given by,

$$\left\{ w_1^+ w_2^-, w_2^+ w_1^-, h_1 z_2, h_2 z_1, z_1 z_2, h_1 h_2, h_1 z_1, h_2 z_2, w_1^+ w_1^-, w_2^+ w_2^-, \frac{z_1 z_1}{\sqrt{2}}, \frac{z_2 z_2}{\sqrt{2}}, \frac{h_1 h_1}{\sqrt{2}}, \frac{h_2 h_2}{\sqrt{2}} \right\} \quad (\text{A.3.1})$$

For the general $\lambda_6, \lambda_7 \neq 0$ case, the (14×14) two-particle scattering matrix is given as follows:

$$\mathcal{M}_{NC} = \begin{pmatrix} \mathcal{A}_{7 \times 7} & \mathcal{B}_{7 \times 7} \\ \mathcal{B}_{7 \times 7}^\dagger & \mathcal{C}_{7 \times 7} \end{pmatrix}, \quad (\text{A.3.2})$$

where \mathcal{A} , \mathcal{B} and \mathcal{C} are given by,

$$\mathcal{A}_{7 \times 7} = \begin{pmatrix} \lambda_3 + \lambda_4 & 2\lambda_5 & \frac{i}{2}(\lambda_4 - \lambda_5) & \frac{i}{2}(-\lambda_4 + \lambda_5) & \frac{1}{2}(\lambda_4 + \lambda_5) & \frac{1}{2}(\lambda_4 + \lambda_5) & 0 \\ 2\lambda_5 & \lambda_3 + \lambda_4 & \frac{i}{2}(-\lambda_4 + \lambda_5) & \frac{i}{2}(\lambda_4 - \lambda_5) & \frac{1}{2}(\lambda_4 + \lambda_5) & \frac{1}{2}(\lambda_4 + \lambda_5) & 0 \\ \frac{i}{2}(-\lambda_4 + \lambda_5) & \frac{i}{2}(\lambda_4 - \lambda_5) & (\lambda_3 + \lambda_4 - \lambda_5) & \lambda_5 & 0 & 0 & \lambda_6 \\ \frac{i}{2}(\lambda_4 - \lambda_5) & \frac{i}{2}(-\lambda_4 + \lambda_5) & \lambda_5 & (\lambda_3 + \lambda_4 - \lambda_5) & 0 & 0 & \lambda_6 \\ \frac{1}{2}(\lambda_4 + \lambda_5) & \frac{1}{2}(\lambda_4 + \lambda_5) & 0 & 0 & (\lambda_3 + \lambda_4 + \lambda_5) & \lambda_5 & 0 \\ \frac{1}{2}(\lambda_4 + \lambda_5) & \frac{1}{2}(\lambda_4 + \lambda_5) & 0 & 0 & \lambda_5 & (\lambda_3 + \lambda_4 + \lambda_5) & 0 \\ 0 & 0 & \lambda_6 & \lambda_6 & 0 & 0 & \lambda_1 \end{pmatrix},$$

$$\mathcal{B}_{7 \times 7} = \begin{pmatrix} 0 & 2\lambda_6 & 2\lambda_7 & \frac{\lambda_6}{\sqrt{2}} & \frac{\lambda_7}{\sqrt{2}} & \frac{\lambda_6}{\sqrt{2}} & \frac{\lambda_7}{\sqrt{2}} \\ 0 & 2\lambda_6 & 2\lambda_7 & \frac{\lambda_6}{\sqrt{2}} & \frac{\lambda_7}{\sqrt{2}} & \frac{\lambda_6}{\sqrt{2}} & \frac{\lambda_7}{\sqrt{2}} \\ \lambda_7 & 0 & 0 & 0 & 0 & 0 & 0 \\ \lambda_7 & 0 & 0 & 0 & 0 & 0 & 0 \\ 0 & \lambda_6 & \lambda_7 & \frac{3\lambda_6}{\sqrt{2}} & \frac{3\lambda_7}{\sqrt{2}} & \frac{\lambda_6}{\sqrt{2}} & \frac{\lambda_7}{\sqrt{2}} \\ 0 & \lambda_6 & \lambda_7 & \frac{\lambda_6}{\sqrt{2}} & \frac{\lambda_7}{\sqrt{2}} & \frac{3\lambda_6}{\sqrt{2}} & \frac{3\lambda_7}{\sqrt{2}} \\ \lambda_5 & 0 & 0 & 0 & 0 & 0 & 0 \end{pmatrix},$$

$$\mathcal{C}_{7 \times 7} = \begin{pmatrix} \lambda_2 & 0 & 0 & 0 & 0 & 0 & 0 \\ 0 & 2\lambda_1 & (\lambda_3 + \lambda_4) & \frac{\lambda_1}{\sqrt{2}} & \frac{\lambda_3}{\sqrt{2}} & \frac{\lambda_1}{\sqrt{2}} & \frac{\lambda_3}{\sqrt{2}} \\ 0 & (\lambda_3 + \lambda_4) & 2\lambda_2 & \frac{\lambda_3}{\sqrt{2}} & \frac{\lambda_2}{\sqrt{2}} & \frac{\lambda_3}{\sqrt{2}} & \frac{\lambda_2}{\sqrt{2}} \\ 0 & \frac{\lambda_1}{\sqrt{2}} & \frac{\lambda_3}{\sqrt{2}} & \frac{3\lambda_1}{2} & \frac{1}{2}(\lambda_3 + \lambda_4 + \lambda_5) & \frac{\lambda_1}{2} & \frac{1}{2}(\lambda_3 + \lambda_4 - \lambda_5) \\ 0 & \frac{\lambda_3}{\sqrt{2}} & \frac{\lambda_2}{\sqrt{2}} & \frac{1}{2}(\lambda_3 + \lambda_4 + \lambda_5) & \frac{3\lambda_2}{2} & \frac{1}{2}(\lambda_3 + \lambda_4 - \lambda_5) & \frac{\lambda_2}{2} \\ 0 & \frac{\lambda_1}{\sqrt{2}} & \frac{\lambda_3}{\sqrt{2}} & \frac{\lambda_1}{2} & \frac{1}{2}(\lambda_3 + \lambda_4 - \lambda_5) & \frac{3\lambda_1}{2} & \frac{1}{2}(\lambda_3 + \lambda_4 + \lambda_5) \\ 0 & \frac{\lambda_3}{\sqrt{2}} & \frac{\lambda_2}{\sqrt{2}} & \frac{1}{2}(\lambda_3 + \lambda_4 - \lambda_5) & \frac{\lambda_2}{2} & \frac{1}{2}(\lambda_3 + \lambda_4 + \lambda_5) & \frac{3\lambda_2}{2} \end{pmatrix}.$$

The constraint imposed by unitarity is then given by $|a_i| \leq 8\pi$, where a_i ($i = 1, \dots, 14$) are eigenvalues of the matrix \mathcal{M} . The eigenvalues of \mathcal{M} are evaluated numerically in the present study. However, in the absence of *hard* \mathbb{Z}_2 breaking, i.e., when $\lambda_6, \lambda_7 = 0$, the matrix decomposes into blocks and analytical expressions for its eigenvalues can be obtained in simple forms which are listed below.

$$a_{\pm} = \frac{3}{2}(\lambda_1 + \lambda_2) \pm \sqrt{\frac{9}{4}(\lambda_1 - \lambda_2)^2 + (2\lambda_3 + \lambda_4)^2}, \quad (\text{A.3.3a})$$

$$b_{\pm} = \frac{1}{2}(\lambda_1 + \lambda_2) \pm \sqrt{\frac{1}{4}(\lambda_1 - \lambda_2)^2 + \lambda_4^2}, \quad (\text{A.3.3b})$$

$$c_{\pm} = d_{\pm} = \frac{1}{2}(\lambda_1 + \lambda_2) \pm \sqrt{\frac{1}{4}(\lambda_1 - \lambda_2)^2 + \lambda_5^2}, \quad (\text{A.3.3c})$$

$$e_1 = (\lambda_3 + 2\lambda_4 - 3\lambda_5), \quad (\text{A.3.3d})$$

$$e_2 = (\lambda_3 - \lambda_5), \quad (\text{A.3.3e})$$

$$f_1 = f_2 = (\lambda_3 + \lambda_4), \quad (\text{A.3.3f})$$

$$f_+ = (\lambda_3 + 2\lambda_4 + 3\lambda_5), \quad (\text{A.3.3g})$$

$$f_- = (\lambda_3 + \lambda_5). \quad (\text{A.3.3h})$$

The matrix corresponding to the overall singly charged states,

$$\{h_1 w_1^+, h_2 w_1^+, z_1 w_1^+, z_2 w_1^+, h_1 w_2^+, h_2 w_2^+, z_1 w_2^+, z_2 w_2^+\} \quad (\text{A.3.4})$$

is given by,

$$\mathcal{M}_{CC} = \begin{pmatrix} \lambda_1 & \lambda_6 & 0 & 0 & \lambda_6 & \frac{1}{2}(\lambda_4 + \lambda_5) & 0 & \frac{i(\lambda_4 - \lambda_5)}{2} \\ \lambda_6 & \lambda_3 & 0 & 0 & \frac{\lambda_4 + \lambda_5}{2} & \lambda_7 & \frac{-i(\lambda_4 - \lambda_5)}{2} & 0 \\ 0 & 0 & \lambda_1 & \lambda_6 & 0 & \frac{-i(\lambda_4 - \lambda_5)}{2} & \lambda_6 & \frac{\lambda_4 + \lambda_5}{2} \\ 0 & 0 & \lambda_6 & \lambda_3 & \frac{i(\lambda_4 - \lambda_5)}{2} & 0 & \frac{\lambda_4 + \lambda_5}{2} & \lambda_7 \\ \lambda_6 & \frac{\lambda_4 + \lambda_5}{2} & 0 & \frac{-i(\lambda_4 - \lambda_5)}{2} & \lambda_3 & \lambda_7 & 0 & 0 \\ \frac{\lambda_4 + \lambda_5}{2} & \lambda_7 & \frac{i(\lambda_4 - \lambda_5)}{2} & 0 & \lambda_7 & \lambda_2 & 0 & 0 \\ 0 & \frac{i(\lambda_4 - \lambda_5)}{2} & \lambda_6 & \frac{\lambda_4 + \lambda_5}{2} & 0 & 0 & \lambda_3 & \lambda_7 \\ \frac{-i(\lambda_4 - \lambda_5)}{2} & 0 & \frac{\lambda_4 + \lambda_5}{2} & \lambda_7 & 0 & 0 & \lambda_7 & \lambda_2 \end{pmatrix}.$$

Again for the case $\lambda_6, \lambda_7 = 0$, the eigenvalues of \mathcal{M}_{CC} are, $b_{\pm}, c_{\pm}, e_2, f_1, f_-$ and $p = (\lambda_3 - \lambda_4)$.

Appendix B

The inert doublet model with right handed neutrinos

B.1 One-loop Renormalisation group (RG) equations

The RG equations for the gauge couplings, for this model, are given by [28],

$$16\pi^2 \frac{dg_3}{dt} = -7g_3^3, \quad (\text{B.1.1a})$$

$$16\pi^2 \frac{dg_2}{dt} = -3g_2^3, \quad (\text{B.1.1b})$$

$$16\pi^2 \frac{dg_1}{dt} = 7g_1^3. \quad (\text{B.1.1c})$$

Here g_1 , g_2 and g_3 denote the $U(1)$, $SU(2)_L$ and $SU(3)_C$ gauge couplings respectively.

The quartic couplings λ_i ($i = 1, \dots, 5$) evolve according to,

$$16\pi^2 \frac{d\lambda_1}{dt} = 12\lambda_1^2 + 4\lambda_3^2 + 4\lambda_3\lambda_4 + 2\lambda_4^2 + 2\lambda_5^2 + \frac{3}{4}(3g_2^4 + g_1^4 + 2g_2^2g_1^2) - \lambda_1(9g_2^2 + 3g_1^2 - 12y_t^2 - 12y_b^2 - 4y_\tau^2) - 12y_t^4, \quad (\text{B.1.2a})$$

$$16\pi^2 \frac{d\lambda_2}{dt} = 12\lambda_2^2 + 4\lambda_3^2 + 4\lambda_3\lambda_4 + 2\lambda_4^2 + 2\lambda_5^2 + \frac{3}{4}(3g_2^4 + g_1^4 + 2g_2^2g_1^2) - 3\lambda_2(3g_2^2 + g_1^2 - \frac{4}{3}y_\nu^2) - 4y_\nu^4, \quad (\text{B.1.2b})$$

$$16\pi^2 \frac{d\lambda_3}{dt} = (\lambda_1 + \lambda_2)(6\lambda_3 + 2\lambda_4) + 4\lambda_3^2 + 2\lambda_4^2 + 2\lambda_5^2 + \frac{3}{4}(3g_2^4 + g_1^4 - 2g_2^2g_1^2) - \lambda_3(9g_2^2 + 3g_1^2 - 6y_t^2 - 6y_b^2 - 2y_\tau^2 - 2y_\nu^2), \quad (\text{B.1.2c})$$

$$16\pi^2 \frac{d\lambda_4}{dt} = 2(\lambda_1 + \lambda_2)\lambda_4 + 8\lambda_3\lambda_4 + 4\lambda_4^2 + 8\lambda_5^2 + 3g_2^2g_1^2 - \lambda_4(9g_2^2 + 3g_1^2 - 6y_t^2 - 6y_b^2 - 2y_\tau^2 - 2y_\nu^2), \quad (\text{B.1.2d})$$

$$\begin{aligned}
16\pi^2 \frac{d\lambda_5}{dt} &= (2\lambda_1 + 2\lambda_2 + 8\lambda_3 + 12\lambda_4) \lambda_5 \\
&\quad - \lambda_5(9g_2^2 + 3g_1^2 - 6y_b^2 - 2y_\tau^2 - 6y_t^2 - 2y_\nu^2),
\end{aligned} \tag{B.1.2e}$$

For the Yukawa couplings the corresponding set of RG equations are,

$$16\pi^2 \frac{dy_b}{dt} = y_b \left(-8g_3^2 - \frac{9}{4}g_2^2 - \frac{5}{12}g_1^2 + \frac{9}{2}y_b^2 + y_\tau^2 + \frac{3}{2}y_t^2 \right), \tag{B.1.3a}$$

$$16\pi^2 \frac{dy_t}{dt} = y_t \left(-8g_3^2 - \frac{9}{4}g_2^2 - \frac{17}{12}g_1^2 + \frac{9}{2}y_t^2 + y_\tau^2 + \frac{3}{2}y_b^2 \right), \tag{B.1.3b}$$

$$16\pi^2 \frac{dy_\tau}{dt} = y_\tau \left(-\frac{9}{4}g_2^2 - \frac{15}{4}g_1^2 + 3y_b^2 + 3y_t^2 + \frac{1}{2}y_\nu^2 + \frac{5}{2}y_\tau^2 \right). \tag{B.1.3c}$$

$$16\pi^2 \frac{dy_\nu}{dt} = y_\nu \left(-\frac{9}{4}g_2^2 - \frac{3}{4}g_1^2 - \frac{3}{4}y_\tau^2 + \frac{5}{2}y_\nu^2 \right). \tag{B.1.3d}$$

Appendix C

S_3 HDM: RG equations and oblique parameters

The expressions for the one-loop beta functions and S, T, U parameters for an S_3 HDM are given below.

C.1 Renormalisation group (RG) equations

We list the one-loop RG equations for the model couplings used throughout the analysis. For the gauge couplings, they are given by [28],

$$16\pi^2 \frac{dg_3}{dt} = -7g_3^3, \quad (\text{C.1.1a})$$

$$16\pi^2 \frac{dg_2}{dt} = -\frac{17}{6}g_2^3, \quad (\text{C.1.1b})$$

$$16\pi^2 \frac{dg_1}{dt} = \frac{43}{6}g_1^3. \quad (\text{C.1.1c})$$

The quartic couplings evolve according to,

$$16\pi^2 \beta_{\lambda_1} = 32\lambda_1^2 + 8\lambda_2^2 + 16\lambda_3^2 + 4\lambda_4^2 + 2\lambda_5^2 + \frac{1}{2}\lambda_6^2 - 8\lambda_1\lambda_2 + 16\lambda_1\lambda_3 + 2\lambda_5\lambda_6 + 2\lambda_7^2 + \frac{3}{8}(g_1^4 + 3g_2^4) - \lambda_1(9g_2^2 + 3g_1^2) \quad (\text{C.1.2a})$$

$$16\pi^2 \beta_{\lambda_2} = 24\lambda_1\lambda_2 - 24\lambda_2^2 - 16\lambda_2\lambda_3 - \frac{1}{2}\lambda_6^2 + 2\lambda_7^2 - \frac{3}{4}g_1^2g_2^2 - \lambda_2(9g_2^2 + 3g_1^2) \quad (\text{C.1.2b})$$

$$16\pi^2 \beta_{\lambda_3} = 16\lambda_3^2 + 8\lambda_4^2 + 24\lambda_1\lambda_3 + 8\lambda_2\lambda_3 + 8\lambda_4^2 + \frac{1}{2}\lambda_6^2 + 2\lambda_7^2 + \frac{3}{4}g_1^2g_2^2$$

$$-\lambda_3(9g_2^2 + 3g_1^2) \quad (\text{C.1.2c})$$

$$16\pi^2\beta_{\lambda_4} = \lambda_4(12\lambda_1 + 4\lambda_2 + 24\lambda_3 + 6\lambda_5 + 8\lambda_6 + 20\lambda_7) - \lambda_4(9g_2^2 + 3g_1^2 - 3y_t^2), \quad (\text{C.1.2d})$$

$$16\pi^2\beta_{\lambda_5} = 4\lambda_5^2 + 2\lambda_6^2 + 8\lambda_4^2 + 8\lambda_7^2 + 20\lambda_1\lambda_5 - 4\lambda_2\lambda_5 + 8\lambda_3\lambda_5 + 8\lambda_1\lambda_6 + 12\lambda_5\lambda_8 + 4\lambda_6\lambda_8 + \frac{3}{4}(g_1^4 - 2g_1^2g_2^2 + 3g_2^4) - \lambda_5(9g_2^2 + 3g_1^2 - 6y_t^2), \quad (\text{C.1.2e})$$

$$16\pi^2\beta_{\lambda_6} = 20\lambda_4^2 + 4\lambda_6^2 + 32\lambda_7^2 + 4\lambda_1\lambda_6 - 4\lambda_2\lambda_6 + 8\lambda_3\lambda_6 + 8\lambda_5\lambda_6 + 4\lambda_8\lambda_6 + 3g_1^2g_2^2 - \lambda_6(9g_2^2 + 3g_1^2 - 6y_t^2), \quad (\text{C.1.2f})$$

$$16\pi^2\beta_{\lambda_7} = 4\lambda_7(\lambda_1 + \lambda_2 + 2\lambda_3 + 2\lambda_5 + 3\lambda_6 + \lambda_8) + 10\lambda_4^2 - \lambda_7(9g_2^2 + 3g_1^2 - 6y_t^2), \quad (\text{C.1.2g})$$

$$16\pi^2\beta_{\lambda_8} = 4\lambda_5^2 + 4\lambda_5\lambda_6 + 2\lambda_6^2 + 8\lambda_7^2 + 24\lambda_8^2 + \frac{3}{8}(g_1^4 + 2g_1^2g_2^2 + 3g_2^4) - \lambda_8(9g_2^2 + 3g_1^2 - 12y_t^2) - 6y_t^4, \quad (\text{C.1.2h})$$

Neglecting the effect of other quarks, the t -quark Yukawa coupling has the beta function,

$$16\pi^2\beta_{y_t} = y_t \left(-8g_3^2 - \frac{9}{4}g_2^2 - \frac{17}{12}g_1^2 + \frac{9}{2}y_t^2 \right) \quad (\text{C.1.3})$$

C.2 Oblique parameters

The expressions for the oblique parameters in the S_3 HDM are given. A shorthand notation $\sin(\beta - \alpha) = s_{\beta-\alpha}$, $\cos(\beta - \alpha) = c_{\beta-\alpha}$ is adopted,

$$24\pi\Delta S = (2s_W^2 - 1)^2 G(m_{H_1^+}^2, m_{H_1^+}^2, m_Z^2) + (2s_W^2 - 1)^2 G(m_{H_2^+}^2, m_{H_2^+}^2, m_Z^2) + G(m_{H_2}^2, m_{A_1}^2, m_Z^2) + c_{\beta-\alpha}^2 G(m_h^2, m_{A_2}^2, m_Z^2) + s_{\beta-\alpha}^2 G(m_{H_1}^2, m_{A_2}^2, m_Z^2) + c_{\beta-\alpha}^2 G(m_{H_1}^2, m_{H_1}^2, m_Z^2) - s_{\beta-\alpha}^2 G(m_h^2, m_h^2, m_Z^2) - 2\ln(m_{H_1^+}^2) - 2\ln(m_{H_2^+}^2) + \ln(m_{H_2}^2) + \ln(m_{H_1}^2) + \ln(m_{A_1}^2) + \ln(m_{A_2}^2) \quad (\text{C.2.1a})$$

$$16\pi s_W^2 m_W^2 \Delta T = F(m_{H_1^+}^2, m_{H_2}^2) + F(m_{H_1^+}^2, m_{A_1}^2) + c_{\beta-\alpha}^2 F(m_{H_2^+}^2, m_h^2) + s_{\beta-\alpha}^2 F(m_{H_2^+}^2, m_{H_1}^2) - F(m_{H_2}^2, m_{A_1}^2) - c_{\beta-\alpha}^2 F(m_h^2, m_{A_2}^2) - s_{\beta-\alpha}^2 F(m_{H_1}^2, m_{A_2}^2) + 3c_{\beta-\alpha}^2 (F(m_Z^2, m_{H_1}^2) - F(m_W^2, m_{H_1}^2)) - 3c_{\beta-\alpha}^2 (F(m_Z^2, m_h^2) - F(m_W^2, m_h^2)) \quad (\text{C.2.1b})$$

$$24\pi\Delta U = \frac{1}{24\pi} [G(m_{H_1^+}^2, m_{H_2}^2, m_W^2) + G(m_{H_1^+}^2, m_{A_1}^2, m_W^2) + c_{\beta-\alpha}^2 G(m_{H_2^+}^2, m_h^2, m_W^2) + s_{\beta-\alpha}^2 G(m_{H_2^+}^2, m_{H_1}^2, m_W^2) + G(m_{H_2^+}^2, m_{A_2}^2, m_W^2) + c_{\beta-\alpha}^2 \hat{G}(m_{H_1}^2, m_W^2) - \hat{G}(m_{H_1}^2, m_Z^2)]$$

$$\begin{aligned}
& -c_{\beta-\alpha}^2 \hat{G}(m_h^2, m_W^2) - \hat{G}(m_h^2, m_Z^2) - G(m_{H_2}^2, m_{A_1}^2, m_Z^2) \\
& -c_{\beta-\alpha}^2 G(m_h^2, m_{A_2}^2, m_Z^2) - s_{\beta-\alpha}^2 G(m_{H_1}^2, m_{A_2}^2, m_Z^2) \\
& -(2s_W^2 - 1)^2 G(m_{H_1^+}^2, m_{H_1^+}^2, m_Z^2) \\
& -(2s_W^2 - 1)^2 G(m_{H_2^+}^2, m_{H_2^+}^2, m_Z^2)
\end{aligned} \tag{C.2.1c}$$

where,

$$F(m_1^2, m_2^2) \equiv \begin{cases} \frac{m_1^2 + m_2^2}{2} - \frac{m_1^2 m_2^2}{m_1^2 - m_2^2} \ln \frac{m_1^2}{m_2^2} & ; m_1^2 \neq m_2^2, \\ 0 & ; m_1^2 = m_2^2. \end{cases} \tag{C.2.2}$$

$$\begin{aligned}
G(m_1^2, m_2^2, q^2) & \equiv -\frac{16}{3} + \frac{5(m_1^2 + m_2^2)}{q^2} - \frac{2(m_1^2 - m_2^2)^2}{(q^2)^2} \\
& + \frac{3}{q^2} \left[\frac{m_1^4 + m_2^4}{m_1^2 - m_2^2} - \frac{m_1^4 - m_2^4}{q^2} + \frac{(m_1^2 - m_2^2)^3}{3q^4} \right] \ln \frac{m_1^2}{m_2^2} + \frac{r}{(q^2)^3} f(t, r)
\end{aligned} \tag{C.2.3}$$

$$\tilde{G}(m_1^2, m_2^2, q^2) \equiv -2 + \left(\frac{m_1^2 - m_2^2}{q^2} - \frac{m_1^2 + m_2^2}{m_1^2 - m_2^2} \right) \ln \frac{m_1^2}{m_2^2} + \frac{f(t, r)}{q^2}. \tag{C.2.4}$$

$$\hat{G}(m^2, q^2) \equiv G(m^2, m^2, q^2) + 12 \tilde{G}(m^2, m^2, q^2) \tag{C.2.5}$$

$$t \equiv m_1^2 + m_2^2 - q^2 \quad \text{and} \quad r \equiv (q^2)^2 - 2q^2(m_1^2 + m_2^2) + (m_1^2 - m_2^2)^2 \tag{C.2.6}$$

$$f(t, r) \equiv \begin{cases} \sqrt{r} \ln \left| \frac{t - \sqrt{r}}{t + \sqrt{r}} \right| & ; r > 0, \\ 0 & ; r = 0, \\ 2\sqrt{-r} \tan^{-1} \frac{\sqrt{-r}}{t} & ; r < 0. \end{cases} \tag{C.2.7}$$

These are standard functions arising in a one-loop calculation.

C.3 $h \rightarrow \gamma\gamma$ decay width

The partial decay width of the SM-like Higgs to a pair of photons in this case has the expression [72],

$$\Gamma(h \rightarrow \gamma\gamma) = \frac{\alpha^2 g_2^2}{2^{10} \pi^3} \frac{m_h^3}{M_W^2} \left| \sin(\beta - \alpha) F_W + \left(-\frac{\sin\alpha}{\cos\beta} \right) \frac{4}{3} F_t + \sum_{i=1}^2 \kappa_i F_{i+} \right|^2, \tag{C.3.1}$$

The functions F_W , F_t and F_{i+} capture the effects of a W -boson, a t -quark and a charged scalar running in the loop and shall be defined as,

$$F_W = 2 + 3\tau_W + 3\tau_W(2 - \tau_W)f(\tau_W), \quad (\text{C.3.2a})$$

$$F_t = -2\tau_t[1 + (1 - \tau_t)f(\tau_t)], \quad (\text{C.3.2b})$$

$$F_{i+} = -\tau_{i+}[1 - \tau_{i+}f(\tau_{i+})]. \quad (\text{C.3.2c})$$

$$f(\tau) = \left[\sin^{-1} \left(\sqrt{1/\tau} \right) \right]^2. \quad (\text{C.3.3})$$

$$\text{with, } \tau = \frac{4m_a^2}{m_h^2} \quad (\text{C.3.4})$$

Here, $a = t, W$ and H_i^+ .

For Scenario A:

$$\begin{aligned} \kappa_1 = & -\frac{1}{6v}(2 \cos \alpha \operatorname{cosec} \beta (-6m_{H_1}^2 + 3m_{H_2}^2 - 3m_h^2 + m_{H_2}^2 + 3m_{H_2^+}^2 \cos 2\beta) + \\ & (6m_{H_2^+}^2 + 2m_{H_2}^2 + m_{H_2^+}^2 \cos 2\beta) \sec \beta \sin \alpha), \end{aligned} \quad (\text{C.3.5a})$$

$$\begin{aligned} \kappa_2 = & \frac{1}{9v}((9(-2m_{H_2^+}^2 + m_h^2) \cos \beta - 9m_h^2 \sec \beta + m_{H_2}^2 \sec^3 \beta) \sin \alpha + \\ & ((9m_h^2 + m_{H_2}^2) \operatorname{cosec} \beta + 18m_{H_2^+}^2 \sin \beta - 9m_h^2 \sin \beta \\ & + m_{H_2}^2 \sec \beta \tan \beta) \cos \alpha) \end{aligned} \quad (\text{C.3.5b})$$

For Scenario B:

$$\kappa_1 = \kappa_2 = -\frac{\lambda_5}{2}. \quad (\text{C.3.6a})$$

Bibliography

- [1] R. P. Feynman and M. Gell-Mann, *Theory of Fermi interaction*, *Phys. Rev.* **109** (1958) 193–198.
- [2] E. C. G. Sudarshan and R. e. Marshak, *Chirality invariance and the universal Fermi interaction*, *Phys. Rev.* **109** (1958) 1860–1860.
- [3] S. L. Glashow, *Partial Symmetries of Weak Interactions*, *Nucl. Phys.* **22** (1961) 579–588.
- [4] S. Weinberg, *A Model of Leptons*, *Phys. Rev. Lett.* **19** (1967) 1264–1266.
- [5] A. Salam, *Weak and electromagnetic interactions*, in *Elementary particle theory* (N. Svartholm, ed.), pp. 367–377, Almquist & Wiksell.
- [6] C.-N. Yang and R. L. Mills, *Conservation of Isotopic Spin and Isotopic Gauge Invariance*, *Phys. Rev.* **96** (1954) 191–195.
- [7] R. M. Godbole, *Lectures on EW Standard Model*, [arXiv:1703.0497](https://arxiv.org/abs/1703.0497).
- [8] G. Bhattacharyya, *A Pedagogical Review of Electroweak Symmetry Breaking Scenarios*, *Rept. Prog. Phys.* **74** (2011) 026201, [[arXiv:0910.5095](https://arxiv.org/abs/0910.5095)].
- [9] J. L. Rosner, *The Standard model in 2001*, in *Heavy flavor physics: Theory and experimental results in heavy quark physics and CP violation. Proceedings, 55th Scottish Universities Summer School in Physics, SUSSP 2001, St. Andrews, UK, August 7-23, 2001*, pp. 1–56, 2001. [hep-ph/0108195](https://arxiv.org/abs/hep-ph/0108195).
- [10] M. Peskin and D. Schroeder, *An Introduction To Quantum Field Theory*. Frontiers in Physics. Avalon Publishing, 1995.
- [11] T. Cheng and L. Li, *Gauge Theory of Elementary Particle Physics*. Oxford science publications. Clarendon Press, 1984.

- [12] M. Schwartz, *Quantum Field Theory and the Standard Model*. Quantum Field Theory and the Standard Model. Cambridge University Press, 2014.
- [13] D. Bailin and A. Love, *Introduction to Gauge Field Theory Revised Edition*. Graduate Student Series in Physics. Taylor & Francis, 1993.
- [14] W. A. Bardeen, *Anomalous Ward identities in spinor field theories*, *Phys. Rev.* **184** (1969) 1848–1857.
- [15] S. L. Adler, *Axial vector vertex in spinor electrodynamics*, *Phys. Rev.* **177** (1969) 2426–2438.
- [16] J. S. Bell and R. Jackiw, *A PCAC puzzle: $\pi^0 \rightarrow \gamma \gamma$ in the sigma model*, *Nuovo Cim.* **A60** (1969) 47–61.
- [17] J. A. Minahan, P. Ramond, and R. C. Warner, *A Comment on Anomaly Cancellation in the Standard Model*, *Phys. Rev.* **D41** (1990) 715.
- [18] F. Englert and R. Brout, *Broken Symmetry and the Mass of Gauge Vector Mesons*, *Phys. Rev. Lett.* **13** (1964) 321–323.
- [19] P. W. Higgs, *Broken Symmetries and the Masses of Gauge Bosons*, *Phys. Rev. Lett.* **13** (1964) 508–509.
- [20] G. S. Guralnik, C. R. Hagen, and T. W. B. Kibble, *Global Conservation Laws and Massless Particles*, *Phys. Rev. Lett.* **13** (1964) 585–587.
- [21] N. Cabibbo, *Unitary symmetry and leptonic decays*, *Phys. Rev. Lett.* **10** (Jun, 1963) 531–533.
- [22] M. Kobayashi and T. Maskawa, *CP Violation in the Renormalizable Theory of Weak Interaction*, *Prog. Theor. Phys.* **49** (1973) 652–657.
- [23] **Particle Data Group** Collaboration, K. A. Olive *et. al.*, *Review of Particle Physics*, *Chin. Phys.* **C38** (2014) 090001.
- [24] **Muon g-2** Collaboration, G. W. Bennett *et. al.*, *Final Report of the Muon E821 Anomalous Magnetic Moment Measurement at BNL*, *Phys. Rev.* **D73** (2006) 072003, [[hep-ex/0602035](https://arxiv.org/abs/hep-ex/0602035)].

- [25] M. J. G. Veltman, *The Infrared - Ultraviolet Connection*, *Acta Phys. Polon.* **B12** (1981) 437.
- [26] V. Barger, P. Langacker, M. McCaskey, M. Ramsey-Musolf, and G. Shaughnessy, *Complex Singlet Extension of the Standard Model*, *Phys. Rev.* **D79** (2009) 015018, [[arXiv:0811.0393](https://arxiv.org/abs/0811.0393)].
- [27] J. C. Montero and V. Pleitez, *Gauging $U(1)$ symmetries and the number of right-handed neutrinos*, *Phys. Lett.* **B675** (2009) 64–68, [[arXiv:0706.0473](https://arxiv.org/abs/0706.0473)].
- [28] G. C. Branco, P. M. Ferreira, L. Lavoura, M. N. Rebelo, M. Sher, and J. P. Silva, *Theory and phenomenology of two-Higgs-doublet models*, *Phys. Rept.* **516** (2012) 1–102, [[arXiv:1106.0034](https://arxiv.org/abs/1106.0034)].
- [29] G. Bhattacharyya and D. Das, *Scalar sector of two-Higgs-doublet models: A minireview*, *Pramana* **87** (2016), no. 3 40, [[arXiv:1507.0642](https://arxiv.org/abs/1507.0642)].
- [30] S. L. Glashow and S. Weinberg, *Natural Conservation Laws for Neutral Currents*, *Phys. Rev.* **D15** (1977) 1958.
- [31] E. A. Paschos, *Diagonal Neutral Currents*, *Phys. Rev.* **D15** (1977) 1966.
- [32] I. P. Ivanov and E. Vdovin, *Classification of finite reparametrization symmetry groups in the three-Higgs-doublet model*, *Eur. Phys. J.* **C73** (2013), no. 2 2309, [[arXiv:1210.6553](https://arxiv.org/abs/1210.6553)].
- [33] I. P. Ivanov, V. Keus, and E. Vdovin, *Abelian symmetries in multi-Higgs-doublet models*, *J. Phys.* **A45** (2012) 215201, [[arXiv:1112.1660](https://arxiv.org/abs/1112.1660)].
- [34] R. Mohapatra and P. Pal, *Massive Neutrinos in Physics and Astrophysics*. Lecture Notes in Physics Series. World Scientific, 1991.
- [35] R. N. Mohapatra and G. Senjanovic, *Neutrino Mass and Spontaneous Parity Violation*, *Phys. Rev. Lett.* **44** (1980) 912.
- [36] D. J. Gross and F. Wilczek, *Ultraviolet Behavior of Nonabelian Gauge Theories*, *Phys. Rev. Lett.* **30** (1973) 1343–1346.
- [37] H. D. Politzer, *Reliable Perturbative Results for Strong Interactions?*, *Phys. Rev. Lett.* **30** (1973) 1346–1349.

- [38] D. R. T. Jones, *Two Loop Diagrams in Yang-Mills Theory*, *Nucl. Phys.* **B75** (1974) 531.
- [39] O. V. Tarasov, A. A. Vladimirov, and A. Yu. Zharkov, *The Gell-Mann-Low Function of QCD in the Three Loop Approximation*, *Phys. Lett.* **B93** (1980) 429–432.
- [40] M. E. Machacek and M. T. Vaughn, *Two Loop Renormalization Group Equations in a General Quantum Field Theory. 1. Wave Function Renormalization*, *Nucl. Phys.* **B222** (1983) 83–103.
- [41] M. E. Machacek and M. T. Vaughn, *Two Loop Renormalization Group Equations in a General Quantum Field Theory. 2. Yukawa Couplings*, *Nucl. Phys.* **B236** (1984) 221–232.
- [42] M. E. Machacek and M. T. Vaughn, *Two Loop Renormalization Group Equations in a General Quantum Field Theory. 3. Scalar Quartic Couplings*, *Nucl. Phys.* **B249** (1985) 70–92.
- [43] L. N. Mihaila, J. Salomon, and M. Steinhauser, *Gauge Coupling Beta Functions in the Standard Model to Three Loops*, *Phys. Rev. Lett.* **108** (2012) 151602, [[arXiv:1201.5868](https://arxiv.org/abs/1201.5868)].
- [44] L. N. Mihaila, J. Salomon, and M. Steinhauser, *Renormalization constants and beta functions for the gauge couplings of the Standard Model to three-loop order*, *Phys. Rev.* **D86** (2012) 096008, [[arXiv:1208.3357](https://arxiv.org/abs/1208.3357)].
- [45] T. P. Cheng, E. Eichten, and L.-F. Li, *Higgs Phenomena in Asymptotically Free Gauge Theories*, *Phys. Rev.* **D9** (1974) 2259.
- [46] A. V. Bednyakov, A. F. Pikelner, and V. N. Velizhanin, *Yukawa coupling beta-functions in the Standard Model at three loops*, *Phys. Lett.* **B722** (2013) 336–340, [[arXiv:1212.6829](https://arxiv.org/abs/1212.6829)].
- [47] A. V. Bednyakov, A. F. Pikelner, and V. N. Velizhanin, *Higgs self-coupling beta-function in the Standard Model at three loops*, *Nucl. Phys.* **B875** (2013) 552–565, [[arXiv:1303.4364](https://arxiv.org/abs/1303.4364)].
- [48] M.-x. Luo and Y. Xiao, *Two loop renormalization group equations in the standard model*, *Phys. Rev. Lett.* **90** (2003) 011601, [[hep-ph/0207271](https://arxiv.org/abs/hep-ph/0207271)].

- [49] B. Schrempp and M. Wimmer, *Top quark and Higgs boson masses: Interplay between infrared and ultraviolet physics*, *Prog. Part. Nucl. Phys.* **37** (1996) 1–90, [[hep-ph/9606386](#)].
- [50] M. Sher, *Precise vacuum stability bound in the standard model*, *Phys. Lett.* **B317** (1993) 159–163, [[hep-ph/9307342](#)]. [Addendum: *Phys. Lett.* **B331**, 448(1994)].
- [51] N. Cabibbo, L. Maiani, G. Parisi, and R. Petronzio, *Bounds on the Fermions and Higgs Boson Masses in Grand Unified Theories*, *Nucl. Phys.* **B158** (1979) 295–305.
- [52] M. Lindner, M. Sher, and H. W. Zaglauer, *Probing Vacuum Stability Bounds at the Fermilab Collider*, *Phys. Lett.* **B228** (1989) 139–143.
- [53] I. V. Krive and A. D. Linde, *On the Vacuum Stability Problem in Gauge Theories*, *Nucl. Phys.* **B117** (1976) 265–268.
- [54] P. B. Arnold, *Can the Electroweak Vacuum Be Unstable?*, *Phys. Rev.* **D40** (1989) 613.
- [55] J. Ellis, J. R. Espinosa, G. F. Giudice, A. Hoecker, and A. Riotto, *The Probable Fate of the Standard Model*, *Phys. Lett.* **B679** (2009) 369–375, [[arXiv:0906.0954](#)].
- [56] J. Elias-Miro, J. R. Espinosa, G. F. Giudice, G. Isidori, A. Riotto, and A. Strumia, *Higgs mass implications on the stability of the electroweak vacuum*, *Phys. Lett.* **B709** (2012) 222–228, [[arXiv:1112.3022](#)].
- [57] K. G. Chetyrkin and M. Steinhauser, *Short distance mass of a heavy quark at order α_s^3* , *Phys. Rev. Lett.* **83** (1999) 4001–4004, [[hep-ph/9907509](#)].
- [58] K. G. Chetyrkin and M. Steinhauser, *The Relation between the \overline{MS} -bar and the on-shell quark mass at order $\alpha(s)^{**3}$* , *Nucl. Phys.* **B573** (2000) 617–651, [[hep-ph/9911434](#)].
- [59] K. Melnikov and T. v. Ritbergen, *The Three loop relation between the \overline{MS} -bar and the pole quark masses*, *Phys. Lett.* **B482** (2000) 99–108, [[hep-ph/9912391](#)].
- [60] A. Fazio and E. R. Rojas, *Vacuum stability and two loop threshold corrections to the higgs quartic coupling*, *Nuclear and Particle Physics Proceedings* **267** (2015) 53 – 59.
- [61] B. A. Kniehl and O. L. Veretin, *Two-loop electroweak threshold corrections to the bottom and top Yukawa couplings*, *Nucl. Phys.* **B885** (2014) 459–480, [[arXiv:1401.1844](#)]. [Erratum: *Nucl. Phys.* **B894**, 56(2015)].

- [62] G. Degrandi, S. Di Vita, J. Elias-Miro, J. R. Espinosa, G. F. Giudice, G. Isidori, and A. Strumia, *Higgs mass and vacuum stability in the Standard Model at NNLO*, *JHEP* **08** (2012) 098, [[arXiv:1205.6497](#)].
- [63] A. Sirlin and R. Zucchini, *Dependence of the Quartic Coupling $H(m)$ on $M(H)$ and the Possible Onset of New Physics in the Higgs Sector of the Standard Model*, *Nucl. Phys.* **B266** (1986) 389–409.
- [64] R. Hempfling and B. A. Kniehl, *On the relation between the fermion pole mass and M_S Yukawa coupling in the standard model*, *Phys. Rev.* **D51** (1995) 1386–1394, [[hep-ph/9408313](#)].
- [65] D. Buttazzo, G. Degrandi, P. P. Giardino, G. F. Giudice, F. Sala, A. Salvio, and A. Strumia, *Investigating the near-criticality of the Higgs boson*, *JHEP* **12** (2013) 089, [[arXiv:1307.3536](#)].
- [66] V. V. Flambaum, D. B. Leinweber, A. W. Thomas, and R. D. Young, *Limits on variations of the quark masses, qcd scale, and fine structure constant*, *Phys. Rev. D* **69** (Jun, 2004) 115006.
- [67] **ATLAS** Collaboration, O. Brandt, *Measurements of the top quark mass with the ATLAS detector*, *PoS EPS-HEP2015* (2015) 324, [[arXiv:1510.0014](#)].
- [68] S. R. Coleman, *The Fate of the False Vacuum. 1. Semiclassical Theory*, *Phys. Rev.* **D15** (1977) 2929–2936. [Erratum: *Phys. Rev.*D16,1248(1977)].
- [69] C. G. Callan, Jr. and S. R. Coleman, *The Fate of the False Vacuum. 2. First Quantum Corrections*, *Phys. Rev.* **D16** (1977) 1762–1768.
- [70] G. Isidori, G. Ridolfi, and A. Strumia, *On the metastability of the standard model vacuum*, *Nucl. Phys.* **B609** (2001) 387–409, [[hep-ph/0104016](#)].
- [71] S. Dawson, *Introduction to electroweak symmetry breaking*, in *Proceedings, Summer School in High-energy physics and cosmology: Trieste, Italy, June 29-July 17, 1998*, pp. 1–83, 1998. [hep-ph/9901280](#).
- [72] A. Djouadi, *The Anatomy of electro-weak symmetry breaking. I: The Higgs boson in the standard model*, *Phys. Rept.* **457** (2008) 1–216, [[hep-ph/0503172](#)].

- [73] J. Kuti, L. Lin, and Y. Shen, *Upper Bound on the Higgs Mass in the Standard Model*, *Phys. Rev. Lett.* **61** (1988) 678.
- [74] B. Grzadkowski and M. Lindner, *Stability of Triviality Mass Bounds in the Standard Model*, *Phys. Lett.* **B178** (1986) 81.
- [75] D. A. Dicus and V. S. Mathur, *Upper bounds on the values of masses in unified gauge theories*, *Phys. Rev. D* **7** (May, 1973) 3111–3114.
- [76] B. W. Lee, C. Quigg, and H. B. Thacker, *Weak interactions at very high energies: The role of the higgs-boson mass*, *Phys. Rev. D* **16** (Sep, 1977) 1519–1531.
- [77] M. Sher, *Electroweak Higgs Potentials and Vacuum Stability*, *Phys. Rept.* **179** (1989) 273–418.
- [78] N. Khan, *Exploring Extensions of the Scalar Sector of the Standard Model*. PhD thesis, Indian Inst. Tech., Indore, 2017. [arXiv:1701.0220](https://arxiv.org/abs/1701.0220).
- [79] B. N. Swiezewska, *Higgs boson and vacuum stability in models with extended scalar sector*. PhD thesis, Warsaw U., 2016.
- [80] **ATLAS** Collaboration, G. Aad *et. al.*, *Observation of a new particle in the search for the Standard Model Higgs boson with the ATLAS detector at the LHC*, *Phys. Lett.* **B716** (2012) 1–29, [[arXiv:1207.7214](https://arxiv.org/abs/1207.7214)].
- [81] **CMS** Collaboration, S. Chatrchyan *et. al.*, *Observation of a new boson at a mass of 125 GeV with the CMS experiment at the LHC*, *Phys.Lett.* **B716** (2012) 30–61, [[arXiv:1207.7235](https://arxiv.org/abs/1207.7235)].
- [82] **ATLAS** Collaboration, G. Aad *et. al.*, *Evidence for the spin-0 nature of the Higgs boson using ATLAS data*, *Phys. Lett.* **B726** (2013) 120–144, [[arXiv:1307.1432](https://arxiv.org/abs/1307.1432)].
- [83] **ATLAS** Collaboration, *Measurements of the properties of the Higgs-like boson in the four lepton decay channel with the ATLAS detector using 25 fb1 of proton-proton collision data*, .
- [84] A. Freitas and P. Schwaller, *Higgs CP Properties From Early LHC Data*, *Phys. Rev.* **D87** (2013), no. 5 055014, [[arXiv:1211.1980](https://arxiv.org/abs/1211.1980)].

- [85] A. Djouadi, R. M. Godbole, B. Mellado, and K. Mohan, *Probing the spin-parity of the Higgs boson via jet kinematics in vector boson fusion*, *Phys. Lett.* **B723** (2013) 307–313, [[arXiv:1301.4965](#)].
- [86] A. Djouadi and G. Moreau, *The couplings of the Higgs boson and its CP properties from fits of the signal strengths and their ratios at the 7+8 TeV LHC*, *Eur. Phys. J.* **C73** (2013), no. 9 2512, [[arXiv:1303.6591](#)].
- [87] J. F. Gunion, H. E. Haber, G. L. Kane, and S. Dawson, *The Higgs Hunter’s Guide*, *Front. Phys.* **80** (2000) 1–404.
- [88] N. G. Deshpande and E. Ma, *Comment on Weinberg’s Gauge Theory of CP Nonconservation*, *Phys. Rev.* **D16** (1977) 1583.
- [89] M. Holthausen, K. S. Lim, and M. Lindner, *Planck scale boundary conditions and the higgs mass*, *Journal of High Energy Physics* **2012** (2012), no. 2 37.
- [90] M. F. Zoller, *Standard Model beta-functions to three-loop order and vacuum stability*, in *17th International Moscow School of Physics and 42nd ITEP Winter School of Physics Moscow, Russia, February 11-18, 2014*, 2014. [arXiv:1411.2843](#).
- [91] M. Zoller, *Beta-function for the Higgs self-interaction in the Standard Model at three-loop level*, *PoS EPS-HEP2013* (2013) 322, [[arXiv:1311.5085](#)].
- [92] N. Chakrabarty, U. K. Dey, and B. Mukhopadhyaya, *High-scale validity of a two-Higgs doublet scenario: a study including LHC data*, *JHEP* **12** (2014) 166, [[arXiv:1407.2145](#)].
- [93] S. Davidson and H. E. Haber, *Basis-independent methods for the two-Higgs-doublet model*, *Phys. Rev.* **D72** (2005) 035004, [[hep-ph/0504050](#)]. [Erratum: *Phys. Rev.*D72,099902(2005)].
- [94] H. E. Haber and D. O’Neil, *Basis-independent methods for the two-Higgs-doublet model. II. The Significance of $\tan\beta$* , *Phys. Rev.* **D74** (2006) 015018, [[hep-ph/0602242](#)]. [Erratum: *Phys. Rev.*D74,no.5,059905(2006)].
- [95] H. E. Haber and D. O’Neil, *Basis-independent methods for the two-Higgs-doublet model III: The CP-conserving limit, custodial symmetry, and the oblique parameters S, T, U*, *Phys. Rev.* **D83** (2011) 055017, [[arXiv:1011.6188](#)].

- [96] A. Barroso, P. M. Ferreira, I. P. Ivanov, and R. Santos, *Metastability bounds on the two Higgs doublet model*, *JHEP* **06** (2013) 045, [[arXiv:1303.5098](#)].
- [97] B. Gorczyca and M. Krawczyk, *Tree-Level Unitarity Constraints for the SM-like 2HDM*, [arXiv:1112.5086](#).
- [98] K. Kannike, *Vacuum Stability Conditions From Copositivity Criteria*, *Eur. Phys. J.* **C72** (2012) 2093, [[arXiv:1205.3781](#)].
- [99] J. Kopp and M. Nardecchia, *Flavor and CP violation in Higgs decays*, *JHEP* **10** (2014) 156, [[arXiv:1406.5303](#)].
- [100] S. Inoue, M. J. Ramsey-Musolf, and Y. Zhang, *CP-violating phenomenology of flavor conserving two Higgs doublet models*, *Phys. Rev.* **D89** (2014), no. 11 115023, [[arXiv:1403.4257](#)].
- [101] A. Arhrib, E. Christova, H. Eberl, and E. Ginina, *CP violation in charged Higgs production and decays in the Complex Two Higgs Doublet Model*, *JHEP* **04** (2011) 089, [[arXiv:1011.6560](#)].
- [102] P. Osland, A. Pukhov, G. M. Pruna, and M. Purmohammadi, *Phenomenology of charged scalars in the CP-Violating Inert-Doublet Model*, *JHEP* **04** (2013) 040, [[arXiv:1302.3713](#)].
- [103] S. L. Glashow and S. Weinberg, *Natural conservation laws for neutral currents*, *Phys. Rev. D* **15** (Apr, 1977) 1958–1965.
- [104] E. A. Paschos, *Diagonal neutral currents*, *Phys. Rev. D* **15** (Apr, 1977) 1966–1972.
- [105] A. Arhrib, *Top and Higgs flavor changing neutral couplings in two Higgs doublets model*, *Phys. Rev.* **D72** (2005) 075016, [[hep-ph/0510107](#)].
- [106] A. Dery, A. Efrati, G. Hiller, Y. Hochberg, and Y. Nir, *Higgs couplings to fermions: 2HDM with MFV*, *JHEP* **08** (2013) 006, [[arXiv:1304.6727](#)].
- [107] G. Cvetič, S. S. Hwang, and C. S. Kim, *One loop renormalization group equations of the general framework with two Higgs doublets*, *Int. J. Mod. Phys.* **A14** (1999) 769–798, [[hep-ph/9706323](#)].

- [108] G. Cvetič, C. S. Kim, and S. S. Hwang, *Higgs mediated flavor changing neutral currents in the general framework with two Higgs doublets: An RGE analysis*, *Phys. Rev.* **D58** (1998) 116003, [[hep-ph/9806282](#)].
- [109] A. Pich and P. Tuzon, *Yukawa Alignment in the Two-Higgs-Doublet Model*, *Phys. Rev.* **D80** (2009) 091702, [[arXiv:0908.1554](#)].
- [110] J. F. Gunion and H. E. Haber, *The CP conserving two Higgs doublet model: The Approach to the decoupling limit*, *Phys. Rev.* **D67** (2003) 075019, [[hep-ph/0207010](#)].
- [111] B. W. Lee, C. Quigg, and H. Thacker, *Weak Interactions at Very High-Energies: The Role of the Higgs Boson Mass*, *Phys. Rev.* **D16** (1977) 1519.
- [112] I. F. Ginzburg and I. P. Ivanov, *Tree-level unitarity constraints in the most general 2HDM*, *Phys. Rev.* **D72** (2005) 115010, [[hep-ph/0508020](#)].
- [113] G. Bhattacharyya, D. Das, P. B. Pal, and M. N. Rebelo, *Scalar sector properties of two-Higgs-doublet models with a global $U(1)$ symmetry*, *JHEP* **10** (2013) 081, [[arXiv:1308.4297](#)].
- [114] B. Grzadkowski, O. M. Ogreid, and P. Osland, *Diagnosing CP properties of the 2HDM*, *JHEP* **01** (2014) 105, [[arXiv:1309.6229](#)].
- [115] L. Basso, A. Lipniacka, F. Mahmoudi, S. Moretti, P. Osland, G. M. Pruna, and M. Purmohammadi, *The CP-violating type-II 2HDM and Charged Higgs boson benchmarks*, *PoS Corfu2012* (2013) 029, [[arXiv:1305.3219](#)].
- [116] S. Kanemura, T. Kubota, and E. Takasugi, *Lee-Quigg-Thacker bounds for Higgs boson masses in a two doublet model*, *Phys. Lett.* **B313** (1993) 155–160, [[hep-ph/9303263](#)].
- [117] A. G. Akeroyd, A. Arhrib, and E.-M. Naimi, *Note on tree level unitarity in the general two Higgs doublet model*, *Phys. Lett.* **B490** (2000) 119–124, [[hep-ph/0006035](#)].
- [118] J. Horejsi and M. Kladiva, *Tree-unitarity bounds for THDM Higgs masses revisited*, *Eur. Phys. J.* **C46** (2006) 81–91, [[hep-ph/0510154](#)].
- [119] S. Nie and M. Sher, *Vacuum stability bounds in the two Higgs doublet model*, *Phys. Lett.* **B449** (1999) 89–92, [[hep-ph/9811234](#)].

- [120] P. M. Ferreira and D. R. T. Jones, *Bounds on scalar masses in two Higgs doublet models*, *JHEP* **08** (2009) 069, [[arXiv:0903.2856](#)].
- [121] P. M. Ferreira, R. Santos, and A. Barroso, *Stability of the tree-level vacuum in two Higgs doublet models against charge or CP spontaneous violation*, *Phys. Lett.* **B603** (2004) 219–229, [[hep-ph/0406231](#)]. [Erratum: *Phys. Lett.*B629,114(2005)].
- [122] J. Bijnens, J. Lu, and J. Rathsman, *Constraining General 2HDM by the Evolution of Yukawa Couplings*, *PoS CHARGED2012* (2012) 023, [[arXiv:1301.7451](#)].
- [123] I. Chakraborty and A. Kundu, *Two-Higgs doublet models confront the naturalness problem*, *Phys. Rev.* **D90** (2014), no. 11 115017, [[arXiv:1404.3038](#)].
- [124] **ATLAS** Collaboration, G. Aad *et. al.*, *Measurement of the Higgs boson mass from the $H \rightarrow \gamma\gamma$ and $H \rightarrow ZZ^* \rightarrow 4\ell$ channels with the ATLAS detector using 25 fb^{-1} of pp collision data*, *Phys. Rev.* **D90** (2014), no. 5 052004, [[arXiv:1406.3827](#)].
- [125] F. Mahmoudi and O. Stal, *Flavor constraints on the two-Higgs-doublet model with general Yukawa couplings*, *Phys. Rev.* **D81** (2010) 035016, [[arXiv:0907.1791](#)].
- [126] O. Deschamps, S. Descotes-Genon, S. Monteil, V. Niess, S. T’Jampens, and V. Tisserand, *The Two Higgs Doublet of Type II facing flavour physics data*, *Phys. Rev.* **D82** (2010) 073012, [[arXiv:0907.5135](#)].
- [127] **Particle Data Group** Collaboration, J. Beringer *et. al.*, *Review of Particle Physics (RPP)*, *Phys. Rev.* **D86** (2012) 010001.
- [128] M. E. Peskin and T. Takeuchi, *Estimation of oblique electroweak corrections*, *Phys. Rev.* **D46** (1992) 381–409.
- [129] H.-J. He, N. Polonsky, and S.-f. Su, *Extra families, Higgs spectrum and oblique corrections*, *Phys. Rev.* **D64** (2001) 053004, [[hep-ph/0102144](#)].
- [130] W. Grimus, L. Lavoura, O. M. Ogreid, and P. Osland, *The Oblique parameters in multi-Higgs-doublet models*, *Nucl. Phys.* **B801** (2008) 81–96, [[arXiv:0802.4353](#)].
- [131] G. Funk, D. O’Neil, and R. M. Winters, *What the Oblique Parameters S , T , and U and Their Extensions Reveal About the 2HDM: A Numerical Analysis*, *Int. J. Mod. Phys.* **A27** (2012) 1250021, [[arXiv:1110.3812](#)].

- [132] **Gfitter Group** Collaboration, M. Baak, J. Cth, J. Haller, A. Hoecker, R. Kogler, K. Mnig, M. Schott, and J. Stelzer, *The global electroweak fit at NNLO and prospects for the LHC and ILC*, *Eur. Phys. J.* **C74** (2014) 3046, [[arXiv:1407.3792](#)].
- [133] **ATLAS** Collaboration, *Search for the Standard Model Higgs boson in $H \rightarrow \tau\tau$ decays in proton-proton collisions with the ATLAS detector*, .
- [134] **ATLAS** Collaboration, T. A. collaboration, *Search for the bb decay of the Standard Model Higgs boson in associated W/ZH production with the ATLAS detector*, .
- [135] **ATLAS** Collaboration, G. Aad *et. al.*, *Measurements of Higgs boson production and couplings in diboson final states with the ATLAS detector at the LHC*, *Phys. Lett.* **B726** (2013) 88–119, [[arXiv:1307.1427](#)]. [Erratum: *Phys. Lett.*B734,406(2014)].
- [136] B. Coleppa, F. Kling, and S. Su, *Constraining Type II 2HDM in Light of LHC Higgs Searches*, *JHEP* **01** (2014) 161, [[arXiv:1305.0002](#)].
- [137] P. M. Ferreira, R. Santos, M. Sher, and J. P. Silva, *Implications of the LHC two-photon signal for two-Higgs-doublet models*, *Phys. Rev.* **D85** (2012) 077703, [[arXiv:1112.3277](#)].
- [138] P. M. Ferreira, R. Santos, M. Sher, and J. P. Silva, *2HDM confronting LHC data*, in *Proceedings, 48th Rencontres de Moriond on QCD and High Energy Interactions: La Thuile, Italy, March 9-16, 2013*, pp. 67–70, 2013. [arXiv:1305.4587](#).
- [139] A. Drozd, B. Grzadkowski, J. F. Gunion, and Y. Jiang, *Two-Higgs-Doublet Models and Enhanced Rates for a 125 GeV Higgs*, *JHEP* **05** (2013) 072, [[arXiv:1211.3580](#)].
- [140] H. S. Cheon and S. K. Kang, *Constraining parameter space in type-II two-Higgs doublet model in light of a 126 GeV Higgs boson*, *JHEP* **09** (2013) 085, [[arXiv:1207.1083](#)].
- [141] A. Drozd, B. Grzadkowski, J. F. Gunion, and Y. Jiang, *2HDM and Enhanced Rates in $\gamma\gamma$ Channel*, *Acta Phys. Polon.* **B44** (2013), no. 7 1417–1428.
- [142] M. Krawczyk, D. Sokoowska, and B. wieewska, *2HDM with Z_2 symmetry in light of new LHC data*, *J. Phys. Conf. Ser.* **447** (2013) 012050, [[arXiv:1303.7102](#)].
- [143] L. Wang and X.-F. Han, *Status of the aligned two-Higgs-doublet model confronted with the Higgs data*, *JHEP* **04** (2014) 128, [[arXiv:1312.4759](#)].

- [144] B. Dumont, J. F. Gunion, Y. Jiang, and S. Kraml, *Constraints on and future prospects for Two-Higgs-Doublet Models in light of the LHC Higgs signal*, *Phys. Rev. D* **90** (2014) 035021, [[arXiv:1405.3584](#)].
- [145] A. Celis, V. Ilisie, and A. Pich, *LHC constraints on two-Higgs doublet models*, *JHEP* **07** (2013) 053, [[arXiv:1302.4022](#)].
- [146] A. Celis, V. Ilisie, and A. Pich, *Towards a general analysis of LHC data within two-Higgs-doublet models*, *JHEP* **12** (2013) 095, [[arXiv:1310.7941](#)].
- [147] O. Eberhardt, U. Nierste, and M. Wiebusch, *Status of the two-Higgs-doublet model of type II*, *JHEP* **07** (2013) 118, [[arXiv:1305.1649](#)].
- [148] S. Kanemura, K. Tsumura, K. Yagyu, and H. Yokoya, *Fingerprinting nonminimal Higgs sectors*, *Phys. Rev. D* **90** (2014) 075001, [[arXiv:1406.3294](#)].
- [149] S. Banerjee, S. Mukhopadhyay, and B. Mukhopadhyaya, *New Higgs interactions and recent data from the LHC and the Tevatron*, *JHEP* **10** (2012) 062, [[arXiv:1207.3588](#)].
- [150] T. Corbett, O. J. P. Eboli, J. Gonzalez-Fraile, and M. C. Gonzalez-Garcia, *Constraining anomalous Higgs interactions*, *Phys. Rev. D* **86** (2012) 075013, [[arXiv:1207.1344](#)].
- [151] J. R. Espinosa, C. Grojean, M. Muhlleitner, and M. Trott, *Fingerprinting Higgs Suspects at the LHC*, *JHEP* **05** (2012) 097, [[arXiv:1202.3697](#)].
- [152] P. P. Giardino, K. Kannike, M. Raidal, and A. Strumia, *Reconstructing Higgs boson properties from the LHC and Tevatron data*, *JHEP* **06** (2012) 117, [[arXiv:1203.4254](#)].
- [153] M. Klute, R. Lafaye, T. Plehn, M. Rauch, and D. Zerwas, *Measuring Higgs Couplings from LHC Data*, *Phys. Rev. Lett.* **109** (2012) 101801, [[arXiv:1205.2699](#)].
- [154] A. Azatov, R. Contino, D. Del Re, J. Galloway, M. Grassi, and S. Rahatlou, *Determining Higgs couplings with a model-independent analysis of $h \rightarrow \gamma\gamma$* , *JHEP* **06** (2012) 134, [[arXiv:1204.4817](#)].
- [155] D. Eriksson, J. Rathsman, and O. Stal, *2HDMC: Two-Higgs-Doublet Model Calculator Physics and Manual*, *Comput. Phys. Commun.* **181** (2010) 189–205, [[arXiv:0902.0851](#)].

- [156] U. Langenfeld, S. Moch, and P. Uwer, *Measuring the running top-quark mass*, *Phys. Rev.* **D80** (2009) 054009, [[arXiv:0906.5273](#)].
- [157] A. V. Bednyakov, B. A. Kniehl, A. F. Pikelner, and O. L. Veretin, *On the b-quark running mass in QCD and the SM*, *Nucl. Phys.* **B916** (2017) 463–483, [[arXiv:1612.0066](#)].
- [158] **D0** Collaboration, V. M. Abazov *et. al.*, *Precision measurement of the top-quark mass in lepton+jets final states*, *Phys. Rev. Lett.* **113** (2014) 032002, [[arXiv:1405.1756](#)].
- [159] L. Basso, A. Lipniacka, F. Mahmoudi, S. Moretti, P. Osland, G. M. Pruna, and M. Purmohammadi, *Probing the charged Higgs boson at the LHC in the CP-violating type-II 2HDM*, *JHEP* **11** (2012) 011, [[arXiv:1205.6569](#)].
- [160] N. Chakrabarty and B. Mukhopadhyaya, *High-scale validity of a two Higgs doublet scenario: metastability included*, *Eur. Phys. J.* **C77** (2017), no. 3 153, [[arXiv:1603.0588](#)].
- [161] P. Ferreira, H. E. Haber, and E. Santos, *Preserving the validity of the Two-Higgs Doublet Model up to the Planck scale*, *Phys. Rev.* **D92** (2015) 033003, [[arXiv:1505.0400](#)].
- [162] E. R. Santos, *Renormalization Group Constraints on the Two-Higgs Doublet Model*. PhD thesis, UC, Santa Cruz, 2015.
- [163] S. Kanemura, T. Kasai, and Y. Okada, *Mass bounds of the lightest cp-even higgs boson in the two-higgs-doublet model*, *Physics Letters B* **471** (1999), no. 23 182 – 190.
- [164] D. Das and I. Saha, *Search for a stable alignment limit in two-Higgs-doublet models*, *Phys. Rev.* **D91** (2015), no. 9 095024, [[arXiv:1503.0213](#)].
- [165] O. Eberhardt, *Fitting the Two-Higgs-Doublet model of type II*, in *Proceedings, 49th Rencontres de Moriond on Electroweak Interactions and Unified Theories*, pp. 523–526, 2014. [arXiv:1405.3181](#).
- [166] N. Chakrabarty, D. K. Ghosh, B. Mukhopadhyaya, and I. Saha, *Dark matter, neutrino masses and high scale validity of an inert Higgs doublet model*, *Phys. Rev.* **D92** (2015), no. 1 015002, [[arXiv:1501.0370](#)].

- [167] V. Branchina and E. Messina, *Stability, Higgs Boson Mass and New Physics*, *Phys. Rev. Lett.* **111** (2013) 241801, [[arXiv:1307.5193](#)].
- [168] V. Branchina, E. Messina, and M. Sher, *Lifetime of the electroweak vacuum and sensitivity to planck scale physics*, *Phys. Rev. D* **91** (Jan, 2015) 013003.
- [169] N. Khan and S. Rakshit, *Constraints on inert dark matter from the metastability of the electroweak vacuum*, *Phys. Rev.* **D92** (2015) 055006, [[arXiv:1503.0308](#)].
- [170] N. G. Deshpande and E. Ma, *Pattern of Symmetry Breaking with Two Higgs Doublets*, *Phys. Rev.* **D18** (1978) 2574.
- [171] I. Chakraborty and A. Kundu, *Scalar potential of two-Higgs doublet models*, *Phys. Rev.* **D92** (2015), no. 9 095023, [[arXiv:1508.0070](#)].
- [172] S. Coleman and E. Weinberg, *Radiative corrections as the origin of spontaneous symmetry breaking*, *Phys. Rev. D* **7** (Mar, 1973) 1888–1910.
- [173] J. S. Lee and A. Pilaftsis, *Radiative Corrections to Scalar Masses and Mixing in a Scale Invariant Two Higgs Doublet Model*, *Phys. Rev.* **D86** (2012) 035004, [[arXiv:1201.4891](#)].
- [174] J. Bernon, J. F. Gunion, H. E. Haber, Y. Jiang, and S. Kraml, *Scrutinizing the alignment limit in two-Higgs-doublet models: $m_h=125\text{GeV}$* , *Phys. Rev.* **D92** (2015), no. 7 075004, [[arXiv:1507.0093](#)].
- [175] J. Bernon, J. F. Gunion, H. E. Haber, Y. Jiang, and S. Kraml, *Scrutinizing the alignment limit in two-Higgs-doublet models. II. $m_H=125\text{GeV}$* , *Phys. Rev.* **D93** (2016), no. 3 035027, [[arXiv:1511.0368](#)].
- [176] K. Cheung, J. S. Lee, and P.-Y. Tseng, *Higgscision in the Two-Higgs Doublet Models*, *JHEP* **01** (2014) 085, [[arXiv:1310.3937](#)].
- [177] M. A. Shifman, A. I. Vainshtein, M. B. Voloshin, and V. I. Zakharov, *Low-Energy Theorems for Higgs Boson Couplings to Photons*, *Sov. J. Nucl. Phys.* **30** (1979) 711–716. [*Yad. Fiz.*30,1368(1979)].
- [178] H. Baer, M. Bisset, C. Kao, and X. Tata, *Observability of $\gamma\gamma$ decays of higgs bosons from supersymmetry at hadron supercolliders*, *Phys. Rev. D* **46** (Aug, 1992) 1067–1075.

- [179] P. Kalyniak, R. Bates, and J. N. Ng, *Two-photon decays of scalar and pseudoscalar bosons in supersymmetry*, *Phys. Rev. D* **33** (Feb, 1986) 755–762.
- [180] **ATLAS** Collaboration, G. Aad *et. al.*, *Measurement of Higgs boson production in the diphoton decay channel in pp collisions at center-of-mass energies of 7 and 8 TeV with the ATLAS detector*, *Phys. Rev.* **D90** (2014), no. 11 112015, [[arXiv:1408.7084](#)].
- [181] N. Chakrabarty and B. Mukhopadhyaya, *High-scale validity of a two Higgs doublet scenario: predicting collider signals*, [arXiv:1702.0826](#).
- [182] J. Baglio, O. Eberhardt, U. Nierste, and M. Wiebusch, *Benchmarks for higgs boson pair production and heavy higgs boson searches in the two-higgs-doublet model of type ii*, *Phys. Rev. D* **90** (Jul, 2014) 015008.
- [183] V. Keus, S. F. King, S. Moretti, and K. Yagyu, *Cp violating two-higgs-doublet model: constraints and lhc predictions*, *Journal of High Energy Physics* **2016** (2016), no. 4 48.
- [184] S. Kanemura, H. Yokoya, and Y.-J. Zheng, *Complementarity in direct searches for additional higgs bosons at the {LHC} and the international linear collider*, *Nuclear Physics B* **886** (2014) 524 – 553.
- [185] D. Gonçalves and D. López-Val, *Pseudoscalar searches with dileptonic tops and jet substructure*, *Phys. Rev. D* **94** (Nov, 2016) 095005.
- [186] R. Patrick, P. Sharma, and A. G. Williams, *Exploring a heavy charged Higgs using jet substructure in a fully hadronic channel*, *Nucl. Phys.* **B917** (2017) 19–30, [[arXiv:1610.0591](#)].
- [187] J. Li, R. Patrick, P. Sharma, and A. G. Williams, *Boosting the charged Higgs search prospects using jet substructure at the LHC*, *JHEP* **11** (2016) 164, [[arXiv:1609.0264](#)].
- [188] A. Arhrib, R. Benbrik, S. J. D. King, B. Manaut, S. Moretti, and C. S. Un, *Phenomenology of 2HDM with VLQs*, [arXiv:1607.0851](#).
- [189] A. G. Akeroyd *et. al.*, *Prospects for charged Higgs searches at the LHC*, [arXiv:1607.0132](#).
- [190] D. Lopez-Val and J. Sola, *Neutral Higgs-pair production at Linear Colliders within the general 2HDM: Quantum effects and triple Higgs boson self-interactions*, *Phys. Rev.* **D81** (2010) 033003, [[arXiv:0908.2898](#)].

- [191] V. Barger, L. L. Everett, H. E. Logan, and G. Shaughnessy, *Scrutinizing the 125 gev higgs boson in two higgs doublet models at the lhc, ilc, and muon collider*, *Phys. Rev. D* **88** (Dec, 2013) 115003.
- [192] C. S. Kim, Y. W. Yoon, and X.-B. Yuan, *Exploring top quark fcnc within 2hdm type iii in association with flavor physics*, *Journal of High Energy Physics* **2015** (2015), no. 12 1–30.
- [193] A. Crivellin, A. Kokulu, and C. Greub, *Flavor-phenomenology of two-Higgs-doublet models with generic Yukawa structure*, *Phys. Rev.* **D87** (2013), no. 9 094031, [[arXiv:1303.5877](#)].
- [194] I. Baum, G. Eilam, and S. Bar-Shalom, *Scalar flavor changing neutral currents and rare top quark decays in a two Higgs doublet model 'for the top quark'*, *Phys. Rev.* **D77** (2008) 113008, [[arXiv:0802.2622](#)].
- [195] G. Cvetič, S. S. Hwang, and C. S. Kim, *Higgs-mediated flavor-changing neutral currents in the general framework with two higgs doublets: An rge analysis*, *Phys. Rev. D* **58** (Oct, 1998) 116003.
- [196] S. Kanemura and K. Yagyu, *Unitarity bound in the most general two Higgs doublet model*, *Phys. Lett.* **B751** (2015) 289–296, [[arXiv:1509.0606](#)].
- [197] B. Grinstein, C. W. Murphy, and P. Uttayarat, *One-loop corrections to the perturbative unitarity bounds in the CP-conserving two-Higgs doublet model with a softly broken \mathbb{Z}_2 symmetry*, *JHEP* **06** (2016) 070, [[arXiv:1512.0456](#)].
- [198] V. Cacchio, D. Chowdhury, O. Eberhardt, and C. W. Murphy, *Next-to-leading order unitarity fits in Two-Higgs-Doublet models with soft \mathbb{Z}_2 breaking*, *JHEP* **11** (2016) 026, [[arXiv:1609.0129](#)].
- [199] N. G. Deshpande and E. Ma, *Pattern of symmetry breaking with two higgs doublets*, *Phys. Rev. D* **18** (Oct, 1978) 2574–2576.
- [200] S. Nie and M. Sher, *Vacuum stability bounds in the two-higgs doublet model*, *Physics Letters B* **449** (1999), no. 12 89 – 92.
- [201] **Particle Data Group** Collaboration, C. Patrignani *et. al.*, *Review of Particle Physics*, *Chin. Phys.* **C40** (2016), no. 10 100001.

- [202] V. Barger, L. L. Everett, C. B. Jackson, A. D. Peterson, and G. Shaughnessy, *Measuring the two-higgs doublet model scalar potential at lhc14*, *Phys. Rev. D* **90** (Nov, 2014) 095006.
- [203] P. S. Bhupal Dev and A. Pilaftsis, *Maximally Symmetric Two Higgs Doublet Model with Natural Standard Model Alignment*, *JHEP* **12** (2014) 024, [[arXiv:1408.3405](#)]. [Erratum: *JHEP*11,147(2015)].
- [204] A. Alloul, N. D. Christensen, C. Degrande, C. Duhr, and B. Fuks, *Feynrules 2.0 a complete toolbox for tree-level phenomenology*, *Computer Physics Communications* **185** (2014), no. 8 2250 – 2300.
- [205] J. Alwall, R. Frederix, S. Frixione, V. Hirschi, F. Maltoni, O. Mattelaer, H. S. Shao, T. Stelzer, P. Torrielli, and M. Zaro, *The automated computation of tree-level and next-to-leading order differential cross sections, and their matching to parton shower simulations*, *JHEP* **07** (2014) 079, [[arXiv:1405.0301](#)].
- [206] T. Sjöstrand, S. Mrenna, and P. Skands, *Pythia 6.4 physics and manual*, *Journal of High Energy Physics* **2006** (2006), no. 05 026.
- [207] J. de Favereau, C. Delaere, P. Demin, A. Giammanco, V. Lemaître, A. Mertens, and M. Selvaggi, *Delphes 3: a modular framework for fast simulation of a generic collider experiment*, *Journal of High Energy Physics* **2014** (2014), no. 2 57.
- [208] **ATLAS** Collaboration, G. Aad *et. al.*, *Search for an additional, heavy Higgs boson in the $H \rightarrow ZZ$ decay channel at $\sqrt{s} = 8$ TeV in pp collision data with the ATLAS detector*, *Eur. Phys. J.* **C76** (2016), no. 1 45, [[arXiv:1507.0593](#)].
- [209] T. Han, *Collider phenomenology: Basic knowledge and techniques*, in *Physics in D $\dot{=} 4$. Proceedings, Theoretical Advanced Study Institute in elementary particle physics, TASI 2004, Boulder, USA, June 6-July 2, 2004*, pp. 407–454, 2005. [hep-ph/0508097](#).
- [210] M. Perelstein, *Introduction to Collider Physics*, in *Physics of the large and the small, TASI 09, proceedings of the Theoretical Advanced Study Institute in Elementary Particle Physics, Boulder, Colorado, USA, 1-26 June 2009*, pp. 421–486, 2011. [arXiv:1002.0274](#).
- [211] D. Zeppenfeld, *Collider physics*, in *Neutrinos in physics and astrophysics from 10^{*-33} to 10^{*28} CM. Proceedings, Conference, TASI'98, Boulder, USA, June 1-26, 1998*, pp. 303–350, 1999. [hep-ph/9902307](#).

- [212] **CMS** Collaboration, V. Khachatryan *et. al.*, *Search for a pseudoscalar boson decaying into a Z boson and the 125 GeV Higgs boson in $^+b\bar{b}$ final states*, *Phys. Lett.* **B748** (2015) 221–243, [[arXiv:1504.0471](#)].
- [213] R. N. Hodgkinson, D. Lopez-Val, and J. Sola, *Higgs boson pair production through gauge boson fusion at linear colliders within the general 2HDM*, *Phys. Lett.* **B673** (2009) 47–56, [[arXiv:0901.2257](#)].
- [214] H. Abramowicz *et. al.*, *The International Linear Collider Technical Design Report - Volume 4: Detectors*, [arXiv:1306.6329](#).
- [215] N. Chakrabarty, T. Han, Z. Liu, and B. Mukhopadhyaya, *Radiative return for heavy higgs boson at a muon collider*, *Phys. Rev. D* **91** (Jan, 2015) 015008.
- [216] F. Zwicky, *Die Rotverschiebung von extragalaktischen Nebeln*, *Helv. Phys. Acta* **6** (1933) 110–127. [Gen. Rel. Grav.41,207(2009)].
- [217] **Planck** Collaboration, P. A. R. Ade *et. al.*, *Planck 2013 results. I. Overview of products and scientific results*, *Astron. Astrophys.* **571** (2014) A1, [[arXiv:1303.5062](#)].
- [218] **Planck** Collaboration, P. A. R. Ade *et. al.*, *Planck 2015 results. XIII. Cosmological parameters*, *Astron. Astrophys.* **594** (2016) A13, [[arXiv:1502.0158](#)].
- [219] A. Liddle, *An introduction to modern cosmology*. 2009.
- [220] A. A. Penzias and R. W. Wilson, *A Measurement of excess antenna temperature at 4080-Mc/s*, *Astrophys. J.* **142** (1965) 419–421.
- [221] M. J. White, *Anisotropies in the CMB*, in *American Physical Society (APS) Meeting of the Division of Particles and Fields (DPF 99) Los Angeles, California, January 5-9, 1999*, 1999. [astro-ph/9903232](#).
- [222] M. Milgrom, *A Modification of the Newtonian dynamics as a possible alternative to the hidden mass hypothesis*, *Astrophys. J.* **270** (1983) 365–370.
- [223] D. A. Schwartz, *The Development and scientific impact of the Chandra X-ray Observatory*, *Int. J. Mod. Phys.* **D13** (2004) 1239–1248, [[astro-ph/0402275](#)].
- [224] M. Markevitch, A. H. Gonzalez, D. Clowe, A. Vikhlinin, L. David, W. Forman, C. Jones, S. Murray, and W. Tucker, *Direct constraints on the dark matter*

- self-interaction cross-section from the merging galaxy cluster 1E0657-56*, *Astrophys. J.* **606** (2004) 819–824, [[astro-ph/0309303](#)].
- [225] D. Clowe, M. Bradac, A. H. Gonzalez, M. Markevitch, S. W. Randall, C. Jones, and D. Zaritsky, *A direct empirical proof of the existence of dark matter*, *Astrophys. J.* **648** (2006) L109–L113, [[astro-ph/0608407](#)].
- [226] J. A. Tyson, G. P. Kochanski, and I. P. Dell’Antonio, *Detailed mass map of CL0024+1654 from strong lensing*, *Astrophys. J.* **498** (1998) L107, [[astro-ph/9801193](#)].
- [227] E. L. Wright, *Theoretical overview of cosmic microwave background anisotropy*, in *Measuring and modeling the universe. Proceedings, Symposium, Pasadena, USA, November 17-22, 2002*, pp. 291–308, 2003. [astro-ph/0305591](#).
- [228] R. Durrer, *The theory of CMB anisotropies*, *J. Phys. Stud.* **5** (2001) 177–215, [[astro-ph/0109522](#)].
- [229] **WMAP** Collaboration, D. N. Spergel *et. al.*, *Wilkinson Microwave Anisotropy Probe (WMAP) three year results: implications for cosmology*, *Astrophys. J. Suppl.* **170** (2007) 377, [[astro-ph/0603449](#)].
- [230] E. Komatsu, K. M. Smith, J. Dunkley, C. L. Bennett, B. Gold, G. Hinshaw, N. Jarosik, D. Larson, M. R. Nolta, L. Page, D. N. Spergel, M. Halpern, R. S. Hill, A. Kogut, M. Limon, S. S. Meyer, N. Odegard, G. S. Tucker, J. L. Weiland, E. Wollack, and E. L. Wright, *Seven-year wilkinson microwave anisotropy probe (wmap) observations: Cosmological interpretation*, *The Astrophysical Journal Supplement Series* **192** (2011), no. 2 18.
- [231] G. Hinshaw, D. Larson, E. Komatsu, D. N. Spergel, C. L. Bennett, J. Dunkley, M. R. Nolta, M. Halpern, R. S. Hill, N. Odegard, L. Page, K. M. Smith, J. L. Weiland, B. Gold, N. Jarosik, A. Kogut, M. Limon, S. S. Meyer, G. S. Tucker, E. Wollack, and E. L. Wright, *Nine-year wilkinson microwave anisotropy probe (wmap) observations: Cosmological parameter results*, *The Astrophysical Journal Supplement Series* **208** (2013), no. 2 19.
- [232] E. W. Otten and C. Weinheimer, *Neutrino mass limit from tritium beta decay*, *Rept. Prog. Phys.* **71** (2008) 086201, [[arXiv:0909.2104](#)].

- [233] S. Tremaine and J. E. Gunn, *Dynamical Role of Light Neutral Leptons in Cosmology*, *Phys. Rev. Lett.* **42** (1979) 407–410.
- [234] H. Okada, Y. Orikasa, and T. Toma, *Nonthermal dark matter models and signals*, *Phys. Rev.* **D93** (2016), no. 5 055007, [[arXiv:1511.0101](#)].
- [235] E. W. Kolb, D. J. H. Chung, and A. Riotto, *WIMPzillas!*, in *Trends in theoretical physics II. Proceedings, 2nd La Plata Meeting, Buenos Aires, Argentina, November 29-December 4, 1998*, pp. 91–105, 1998. [hep-ph/9810361](#). [,91(1998)].
- [236] A. Dar, *Dark matter and big bang nucleosynthesis*, *Astrophys. J.* **449** (1995) 550, [[astro-ph/9504082](#)]. [,21(1995)].
- [237] K. Jedamzik and M. Pospelov, *Big Bang Nucleosynthesis and Particle Dark Matter*, *New J. Phys.* **11** (2009) 105028, [[arXiv:0906.2087](#)].
- [238] B. J. Carr, *Baryonic dark matter*, *Ann. Rev. Astron. Astrophys.* **32** (1994) 531–590.
- [239] J. Silk *et. al.*, *Particle Dark Matter: Observations, Models and Searches*. Cambridge Univ. Press, Cambridge, 2010.
- [240] G. Bertone, D. Hooper, and J. Silk, *Particle dark matter: Evidence, candidates and constraints*, *Phys. Rept.* **405** (2005) 279–390, [[hep-ph/0404175](#)].
- [241] R. K. Schaefer, Q. Shafi, and F. W. Stecker, *Large Scale Structure Formation and Cosmic Microwave Anisotropy in a Cold Plus Hot Dark Matter Universe*, *Astrophys. J.* **347** (1989) 575.
- [242] S. F. King and A. Merle, *Warm Dark Matter from keVins*, *JCAP* **1208** (2012) 016, [[arXiv:1205.0551](#)].
- [243] M. Drees, R. Godbole, and P. Roy, *Theory and phenomenology of sparticles: An account of four-dimensional $N=1$ supersymmetry in high energy physics*. 2004.
- [244] H. Baer and X. Tata, *Weak Scale Supersymmetry: From Superfields to Scattering Events*. Cambridge University Press, 2006.
- [245] L. Calibbi, J. M. Lindert, T. Ota, and Y. Takanishi, *Cornering light Neutralino Dark Matter at the LHC*, *JHEP* **10** (2013) 132, [[arXiv:1307.4119](#)].

- [246] G. Blanger, G. Drieu La Rochelle, B. Dumont, R. M. Godbole, S. Kraml, and S. Kulkarni, *LHC constraints on light neutralino dark matter in the MSSM*, *Phys. Lett.* **B726** (2013) 773–780, [[arXiv:1308.3735](#)].
- [247] T. Han, Z. Liu, and S. Su, *Light Neutralino Dark Matter: Direct/Indirect Detection and Collider Searches*, *JHEP* **08** (2014) 093, [[arXiv:1406.1181](#)].
- [248] M. Low and L.-T. Wang, *Neutralino dark matter at 14 TeV and 100 TeV*, *JHEP* **08** (2014) 161, [[arXiv:1404.0682](#)].
- [249] J. L. Feng, S.-f. Su, and F. Takayama, *SuperWIMP gravitino dark matter from slepton and sneutrino decays*, *Phys. Rev.* **D70** (2004) 063514, [[hep-ph/0404198](#)].
- [250] G. Arcadi, L. Covi, and M. Nardecchia, *Gravitino Dark Matter and low-scale Baryogenesis*, *Phys. Rev.* **D92** (2015), no. 11 115006, [[arXiv:1507.0558](#)].
- [251] F. D. Steffen, *Gravitino dark matter and cosmological constraints*, *JCAP* **0609** (2006) 001, [[hep-ph/0605306](#)].
- [252] S. Khalil, H. Okada, and T. Toma, *Right-handed Sneutrino Dark Matter in Supersymmetric B-L Model*, *JHEP* **07** (2011) 026, [[arXiv:1102.4249](#)].
- [253] A. Chatterjee, D. Das, B. Mukhopadhyaya, and S. K. Rai, *Right Sneutrino Dark Matter and a Monochromatic Photon Line*, *JCAP* **1407** (2014) 023, [[arXiv:1401.2527](#)].
- [254] D. G. Cerdeno and O. Seto, *Right-handed sneutrino dark matter in the NMSSM*, *JCAP* **0908** (2009) 032, [[arXiv:0903.4677](#)].
- [255] T. Appelquist, H.-C. Cheng, and B. A. Dobrescu, *Bounds on universal extra dimensions*, *Phys. Rev.* **D64** (2001) 035002, [[hep-ph/0012100](#)].
- [256] G. Servant and T. M. P. Tait, *Is the lightest Kaluza-Klein particle a viable dark matter candidate?*, *Nucl. Phys.* **B650** (2003) 391–419, [[hep-ph/0206071](#)].
- [257] K. Kong and K. T. Matchev, *Precise calculation of the relic density of Kaluza-Klein dark matter in universal extra dimensions*, *JHEP* **01** (2006) 038, [[hep-ph/0509119](#)].
- [258] M. Kakizaki, S. Matsumoto, Y. Sato, and M. Senami, *Relic abundance of LKP dark matter in UED model including effects of second KK resonances*, *Nucl. Phys.* **B735** (2006) 84–95, [[hep-ph/0508283](#)].

- [259] M. Kakizaki, S. Matsumoto, Y. Sato, and M. Senami, *Significant effects of second KK particles on LKP dark matter physics*, *Phys. Rev.* **D71** (2005) 123522, [[hep-ph/0502059](#)].
- [260] T. Flacke, D. Hooper, and J. March-Russell, *Improved bounds on universal extra dimensions and consequences for LKP dark matter*, *Phys. Rev.* **D73** (2006) 095002, [[hep-ph/0509352](#)]. [Erratum: *Phys. Rev.* **D74**, 019902(2006)].
- [261] F. Burnell and G. D. Kribs, *The Abundance of Kaluza-Klein dark matter with coannihilation*, *Phys. Rev.* **D73** (2006) 015001, [[hep-ph/0509118](#)].
- [262] T. Flacke and D. W. Maybury, *Constraints on UED KK-neutrino dark matter from magnetic dipole moments*, *Int. J. Mod. Phys.* **D16** (2007) 1593–1600, [[hep-ph/0601161](#)].
- [263] S. Arrenberg, L. Baudis, K. Kong, K. T. Matchev, and J. Yoo, *Kaluza-Klein Dark Matter: Direct Detection vis-a-vis LHC*, *Phys. Rev.* **D78** (2008) 056002, [[arXiv:0805.4210](#)].
- [264] G. Belanger, M. Kakizaki, and A. Pukhov, *Dark matter in UED: The Role of the second KK level*, *JCAP* **1102** (2011) 009, [[arXiv:1012.2577](#)].
- [265] S. Arrenberg, L. Baudis, K. Kong, K. T. Matchev, and J. Yoo, *Kaluza-Klein Dark Matter: Direct Detection vis-a-vis LHC (2013 update)*, [arXiv:1307.6581](#).
- [266] R. D. Peccei and H. R. Quinn, *CP Conservation in the Presence of Instantons*, *Phys. Rev. Lett.* **38** (1977) 1440–1443.
- [267] M. S. Turner, *Windows on the Axion*, *Phys. Rept.* **197** (1990) 67–97.
- [268] G. G. Raffelt, *Astrophysical methods to constrain axions and other novel particle phenomena*, *Phys. Rept.* **198** (1990) 1–113.
- [269] L. Visinelli and P. Gondolo, *Dark Matter Axions Revisited*, *Phys. Rev.* **D80** (2009) 035024, [[arXiv:0903.4377](#)].
- [270] P. Sikivie, *Dark matter axions*, *Int. J. Mod. Phys.* **A25** (2010) 554–563, [[arXiv:0909.0949](#)].

- [271] E. Di Valentino, E. Giusarma, M. Lattanzi, O. Mena, A. Melchiorri, and J. Silk, *Cosmological Axion and neutrino mass constraints from Planck 2015 temperature and polarization data*, *Phys. Lett.* **B752** (2016) 182–185, [[arXiv:1507.0866](#)].
- [272] K. S. Jeong, M. Kawasaki, and F. Takahashi, *Axions as Hot and Cold Dark Matter*, *JCAP* **1402** (2014) 046, [[arXiv:1310.1774](#)].
- [273] E. Di Valentino, E. Giusarma, M. Lattanzi, A. Melchiorri, and O. Mena, *Axion cold dark matter: status after Planck and BICEP2*, *Phys. Rev.* **D90** (2014), no. 4 043534, [[arXiv:1405.1860](#)].
- [274] J. McDonald, *Electroweak baryogenesis and dark matter via a gauge singlet scalar*, *Phys. Lett.* **B323** (1994) 339–346.
- [275] L. Lopez Honorez, E. Nezri, J. F. Oliver, and M. H. G. Tytgat, *The Inert Doublet Model: An Archetype for Dark Matter*, *JCAP* **0702** (2007) 028, [[hep-ph/0612275](#)].
- [276] E. W. Kolb and M. S. Turner, *The Early Universe*, *Front. Phys.* **69** (1990) 1–547.
- [277] S. Dodelson, *Modern Cosmology*. Academic Press, Amsterdam, 2003.
- [278] D. Majumdar, *Dark Matter: An Introduction*. Taylor & Francis, 2014.
- [279] P. Gondolo and G. Gelmini, *Cosmic abundances of stable particles: Improved analysis*, *Nucl. Phys.* **B360** (1991) 145–179.
- [280] J. D. Wells, *Annihilation cross-sections for relic densities in the low velocity limit*, [hep-ph/9404219](#).
- [281] K. Griest and D. Seckel, *Three exceptions in the calculation of relic abundances*, *Phys. Rev.* **D43** (1991) 3191–3203.
- [282] T. Plehn, *Yet Another Introduction to Dark Matter*, [arXiv:1705.0198](#).
- [283] **LUX** Collaboration, D. S. Akerib *et. al.*, *First results from the LUX dark matter experiment at the Sanford Underground Research Facility*, *Phys. Rev. Lett.* **112** (2014) 091303, [[arXiv:1310.8214](#)].
- [284] **XENON10** Collaboration, J. Angle *et. al.*, *A search for light dark matter in XENON10 data*, *Phys. Rev. Lett.* **107** (2011) 051301, [[arXiv:1104.3088](#)]. [Erratum: *Phys. Rev. Lett.*110,249901(2013)].

- [285] **XENON100** Collaboration, E. Aprile *et. al.*, *Dark Matter Results from 225 Live Days of XENON100 Data*, *Phys. Rev. Lett.* **109** (2012) 181301, [[arXiv:1207.5988](#)].
- [286] **DAMA** Collaboration, R. Bernabei *et. al.*, *First results from DAMA/LIBRA and the combined results with DAMA/NaI*, *Eur. Phys. J.* **C56** (2008) 333–355, [[arXiv:0804.2741](#)].
- [287] **CoGeNT Collaboration** Collaboration, C. E. Aalseth, P. S. Barbeau, N. S. Bowden, B. Cabrera-Palmer, J. Colaresi, J. I. Collar, S. Dazeley, P. de Lurgio, J. E. Fast, N. Fields, C. H. Greenberg, T. W. Hossbach, M. E. Keillor, J. D. Kephart, M. G. Marino, H. S. Miley, M. L. Miller, J. L. Orrell, D. C. Radford, D. Reyna, O. Tench, T. D. Van Wechel, J. F. Wilkerson, and K. M. Yocum, *Results from a search for light-mass dark matter with a p-type point contact germanium detector*, *Phys. Rev. Lett.* **106** (Mar, 2011) 131301.
- [288] **CDMS** Collaboration, R. Agnese *et. al.*, *Silicon Detector Dark Matter Results from the Final Exposure of CDMS II*, *Phys. Rev. Lett.* **111** (2013), no. 25 251301, [[arXiv:1304.4279](#)].
- [289] J. M. Gaskins, *A review of indirect searches for particle dark matter*, *Contemp. Phys.* **57** (2016), no. 4 496–525, [[arXiv:1604.0001](#)].
- [290] T. Gherghetta, B. von Harling, A. D. Medina, M. A. Schmidt, and T. Trott, *SUSY implications from WIMP annihilation into scalars at the Galactic Center*, *Phys. Rev.* **D91** (2015) 105004, [[arXiv:1502.0717](#)].
- [291] A. Hektor, K. Kannike, and L. Marzola, *Muon $g - 2$ and Galactic Centre γ -ray excess in a scalar extension of the 2HDM type-X*, *JCAP* **1510** (2015), no. 10 025, [[arXiv:1507.0509](#)].
- [292] A. J. Williams, *Explaining the Fermi Galactic Centre Excess in the CMSSM*, [[arXiv:1510.0071](#)].
- [293] K. P. Modak and D. Majumdar, *Confronting Galactic and Extragalactic γ -rays Observed by Fermi-lat With Annihilating Dark Matter in an Inert Higgs Doublet Model*, *Astrophys. J. Suppl.* **219** (2015), no. 2 37, [[arXiv:1502.0568](#)].
- [294] L. Goodenough and D. Hooper, *Possible Evidence For Dark Matter Annihilation In The Inner Milky Way From The Fermi Gamma Ray Space Telescope*, [[arXiv:0910.2998](#)].

- [295] **PAMELA** Collaboration, O. Adriani *et. al.*, *An anomalous positron abundance in cosmic rays with energies 1.5-100 GeV*, *Nature* **458** (2009) 607–609, [[arXiv:0810.4995](#)].
- [296] **AMS** Collaboration, M. Aguilar *et. al.*, *First Result from the Alpha Magnetic Spectrometer on the International Space Station: Precision Measurement of the Positron Fraction in Primary Cosmic Rays of 0.5350 GeV*, *Phys. Rev. Lett.* **110** (2013) 141102.
- [297] **ATLAS** Collaboration, M. Aaboud *et. al.*, *Search for dark matter at $\sqrt{s} = 13$ TeV in final states containing an energetic photon and large missing transverse momentum with the ATLAS detector*, [arXiv:1704.0384](#).
- [298] **ATLAS Collaboration** Collaboration, *Search for New Phenomena in Monojet plus Missing Transverse Momentum Final States using 10fb-1 of pp Collisions at $\sqrt{s}=8$ TeV with the ATLAS detector at the LHC*, Tech. Rep. ATLAS-CONF-2012-147, CERN, Geneva, Nov, 2012.
- [299] E. Ma, *Verifiable radiative seesaw mechanism of neutrino mass and dark matter*, *Phys.Rev.* **D73** (2006) 077301, [[hep-ph/0601225](#)].
- [300] R. Barbieri, L. J. Hall, and V. S. Rychkov, *Improved naturalness with a heavy Higgs: An Alternative road to LHC physics*, *Phys.Rev.* **D74** (2006) 015007, [[hep-ph/0603188](#)].
- [301] Q.-H. Cao, E. Ma, and G. Rajasekaran, *Observing the Dark Scalar Doublet and its Impact on the Standard-Model Higgs Boson at Colliders*, *Phys.Rev.* **D76** (2007) 095011, [[arXiv:0708.2939](#)].
- [302] S. Andreas, M. H. Tytgat, and Q. Swillens, *Neutrinos from Inert Doublet Dark Matter*, *JCAP* **0904** (2009) 004, [[arXiv:0901.1750](#)].
- [303] E. Nezri, M. H. Tytgat, and G. Vertongen, *$e+$ and anti- p from inert doublet model dark matter*, *JCAP* **0904** (2009) 014, [[arXiv:0901.2556](#)].
- [304] T. Hambye, F.-S. Ling, L. Lopez Honorez, and J. Rocher, *Scalar Multiplet Dark Matter*, *JHEP* **0907** (2009) 090, [[arXiv:0903.4010](#)].
- [305] L. Lopez Honorez and C. E. Yaguna, *The inert doublet model of dark matter revisited*, *JHEP* **1009** (2010) 046, [[arXiv:1003.3125](#)].

- [306] L. Lopez Honorez and C. E. Yaguna, *A new viable region of the inert doublet model*, *JCAP* **1101** (2011) 002, [[arXiv:1011.1411](#)].
- [307] E. Dolle, X. Miao, S. Su, and B. Thomas, *Dilepton Signals in the Inert Doublet Model*, *Phys.Rev.* **D81** (2010) 035003, [[arXiv:0909.3094](#)].
- [308] X. Miao, S. Su, and B. Thomas, *Trilepton Signals in the Inert Doublet Model*, *Phys.Rev.* **D82** (2010) 035009, [[arXiv:1005.0090](#)].
- [309] A. Arhrib, R. Benbrik, and N. Gaur, *$H \rightarrow \gamma\gamma$ in Inert Higgs Doublet Model*, *Phys.Rev.* **D85** (2012) 095021, [[arXiv:1201.2644](#)].
- [310] M. Gustafsson, S. Rydbeck, L. Lopez-Honorez, and E. Lundstrom, *Status of the Inert Doublet Model and the Role of multileptons at the LHC*, *Phys.Rev.* **D86** (2012) 075019, [[arXiv:1206.6316](#)].
- [311] B. Swiezewska and M. Krawczyk, *Diphoton rate in the inert doublet model with a 125 GeV Higgs boson*, *Phys.Rev.* **D88** (2013), no. 3 035019, [[arXiv:1212.4100](#)].
- [312] A. Goudelis, B. Herrmann, and O. Stl, *Dark matter in the Inert Doublet Model after the discovery of a Higgs-like boson at the LHC*, *JHEP* **1309** (2013) 106, [[arXiv:1303.3010](#)].
- [313] M. Krawczyk, D. Sokolowska, and B. Swiezewska, *Inert Doublet Model with a 125 GeV Higgs*, [arXiv:1304.7757](#).
- [314] M. Krawczyk, D. Sokoowska, P. Swaczyna, and B. wieewska, *Higgs $\rightarrow \gamma\gamma$, $Z\gamma$ in the Inert Doublet Model*, *Acta Phys.Polon.* **B44** (2013), no. 11 2163–2170, [[arXiv:1309.7880](#)].
- [315] A. Arhrib, Y.-L. S. Tsai, Q. Yuan, and T.-C. Yuan, *An Updated Analysis of Inert Higgs Doublet Model in light of the Recent Results from LUX, PLANCK, AMS-02 and LHC*, [arXiv:1310.0358](#).
- [316] A. Arhrib, R. Benbrik, and T.-C. Yuan, *Associated Production of Higgs at Linear Collider in the Inert Higgs Doublet Model*, *Eur.Phys.J.* **C74** (2014) 2892, [[arXiv:1401.6698](#)].
- [317] E. Ma, *Common origin of neutrino mass, dark matter, and baryogenesis*, *Mod.Phys.Lett.* **A21** (2006) 1777–1782, [[hep-ph/0605180](#)].

- [318] L. M. Krauss, S. Nasri, and M. Trodden, *A Model for neutrino masses and dark matter*, *Phys.Rev.* **D67** (2003) 085002, [[hep-ph/0210389](#)].
- [319] J. Kubo, E. Ma, and D. Suematsu, *Cold Dark Matter, Radiative Neutrino Mass, $\mu \rightarrow e\gamma$, and Neutrinoless Double Beta Decay*, *Phys.Lett.* **B642** (2006) 18–23, [[hep-ph/0604114](#)].
- [320] D. Aristizabal Sierra, J. Kubo, D. Restrepo, D. Suematsu, and O. Zapata, *Radiative seesaw: Warm dark matter, collider and lepton flavour violating signals*, *Phys.Rev.* **D79** (2009) 013011, [[arXiv:0808.3340](#)].
- [321] D. Suematsu, T. Toma, and T. Yoshida, *Reconciliation of CDM abundance and $\mu \rightarrow e\gamma$ in a radiative seesaw model*, *Phys.Rev.* **D79** (2009) 093004, [[arXiv:0903.0287](#)].
- [322] D. Suematsu, T. Toma, and T. Yoshida, *Enhancement of the annihilation of dark matter in a radiative seesaw model*, *Phys.Rev.* **D82** (2010) 013012, [[arXiv:1002.3225](#)].
- [323] D. Suematsu, *Thermal Leptogenesis in a TeV Scale Model for Neutrino Masses*, *Eur.Phys.J.* **C72** (2012) 1951, [[arXiv:1103.0857](#)].
- [324] R. Bouchand and A. Merle, *Running of Radiative Neutrino Masses: The Scotogenic Model*, *JHEP* **1207** (2012) 084, [[arXiv:1205.0008](#)].
- [325] S. Kashiwase and D. Suematsu, *Baryon number asymmetry and dark matter in the neutrino mass model with an inert doublet*, *Phys.Rev.* **D86** (2012) 053001, [[arXiv:1207.2594](#)].
- [326] S. Kashiwase and D. Suematsu, *Leptogenesis and dark matter detection in a TeV scale neutrino mass model with inverted mass hierarchy*, *Eur.Phys.J.* **C73** (2013) 2484, [[arXiv:1301.2087](#)].
- [327] T. Toma and A. Vicente, *Lepton Flavor Violation in the Scotogenic Model*, *JHEP* **1401** (2014) 160, [[arXiv:1312.2840](#)].
- [328] H. Davoudiasl and I. M. Lewis, *Right-Handed Neutrinos as the Origin of the Electroweak Scale*, *Phys.Rev.* **D90** (2014), no. 3 033003, [[arXiv:1404.6260](#)].

- [329] M. Fukugita and T. Yanagida, *Baryogenesis Without Grand Unification*, *Phys.Lett.* **B174** (1986) 45.
- [330] A. Pilaftsis, *CP violation and baryogenesis due to heavy Majorana neutrinos*, *Phys.Rev.* **D56** (1997) 5431–5451, [[hep-ph/9707235](#)].
- [331] J. Racker, *Mass bounds for baryogenesis from particle decays and the inert doublet model*, *JCAP* **1403** (2014) 025, [[arXiv:1308.1840](#)].
- [332] E. Lundstrom, M. Gustafsson, and J. Edsjo, *The Inert Doublet Model and LEP II Limits*, *Phys.Rev.* **D79** (2009) 035013, [[arXiv:0810.3924](#)].
- [333] A. Pierce and J. Thaler, *Natural Dark Matter from an Unnatural Higgs Boson and New Colored Particles at the TeV Scale*, *JHEP* **0708** (2007) 026, [[hep-ph/0703056](#)].
- [334] J. R. Ellis, M. K. Gaillard, and D. V. Nanopoulos, *A Phenomenological Profile of the Higgs Boson*, *Nucl.Phys.* **B106** (1976) 292.
- [335] R. Cahn, M. S. Chanowitz, and N. Fleishon, *Higgs Particle Production by $Z \rightarrow H\gamma$* , *Phys.Lett.* **B82** (1979) 113.
- [336] L. Bergstrom and G. Hulth, *Induced Higgs Couplings to Neutral Bosons in e^+e^- Collisions*, *Nucl.Phys.* **B259** (1985) 137.
- [337] A. Djouadi, *The Anatomy of electro-weak symmetry breaking. II. The Higgs bosons in the minimal supersymmetric model*, *Phys.Rept.* **459** (2008) 1–241, [[hep-ph/0503173](#)].
- [338] **CMS** Collaboration, V. Khachatryan *et. al.*, *Observation of the diphoton decay of the Higgs boson and measurement of its properties*, *Eur.Phys.J.* **C74** (2014), no. 10 3076, [[arXiv:1407.0558](#)].
- [339] **Planck** Collaboration, P. A. R. Ade *et. al.*, *Planck 2013 results. XVI. Cosmological parameters*, *Astron. Astrophys.* **571** (2014) A16, [[arXiv:1303.5076](#)].
- [340] K. Cheung, J. S. Lee, and P.-Y. Tseng, *Higgs precision analysis updates 2014*, *Phys.Rev.* **D90** (2014), no. 9 095009, [[arXiv:1407.8236](#)].
- [341] G. Belanger, F. Boudjema, A. Pukhov, and A. Semenov, *micrOMEGAs_3 : A program for calculating dark matter observables*, *Comput.Phys.Commun.* **185** (2014) 960–985, [[arXiv:1305.0237](#)].

- [342] CMS Collaboration, S. Chatrchyan *et. al.*, *Observation of a new boson at a mass of 125 GeV with the CMS experiment at the LHC*, *Phys. Lett.* **B716** (2012) 30–61, [[arXiv:1207.7235](#)].
- [343] N. Chakrabarty, *High-scale validity of a model with Three-Higgs-doublets*, *Phys. Rev.* **D93** (2016), no. 7 075025, [[arXiv:1511.0813](#)].
- [344] A. Aranda, C. Bonilla, and J. L. Diaz-Cruz, *Three generations of Higgses and the cyclic groups*, *Phys. Lett.* **B717** (2012) 248–251, [[arXiv:1204.5558](#)].
- [345] S. Moretti, D. Rojas, and K. Yagyu, *Enhancement of the $H^\pm W^\mp Z$ vertex in the three scalar doublet model*, *JHEP* **08** (2015) 116, [[arXiv:1504.0643](#)].
- [346] I. P. Ivanov and E. Vdovin, *Discrete symmetries in the three-Higgs-doublet model*, *Phys. Rev.* **D86** (2012) 095030, [[arXiv:1206.7108](#)].
- [347] M. Maniatis, D. Mehta, and C. M. Reyes, *Stability and symmetry breaking in a three-Higgs-doublet model with lepton family symmetry $O(2)\mathbb{Z}_2$* , *Phys. Rev.* **D92** (2015), no. 3 035017, [[arXiv:1503.0594](#)].
- [348] S. Moretti and K. Yagyu, *Constraints on Parameter Space from Perturbative Unitarity in Models with Three Scalar Doublets*, *Phys. Rev.* **D91** (2015) 055022, [[arXiv:1501.0654](#)].
- [349] S. Pramanick and A. Raychaudhuri, *A_4 -based seesaw model for realistic neutrino masses and mixing*, *Phys. Rev.* **D93** (2016), no. 3 033007, [[arXiv:1508.0233](#)].
- [350] V. Keus, S. F. King, S. Moretti, and D. Sokolowska, *Observable Heavy Higgs Dark Matter*, *JHEP* **11** (2015) 003, [[arXiv:1507.0843](#)].
- [351] V. Keus, S. F. King, S. Moretti, and D. Sokolowska, *Dark Matter with Two Inert Doublets plus One Higgs Doublet*, *JHEP* **11** (2014) 016, [[arXiv:1407.7859](#)].
- [352] V. Keus, S. F. King, and S. Moretti, *Three-Higgs-doublet models: symmetries, potentials and Higgs boson masses*, *JHEP* **01** (2014) 052, [[arXiv:1310.8253](#)].
- [353] I. de Medeiros Varzielas, O. Fischer, and V. Maurer, *A_4 symmetry at colliders and in the universe*, *JHEP* **08** (2015) 080, [[arXiv:1504.0395](#)].
- [354] G. Bhattacharyya, P. Leser, and H. Pas, *Novel signatures of the Higgs sector from S_3 flavor symmetry*, *Phys. Rev.* **D86** (2012) 036009, [[arXiv:1206.4202](#)].

- [355] G. Bhattacharyya, P. Leser, and H. Pas, *Exotic Higgs boson decay modes as a harbinger of S_3 flavor symmetry*, *Phys. Rev.* **D83** (2011) 011701, [[arXiv:1006.5597](#)].
- [356] E. Barradas-Guevara, O. Flix-Beltrn, and E. Rodriguez-Juregui, *Trilinear self-couplings in an $S(3)$ flavored Higgs model*, *Phys. Rev.* **D90** (2014), no. 9 095001, [[arXiv:1402.2244](#)].
- [357] J. Kubo, H. Okada, and F. Sakamaki, *Higgs potential in minimal $S(3)$ invariant extension of the standard model*, *Phys. Rev.* **D70** (2004) 036007, [[hep-ph/0402089](#)].
- [358] Y. Koide, *Permutation symmetry $S(3)$ and VEV structure of flavor-triplet Higgs scalars*, *Phys. Rev.* **D73** (2006) 057901, [[hep-ph/0509214](#)].
- [359] A. C. B. Machado and V. Pleitez, *A model with two inert scalar doublets*, *Annals Phys.* **364** (2016) 53–67, [[arXiv:1205.0995](#)].
- [360] P. F. Harrison and W. G. Scott, *Permutation symmetry, tri - bimaximal neutrino mixing and the $S3$ group characters*, *Phys. Lett.* **B557** (2003) 76, [[hep-ph/0302025](#)].
- [361] J. Kubo, A. Mondragon, M. Mondragon, and E. Rodriguez-Jauregui, *The Flavor symmetry*, *Prog. Theor. Phys.* **109** (2003) 795–807, [[hep-ph/0302196](#)]. [Erratum: *Prog. Theor. Phys.*114,287(2005)].
- [362] T. Teshima, *Flavor mass and mixing and $S(3)$ symmetry: An $S(3)$ invariant model reasonable to all*, *Phys. Rev.* **D73** (2006) 045019, [[hep-ph/0509094](#)].
- [363] Y. Koide, *$S(3)$ symmetry and neutrino masses and mixings*, *Eur. Phys. J.* **C50** (2007) 809–816, [[hep-ph/0612058](#)].
- [364] S.-L. Chen, M. Frigerio, and E. Ma, *Large neutrino mixing and normal mass hierarchy: A Discrete understanding*, *Phys. Rev.* **D70** (2004) 073008, [[hep-ph/0404084](#)]. [Erratum: *Phys. Rev.*D70,079905(2004)].
- [365] A. Mondragon, M. Mondragon, and E. Peinado, *Lepton masses, mixings and FCNC in a minimal $S(3)$ -invariant extension of the Standard Model*, *Phys. Rev.* **D76** (2007) 076003, [[arXiv:0706.0354](#)].
- [366] E. C. F. S. Fortes, A. C. B. Machado, J. Montao, and V. Pleitez, *Scalar dark matter candidates in a two inert Higgs doublet model*, *J. Phys.* **G42** (2015), no. 10 105003, [[arXiv:1407.4749](#)].

- [367] A. Aranda, C. Bonilla, F. de Anda, A. Delgado, and J. Hernandez-Sanchez, *Higgs decay into two photons from a 3HDM with flavor symmetry*, *Phys. Lett.* **B725** (2013) 97–100, [[arXiv:1302.1060](#)].
- [368] I. P. Ivanov and C. C. Nishi, *Symmetry breaking patterns in 3HDM*, *JHEP* **01** (2015) 021, [[arXiv:1410.6139](#)].
- [369] A. P. Serebrov *et. al.*, *New measurements of the neutron electric dipole moment*, *JETP Lett.* **99** (2014) 4–8, [[arXiv:1310.5588](#)].
- [370] D. Das and U. K. Dey, *Analysis of an extended scalar sector with S_3 symmetry*, *Phys. Rev.* **D89** (2014), no. 9 095025, [[arXiv:1404.2491](#)]. [Erratum: *Phys. Rev.* **D91**, no. 3, 039905 (2015)].
- [371] **OPAL, DELPHI, L3, ALEPH, LEP Higgs Working Group for Higgs boson searches** Collaboration, *Search for charged Higgs bosons: Preliminary combined results using LEP data collected at energies up to 209-GeV*, in *Lepton and photon interactions at high energies. Proceedings, 20th International Symposium, LP 2001, Rome, Italy, July 23-28, 2001*, 2001. [hep-ex/0107031](#).
- [372] D. Das, U. K. Dey, and P. B. Pal, *S_3 symmetry and the quark mixing matrix*, *Phys. Lett.* **B753** (2016) 315–318, [[arXiv:1507.0650](#)].
- [373] F. Gonzalez Canales, A. Mondragn, M. Mondragn, U. J. Saldaa Salazar, and L. Velasco-Sevilla, *Quark sector of S_3 models: classification and comparison with experimental data*, *Phys. Rev.* **D88** (2013) 096004, [[arXiv:1304.6644](#)].
- [374] E. Ma and B. Melic, *Updated S_3 model of quarks*, *Phys. Lett.* **B725** (2013) 402–406, [[arXiv:1303.6928](#)].
- [375] T. Teshima and Y. Okumura, *Quark/lepton mass and mixing in S_3 invariant model and CP-violation of neutrino*, *Phys. Rev.* **D84** (2011) 016003, [[arXiv:1103.6127](#)].
- [376] M. Baak and R. Kogler, *The global electroweak Standard Model fit after the Higgs discovery*, in *Proceedings, 48th Rencontres de Moriond on Electroweak Interactions and Unified Theories: La Thuile, Italy, March 2-9, 2013*, pp. 349–358, 2013. [arXiv:1306.0571](#). [,45(2013)].
- [377] **CMS** Collaboration, V. Khachatryan *et. al.*, *Precise determination of the mass of the Higgs boson and tests of compatibility of its couplings with the standard model*

- predictions using proton collisions at 7 and 8 TeV*, *Eur. Phys. J.* **C75** (2015), no. 5 212, [[arXiv:1412.8662](#)].
- [378] S. Pakvasa and H. Sugawara, *Discrete Symmetry and Cabibbo Angle*, *Phys. Lett.* **B73** (1978) 61–64.
- [379] A. Ahriche, G. Faisel, S.-Y. Ho, S. Nasri, and J. Tandean, *Effects of two inert scalar doublets on Higgs boson interactions and the electroweak phase transition*, *Phys. Rev.* **D92** (2015), no. 3 035020, [[arXiv:1501.0660](#)].